

SLOW AND STORED LIGHT UNDER CONDITIONS OF
ELECTROMAGNETICALLY INDUCED TRANSPARENCY AND
FOUR WAVE MIXING IN AN ATOMIC VAPOR

Nathaniel Blair Phillips

Lancaster, Pennsylvania

Master of Science, College of William and Mary, 2006
Bachelor of Arts, Millersville University, Millersville PA, 2004

A Dissertation presented to the Graduate Faculty
of the College of William and Mary in Candidacy for the Degree of
Doctor of Philosophy

Department of Physics

The College of William and Mary
August 2011

©2011
Nathaniel Blair Phillips
All rights reserved.

APPROVAL PAGE

This Dissertation is submitted in partial fulfillment of
the requirements for the degree of

Doctor of Philosophy

Nathaniel Blair Phillips

Approved by the Committee, June, 2011

Committee Chair

Assistant Professor Irina Novikova, Physics
The College of William and Mary

Assistant Professor Seth Aubin, Physics
The College of William and Mary

Professor John Delos, Physics
The College of William and Mary

Professor Gina Hoatson, Physics
The College of William and Mary

Eminent Professor Mark Havey, Physics
Old Dominion University

ABSTRACT PAGE

The recent prospect of efficient, reliable, and secure quantum communication relies on the ability to coherently and reversibly map nonclassical states of light onto long-lived atomic states. A promising technique that accomplishes this employs Electromagnetically Induced Transparency (EIT), in which a strong classical control field modifies the optical properties of a weak signal field in such a way that a previously opaque medium becomes transparent to the signal field. The accompanying steep dispersion in the index of refraction allows for pulses of light to be decelerated, then stored as an atomic excitation, and later retrieved as a photonic mode. This dissertation presents the results of investigations into methods for optimizing the memory efficiency of this process in an ensemble of hot Rb atoms. We have experimentally demonstrated the effectiveness of two protocols for yielding the best memory efficiency possible at a given atomic density. Improving memory efficiency requires operation at higher optical depths, where undesired effects such as four-wave mixing (FWM) become enhanced and can spontaneously produce a new optical mode (Stokes field). We present the results of experimental and theoretical investigations of the FWM-EIT interaction under continuous-wave (cw), slow light, and stored light conditions. In particular, we provide evidence that indicates that while a Stokes field is generated upon retrieval of the signal field, any information originally encoded in a seeded Stokes field is not independently preserved during the storage process. We present a simple model that describes the propagation dynamics and provides an intuitive description of the EIT-FWM process.

TABLE OF CONTENTS

	Page
Acknowledgments	x
List of Tables	xii
List of Figures	xiii
CHAPTER	
1 Introduction	2
1.1 Optical quantum memory	4
1.2 Electromagnetically induced transparency	5
1.3 Performance criteria for optical quantum memory	8
1.4 Experimental demonstrations of EIT	10
1.5 Progress towards long distance quantum communication using atomic ensembles	12
1.5.1 Experimental demonstration of DLCZ components	15
1.5.2 Towards storage of single photons	16
1.6 Outline of this dissertation	17
2 Review of the theory	19
2.1 Maxwell's Equations	20
2.2 General model of the atomic system	21
2.3 Interaction of a bichromatic electromagnetic field with a three- level Λ system	24

2.4	Electromagnetically Induced Transparency	29
2.4.1	A brief aside on two-level atoms in a resonant laser field . . .	30
2.4.2	Complex refractive index of a three-level Λ system	32
2.5	Dark state description of EIT	34
2.6	Slow light and stored light	35
2.7	Dark state polariton description of stored light	39
2.8	Efficiency of EIT-based storage	42
2.9	The effects of four-wave mixing	43
3	Experimental Arrangements	50
3.1	The atoms	50
3.1.1	Zeeman sub-structure and transitions	53
3.1.2	Vapor cells	55
3.1.3	Neon buffer gas	57
3.1.4	Diffusion time	58
3.1.5	Collisional broadening	60
3.1.6	Doppler broadening	62
3.1.7	Optical pumping	63
3.1.8	Optical depth	65
3.1.9	Rabi frequency of the control field	69
3.2	Experimental description	69
3.3	The light fields	73
3.3.1	Light field modulation	73
3.3.2	Spectral filtering with a temperature-tunable Fabry-Pérot Filter	76
3.3.3	Vapor cell enclosure	79
3.3.4	Light detection	79

3.3.5	Control of AOM and EOM inputs	81
3.3.6	Calibration of AOM and EOM	82
3.3.7	A typical cw (EIT) experiment	84
3.3.8	A typical slow/stored light experiment	86
3.3.9	Measuring spin decay time	89
4	Optimization of memory efficiency	91
4.1	Signal pulse optimization	92
4.2	Control pulse optimization	96
4.3	Dependence of memory efficiency on the optical depth	99
5	Full control over storage and retrieval	106
6	The effects of four-wave mixing on pulse propagation through an EIT medium	114
6.1	Theoretical description of FWM in the steady-state	115
6.2	Spectral Measurements	119
6.3	Slow Light Measurements	122
6.3.1	Case I: $\delta = 2 \Delta_R $	125
6.3.2	Case II: $\delta = 2\delta_s$	126
6.3.3	Case III: $\delta = 0$	126
6.4	FWM under Stored Light conditions	127
6.4.1	Coupled propagation of signal and Stokes fields in a double- Λ system	128
6.4.2	Correspondence between experiment and theory	129
6.4.3	The effect of four-wave mixing on the spin wave	132
6.5	Optical depth dependence of the Stokes field	141
7	Experimental investigations of spin decay mechanisms	144
7.1	Mechanisms that affect the rate of spin decay	145
7.1.1	Diffusion and $2d$ -dependence	145

7.1.2	Collisions	146
7.1.3	Magnetic fields	148
7.2	Experimental evidence for spin decay mechanisms	148
7.2.1	Ω and \mathcal{E}_{in} dependences	148
7.3	Possible physical mechanisms	151
7.3.1	Power broadening	151
7.3.2	Radiation trapping and diffusion effects	151
7.3.3	Transverse AC Stark shifts	154
7.3.4	Two-photon detuning (δ) dependence	155
7.3.5	FWM dependence	158
7.4	Summary and conclusions	161
8	Conclusion and Outlook	162
APPENDIX A		
	Details of control field shaping	165
APPENDIX B		
	Derivation of Eqs. 6.20, 6.21, 6.29, and 6.30	171
	Bibliography	178
	Vita	191

DEDICATION

I present this thesis in honor of my AP physics teacher, Mr. Jeffrey A. Way.

ACKNOWLEDGMENTS

I could not have completed this research without the support and guidance of my advisor, Dr. Irina Novikova. I value the patience with which you taught me how to align (and re-align) optics, and am continuously impressed with your knack for creating clever and compact experiments. In addition, much of this work could not have been completed without our theorist collaborator, the inimitable Dr. Alexey Gorshkov, who developed the optimization protocols and provided essential support for the theoretical modeling of the FWM-EIT interaction. It has been a pleasure to work with my lab colleagues, Nathan, Will, Kevin, Gleb, Matt, Travis, Francesca, Quint, Joe, and Eugeni.

I am forever in debt to my good friend, Mr. Jeff Fuhrman, who fostered my interest in science over many trips to Hershey Park, various volunteer adventures involving technology support at concerts, and vital advice when life wasn't always easy. My interest in science and math stemmed from several awesome teachers that I met in high school. To Dr. Bill Grove, who taught me the importance of memorizing trigonometric values and identities. To my 11th grade Chemistry teacher, Mr. Glen Shaffer, who taught me that I can be a better student if I just studied. To my AP Statistics teacher, Mr. Steve Haldeman, and my AP Calculus teacher, Mr. Mark Rorabaugh, who pushed me to strive for perfection. And especially to my AP Physics teacher and good friend, the late Mr. Jeff Way, who taught me to believe that I was capable of learning something difficult like physics, and whose positive personality inspired many.

I would not be at William and Mary if it weren't for my undergraduate advisor, Dr. Zenaida Uy, who insisted that I apply to at least one graduate school. My life would be incomplete if I had never met Ken, Diane, Jennie, and Trent Keifer, who, with their vast knowledge of all things colonial, suggested that I apply to W&M.

Graduate school isn't always super-fun times. I'd like to thank the people who tried to make it more fun. Thanks to the friends who risked heat stroke to play weekend "touch" football (that is, when they weren't working on their glamour muscles), played 3-on-3-on-3 softball, philosophized about many mock sports, and played (and even occasionally won) intramural soccer, volleyball, softball, and hockey. Thanks to the Thursday-TV club: Stephen, Carla, Chris, Aidan, and sometimes Doug, with whom I've been honored to enjoy a few laughs and a few beers.

Finally, no list of acknowledgments would be complete without my family, who has supported me always. Dad, Mom, Melissa, Jonathan, and Adam—I love you guys (and frankly, I'm impressed that you're reading this). If it were physically

possible, I would to express infinite thanks to my lovely wife and best friend, Kelly, and my two cats, Batman the Cat and the late Gravy, for continuous moral support through this entire process.

LIST OF TABLES

Table		Page
3.1	$^{87}\text{Rb } D_1 (5^2S_{1/2} \rightarrow 5^2P_{1/2})$ Clebsch-Gordan coefficients for σ^+ transitions, $ F = 1, m_F\rangle \rightarrow F', m_{F'} = m_F + 1\rangle$	56
3.2	$^{87}\text{Rb } D_1 (5^2S_{1/2} \rightarrow 5^2P_{1/2})$ Clebsch-Gordan coefficients for σ^+ transitions, $ F = 2, m_F\rangle \rightarrow F', m_{F'} = m_F + 1\rangle$	56

LIST OF FIGURES

Figure	Page
1.1 (a) Three-level Λ system under EIT conditions. (b) Absorption and (c) refractive index seen by the signal field	6
1.2 A schematic of the (a) entanglement creation, and (b) entanglement swapping stages of the DLCZ protocol.	14
2.1 A simple three-level Λ -type atom	24
2.2 Absorption and refraction of the signal field	33
2.3 An illustration of stored light.	37
2.4 The double- Λ system used in theoretical modeling of the FWM interaction with EIT.	44
3.1 ^{87}Rb D_1 hyperfine structure with frequency splitting between the hyperfine energy levels [1].	52
3.2 ^{87}Rb D_1 hyperfine structure and Zeeman substructure with σ^+ light resonant to the $F = 2 \rightarrow F' = 2$ transition.	64
3.3 Optical depth of the ^{87}Rb $F = 1 \rightarrow F' = 2$ ^{87}Rb D_1 transition as a function of temperature.	67
3.4 Contributions to the D_1 transition optical depth from the various m_F sublevels	68
3.5 A schematic of the experimental arrangements. See text for abbreviations.	70

3.6	Saturated absorption spectrum for a vapor cell containing natural abundance Rb under conditions relevant to our experiment.	71
3.7	A diagram of the Fabry-Pérot under filtering operation.	76
3.8	Transmission spectrum of the Fabry-Pérot filter tuned to the signal field frequency.	78
3.9	Sample data from the calibration of the AOM and EOM.	84
3.10	Signal spectra at an optical depth of $2d = 52$ with a beam diameter of 4 mm and $\Omega = (2\pi) 9$ MHz.	85
3.11	The shapes of the control field train and the signal field train sent to the AOM and EOM function generators, respectively, during a typical stored light experiment.	87
3.12	An example trace from the oscilloscope which depicts the raw data obtained during a stored light experiment.	88
3.13	Normalized off-resonant pulse, \mathcal{E}_{in} , the leakage, and the retrieval from storage, \mathcal{E}_{out} during a typical stored light experiment.	89
3.14	Dependence of retrieved signal energies as a function of storage time at $T = 70^\circ\text{C}$ ($\alpha_0 L = 52$)	90
4.1	Experimental and numerical results of iterative signal pulse optimization at $T = 60.5^\circ\text{C}$ ($\alpha_0 L = 24$) using 16 mW constant control field during writing and retrieval with a $\tau = 100 \mu\text{s}$ storage interval	94
4.2	(a) Experimental and theoretical optimized signal pulses obtained after five steps of the iteration procedure for three different powers of the constant control fields during writing and retrieval stages. (b) Corresponding memory efficiencies determined for each iteration step.	95
4.3	Storage of three signal pulses (a' , b' , c') using calculated optimal storage ($t < 0$) control fields (a), (b), (c). Graphs (a'' , b'' , c'') show the results of numerical calculations of (a' , b' , c').	96
4.4	(a) Eight randomly selected signal pulse shapes and their corresponding optimal control fields. (b) Memory efficiency for each case.	98

4.5	Memory efficiency as a function of optical depth obtained by carrying out iterative signal optimization until convergence. (a) Experimental data. (b) Theoretical predictions.	100
4.6	Results of the optimization procedures for different optical depths: $\alpha_0 L = 24$, $\alpha_0 L = 40$, and $\alpha_0 L = 50$	101
4.7	(a) Level diagram illustrating Stokes field (\mathcal{E}') generation due to resonant four-wave mixing. (b) Memory efficiency for retrieval in the signal channel, Stokes channel, and the total for both channels.	105
5.1	(a) Schematic of the three-level Λ interaction scheme. (b, c) Control and signal fields in pulse-shape-preserving storage of a "positive-ramp" pulse using a calculated optimal control field envelope $\Omega(t)$	107
5.2	An input Gaussian pulse was optimally stored and retrieved either into its original pulse shape (a) or into a ramp pulse shape (b). Similarly, the incoming ramp pulse was optimally stored and retrieved into a Gaussian (c) or into an identical ramp (d).	108
5.3	Examples of storage of signal input pulses with Gaussian and triangular envelopes, followed by retrieval in a linear combination of two time-resolved Gaussian pulse shapes $g_1(t)$ and $g_2(t)$	111
6.1	(a, b) Signal and Stokes amplitude spectra at an optical depth of $2d = 52$ with a beam diameter of 4 mm and $\Omega/2\pi = 9$ MHz under two different Stokes filtering conditions. (a', b') Corresponding theoretical predictions.	120
6.2	Same as Fig. 6.1, but at with an optical depth of $2d = 98$	121
6.3	(a, b) Signal and Stokes amplitude spectra at an optical depth of $2d = 52$ with a beam diameter of 2.6 mm and $\Omega/2\pi = 14$ MHz under two different Stokes filtering conditions. (a', b') Corresponding theoretical predictions.	122
6.4	Same as Fig. 6.3, but at with an optical depth of $2d = 98$	123

6.5	Slow light on the (a) signal, and (b) Stokes channels at an optical depth of $2d = 110$ with no Stokes seed attenuation for several values of δ . (a', b') Theoretical predictions. Theoretical signal (c) delay dispersion, and (d) gain dispersion.	124
6.6	Same as Fig. 6.5, but with Stokes seed attenuation ($f = \sqrt{0.05}$).	125
6.7	Experimental and theoretical results for the storage and retrieval of $16 \mu\text{s}$ -long (FWHM) truncated Gaussian pulses at $T = 70^\circ\text{C}$ ($\alpha_0 L = 52$) at various values of δ	129
6.8	Results of a numerical investigation of pulse propagation and spin-wave dynamics under conditions of slow light with a $6.6 \mu\text{s}$ -long pulse, with $\Omega/(2\pi) = 10 \text{ MHz}$ and $\alpha_0 L = 80$, so that the bandwidth of the pulse $\Delta\omega = 0.1\Gamma_E$. The various levels of theoretical approximations are discussed in the text.	133
6.9	Results from numerical evaluation of Eqs. 6.17, 6.23 and 6.28 and of the homogeneous version of Eq. 6.28 for a range of optical depths $\alpha_0 L$, as indicated in the legends.	136
6.10	An illustration of the modified storage description under FWM conditions.	137
6.11	Storage of a $15 \mu\text{s}$ (FWHM) truncated Gaussian pulse at $T = 70^\circ\text{C}$ ($\alpha_0 L = 52$) under different Stokes seeding conditions.	140
6.12	Stokes behavior upon retrieval for increasing optical depths.	141
7.1	The dependence of spin decay time, τ_s	147
7.2	The dependence of spin decay during storage time as a function of the Rabi frequency of the writing control field, Ω	149
7.3	The dependence of spin decay on the bandwidth of the input signal pulse.	150
7.4	Numerically-computed spin wave (a) shape and (b) phase under conditions corresponding to Fig. 7.2.	153
7.5	Numerically-computed spin-wave (a) shape and (b) phase under conditions corresponding to Fig. 7.3	154

7.6	Results from an investigation of the dependence of spin decay time on the amplitude of the seeded Stokes pulse and the dialed two-photon detuning, δ	156
7.7	The memory efficiency obtained by storing a 17 μ s-long signal pulse with $\Omega = 7$ MHz (red) and $\Omega = 10$ MHz (black) as a function of two-photon detuning (δ) and the amplitude of the seeded Stokes field.	157
7.8	Dependence of retrieved signal and Stokes pulse energies as a function of storage time at $T = 70^\circ\text{C}$ ($\alpha_0 L = 52$).	158
7.9	Numerical solutions to Eqs. 6.16-6.19 provide the calculated spin-wave (<i>top</i>) shapes and (<i>bottom</i>) phases for various two-photon detunings.	159
B.1	Graphs of (a) $f_1(L, t)$, (a') $-h_1(L, t)$, (b) $f_2(L, t)$, (b') $-h_2(L, t)$, (c) $\text{Im}[f_3(L, t)] = -\text{Im}[g_3(L, t)]$, (c') $-\text{Im}[h_3(L, t)]$, and (d) $g_2(L, t)$ under the different levels of approximation described in the text.	174

SLOW AND STORED LIGHT UNDER CONDITIONS OF
ELECTROMAGNETICALLY INDUCED TRANSPARENCY AND FOUR WAVE
MIXING IN AN ATOMIC VAPOR

CHAPTER 1

Introduction

Technologies that enable perfect encryption and transmission of sensitive information will harness the quantum world. While current classical encryption schemes are generally successful because of the difficulty of performing certain mathematical tasks—like finding the prime factors of a very large number—these schemes have limitations. In general, if a person (Alice) wants to send a secure message to another person (Bob), they must share a secret key that allows Alice to encrypt the message and Bob to decode the message. A secure, but impractical, method of key sharing would be for the two parties to meet and exchange a key. Since this protocol is inefficient, other methods are used wherein a key must also be transmitted between the parties. A malevolent stranger, Eve, could intercept the transmissions via eavesdropping techniques and, given enough time and resources, possibly crack the encryption scheme—all without Alice and Bob realizing that their security was jeopardized. Thus, the problem of secure communication reduces to the secure distribution of a shared key.

An alternative, absolutely secure, means of key distribution binds Eve to the laws of quantum mechanics—specifically the fact that it is impossible to perfectly

copy a quantum state, a quantum mechanical phenomenon described by the *no-cloning theorem* [2, 3]. In so-called Quantum Key Distribution (QKD) protocols, the secret key is transmitted between Alice and Bob as a series of quantum states. If Eve attempts to intercept the key, she destroys the quantum state, and thereby alerts Alice and Bob of the attack.

More precisely, we draw an analogy between QKD and conventional classical key distribution, the latter of which employs a series of bits, each one of which can take one of two values, 0 or 1. Quantum bits, or qubits, can be in both states $|0\rangle$ and $|1\rangle$ at the same time—a phenomenon known as quantum superposition. In other words, we can write a qubit as $|\psi\rangle = c_0|0\rangle + c_1|1\rangle$; a measurement on this qubit will cause it to “collapse” into one of its observable states, and will yield an outcome of either $|0\rangle$ or $|1\rangle$, with the probability of each outcome determined by the prefactors, as $|c_0|^2$ or $|c_1|^2$, respectively. Since the measurement is not deterministic, it is impossible to faithfully reconstruct the original qubit after a single measurement. Herein lies the difficulty of Eve’s task. Since Eve destroys the underlying quantum state when she detects it, she cannot create a perfect clone to reconstruct it, and thereby alerts Alice and Bob of her attack [4].

Current communications architectures use light to transmit classical information through fiber optics networks. Corpuscles of light—photons—are a natural choice for transmitting a quantum state, since they travel quickly and generally do not interact with other photons [5]. For example, the states $|0\rangle$ and $|1\rangle$ can correspond to the polarization state of a single photon (*e.g.*, either left- or right-circularly polarized). Other representations include photon path [6], photon-number [7, 8], or time-bin encodings [9].

However, imperfect transmission lines can cause photonic quantum states to degrade after a finite distance (typically several hundred kilometers in an optical fiber) [5]. In classical communication, this attenuation problem is curtailed with

a series of electronic repeaters, which amplifies the signal along the transmission path. However, the same phenomenon that prevents Eve from perfectly copying a quantum state also renders traditional amplification useless.

One solution employs a series of so-called *quantum repeaters* [10–12] along the transmission line, which can permit quantum communication over arbitrary distances. Essentially, quantum repeaters must have sufficiently long coherence times in order to entangle adjacent nodes together [13]. By using entanglement swapping (*i.e.*, teleportation), the shorter segments will all be linked to a single entangled state containing Alice and Bob. One essential component of a quantum repeater is a reliable quantum memory, which would store a photon’s quantum state at one of the nodes for a controllable period of time and allow for synchronization between adjacent quantum repeaters. This requires coherent control over the light-matter interaction at the single photon level [14].

1.1 Optical quantum memory

As we have already mentioned, since they weakly interact with the environment and travel quickly, photons are the only viable information carrier in long-distance quantum communication schemes. There are many promising systems that readily couple with photons and are good candidates for the building blocks of quantum memory devices. For instance, experiments with cavity quantum electrodynamics (QED) [15–17] have demonstrated the strong coupling between single optical or microwave photons and individual atoms in high-finesse ($Q \sim 10^7 - 10^{11}$) microcavities, which in itself requires the strong coupling of a single atom to a single cavity mode. In this approach, the absorption and emission of single photons by an atom is coherently controlled by a classical external control field. By cleverly manipulating the control field’s temporal structure, it is possible to generate single, heralded

photons on-demand [18–20]. Other promising avenues involves the manipulation of pulses of light in an optically thick ensemble of atoms—either a warm or cold atomic gas [21–31], in “atom-like” defects in solid-state systems [*e.g.*, nitrogen vacancy (NV) centers in diamond] [32–34], or nanostructures like quantum dots [35].

The interaction between light and atoms is very well understood: atoms strongly couple to specific frequencies of light, exchanging information based on the atoms’ spin and orbital angular momentum and light polarization. Typically, when the frequency of a light field is tuned near an atomic transition, the atomic medium responds by strongly absorbing the light and then scattering it in all directions. Thus, the challenge is to coherently control this interaction and mitigate any decoherent effects that result from spontaneous decay, atom-atom interactions, or other dissipative processes.

Quantum interference makes this possible. Through a phenomenon called Electromagnetically Induced Transparency (EIT), the absorption pathways of two resonant fields are canceled [36], and one can coherently control the propagation of light through a near-resonant medium. We explore this effect briefly in the next section and in more detail in Ch. 2.

1.2 Electromagnetically induced transparency

The prototypical atomic system for EIT is shown in Fig. 1.1(a). The atom is modeled as a three-level Λ -type, comprised of two long-lived electronic ground states, $|g\rangle$ and $|s\rangle$, and an excited electronic state, $|e\rangle$, which is the case, for example, for sublevels of different angular momentum or spin within the electronic ground state of alkali atoms. A weak optical signal field is tuned near the $|g\rangle \rightarrow |e\rangle$ transition. A strong optical control field is tuned near the $|s\rangle \rightarrow |e\rangle$ transition.

The two fields collaborate to place an atom into a coherent superposition of the

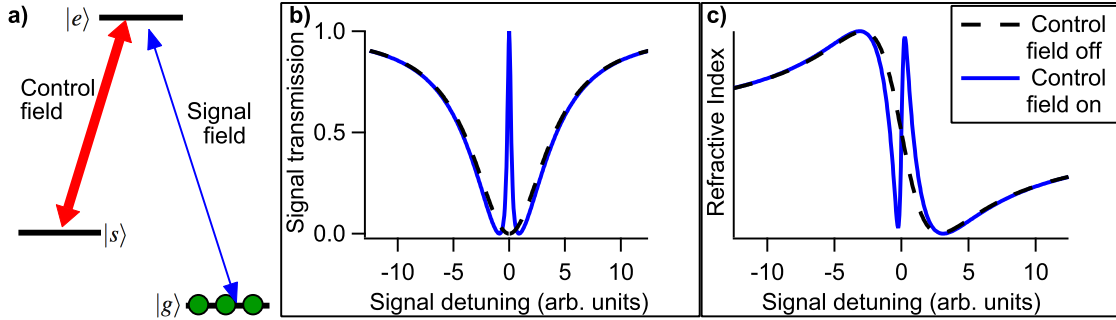


FIG. 1.1: (a) Three-level Λ system under EIT conditions. (b) In the absence of the control field (dashed black lines), a broad range of signal frequencies is absorbed by the medium. When the control field is illuminated (solid blue lines), a narrow transparency window is created. (c) Refractive index seen by the signal field.

two ground states, which no longer interacts with the optical fields. In fact, despite both fields being resonant, the atom ideally never occupies the excited state. Thus, for a narrow range of signal frequencies, the previously-opaque medium is rendered transparent. The width of this so-called *EIT window* is determined by the strength of the control field, but is much narrower than the typically Doppler- or pressure-broadened natural resonance. Fig. 1.1(b) depicts the transmission spectrum of the signal pulse as a function of its detuning from resonance in the absence of the control field (dashed black line) and the presence of the control field (solid blue line), the latter of which clearly shows that EIT peak.

Because the atoms are decoupled from the light fields, the refractive index experienced by the signal field during propagation is near unity. However, according to the Kramers-Kronig relations, an anomaly in the absorption spectrum is accompanied by an anomaly in the dispersion. Thus, the narrow transparency window is accompanied by a very steep, linear change in the refractive index, as we see in Fig. 1.1(c). Since different Fourier frequencies of a pulse of signal light experience different indices of refraction, the pulse will travel with a group velocity, v_g , which can be much less than the speed of light—an effect known as *slow light*.

During slow light propagation, information is coherently shared between the signal field and the collective spin coherence (“spin wave”). Thus, slow light can be the basis for a quantum memory. In essence, the EIT medium “remembers” the incident photon’s quantum state for the duration of the propagation, but these times are far too brief for practical purposes. We can write the photon’s quantum state as [37],

$$|\Psi_\phi(t)\rangle = \sum_k c_k(t) a_k^\dagger |0\rangle, \quad (1.1)$$

where $c_k(t)$ is an amplitude coefficient for photon mode k , a_k^\dagger is the creation operator for mode k , and $|0\rangle$ is the vacuum state.

In order to extend the storage time of this type of quantum memory, a dynamic form of EIT is employed. Specifically, as a signal pulse enters an EIT region, the reduction in group velocity will result in pulse compression. Ideally, the entire pulse would be spatially compressed inside the medium. At this time, the control field can be turned off, thereby reducing v_g to zero, collapsing the EIT window, and completely mapping the signal pulse to the spin coherence. When the information needs to be retrieved, the control field is turned on, and the spin wave is converted into an optical signal pulse, which propagates out of the medium.

If, rather than using a classical pulse, one uses a single-photon wave packet, then the above EIT description remains intact, but the spin wave and the photon share the same quantum state. More precisely, prior to the arrival of the signal pulse, all N atoms are prepared (*e.g.*, by optical pumping) in the ground state, $|g\rangle$, producing an initial collective atomic state of

$$|\psi_0\rangle = |g_1 \dots g_N\rangle. \quad (1.2)$$

When a signal photon is stored, its quantum state is transferred to the collective

spin excitation of the atoms,

$$|\psi_1\rangle = \sum_j \psi_j e^{i\Delta k z_j} |g_1 \dots s_j \dots g_N\rangle, \quad (1.3)$$

where z_j is the position of atom j along the field propagation direction, Δk is the difference in signal and control field wavevectors, and ψ_j is an amplitude chosen to ensure normalization. In other words, one of the atom's spin is flipped from $|g\rangle$ to $|s\rangle$, but it is not known which one. Later, a pulse of the control field can read out this coherence into an optical signal field.

1.3 Performance criteria for optical quantum memory

The above discussion is valid in a fictional world in which no dephasing or decoherence mechanisms conspire to destroy a quantum memory. We can quantify the extent of these effects by requiring the quantum memory to achieve certain performance criteria, which we discuss in this section [12, 38].

The figure of merit for any memory device is the storage efficiency, which is a measure of the total retrieved information or the probability of retrieving an incoming photon after some time. Equivalently, this is the energy ratio between retrieved signal pulse, $\mathcal{E}_{\text{out}}(t)$, and initial signal pulse, $\mathcal{E}_{\text{in}}(t)$:

$$\eta = \frac{\int_{\tau}^{\tau+T} |\mathcal{E}_{\text{out}}(t)|^2 dt}{\int_0^T |\mathcal{E}_{\text{in}}(t)|^2 dt}, \quad (1.4)$$

where τ is the storage time and T is the pulse duration.

This metric is fairly easy to determine experimentally with weak classical pulses, but it does not account for possible detrimental effects such as excess noise from

the storage medium, which would affect the shape of the output. To quantify any distortion effects and to characterize the quality of the pulse shape generation, we define an overlap integral J^2 as [39]

$$J^2 = \frac{|\int_{\tau}^{\tau+T} \mathcal{E}_{\text{out}}(t)\mathcal{E}_{\text{tgt}}(t)dt|^2}{\int_{\tau}^{\tau+T} |\mathcal{E}_{\text{out}}(t)|^2 dt \int_{\tau}^{\tau+T} |\mathcal{E}_{\text{tgt}}(t)|^2 dt}, \quad (1.5)$$

where $\mathcal{E}_{\text{tgt}}(t)$ is the desired (target) shape.

The storage and retrieval of a signal photon in a nonideal passive quantum memory produces a mixed state that is described by a density matrix [40]

$$\rho = (1 - \eta)|0\rangle\langle 0| + \eta|\phi\rangle\langle\phi|, \quad (1.6)$$

where $|\phi\rangle$ is a single-photon state with envelope $\mathcal{E}_{\text{out}}(t)$ and $|0\rangle$ is the zero-photon (vacuum) state. In general, a quantum memory stores a pure state or mixed state that is represented by a density matrix, ρ . The output state, represented as ρ' , should be “close” to ρ . The fidelity between the target single-photon state $|\psi\rangle$ with envelope \mathcal{E}_{tgt} and the single-photon state $|\phi\rangle$ is given by the overlap integral J^2 [Eq. (1.5)], while

$$F = \langle\psi|\rho'|\psi\rangle = \eta J^2 \quad (1.7)$$

is the fidelity of the output state ρ' with respect to the target state.

A final criteria for quantum memory performance is the storage time. A practical quantum memory must be able to faithfully store a state for long enough to perform a particular task, which in the case of quantum repeaters, is how long it takes to perform entanglement swapping. This, of course, depends on the number of quantum repeaters (and thus the number of desired entangled photons) and the distance between them. Jiang, *et al.* [41] have presented an analysis of the DLCZ protocol (see Sec. 1.2) and found that with $\eta = 90\%$, it is possible to generate one

pair of entangled photons (and hence one pair of entangled quantum repeaters) per three minutes over a distance of 1280 km with $F = 78\%$, which is greater than the classical limit of 67%.

For EIT-based light storage, the fulfillment of sufficiently high efficiency requires the simultaneous balancing of two competing loss mechanisms that exist even in the ideal case of no ground-state (spin-wave) decoherence. First, the group velocity of the signal pulse must be low enough so that the entire pulse is compressed inside the EIT medium of length L . If this requirement is not met, then the front part of the pulse can exit the other side of a finite-sized medium (*i.e.*, “leak”) and take information with it before the control field is turned off. One might suspect that the use of short pulses may curtail this problem, such that the duration of the pulse, T , satisfies the condition $T \ll L/v_g$. However, the second requirement is that the bandwidth of the signal pulse fit inside the narrow EIT window in order to minimize absorption and spontaneous losses. Thus, $1/T \ll \sqrt{d}v_g/L$ [22, 42]. The simultaneous fulfillment of both requirements is only possible at high optical depths $d \gg 1$ [22, 42, 43].

1.4 Experimental demonstrations of EIT

In 1999, a collaboration between Harvard and Stanford Universities, under the direction of Stephen Harris, demonstrated slow light speeds of 17 m/s with weak classical pulses through an ensemble of ultracold sodium atoms prepared under EIT conditions [44]. Later that year, a research group at University of California, Berkeley demonstrated weak classical light propagation at speeds of 8 m/s in an ensemble of room temperature ^{85}Rb [45]. Also in 1999, Marlan Scully’s group at Texas A&M University demonstrated a group velocity reduction to $v_g = 90$ m/s in a hot ($T = 320$ K) vapor of ^{87}Rb atoms, and demonstrated that the group velocity

could be controlled by adjusting the intensity of the control field [46].

In 2001, L. V. Hau’s group at Harvard demonstrated the storage of weak classical pulses of light in cold ($T = 0.9 \mu\text{K}$) Sodium atoms. After 1 ms, they retrieved the pulses with efficiencies of a few percent [24]. Also in 2001, Ronald Walsworth’s group at Harvard demonstrated storage of weak pulses for up to 0.5 ms in hot ^{87}Rb vapor, with retrieval efficiencies of a few percent [25]. Later, the Texas A& M group demonstrated that the storage process obeyed time-reversal symmetry—an important step towards the optimization of memory efficiency [47], which we will discuss in Ch. 4.

Storage of nonclassical states of light is a technologically challenging feat. While lasers are adept at supplying light comprised of trillions of photons per second, single photons and other nonclassical states of light are notoriously difficult to produce and detect. In particular, since optical losses degrade quantum states, loss mechanisms at all system components must be minimized. Further, detection of quantum states of light, and measurement of the quantum properties, requires detectors with very high quantum efficiency [48].

Moreover, the relatively narrow EIT window restricts the bandwidth of nonclassical optical fields to several MHz, and requires that the associated frequency be near the two-photon resonance. Currently, the most common single photon source—parametric down conversion in nonlinear crystals [48]—produces bandwidths that are insufficiently high, due in part to the large spectral bandwidth of the optical nonlinearity of the crystals. Narrow-band pump lasers and the use of high-quality cavities is a promising, albeit challenging, avenue for spectrally narrow single photons [49–53].

Despite these challenges, important steps towards the storage of quantum states of light were made in 2004, when Akamatsu, *et al.* observed a squeezed vacuum state under EIT conditions [54]. Since 2008, several research groups have demonstrated

that the storage process preserves the nonclassical quadrature noise properties of squeezed light [55–58]. Progress in the storage of single photons will be discussed briefly in Sec. 1.5.2.

The problem inherent to all of these demonstrations is that the memory efficiency is low. On one hand, this is not surprising, since EIT-based storage of quantum light suffers from background noise from the repopulation of $|s\rangle$ due to atomic diffusion [59], which results in absorption of the control field upon retrieval, and producing thermal photons via spontaneous decay from $|e\rangle$. On the other hand, the detrimental effects of this noise become significant in the experimental parameter space of interest. In order to combat this problem, memory efficiency protocols must be established. We discuss an important optimization protocol and demonstration thereof in Ch. 4.

Another drawback of these memory demonstrations is that they rely on the coupling of photons to a single ensemble of atoms. Thus, EIT-based quantum memory of the type described above does not clearly lend itself to long-distance quantum communication protocols.

1.5 Progress towards long distance quantum communication using atomic ensembles

In 2001, Luming Duan, Mikhail Lukin, Juan Ignacio Cirac, and Peter Zoller (DLCZ) published a theoretical protocol for achieving a realistic quantum repeater scheme, which would enable long-distance quantum communication by entangling adjacent ensembles of atoms [13]. Their proposal has similarities to the EIT scheme. They consider two identical atomic ensembles, separated by some distance, which is less than the decoherence length of photons through an optical fiber, of three-level

Λ -type atoms [see Fig. 1.2(a)] each possessing a single excited state $|e\rangle$, and two ground states, $|g\rangle$ and $|s\rangle$. An initiatory step of the DLCZ procedure involves the creation of a spin excitation of the type described by Eq. 1.3. In contrast with EIT, the spin excitation is created not by an incoming signal field, but by the ensemble interacting with a far-detuned control field.

More precisely, a far detuned Raman pulse of light, as shown in Fig. 1.2(a) is sent through two atomic ensembles, labeled L_1 and R_1 . This procedure is repeated at adjacent pairs of ensembles. There is a small but finite probability that an atom in one of the ensembles will complete a virtual transition and flip its spin state from $|g\rangle$ to $|s\rangle$, thereby creating a spin excitation and releasing a Stokes photon. The probability of this event occurring in both ensembles is low. Thus, it is impossible to know which atom has completed this transition; consequently, one of the ensembles can be described by the wavefunction in Eq. 1.3.

The outputs from both ensembles are coupled to optical fibers and interferes on a 50/50 beam-splitter. Two photodetectors, D_1 and D_2 monitor the ports of the beam-splitter, such that if there is a ‘click’ in either detector, it is impossible to ascertain whether the detected photon originated in either the left or the right ensemble, and thus L_1 and R_1 (and, by similar results, L_2 and R_2 , and L_3 and R_3) become entangled by post-selection. The detection of a ‘click’ heralds this phenomenon. Since this protocol is probabilistic, one can repeat it until a ‘click’ in either detector is registered.

At this point, adjacent pairs of ensembles are mutually entangled. The second step in the DLCZ protocol is to swap the entanglement, for instance from entangled pair 1 to entangled pair 2 [see Fig. 1.2(b)]. This is performed by sending an EIT-like “read” pulse of light tuned on the $|s\rangle \rightarrow |e\rangle$ transition. This reads out the spin excitations and produces an anti-Stokes pulse. As before, the outputs from adjacent ensembles (*e.g.*, R_1 and L_2) are coupled into optical fibers, and the signals interfere

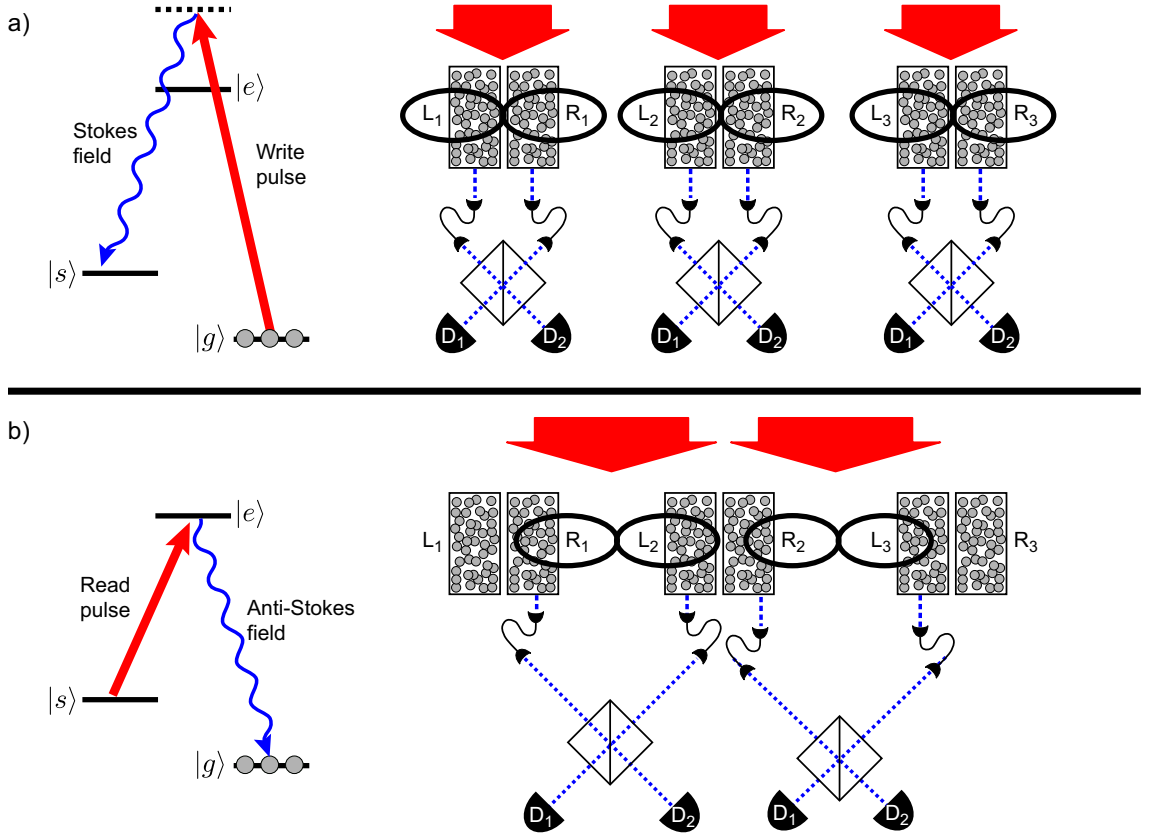


FIG. 1.2: A schematic of the (a) entanglement creation, and (b) entanglement swapping stages of the DLCZ protocol. (a) All atoms in identical ensembles $L_{1,2,3}$ and $R_{1,2,3}$ are prepared in the ground state $|g\rangle$. A far-detuned ‘write’ pulse incident on adjacent ensembles can, with a finite probability, induce a spin flip in one of the ensembles. This spin flip is accompanied by the release of a Stokes photon, which leaves the ensemble and is split at a 50/50 beamsplitter. Since the likelihood of this process happening in both ensembles is low, then the detection of a ‘click’ at detector D_1 or D_2 will create entanglement of ensembles L_1 and L_2 via post-selection. (b) Entanglement is swapped by sending an EIT-like ‘read’ pulse on adjacent ensembles (*e.g.*, R_1 and L_2). This reads out the spin excitation and creates an anti-Stokes field. The anti-Stokes fields from adjacent ensembles interfere at a 50/50 beamsplitter, and the detection of a ‘click’ signifies that the entanglement has been extended, for instance, from L_1 to R_2 . This process can be repeated to extend the entanglement farther.

at a 50/50 beamsplitter.

Since each photon is still entangled with the corresponding atomic spin excitation in each pair of ensembles, a ‘click’ at either detector signifies the entanglement between the two distant ensembles (*e.g.*, L_1 and R_2). This process can be repeated and the entanglement can be spread over a longer distance. The readout of the spin wave can be used to swap entanglement between different adjacent states, thereby enabling teleportation of quantum data [60].

1.5.1 Experimental demonstration of DLCZ components

The promise of the DLCZ protocol has led to much experimental interest. While the current state of the art has not produced a DLCZ quantum repeater scheme in full, many important building blocks have already been experimentally demonstrated.

In 2003, two research groups experimentally demonstrated quantum correlations between the incoming Stokes and outgoing anti-Stokes photons by measuring the photon-number fluctuations using a Hanbury-Brown-Twiss type of experiment [61] to compute the second-order correlation function [62–64],

$$g^{(2)} = (n_{AS}, n_S) = \frac{\langle : \hat{n}_{AS} \hat{n}_S : \rangle}{\langle \hat{n}_{AS} \rangle \langle \hat{n}_S \rangle}, \quad (1.8)$$

where $\hat{n}_i = a_i^\dagger a_i$ is the photon number operator for either the Stokes or anti-Stokes fields, and $: \dots :$ denotes operator normal ordering. For classical sources of light, the value of the correlation function is $g_{\text{class.}}^{(2)} \geq 1$, while for ideally correlated photons, $g_{\text{ideal}}^{(2)} = 0$. Smaller values of $g^{(2)} < 1$ indicate stronger non-classical correlations between the fields.

H. Jeffrey Kimble’s group at the California Institute of Technology demonstrated correlations below the classical limit in the photon number of fields associ-

ated with the retrieval of atomic coherences of Cs in a magneto-optical trap (MOT) [65]. In the same year, Ronald Walsworth’s group at Harvard University demonstrated nonclassical intensity correlations between two photon fields comprised of a large number of photons ($10^3 - 10^4$), which were retrieved from an atomic coherence in a warm vapor of ^{87}Rb [66]. Since these two proof-of-principle experiments were conducted, several other experiments have demonstrated the quantum correlations and similar entanglement with controllable waveform shapes in ensembles of cold [67–69] and hot atoms [26, 70].

Later experiments demonstrated that entanglement exists between the spin excitation and the released Stokes field. These results confirmed the feasibility of the DLCZ protocol within long-lived spin coherences in ensembles of alkali atoms [71–73] and led to the demonstration of entanglement between adjacent atomic ensembles [74–78].

1.5.2 Towards storage of single photons

Quantum repeaters require the development of long-lived quantum memories for few-photon pulses of light. Several research groups have directed the output from DLCZ-type experiments to quantum memory devices. Essentially, the outgoing quantum state could be stored for long enough to ensure that entanglement swapping has produced a network of entangled quantum repeaters. As discussed above, a significant hurdle to quantum memory based on EIT is that the bandwidth and frequency associated with a few-photon wavepacket must match the EIT window in order to achieve optimal storage. Using the heralded photons from DCLZ-based entanglement as a source for EIT-based storage can alleviate this problem, since the bandwidth of the retrieved anti-Stokes photon (which was retrieved with EIT techniques) matches the EIT bandwidth used for storage in a different, but identical

atomic ensemble [77, 79, 80].

In 2005, Alexander Kuzmich’s group at the Georgia Institute of Technology demonstrated the storage of single photons in a magneto-optical trap (MOT) of cold ^{85}Rb atoms for 15 μs with a retrieval efficiency of a few percent [27]. Also that year, Eisaman, *et al.* produced single photons in one laboratory, sent them 100 m via an optical fiber and stored them in a vapor cell containing hot ^{87}Rb atoms for a few microseconds, with approximately 10% memory efficiency [26]. Other experiments have refined these techniques using ensembles of cold atoms [81–83] hot atoms [28], and atoms trapped in an optical lattice [84].

However, all of these demonstrations suffer from a similar fate—the retrieval efficiency is too low for practical purposes. As discussed above, the memory efficiency for EIT-based devices is improved by increasing the optical depth (or, equivalently the atomic concentration) of the ensemble. This is technologically challenging with cold trapped atoms (although it has recently been demonstrated [85]), but readily achievable in hot atomic vapors.

1.6 Outline of this dissertation

This thesis presents experiments that investigate the optimization of storage efficiency using EIT in a hot vapor of ^{87}Rb atoms. We exploit the correspondence between the quantum and the classical equations of motion and use weak classical signal pulses of light to demonstrate the efficacy of two memory optimization protocols. Large optical depth is readily achieved with hot atoms, but this can lead to unwanted effects, which we explore in more detail.

Chapter 2 presents a detailed semi-classical theoretical derivation and discussion of EIT and the stored light phenomenon. Chapter 3 discusses how ^{87}Rb is a fairly good approximation for a three-level Λ atom and describes the basic experimental

apparatus used in this investigation. In Ch. 4, we present the results of experiments that tested two proposals to achieve optimal efficiency. One technique involves optimizing the envelope of the input signal field. The second technique involves shaping the control field temporal profile to achieve optimal storage of a desired input field. We also tested the time-reversal of the storage protocol and show that it is possible to have full control over the output. We show that both of these protocols are successful for achieving the memory efficiency that is predicted by the theoretical model, up to an optical depth of $\alpha L \lesssim 25$. In Ch. 5, we show that the ability to shape the output can be used to generate time-bin qubits of sufficiently high fidelity. Thus, EIT based quantum memory can also be a source for non-classical states of light. Chapter 6 presents a detailed investigation of one effect that we suspected resulted in the degradation of memory efficiency at high optical depths: resonant four-wave mixing (FWM). We present experimental results of FWM in the continuous-wave (cw), slow light, and stored light regimes, and present a novel theoretical model of the FWM-EIT interference effect that successfully describes all three regimes. Chapter 7 discusses the results of experiments that investigated sources for spin-wave decay. Finally, Ch. 8 summarizes the findings. We include the details of the control pulse shaping algorithm in Appendix A. Appendix B provides some of the details of the FWM model that were omitted from Ch. 6.

CHAPTER 2

Review of the theory

In this chapter, we review the theoretical concepts governing the propagation of light through a medium comprised of three-level Λ -type atoms. The analysis presented in this thesis is conducted mostly within the semiclassical approximation, wherein the electromagnetic field is treated classically while the atomic medium is quantized. However the quantum treatment of light fields produces similar results, as we will briefly outline [43].

The chapter is organized as follows. First, we work from Maxwell's Equations to describe light propagation through an atomic medium in terms of slowly-varying electric field envelopes. We then derive the Hamiltonian in the dipole and rotating wave approximations, for a simple three-level Λ atom illuminated simultaneously by a strong control field and a weak signal field. We derive the time evolution equations for the density matrix elements and use them to show that, for a narrow range of signal field frequencies, the near-resonant signal field propagates with minimal loss—a phenomenon known as electromagnetically induced transparency. As a result of this narrow transparency window, there is a steep change in the medium's index of refraction, which results in a reduced group velocity of the signal field (“slow light”).

We find that the group velocity of the signal pulse is determined by the intensity of the control field, indicating that a signal pulse can essentially be slowed to zero group velocity and preserved in a long-lived collective atomic coherence (“stored light”). At high optical depth of the medium, the effects of four-wave mixing become relevant and can interfere with EIT. We derive the effective Hamiltonian for this system using Floquet theory and derive density matrix evolution equations and propagation equations for the signal and Stokes fields.

2.1 Maxwell’s Equations

The propagation of an electromagnetic field propagating in atomic vapor is described by Maxwell’s Equations (in SI units) [86]:

$$\nabla \times \mathbf{E} = -\frac{\partial \mathbf{B}}{\partial t} \quad (2.1)$$

$$\nabla \cdot \mathbf{D} = \rho_f \quad (2.2)$$

$$\nabla \times \mathbf{H} = \mathbf{J}_f + \frac{\partial \mathbf{D}}{\partial t} \quad (2.3)$$

$$\nabla \cdot \mathbf{B} = 0. \quad (2.4)$$

Here, \mathbf{E} is the electric field, \mathbf{H} is the magnetic field, $\mathbf{D} = \epsilon_0 \mathbf{E} + \mathbf{P}$ is the electric displacement, \mathbf{P} is the medium’s macroscopic polarization, $\mathbf{B} = \mu_0(\mathbf{H} + \mathbf{M})$ is the magnetic induction, and \mathbf{M} is the medium’s magnetization. ρ_f and \mathbf{J}_f are the free electric charge and current densities inside the medium. Since there are typically no unbound charges or currents in an atomic vapor, $\rho_f = 0$ and $\mathbf{J}_f = 0$. Further, we are interested only in the effects on the electric polarization, and ignore any effects arising from magnetization. Hence, $\mathbf{M} = 0$ and $\mathbf{B} = \mu_0 \mathbf{H}$. As usual, ϵ_0 and μ_0 are the vacuum permittivity and permeability, respectively. Under these assumptions, we find from taking the curl of Eq. 2.1, employing the vector identity

$\nabla \times (\nabla \times \mathbf{E}) = \nabla(\nabla \cdot \mathbf{E}) - \nabla^2 \mathbf{E}$, and inserting the corresponding expression from Eq. 2.3:

$$\begin{aligned} \nabla \times (\nabla \times \mathbf{E}) &= -\frac{\partial}{\partial t}(\nabla \times \mathbf{B}) \\ \nabla(\nabla \cdot \mathbf{E}) - \nabla^2 \mathbf{E} &= -\mu_0 \epsilon_0 \frac{\partial^2 \mathbf{E}}{\partial t^2} - \mu_0 \frac{\partial^2 \mathbf{P}}{\partial t^2}, \end{aligned} \quad (2.5)$$

Let us assume that the electromagnetic field is a plane wave propagating along the z -direction, so we neglect the x - and y - dependence of \mathbf{E} . Thus, $\nabla \cdot \mathbf{E} = 0$, and Eq. 2.5 then reduces to

$$\left(\frac{\partial^2}{\partial z^2} - \frac{1}{c^2} \frac{\partial^2}{\partial t^2} \right) \mathbf{E} = \frac{1}{c^2 \epsilon_0} \frac{\partial^2 \mathbf{P}}{\partial t^2}, \quad (2.6)$$

where we have used $c = 1/\sqrt{\epsilon_0 \mu_0}$. This is the wave equation for the electromagnetic field, where the polarization \mathbf{P} acts as a source term for the radiation field. If we were to treat the medium macroscopically, we would relate the material's polarization to the electric field via the electric susceptibility tensor, χ , via

$$\mathbf{P} = \epsilon_0 \chi \mathbf{E}, \quad (2.7)$$

however, since χ is presently unspecified, the problem remains unresolved. Rather, in what follows, we relate the macroscopic polarization, \mathbf{P} , to the quantum mechanical dipole moment of the atom.

2.2 General model of the atomic system

\mathbf{P} is the induced macroscopic polarization of the atomic vapor, which can be written as the average per unit volume of the dipole moments of the atoms in the interaction region, assuming that there is no mutual phasing of the dipole moments.

Specifically,

$$\mathbf{P} = \frac{N}{V} \langle \mathbf{d} \rangle = -e \frac{N}{V} \langle \mathbf{r} \rangle, \quad (2.8)$$

where N is the number of atoms in volume V and $\langle \mathbf{d} \rangle = -e \langle \mathbf{r} \rangle$ is the dipole moment of an individual atom averaged over the ensemble. Here, e is the charge of the electron, and \mathbf{r} is taken to be a Hermitian operator describing the position of the electron. In the Schrödinger picture,

$$\begin{aligned} \langle \mathbf{r} \rangle &= \langle \psi(t) | \mathbf{r} | \psi(t) \rangle \\ &= \sum_{n,m} a_m^*(t) a_n(t) \langle m | \mathbf{r} | n \rangle, \end{aligned} \quad (2.9)$$

where a_i are the amplitudes of basis state $|i\rangle$. At this point, we introduce the density matrix,

$$\hat{\rho}(t) = |\psi(t)\rangle \langle \psi(t)|, \quad (2.10)$$

which has the property

$$\rho_{nm} = \langle n | \hat{\rho}(t) | m \rangle = \langle n | \psi(t) \rangle \langle \psi(t) | m \rangle = \sum_{p,p'} \langle n | a_p(t) | p \rangle \langle p' | a_{p'}^*(t) | m \rangle = a_n(t) a_m^*(t). \quad (2.11)$$

Diagonal elements of the density operator, $\rho_{nn} = \langle n | n \rangle$, correspond to the probability that the atom occupies state $|n\rangle$. Off-diagonal elements, $\rho_{nm} = \langle m | n \rangle$, correspond to the expectation value of the coherence between levels $|n\rangle$ and $|m\rangle$, *e.g.*, the atomic dipole, in the case of an electric dipole transition.

Inserting Eq. 2.11 into Eq. 2.9, $\langle \mathbf{d} \rangle$ can be written in terms of the density matrix as,

$$\langle \mathbf{d} \rangle = -e \sum_{n,m} \rho_{nm} \langle m | \mathbf{r} | n \rangle = \sum_{n,m} \rho_{nm} \wp_{nm} = \text{Tr} [-e \hat{\rho}(t) \mathbf{r}], \quad (2.12)$$

where we define $\wp_{nm} = -e \langle m | \mathbf{r} | n \rangle$ as the dipole moment corresponding to the

$|n\rangle \rightarrow |m\rangle$ atomic transition and we assume it to be real. We recognize that the sum is simply the trace of the product of the density and position operators.

Using Eq. 2.12, the propagation of the electric field (Eq. 2.6) can be described with,

$$\left(\frac{\partial^2}{\partial z^2} - \frac{1}{c^2} \frac{\partial^2}{\partial t^2} \right) \mathbf{E} = \frac{1}{c^2 \epsilon_0} \frac{N}{V} \sum_{n,m} \wp_{nm} \frac{\partial^2}{\partial t^2} \rho_{nm}, \quad (2.13)$$

where the time evolution of the density operator is determined by the Liouville-Von Neumann equation:

$$\frac{\partial}{\partial t} \hat{\rho}(t) = -\frac{i}{\hbar} \left[\hat{H}, \hat{\rho}(t) \right], \quad (2.14)$$

where \hat{H} is the Hamiltonian describing the atomic response to the electric field.

It is convenient to extract the fast-oscillating time dependence of the electric field and the polarization by employing the slowly-varying amplitude and phase approximation (SVAPA) [87]. A nearly-monochromatic electric field can be parameterized as the product of its polarization unit vector, $\hat{\epsilon}$, and an envelope function, $\mathcal{E}(z, t)$,

$$\mathbf{E}(z, t) = \mathcal{E}(z, t) e^{ikz - i\nu t} \hat{\epsilon} + \text{complex conjugate}, \quad (2.15)$$

where \mathcal{E} varies slowly in t and z , when compared to the optical frequency ν and the wavevector $k = \nu/c$:

$$\frac{\partial \mathcal{E}}{\partial z} \ll k \mathcal{E}; \quad \frac{\partial \mathcal{E}}{\partial t} \ll \nu \mathcal{E} \quad (2.16)$$

Similarly, the oscillation frequency of the electric dipole moment is largely determined by the frequency of the electric field, and we can write the density matrix elements in the SVAPA

$$\hat{\rho}(z, t) = \tilde{\rho}(z, t) e^{ikz - i\nu t} + \text{c.c.}, \quad (2.17)$$

where c.c. indicates usage of the complex conjugate.

Substituting Eqs. 2.15 and 2.17 into Eq. 2.13 and ignoring higher order derivatives, we obtain a wave equation for the slowly-varying envelopes [87]:

$$\left(\frac{\partial}{\partial z} + \frac{1}{c}\frac{\partial}{\partial t}\right)\mathcal{E}(z,t) = i\frac{k}{2\epsilon_0}\frac{N}{V}\sum_{m,n}\wp_{nm}\tilde{\rho}(z,t). \quad (2.18)$$

2.3 Interaction of a bichromatic electromagnetic field with a three-level Λ system

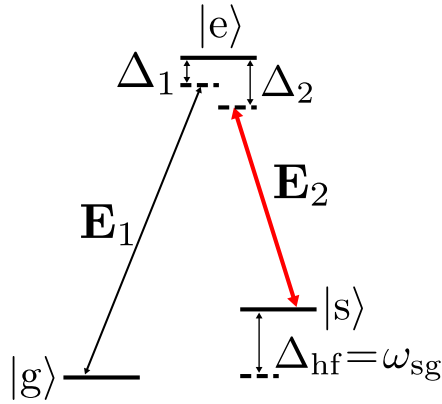


FIG. 2.1: A three-level Λ -type atom comprised of two ground states, $|g\rangle$ and $|s\rangle$, which in our case are separated in energy by the hyperfine interaction, and a single excited state $|e\rangle$. One optical light field, \mathbf{E}_1 at frequency ν_1 is near resonance with the $|g\rangle \rightarrow |e\rangle$ transition, so that its single-photon detuning is $\Delta_1 = \nu_1 - \omega_{eg}$. A second optical light field, \mathbf{E}_2 at frequency ν_2 is near resonance with the $|s\rangle \rightarrow |e\rangle$ transition, so that its single-photon detuning is $\Delta_2 = \nu_2 - \omega_{es}$.

In this section, we derive the time evolution equations for the density matrix elements in a general three-level Λ scheme, which is depicted in Fig. 2.1. In the case of interest, a signal optical field, $\mathbf{E}_1 = \hat{\epsilon}_1 \mathcal{E}_1(z,t)e^{ik_1z - i\nu_1t} + \text{c. c.}$ couples the ground state $|g\rangle$ to the excited state $|e\rangle$. A control optical field, $\mathbf{E}_2 = \hat{\epsilon}_2 \mathcal{E}_2(z,t)e^{ik_2z - i\nu_2t} + \text{c. c.}$ couples the second ground state $|s\rangle$ to the excited state. $\hat{\epsilon}_{1,2}$ are the optical

field polarization unit vectors. The combined optical field has the form

$$\begin{aligned}\mathbf{E}(z, t) &= \hat{\varepsilon}_1 \mathcal{E}_1(z, t) e^{ik_1 z - i\nu_1 t} + \hat{\varepsilon}_2 \mathcal{E}_2(z, t) e^{ik_2 z - i\nu_2 t} + \text{c.c.} \\ &= \mathbf{E}^{(+)}(z, t) + \mathbf{E}^{(-)}(z, t),\end{aligned}\tag{2.19}$$

where we have introduced $\mathbf{E}^{(\pm)}$ as the positive and negative rotating components of the field [88]:

$$\mathbf{E}^{(\pm)} = \hat{\varepsilon}_1 \mathcal{E}_1(z, t) e^{\pm ik_1 z} e^{\mp i\nu_1 t} + \hat{\varepsilon}_2 \mathcal{E}_2(z, t) e^{\pm ik_2 z} e^{\mp i\nu_2 t}.\tag{2.20}$$

The atomic Hamiltonian for a three-level atom at rest is

$$\hat{H}_0 = \hbar\omega_{sg} \hat{\sigma}_{ss} + \hbar\omega_{eg} \hat{\sigma}_{ee},\tag{2.21}$$

where we have taken the ground state to have zero energy. $\hat{\sigma}_{ij} = |i\rangle\langle j|$ is the atomic spin-flip operator.

In the dipole approximation, the Hamiltonian describing the atom-field interaction is

$$\hat{H}_1 = -\hat{d} \cdot \mathbf{E}.\tag{2.22}$$

By applying the completeness relationship, $|g\rangle\langle g| + |s\rangle\langle s| + |e\rangle\langle e| = \mathbf{1}$, to both sides of \hat{d} , and observing that $\langle i|\hat{d}|i\rangle = 0$ for $i = (g, s, e)$ by symmetry, and selecting $|g\rangle$ and $|s\rangle$ such that the transition between the two is electric dipole forbidden, so that $\langle s|\hat{d}|g\rangle = \langle g|\hat{d}|s\rangle = 0$, we find that

$$\begin{aligned}\hat{d} &= |e\rangle\langle e|\hat{d}|g\rangle\langle g| + |e\rangle\langle e|\hat{d}|s\rangle\langle s| + \text{H.c.} \\ &= \wp_{eg} \hat{\sigma}_{eg} + \wp_{es} \hat{\sigma}_{es} + \text{H.c.},\end{aligned}\tag{2.23}$$

where \wp_{ij} is the matrix element of the electric dipole moment of the transition and

H.c. indicates usage of the Hermitian conjugate.

As we did with the electric field, we can decompose \mathbf{d} into positive and negative rotating components by observing that the expectation value of, for instance $\hat{\sigma}_{ge} = |g\rangle\langle e|$ has the unperturbed time dependence $e^{-i\omega_{eg}t}$, while $\hat{\sigma}_{ge}^\dagger = \hat{\sigma}_{eg} = |e\rangle\langle g|$ rotates oppositely, $\sim e^{+i\omega_{eg}t}$. Thus, the quantity $\mathbf{d} \cdot \mathbf{E}$ is rewritten:

$$\begin{aligned} \mathbf{d} \cdot \mathbf{E} &= (\mathbf{d}^{(+)} + \mathbf{d}^{(-)}) \cdot (\mathbf{E}^{(+)} + \mathbf{E}^{(-)}) \\ &= \mathbf{d}^{(+)} \cdot \mathbf{E}^{(+)} + \mathbf{d}^{(+)} \cdot \mathbf{E}^{(-)} + \mathbf{d}^{(-)} \cdot \mathbf{E}^{(+)} + \mathbf{d}^{(-)} \cdot \mathbf{E}^{(-)}. \end{aligned} \quad (2.24)$$

At this point, we implement the assumption that $\mathbf{E}_{1(2)}$ couples near-resonantly to the $|g\rangle \rightarrow |e\rangle$ ($|s\rangle \rightarrow |e\rangle$) transition, although we will later relax this assumption and treat off-resonant interactions perturbatively, as in Ch. 6. Additionally, we can perform the rotating wave approximation and replace rapidly oscillating terms in Eq. 2.24 [e.g., $e^{\pm i(\nu_{1,2} + \omega_{eg})t}$, $e^{\pm i(\nu_{1,2} + \omega_{es})t}$] with their time average value, 0. Thus,

$$\hat{H}_1 = \langle e | \mathbf{d} \cdot \hat{\varepsilon}_1 | g \rangle \mathcal{E}_1(z, t) \hat{\sigma}_{eg} e^{ik_1 z} e^{-i\nu_1 t} + \langle e | \mathbf{d} \cdot \hat{\varepsilon}_2 | s \rangle \mathcal{E}_2(z, t) \hat{\sigma}_{es} e^{ik_2 z} e^{-i\nu_2 t} + \text{H.c.} \quad (2.25)$$

We define the Rabi frequencies of the fields as follows:

$$\Omega = \langle e | \mathbf{d} \cdot \hat{\varepsilon}_2 | s \rangle \mathcal{E}_2 / \hbar \quad (2.26)$$

$$\alpha = \langle e | \mathbf{d} \cdot \hat{\varepsilon}_1 | g \rangle \mathcal{E}_1 / \hbar, \quad (2.27)$$

so that the full atomic Hamiltonian in the dipole approximation is

$$\frac{\hat{H}}{\hbar} = \omega_{sg} \hat{\sigma}_{ss} + \omega_{eg} \hat{\sigma}_{ee} - \left(\Omega \hat{\sigma}_{es} e^{ik_2 z - i\nu_2 t} + \alpha \hat{\sigma}_{eg} e^{ik_1 z - i\nu_1 t} + \text{H.c.} \right). \quad (2.28)$$

It is helpful to remove the explicit time dependence from the Hamiltonian by

moving to a rotating frame. We do this by applying the unitary transformation

$$U = e^{-i\nu_1 t|e\rangle\langle e| - i(\nu_1 - \nu_2)|s\rangle\langle s|}. \quad (2.29)$$

Specifically, the wavefunction $|\psi\rangle \rightarrow |\tilde{\psi}\rangle \equiv U^\dagger|\psi\rangle$. Schrödinger's Equation is modified to be

$$\begin{aligned} i\hbar \frac{\partial}{\partial t} |\tilde{\psi}\rangle &= \left(i\hbar \dot{U}^\dagger U + U^\dagger \hat{H} U \right) |\tilde{\psi}\rangle \\ &= \tilde{H} |\tilde{\psi}\rangle. \end{aligned} \quad (2.30)$$

Observing that

$$i\dot{U}^\dagger U = -[\nu_1 \hat{\sigma}_{ee} + (\nu_1 - \nu_2) \hat{\sigma}_{ss}] \quad (2.31a)$$

$$U^\dagger \hat{\sigma}_{eg} U = e^{i\nu_1 t} \hat{\sigma}_{eg} \quad (2.31b)$$

$$U^\dagger \hat{\sigma}_{es} U = e^{i\nu_2 t} \hat{\sigma}_{es} \quad (2.31c)$$

$$U^\dagger \hat{\sigma}_{ee} U = \hat{\sigma}_{ee} \quad (2.31d)$$

$$U^\dagger \hat{\sigma}_{ss} U = \hat{\sigma}_{ss}, \quad (2.31e)$$

and defining the two-photon detuning $\delta = \nu_1 - \nu_2 - \omega_{sg}$ and simplifying the notation for the control field single-photon detuning: $\Delta \equiv \Delta_2$, the Hamiltonian becomes

$$\tilde{H} = -\hbar(\Delta + \delta) \hat{\sigma}_{ee} - \hbar\delta \hat{\sigma}_{ss} - \hbar(\Omega \hat{\sigma}_{es} + \alpha \hat{\sigma}_{eg} + \text{H.c.}). \quad (2.32)$$

To meticulously account for decay and dephasing mechanisms that affect the atomic equations of motion, we employ a master equation [89, 90],

$$\begin{aligned} \frac{\partial \tilde{\rho}}{\partial t} &= \frac{1}{i\hbar} \left[\tilde{H}, \tilde{\rho} \right] + \frac{\Gamma_{e \rightarrow g}}{2} [2\hat{\sigma}_{ge} \tilde{\rho} \hat{\sigma}_{eg} - \{\hat{\sigma}_{ee}, \tilde{\rho}\}] + \frac{\Gamma_{e \rightarrow s}}{2} [2\hat{\sigma}_{se} \tilde{\rho} \hat{\sigma}_{es} - \{\hat{\sigma}_{ss}, \tilde{\rho}\}] \\ &\quad + \frac{\gamma_{s, \text{deph}}}{2} [2\hat{\sigma}_{ss} \tilde{\rho} \hat{\sigma}_{ss} - \{\hat{\sigma}_{ss}, \tilde{\rho}\}] + \frac{\gamma_{e, \text{deph}}}{2} [2\hat{\sigma}_{ee} \tilde{\rho} \hat{\sigma}_{ee} - \{\hat{\sigma}_{ee}, \tilde{\rho}\}]. \end{aligned} \quad (2.33)$$

The second and third terms on the right-hand side describe spontaneous emission from states $|e\rangle$ to $|g\rangle$ and states $|e\rangle$ to $|s\rangle$ at rates $\Gamma_{e\rightarrow g}$ and $\Gamma_{e\rightarrow s}$, respectively, such that $\Gamma_e \equiv \Gamma_{e\rightarrow g} + \Gamma_{e\rightarrow s}$ is the total spontaneous emission rate out of $|e\rangle$, and thus $1/\Gamma_e$ is its lifetime. Additionally, we have phenomenologically introduced energy-conserving dephasing processes (*e.g.* collisions with inert atomic species) with rates $\gamma_{s,\text{deph}}$ and $\gamma_{e,\text{deph}}$. We further define the coherence decay rates as

$$\gamma_{eg} = \frac{1}{2}(\Gamma_e + \gamma_{e,\text{deph}}) \equiv \gamma \quad (2.34a)$$

$$\gamma_{sg} = \frac{1}{2}\gamma_{s,\text{deph}} \equiv \gamma_0 \quad (2.34b)$$

$$\gamma_{es} = \frac{1}{2}(\Gamma_e + \gamma_{s,\text{deph}} + \gamma_{e,\text{deph}}). \quad (2.34c)$$

It is notable that in the limit of radiative decoherence ($\gamma_{i,\text{deph}} = 0$), γ_{ej} will be equal to half of the spontaneous decay rate out of $|e\rangle$. The density matrix equations of motion are

$$\partial_t \tilde{\rho}_{gg} = \Gamma_{31} \tilde{\rho}_{ee} - i\alpha \tilde{\rho}_{ge} + i\alpha^* \tilde{\rho}_{eg} \quad (2.35)$$

$$\partial_t \tilde{\rho}_{ss} = \Gamma_{32} \tilde{\rho}_{ee} - i\Omega \tilde{\rho}_{se} + i\Omega^* \tilde{\rho}_{es} \quad (2.36)$$

$$\partial_t \tilde{\rho}_{eg} = -[\gamma - i(\Delta + \delta)] \tilde{\rho}_{eg} + i\Omega \tilde{\rho}_{sg} + i\alpha(\tilde{\rho}_{gg} - \tilde{\rho}_{ee}) \quad (2.37)$$

$$\partial_t \tilde{\rho}_{es} = -(\gamma_{es} - i\Delta) \tilde{\rho}_{es} + i\alpha \tilde{\rho}_{gs} + i\Omega(\tilde{\rho}_{ss} - \tilde{\rho}_{ee}) \quad (2.38)$$

$$\partial_t \tilde{\rho}_{sg} = -(\gamma_0 - i\delta) \tilde{\rho}_{sg} + i\Omega^* \tilde{\rho}_{eg} - i\alpha \tilde{\rho}_{se}. \quad (2.39)$$

We are interested in the case of a sufficiently weak signal field, so that $\alpha \ll \Omega$. Under this condition, the atom is quickly prepared in $|g\rangle$, so that the density matrix populations are $\rho_{gg} \approx 1$ and $\rho_{ss} = \rho_{ee} \approx 0$. Additionally, we set $\tilde{\rho}_{es} = 0$, since $|s\rangle$ and $|e\rangle$ are unpopulated to lowest order in α . Under this approximation, we note that the control field propagates at a speed of c without absorption, since its

propagation equation is (*c.f.*, Eq. 2.18),

$$(\partial_t + c\partial_z)\Omega(z, t) = i\frac{\omega_2}{2\epsilon_0} \frac{N}{V} \wp_{es} \tilde{\rho}_{es}(z, t) = 0. \quad (2.40)$$

This is the celebrated *undepleted pump approximation*.

We define the optical polarization $P(z, t) = \sqrt{N}\tilde{\rho}_{eg}(z, t)$ and the collective spin wave of the atomic ensemble $S(z, t) = \sqrt{N}\tilde{\rho}_{sg}(z, t)$, where N is the number of atoms in the interaction region of volume V . We define $g\sqrt{N} = \wp_{eg}\sqrt{\frac{\omega N}{2\hbar\epsilon_0 V}}$ as the collectively enhanced coupling constant between the signal field and the atomic medium [87], and redefine the signal field amplitude as $\mathcal{E} \equiv \mathcal{E}_1\wp_{eg}/(g\hbar)$. Under these approximations, the three equations that govern light propagation and the atomic response are:

$$(\partial_t + c\partial_z)\mathcal{E}(z, t) = ig\sqrt{N}P(z, t), \quad (2.41)$$

$$\begin{aligned} \partial_t P(z, t) &= -[\gamma - i(\Delta + \delta)]P(z, t) + i\Omega(z, t)S(z, t) \\ &\quad + ig\sqrt{N}\mathcal{E}(z, t), \end{aligned} \quad (2.42)$$

$$\partial_t S(z, t) = -(\gamma_0 - i\delta)S(z, t) + i\Omega^*(z, t)P(z, t). \quad (2.43)$$

2.4 Electromagnetically Induced Transparency

Equations 2.41–2.43 fully describe the time evolution of the two atomic coherences—the optical coherence, $P(z, t)$, and the spin coherence, $S(z, t)$ —and a weak signal field. At this point, we restrict ourselves to cases where the control field intensity is constant in time, so that $\Omega(z, t) = \bar{\Omega}(z)$. We can perform a Fourier transform

($t \rightarrow \omega$, $\partial_t \rightarrow -i\omega$), so that Eqs. 2.41–2.43 become:

$$(-i\omega + c\partial_z)\mathcal{E}(z, \omega) = ig\sqrt{N}P(z, \omega), \quad (2.44)$$

$$\begin{aligned} -i\omega P(z, \omega) &= -[\gamma - i(\Delta + \delta)]P(z, \omega) + i\Omega(z)S(z, \omega) \\ &\quad + ig\sqrt{N}\mathcal{E}(z, \omega), \end{aligned} \quad (2.45)$$

$$-i\omega S(z, \omega) = -(\gamma_0 - i\delta)S(z, \omega) + i\Omega^*(z)P(z, \omega). \quad (2.46)$$

It is straight-forward to solve the algebraic expression in Eqs. 2.45–2.46 for the coherences,

$$P(z, \omega) = i\frac{\Gamma_0}{F}g\sqrt{N}\mathcal{E}(z, \omega) \quad (2.47)$$

$$S(z, \omega) = -\frac{\Omega^*(z)}{F}\mathcal{E}(z, \omega), \quad (2.48)$$

where we have defined $\Gamma_0 \equiv [\gamma_0 - i(\delta + \omega)]$, $\Gamma \equiv [\gamma - i(\Delta + \delta + \omega)]$, and $F \equiv |\Omega(z)|^2 + \Gamma_0\Gamma$. The induced polarization in Eq. 2.47 determines the optical properties of the medium, as far as the signal field is concerned. Recalling that the induced polarization is (*c.f.*, Eq. 2.7)

$$P_{\text{ind.}}(\omega) = N\langle g|\hat{\epsilon}_1 \cdot \mathbf{d}|e\rangle\tilde{\rho}_{eg}(\omega) = \epsilon_0\chi(\omega)E(\omega), \quad (2.49)$$

we find the following expression for the electric susceptibility, $\chi(\omega)$ of the medium:

$$\chi(\omega) = \frac{N\wp_{eg}^2}{V\epsilon_0\hbar} \frac{\delta + \omega + i\gamma_0}{|\Omega(z)|^2 + \Gamma_0\Gamma}. \quad (2.50)$$

2.4.1 A brief aside on two-level atoms in a resonant laser field

We wish to contrast the effects of EIT with the response of a two-level atom in a near-resonant field. In this limit, there is a single optical polarization, which

evolves according to (*c.f.* Eq. 2.37 with $\tilde{\rho}_{sg} = 0$, $\tilde{\rho}_{gg} - \tilde{\rho}_{ee} = 1$, $\Omega = 0$, and $\Delta_2 = 0$):

$$\partial_t \tilde{\rho}_{eg} = -(\gamma - i\Delta_1)\tilde{\rho}_{eg} + i\wp_{eg}\mathcal{E}_1/\hbar, \quad (2.51)$$

so that the steady-state optical polarization, when atoms populate the ground state $|g\rangle$ is,

$$\tilde{\rho}_{eg} = \frac{i\wp_{eg}}{\hbar(\gamma - i\Delta_1)}\mathcal{E}_1 \quad (2.52)$$

The propagation of the single near-resonant laser field envelope (*c.f.*, Eq. 2.18), in a co-moving frame is:

$$\begin{aligned} \partial_z \mathcal{E}_1 &= i \frac{k\wp_{eg}}{2\epsilon_0} \frac{N}{V} \tilde{\rho}_{eg} \\ &= -\frac{k}{2\epsilon_0} \frac{N}{V} \frac{\wp_{eg}^2}{\hbar(\gamma - i\Delta_1)} \mathcal{E}_1. \end{aligned} \quad (2.53)$$

where we have used Eq. 2.52. The imaginary part of the term on the right-hand side changes the refractive index, while the real part defines the *optical depth*, $2d$, via

$$\partial_z \mathcal{E}_1 = -\frac{d}{L} \mathcal{E}_1, \quad (2.54)$$

where

$$d = \frac{kL}{2\epsilon_0} \frac{N}{V} \frac{\wp_{eg}^2}{\hbar} \frac{\gamma}{\gamma^2 + \Delta_1^2} \quad (2.55)$$

Notice that by integrating Eq. 2.54 from 0 to L , we find that the amplitude of resonant light has been attenuated according to $\mathcal{E}_1(L) = \mathcal{E}_1(0)e^{-d}$, or that the intensity becomes attenuated by a factor $2d = \alpha_0 L$, where α_0 can be thought of as the on-resonant absorption coefficient. We note that in this dissertation, we use both $2d$ and $\alpha_0 L$ terminologies when referring to the optical depth.

We can write the dipole matrix element of a real atom as the product of a

reduced dipole moment [89], \wp_0 , and a Clebsch-Gordan coefficient: $\wp_{eg} = \text{CG}_{eg}\wp_0$. Using $k = \nu_1/c$, $\lambda = 2\pi/k$, and recognizing the spontaneous emission rate as [89, 91]

$$\Gamma_{\text{sp}} = \frac{\nu_1^3 \wp_{eg}^2}{3\pi\epsilon_0 \hbar c^3}, \quad (2.56)$$

we obtain the following expression for the optical depth of a two-level atom,

$$d = \frac{3}{8\pi} \lambda^2 L \frac{N}{V} \frac{\Gamma_{\text{sp}}}{\gamma} \text{CG}^2 \frac{\gamma^2}{\gamma^2 + \Delta_1^2}. \quad (2.57)$$

Furthermore, it can be shown that

$$g\sqrt{N} = \sqrt{\gamma cd/L}. \quad (2.58)$$

2.4.2 Complex refractive index of a three-level Λ system

We now return to the case of a three-level system with a resonant control field ($\Delta_2 = \Delta = 0$), in which case the two-photon detuning, δ , and the signal field's single-photon detuning, Δ_1 , have the same interpretation. We rewrite the electric susceptibility in Eq. 2.50 in terms of the optical depth, in order to contrast the three-level case with the two-level case,

$$\chi = \frac{2c(\delta + i\gamma_0)}{\nu_1 FL} \left(\frac{\wp_{eg}^2}{\epsilon_0 \hbar} \frac{\nu_1^3}{3\pi c^3} \right) \left(\frac{3\pi c^2 L N}{2\nu_1^2 V} \right) \quad (2.59a)$$

$$= \frac{2}{k_1} \gamma \frac{d}{FL} (\delta + i\gamma_0), \quad (2.59b)$$

Recalling that the complex refractive index is related to the square root of the dielectric constant, $n = \sqrt{1 + \chi} \approx 1 + \frac{\chi}{2}$, limiting ourselves to the continuous-wave

case ($\omega = 0$), and expanding Eq. 2.59b to $\mathcal{O}(\delta^2)$, we obtain [89, 90],

$$\tilde{n}(\delta) \approx 1 + \frac{d/Lc\gamma}{\nu_1|\Omega(z)|^2} \left(\delta + i \frac{\gamma\delta^2}{|\Omega(z)|^2} + \mathcal{O}(\delta^3) \right). \quad (2.60)$$

We find that the transmission of the signal field, as a function of the two-photon detuning is

$$T(\delta, z) = \exp \{ -kz \operatorname{Im}[\chi] \} \approx \exp[-\delta^2/\Gamma_E^2], \quad (2.61)$$

where

$$\Gamma_E = |\Omega|^2 / (\gamma \sqrt{dz/L}) \quad (2.62)$$

is the characteristic width of the EIT transmission resonance [90].

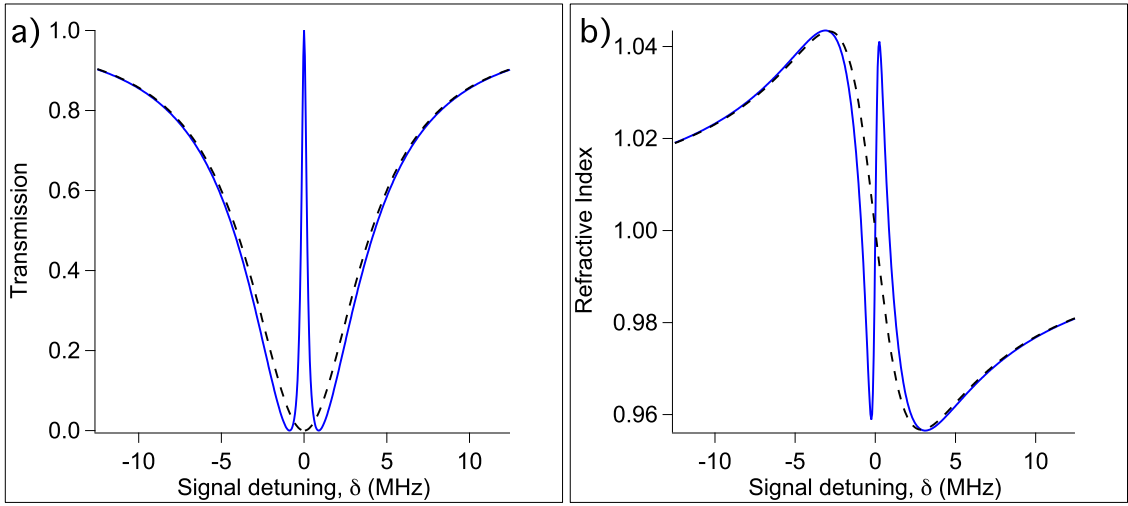


FIG. 2.2: (a) In the absence of a control field (dashed black lines), a broad range of frequencies is absorbed by the atomic medium, as is characteristic of a two-level system in a near-resonant field. When the control field is illuminated (solid blue line), a narrow window of transparency is created for the signal field. (b) The refractive index seen by the signal field. We note that the presence of the control field produces a steep, linear change in the refractive index near the two-photon resonance (see solid blue line), which leads to a dramatic reduction in the signal field group velocity.

Contrast this with the two-level, near-resonant field case, where a broad range of signal frequencies are absorbed by the atoms. We show the typical transmission

of a near-resonant light field as a function of detuning in the dashed black curves in Fig. 2.2(a). We note that on resonance ($\delta = 0$), there is no transmission. The blue curve in Fig. 2.2(a) depicts the transmission of the signal field through an ensemble of three-level Λ -type atoms. Here, we see that the presence of the control field has opened a narrow window of transparency, of width Γ_E around the two-photon resonance—this phenomenon is known as *Electromagnetically Induced Transparency* (EIT). We note an important result—that on the two-photon resonance, $\delta = 0$, Eq. 2.61 predicts perfect signal field transmission under EIT conditions. We remind the reader that Eq. 2.61 is valid for the ideal case of no spin-wave decay ($\gamma_0 = 0$). Inclusion of decoherence mechanisms will transform the EIT window from a Gaussian to a Lorentzian profile, and will limit the maximum value of transmission.

2.5 Dark state description of EIT

It is convenient to describe the effects of EIT by considering the response of the atoms to the presence of both fields. It is a straight-forward exercise to show that there is an eigenfunction, $|D\rangle$, of the Hamiltonian (Eq. 2.32) with a corresponding eigenvalue of 0, *i.e.*, $\hat{H}|D\rangle = 0$. This so-called dark-state is,

$$|D\rangle = \frac{\Omega|g\rangle - \alpha e^{i\phi}|s\rangle}{\sqrt{|\Omega|^2 + |\alpha|^2}}, \quad (2.63)$$

where we have introduced ϕ as the phase difference between the signal and control fields. If $\phi = 0$, then the eigenenergy of this state is 0, and once an atom is prepared in this state, it will stay there indefinitely (in the absence of any decoherence mechanisms). Since this new state is no longer coupled to either field, it does not interact with them. In other words, the two resonant absorption pathways interfere destructively. Thus, none of the atoms are promoted to the excited state and the

usual resonant absorption of the light fields vanishes.

2.6 Slow light and stored light

Since the atomic response is causal—an atom does not respond until it sees light—the absorption and index of refraction (*i.e.* the imaginary and real parts of the linear susceptibility) are related by the Kramers-Kronig relations [86],

$$\operatorname{Re}[\chi(\omega)] = 1 + \frac{1}{\pi} P \int_{-\infty}^{+\infty} \frac{\operatorname{Im}[\chi(\omega')]}{\omega' - \omega} d\omega' \quad (2.64)$$

$$\operatorname{Im}[\chi(\omega)] = \frac{1}{\pi} P \int_{-\infty}^{+\infty} \frac{\operatorname{Re}[\chi(\omega')] - 1}{\omega' - \omega} d\omega', \quad (2.65)$$

where P denotes that the Cauchy principal-values should be taken. Thus, we expect that the narrow window of transparency will be accompanied by a steep dispersion in the material's index of refraction $\frac{dn}{d\delta}$. Figure 2.2(b) depicts the refractive index experienced by the control field in the absence of the control field (dashed black line) and in the presence of the control field (solid blue lines). Indeed, near the two-photon resonance, the refractive index changes rapidly and linearly with respect to ω . This leads to a modification of the group velocity experienced by the signal pulse [86, 92]

$$v_g = \frac{c}{n(\omega) + \omega \frac{dn}{d\omega}}. \quad (2.66)$$

We see from the expression for the complex refractive index in Eq. 2.60, that

$$n_g = n + \nu_1 \frac{dn}{d\nu_1} = n + \nu_1 \frac{dn}{d\delta} \quad (2.67a)$$

$$\approx 1 + \frac{d\gamma c \delta}{\nu_1 L |\Omega|^2} + \frac{d\gamma c}{L |\Omega|^2} \quad (2.67b)$$

Near the two-photon resonance, n_g is dominated by the third term, so that the

group velocity experienced by a pulsed signal field is

$$v_g = c/n_g \approx \frac{|\Omega|^2 L}{\gamma d}. \quad (2.68)$$

In other words, the presence of the control field results in a dramatic reduction of the signal field's group velocity. Importantly, the intensity of the control field dictates the propagation velocity of the signal field (Eq. 2.68) by determining the spectral width of the EIT window (Eq. 2.62).

We can clearly see this by returning to the time domain, and considering a resonant ($\delta = 0$) signal field in the absence of any ground state decoherence mechanisms ($\gamma_0 = 0$), we find via Eq. 2.43 that

$$P(z, t) = -\frac{i}{\Omega^*(z)} \frac{\partial}{\partial t} S(z, t), \quad (2.69)$$

so that Eq. 2.41 becomes,

$$\left(\frac{\partial}{\partial t} + c \frac{\partial}{\partial z} \right) \mathcal{E}(z, t) = -\frac{g^2 N}{|\Omega(z)|^2} \frac{\partial}{\partial t} \mathcal{E}(z, t), \quad (2.70)$$

which, with Eqs. 2.58 and 2.68, can be written as

$$\left(\frac{\partial}{\partial t} + v_g \frac{\partial}{\partial z} \right) \mathcal{E}(z, t) = 0. \quad (2.71)$$

This equation describes the lossless, distortion-free propagation of a light field \mathcal{E} at a reduced group velocity v_g , and confirms the interpretation of the expression for $\chi(\omega)$ in Eq. 2.59b. We note an additional important distinction: under these conditions, the spin coherence is

$$S(z, t) = -\frac{g\sqrt{N}}{\Omega} \mathcal{E}(z, t). \quad (2.72)$$

In other words, there is a one-to-one correspondence between the spin wave and the signal field. In fact, since it is proportional to its amplitude, the spin coherence simply propagates alongside the signal field at the same reduced group velocity.

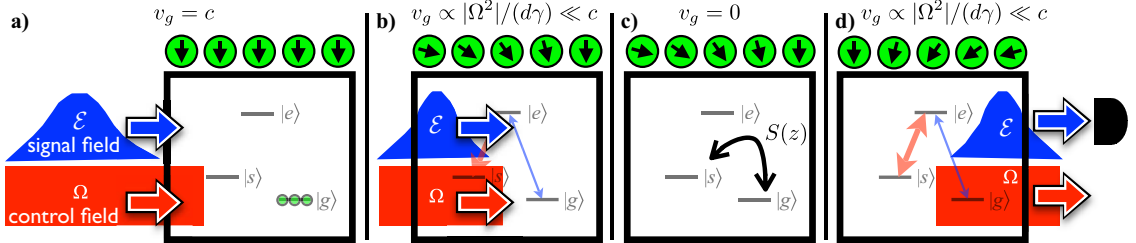


FIG. 2.3: (a) The control field (red) optically pumps all of the atoms (green dots) into the ground state $|g\rangle$. Before the EIT medium, the signal pulse (blue) propagates with $v_g \approx c$. (b) The intensity of the control field remains constant. Upon entering the cell, the signal pulse experiences a reduced $v_g \ll c$, causing the signal pulse to spatially compress. An atomic spin wave is created along the cell in the direction of the pulse propagation, as illustrated by the rotated atomic spins. (c) When most of the signal pulse is inside the cell, the control field is extinguished, which sends $v_g = 0$, and maps any information encoded in the signal pulse onto the spin wave. (d) After a prescribed amount of time, the control field is turned on, releasing the spin wave into the signal field, which leaves the cell.

We now consider the dynamics experienced by a pulsed signal field whose bandwidth fits inside the EIT window Γ_E . As portrayed in Fig. 2.3(a), Λ -type atoms are initially pumped into ground state $|g\rangle$ by the strong control field, represented in red. Outside of the interaction region, the signal pulse (blue) propagates with $v_g \approx c$. Upon entering the atomic region, the front portion of the signal field abruptly slows down because of the medium's low group velocity. Since the rear portion of the signal pulse still travels with an unaltered group velocity, the spatial length of the pulse, Δl is compressed according to

$$\Delta l = \frac{v_g}{c} \Delta l_0, \quad (2.73)$$

as compared to a free-space value Δl_0 . As the pulse propagates through the medium [see Fig. 2.3(b)], the atoms respond by being in a superposition of ground states

$|g\rangle$ and $|s\rangle$, thereby creating the spin coherence, $S(z)$, which shares a mapping with the signal field. As a result, the spin wave travels along with the signal field, until \mathcal{E} reaches the end of the interaction region and reaccelerates to $v_g \approx c$ (see Fig. 2.3). As a result of the reduced group velocity, this pulse has been delayed by a time

$$\tau_D = \frac{L}{v_g} - \frac{L}{c} \approx \frac{L}{v_g} = \frac{d\gamma}{|\Omega|^2}, \quad (2.74)$$

when compared to a pulse that propagated through vacuum.

Slow light can be a basis for quantum memory. If, rather than using a classical signal pulse, one uses a quantum state of light (*i.e.*, single photon wavepackets, squeezed states, *etc.*), then the above EIT description remains intact, due to the linearity of the equations of motion. We discuss this correspondence more precisely in Sec. 2.7. The only difference is that the signal field must be described in terms of field creation and annihilation operators, and appropriate Langevin noise operators must be used to account for the effects of quantum noise fluctuations [93–95]. Since the information originally encoded in the signal pulse was shared with the spin coherence during propagation, in essence, the EIT medium “remembers” the incident state for a time τ_D .

In order to extend the storage time of this type of quantum memory, a dynamic form of EIT is used. As we discussed earlier, it is notable that the group velocity, and hence the delay time, is dictated by the intensity of the control field. Therefore, by varying the control field’s intensity, one is able to control the dynamics of the signal pulse. In particular, reducing the control field intensity to zero reduces the group velocity to zero [see Fig. 2.3(c)]. At this point, all of the information about the signal field’s quantum state is mapped onto the atomic spin wave, which, in the absence of dephasing mechanisms, is frozen for a prescribed period of time, a phenomenon known as *stored light*. In order to retrieve this information, the control

field is turned on, thereby increasing v_g from zero and converting the spin wave back into a pulse of signal field light, which propagates out of the medium.

2.7 Dark state polariton description of stored light

For the above case of no decoherence between states $|g\rangle$ and $|s\rangle$, it is helpful to describe light storage by introducing a quasi-particle called a dark-state polariton [22, 23, 42], which has contributions from both photons and atoms. Here, we treat the signal field quantum mechanically, although we will find that the resulting equations of motion are identical to the semi-classical picture. We can describe the signal field by the electric field operator [87],

$$\hat{\mathcal{E}}(z, t) = \sum_k \hat{a}_k(t) e^{ikz} + \text{H.a.}, \quad (2.75)$$

where the sum is over the free-space photonic modes, \hat{a}_k are the corresponding bosonic field annihilation operators, and H.a. indicates usage of the Hermitian adjoint. The quantum properties of the medium are described by the collective atomic spin-flip slowly-varying operators,

$$\hat{\sigma}_{\mu\nu}(z, t) = \frac{1}{N_z} \sum_{j=1}^{N_z} |\mu_j\rangle \langle \nu_j| e^{-i\omega_{\mu\nu}t}, \quad (2.76)$$

where the sums are over all N_z atoms in a slice of atoms at position z that is thick enough so that $N_z \gg 1$ but thin enough so that the resulting collective fields are continuous [96]. In particular, the atomic polarization is described by the operator $\hat{P}(z, t) = \sqrt{N} \hat{\sigma}_{ge}(t)$, which oscillates at the optical frequency. The spin coherence (spin wave) is described by the operator $\hat{S}(z, t) = \sqrt{N} \hat{\sigma}_{gs}(z, t)$ which oscillates at the frequency splitting of $|g\rangle$ and $|s\rangle$. We treat the control field classically.

The effective rotating frame Hamiltonian is [96],

$$\hat{H} = -\hbar g\sqrt{N} \sum_j \left[\sigma_{eg}^j \hat{\mathcal{E}}(z_j) + \text{H.a.} \right] - \hbar \sum_j \left[\sigma_{es}^j \Omega(z_j, t) + \text{H.a.} \right], \quad (2.77)$$

where $g\sqrt{N}$ is the collectively enhanced coupling constant of atoms with the signal field. The evolution of the atomic coherences is governed by a set of Heisenberg equations,

$$i\hbar\partial_t \hat{A} = \left[\hat{A}, \hat{H} \right] + \hat{\Gamma} + \hat{F}, \quad (2.78)$$

where $\hat{A} \in \{\hat{P}, \hat{S}\}$ and \hat{H} is the atom-field interaction Hamiltonian, $\hat{\Gamma}$ describes decay and decoherence processes, and \hat{F} is describes the Langevin noise operators for the atomic operators [87, 89].

We assume that the signal field is weak (which is valid in the case of few photons) and that $\hat{\mathcal{E}}$ and Ω vary adiabatically. Under reasonable experimental conditions, the normally-ordered noise correlations of the Langevin operators are zero, such that the incoming noise is vacuum [40, 43, 97–99]. Thus, to leading order in $\hat{\mathcal{E}}$, we find [96],

$$(\partial_t + c\partial_z) \hat{\mathcal{E}}(z, t) = ig\sqrt{N} \hat{P}(z, t) \quad (2.79)$$

$$\hat{P}(z, t) = -\frac{i}{\Omega} \partial_t \hat{S} \quad (2.80)$$

$$\hat{S}(z, t) = -\frac{g\sqrt{N} \hat{\mathcal{E}}}{\Omega}. \quad (2.81)$$

These three equations are exactly analogous to their semi-classical counterparts in Eqs. 2.41–2.43. This is precisely the reason why we justify using weak pulses of light to study quantum memory experimentally; at least theoretically, there is a direct applicability of any findings to the realm of non-classical light.

We can obtain a solution to Eqs. 2.79–2.81 by introducing a new quantum field,

the dark-state polariton [22, 23, 42]

$$\hat{\Psi}(z, t) = \cos \theta \hat{\mathcal{E}}(z, t) - \sin \theta \hat{S}(z, t). \quad (2.82)$$

The mixing angle θ determines the weighting of the photonic and atomic contributions and is defined as,

$$\tan \theta = \frac{g\sqrt{N}}{\Omega}. \quad (2.83)$$

It can be shown that the dark-state polariton's time evolution is described by [22, 23, 42]

$$[\partial_t + c \cos^2 \theta \partial_z] \hat{\Psi}(z, t) = 0. \quad (2.84)$$

This equation describes the shape-preserving propagation of a field that moves with velocity $v_g = c \cos^2 \theta \approx c|\Omega|^2/(g^2N)$:

$$\hat{\Psi}(z, t) = \hat{\Psi} \left(z - c \int_0^t dt' \cos^2 \theta(t'), t = 0 \right). \quad (2.85)$$

The dark-state polariton picture allows us to see clearly how it is possible to control the polariton properties via the control field intensity. Specifically, by reducing Ω to 0, the group velocity is reduced to zero, and θ is rotated to $\pi/2$. Thus, the polariton is purely spin-wave-like when the control field is off. Likewise, in the limit of a strong control field, $|\Omega|^2 \gg g^2N$, then $\theta \rightarrow 0$, and the polariton has purely photonic character with $v_g \rightarrow c$. This suggests that a stationary (spin wave) polariton can be reaccelerated to the vacuum speed of light. *i.e.*, The stored quantum state is transferred back to the light field. Recent experiments have shown the efficacy of dynamic EIT for storing and retrieving classical light pulses [24, 25] and preserving phase coherence [100].

2.8 Efficiency of EIT-based storage

The figure of merit of any memory device is its memory efficiency, or the probability of retrieving an incoming single photon after storage for a time τ_s . Equivalently, this is the energy ratio of the initial and retrieved signal pulses,

$$\eta = \frac{\int_{\tau_s}^{\tau_s+T} |\mathcal{E}_{\text{out}}(t)|^2 dt}{\int_{-T}^0 |\mathcal{E}_{\text{in}}(t)|^2 dt}, \quad (2.86)$$

where the variable T is the pulse duration.

Even under the assumption of no atomic decoherence, achievement of 100% memory efficiency requires the simultaneous balancing of losses due to the finite EIT window $\Gamma_E = |\Omega|^2/(\gamma\sqrt{d})$ and a finite $v_g/L = |\Omega|^2/\gamma d$ [43, 99].

On one hand, the group velocity v_g must be low enough to compress the entire signal pulse into the interaction region of length L . If v_g is too high during the writing stage of storage, then the pulse can “leak” out of the end of the cell before the control field is turned off—taking information with it. Thus, we require that $v_g T \ll L$. On the other hand, if one shortens the temporal length of the pulse to compensate for this effect, then its bandwidth increases, possibly extending outside of the EIT window, so parts of the pulse are lost to absorption. Thus, $1/T \ll \Gamma_E$. The simultaneous satisfaction of these criteria is possible at very high optical depth $d \gg 1$ [43, 99].

Further decohering physical effects conspire to limit the efficiency. For instance, gas atoms can diffuse during all stages of storage, but most importantly during the waiting time. If the diameters of the light beams are smaller than the diameter of the vapor cell used to contain the atoms, then the atoms can leave the interaction region and take information away [101]. Additionally, atomic collisions cause the spin coherence to dephase and thus negatively effect the fidelity of retrieval [102,

103]. Unfortunately, many of these degradation factors are more prominent at high atomic densities. Furthermore, the off-resonant interaction of the control field on the $|g\rangle \rightarrow |e\rangle$ transition can spontaneously produce a new Stokes light field at an optical frequency of $(\nu_2 - \Delta_{\text{hf}})$ via four-wave mixing.

2.9 The effects of four-wave mixing

In the limit of low optical depth, it is sufficient to take into account only the effects of the single Λ system described above. However, many applications require operation at high optical depth [43, 104], where additional nonlinear effects may become important [105–108]. One such effect is resonant four-wave mixing (FWM)—a nonlinear process arising from the far off-resonant interaction of the control field. Earlier studies [109, 110, 110–119] found that the propagation of the signal field in this case is strongly affected by the presence of the Stokes field.

The effect of four-wave mixing can be advantageous or detrimental, depending on the details of the application. For example, in quantum memory applications, the resonant mixing reduces the fidelity by adding extra noise into the signal field. In addition, FWM may limit the storage efficiency at higher optical depth [120]. On the other hand, non-classical correlations between the signal and Stokes fields can individually carry quantum information and produce entangled photons [53, 121] and images [122]. Similarly, for slow light applications, the conversion of an original pulse from the signal to Stokes channel may reduce the readout efficiency [123]. However, under certain conditions, FWM may lead to gain for both the signal and Stokes fields, which could compensate for any optical losses [124].

In this section, we review the relevant theory governing the off-resonant interaction of the control field on the $|g\rangle \rightarrow |e\rangle$ transition, which can coherently and efficiently create a new Stokes field, which is detuned from the $|s\rangle \rightarrow |e\rangle$ transition. We

theoretically model this effect by considering a double- Λ configuration, consisting of a near-resonant Λ system formed by the control and signal fields and of the additional far-detuned Λ system formed by the same control field ($\nu_C = \omega_{es}$, Rabi frequency Ω'), applied to the state $|g\rangle$ and by an additional Stokes field ($\nu' = \omega_{es} - \Delta_{\text{hf}} - \delta$, Rabi frequency α'). In Fig. 2.4, we provide an illustration of the double- Λ system.

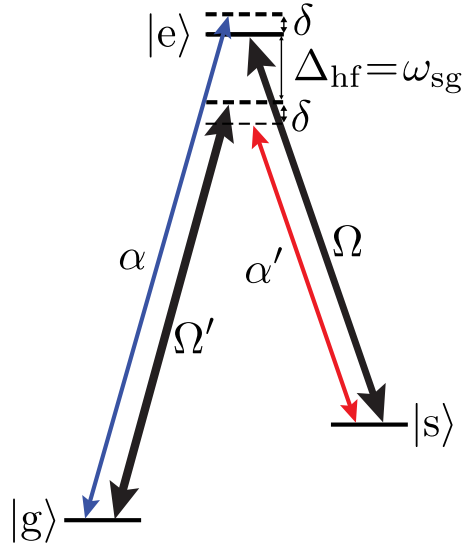


FIG. 2.4: The double- Λ system used in theoretical modeling of the FWM interaction with EIT. In our case, $|g\rangle$ and $|s\rangle$ correspond to the ^{87}Rb ground state sublevels $|F, m_F\rangle = |1, 1\rangle, |2, 2\rangle$, respectively; $|e\rangle$ corresponds to the excited state $|F', m_F\rangle = |2, 2\rangle$. Ω and Ω' (in black) represent the Rabi frequencies of the same control field applied to two different transitions, as depicted. α (in blue) and α' (red) represent the Rabi frequencies associated with the signal and Stokes fields, respectively.

To account for such an interaction, we must append to the original Hamiltonian (Eq. 2.28) terms that describe the interaction of Ω' and α' with the corresponding atomic levels. In what follows, we consider an atom at position $z = 0$ for simplicity, and find

$$\hat{H} = \omega_{sg}\hat{\sigma}_{ss} + \omega_{eg}\hat{\sigma}_{ee} - \left[\alpha e^{-i\nu t}\hat{\sigma}_{eg} + \alpha' e^{-i\nu' t}\hat{\sigma}_{es} + \Omega e^{-i\nu_{at}t}\hat{\sigma}_{es} + \Omega' e^{-i\nu_{at}t}\hat{\sigma}_{eg} + \text{H.c.} \right] \quad (2.87)$$

As before, we seek to remove the optical frequencies and time dependence by

use of a rotating frame, which is invoked via the unitary transformation in Eq. 2.29. Employing this, and assuming resonant control fields, we find that

$$\tilde{H}/\hbar = -\delta\hat{\sigma}_{ss} - \delta\hat{\sigma}_{ee} - [\alpha\hat{\sigma}_{eg} + \Omega\hat{\sigma}_{es} + \alpha'e^{i(\Delta_{\text{hf}}+\delta)t}\hat{\sigma}_{es} + \Omega'e^{i(\Delta_{\text{hf}}+\delta)t}\hat{\sigma}_{eg} + \text{H.c.}]. \quad (2.88)$$

It is clear in this case that a rotating frame, in which the Hamiltonian is time-independent, does not exist. In order to remedy this, it is necessary to employ a Floquet basis [125]. In what follows, we work with Schrödinger's equation and wavefunctions, rather than the Master Equation for the density matrix, for simplicity. We can expand the wavefunction $|\tilde{\psi}\rangle$ as an infinite series representation as,

$$\begin{aligned} |\tilde{\psi}\rangle &= (\dots + c_g^{(-1)}e^{i(\Delta_{\text{hf}}+\delta)t} + c_g^{(0)} + c_g^{(+1)}e^{-i(\Delta_{\text{hf}}+\delta)t} + \dots) |g\rangle \\ &\quad (\dots + c_s^{(-1)}e^{i(\Delta_{\text{hf}}+\delta)t} + c_s^{(0)} + c_s^{(+1)}e^{-i(\Delta_{\text{hf}}+\delta)t} + \dots) |s\rangle \\ &\quad (\dots + c_e^{(-1)}e^{i(\Delta_{\text{hf}}+\delta)t} + c_e^{(0)} + c_e^{(+1)}e^{-i(\Delta_{\text{hf}}+\delta)t} + \dots) |e\rangle. \end{aligned} \quad (2.89)$$

We now equate $i\hbar\partial_t|\tilde{\psi}\rangle = \tilde{H}|\tilde{\psi}\rangle$ and collect terms in the same power of $e^{i(\Delta_{\text{hf}}+\delta)t}$.

Doing so, we find the following recursion relations,

$$i\dot{c}_g^{(n)} = -n(\Delta_{\text{hf}} + \delta)c_g^{(n)} - \alpha^*c_e^{(n)} - \Omega'^*c_e^{(n-1)} \quad (2.90)$$

$$i\dot{c}_s^{(n)} = -[n(\Delta_{\text{hf}} + \delta) + \delta]c_s^{(n)} - \Omega^*c_e^{(n)} - \alpha'^*c_e^{(n-1)} \quad (2.91)$$

$$i\dot{c}_e^{(n)} = -[n(\Delta_{\text{hf}} + \delta) + \delta]c_e^{(n)} - \alpha'^*c_g^{(n)} - \Omega c_s^{(n)} - \alpha'c_s^{(n+1)} - \Omega'c_g^{(n+1)}. \quad (2.92)$$

We've now essentially exchanged time-dependence for an $\infty \times \infty$ matrix,

$$i \frac{d}{dt} \begin{pmatrix} \vdots \\ c_g^{(-1)} \\ c_s^{(-1)} \\ c_e^{(-1)} \\ c_g^{(0)} \\ c_s^{(0)} \\ c_e^{(0)} \\ c_g^{(+1)} \\ c_s^{(+1)} \\ c_e^{(+1)} \\ \vdots \end{pmatrix} = \begin{pmatrix} \ddots & \vdots & \ddots \\ \dots & \boxed{\Delta_{\text{hf}} + \delta} & 0 & -\alpha^* & 0 & 0 & 0 & 0 & 0 & 0 & \dots \\ \dots & 0 & \Delta_{\text{hf}} & -\Omega^* & 0 & 0 & 0 & 0 & 0 & 0 & \dots \\ \dots & -\alpha & -\Omega & \Delta_{\text{hf}} - \delta & -\Omega' & -\alpha' & 0 & 0 & 0 & 0 & \dots \\ \dots & 0 & 0 & -\Omega'^* & \boxed{0} & \boxed{0} & -\alpha^* & 0 & 0 & 0 & \dots \\ \dots & 0 & 0 & -\alpha'^* & \boxed{0} & \boxed{-\delta} & -\Omega^* & 0 & 0 & 0 & \dots \\ \dots & 0 & 0 & 0 & \boxed{-\alpha} & \boxed{-\Omega} & \boxed{-\delta} & -\Omega' & -\alpha' & 0 & \dots \\ \dots & 0 & 0 & 0 & 0 & 0 & -\Omega'^* & \boxed{-(\Delta_{\text{hf}} + \delta)} & 0 & -\alpha^* & \dots \\ \dots & 0 & 0 & 0 & 0 & 0 & -\alpha'^* & 0 & \boxed{-(\Delta_{\text{hf}} + 2\delta)} & -\Omega^* & \dots \\ \dots & 0 & 0 & 0 & 0 & 0 & 0 & -\alpha & -\Omega & \boxed{-(\Delta_{\text{hf}} + 2\delta)} & \dots \\ \ddots & \vdots & \ddots \end{pmatrix} \begin{pmatrix} \vdots \\ c_g^{(-1)} \\ c_s^{(-1)} \\ c_e^{(-1)} \\ c_g^{(0)} \\ c_s^{(0)} \\ c_e^{(0)} \\ c_g^{(+1)} \\ c_s^{(+1)} \\ c_e^{(+1)} \\ \vdots \end{pmatrix} \quad (2.93)$$

It is notable that the diagonal blocks are identical but shifted relative to each other by multiples of $(\Delta_{\text{hf}} + \delta)$. The off-diagonal blocks connect the nearest diagonal blocks and are identical. At this point, we elect to adiabatically eliminate all of the Hilbert space except for $\{|g\rangle^{(0)}, |s\rangle^{(0)}, |e\rangle^{(0)}\}$, which provides an effective Hamiltonian to lowest order in the small parameter Δ_{hf}^{-1} . The result is,

$$i \frac{d}{dt} \begin{pmatrix} c_g^{(0)} \\ c_s^{(0)} \\ c_e^{(0)} \end{pmatrix} = \begin{pmatrix} \frac{-|\Omega'|^2}{\Delta_{\text{hf}}} & -\frac{\Omega'^* \alpha'}{\Delta_{\text{hf}}} & -\alpha^* \\ -\frac{\Omega' \alpha'^*}{\Delta_{\text{hf}}} & -\delta - \frac{|\alpha'|^2}{\Delta_{\text{hf}}} & -\Omega^* \\ -\alpha & -\Omega & -\delta + \frac{|\Omega'|^2}{\Delta_{\text{hf}}} + \frac{|\alpha'|^2}{\Delta_{\text{hf}}} \end{pmatrix} \begin{pmatrix} c_g^{(0)} \\ c_s^{(0)} \\ c_e^{(0)} \end{pmatrix}. \quad (2.94)$$

Here, we see that the presence of Ω' results in AC-Stark shifts of levels $|e\rangle$ and $|g\rangle$ by $\delta_s = |\Omega'|^2/\Delta_{\text{hf}}$ and $-\delta_s$, respectively, and an effective Rabi frequency $\Omega' \alpha'/\Delta_{\text{hf}}$, which couples $|g\rangle$ to $|s\rangle$. Further, the presence of α' results in small AC-Stark shifts of levels $|s\rangle$ and $|g\rangle$ of $\mathcal{O}(|\alpha'|^2)$, which we elect to ignore, since α and α' are sufficiently weak. We shift all energy levels down by δ_s , so that $|g\rangle$ has zero energy. This gives an effective time-independent Hamiltonian,

$$H = -(\delta - \delta_s)|s\rangle\langle s| - (\delta - 2\delta_s)|e\rangle\langle e| - \left[\alpha|e\rangle\langle g| + \Omega|e\rangle\langle s| + \frac{\Omega' \alpha'^*}{\Delta_{\text{hf}}}|s\rangle\langle g| + \text{H.c.} \right]. \quad (2.95)$$

As before, we can solve for the time evolution of the density matrix elements to find,

$$\partial_t \tilde{\rho}_{sg} = -[\gamma_0 - i(\delta - \delta_s)]\tilde{\rho}_{sg} + i\Omega^* \tilde{\rho}_{eg} + i\frac{\Omega'}{\Delta_{\text{hf}}}\alpha'^*(\tilde{\rho}_{gg} - \tilde{\rho}_{ss}) - i\alpha\tilde{\rho}_{se} \quad (2.96)$$

$$\partial_t \tilde{\rho}_{eg} = -[\gamma - i(\delta - 2\delta_s)]\tilde{\rho}_{eg} + i\Omega\tilde{\rho}_{sg} + i\alpha(\tilde{\rho}_{gg} - \tilde{\rho}_{ee}) - i\frac{\Omega'}{\Delta_{\text{hf}}}\alpha'^* \tilde{\rho}_{es} \quad (2.97)$$

$$\partial_t \tilde{\rho}_{es} = -(\gamma_{es} + i\delta_s)\tilde{\rho}_{es} + i\alpha\tilde{\rho}_{gs} - i\frac{\Omega^*}{\Delta_{\text{hf}}}\alpha' \tilde{\rho}_{eg} - i\Omega(\tilde{\rho}_{ee} - \tilde{\rho}_{ss}) \quad (2.98)$$

$$\partial_t \tilde{\rho}_{gg} = \Gamma_{eg}\tilde{\rho}_{ee} + i(\alpha^* \tilde{\rho}_{eg} - \alpha\tilde{\rho}_{ge}) + i\left(\frac{\alpha'\Omega'^*}{\Delta_{\text{hf}}}\tilde{\rho}_{sg} - \frac{\alpha'^*\Omega'}{\Delta_{\text{hf}}}\tilde{\rho}_{gs}\right) \quad (2.99)$$

$$\partial_t \tilde{\rho}_{ss} = \Gamma_{es}\tilde{\rho}_{ee} + i(\Omega^* \tilde{\rho}_{es} - \Omega\tilde{\rho}_{se}) - i\left(\frac{\alpha'\Omega'^*}{\Delta_{\text{hf}}}\tilde{\rho}_{sg} - \frac{\alpha'^*\Omega'}{\Delta_{\text{hf}}}\tilde{\rho}_{gs}\right). \quad (2.100)$$

For completeness, we remark that the coherences above are related to the zeroth order amplitude coefficients from Eq. 2.89, *i.e.*, $\tilde{\rho}_{ij} = c_i^{(0)}c_j^{*(0)}$. To first order in the weak light fields α and α' , we find that all of the atoms are prepared in $|g\rangle$, so that $\tilde{\rho}_{gg} \approx 1$, and $\tilde{\rho}_{ee} = \tilde{\rho}_{ss} = 0$. In other words, the off-resonant interaction of Ω' on the $|g\rangle \rightarrow |e\rangle$ transition does not result in significant optical pumping out of $|g\rangle$. With this approximation, we can adiabatically eliminate $\tilde{\rho}_{es}$ by setting the right hand side of Eq. 2.98 to zero. We find that it contributes at first order in the weak like fields α and α' . Thus, contributions involving this coherence in Eqs. 2.96 and 2.97 contribute at second order of these light fields, so we can ignore them.

The propagation of the signal field through these atoms is described by Eq. 2.18. Correspondingly, the Stokes field propagates according to a form like

$$\left(\frac{\partial}{\partial t} + c\frac{\partial}{\partial z}\right)\mathcal{E}'^*(z, t) = -\frac{i\nu_1 N}{2\epsilon_0 V}\wp_{es}\tilde{\rho}_{se}, \quad (2.101)$$

however, we must be careful about the coherence $\tilde{\rho}_{se}$. The polarization that drives the Stokes field is the one that oscillates at a similar frequency, which, in the rotating frame is $\Delta + \delta$ (see Fig. 2.4). In particular, from the Floquet decomposition in Eq. 2.89, we are looking for products of amplitude coefficients of the form $c_s^{(-1)}c_e^{*(0)}$

or $c_s^{(0)}c_e^{*(-1)}$. By analyzing the recursion relations in Eqs. 2.90–2.92, we observe that $c_s^{-1} \propto 1/\Delta_{\text{hf}}^2 \approx 0$ to our degree of expansion. We also find that $c_e^{(-1)} \approx \frac{\alpha'}{\Delta_{\text{hf}}}c_s^{(0)} + \frac{\Omega'}{\Delta_{\text{hf}}}c_g^{(0)}$. Therefore,

$$\tilde{\rho}_{se} = c_s^{(0)}c_e^{*(-1)} \approx \frac{\alpha'^*}{\Delta_{\text{hf}}}|c_s^{(0)}|^2 + \frac{\Omega'^*}{\Delta_{\text{hf}}}c_s^{(0)}c_g^{*(0)} \approx \frac{\Omega'^*}{\Delta_{\text{hf}}}\tilde{\rho}_{sg}. \quad (2.102)$$

Thus, the following four equations suffice to describe the interaction of two weak light pulses through a collection of Λ -type atoms:

$$\left(\frac{\partial}{\partial t} + c\frac{\partial}{\partial z}\right)\mathcal{E}(z, t) = \frac{i\nu_1 N}{2\epsilon_0 V}\wp_{eg}\tilde{\rho}_{eg} \quad (2.103)$$

$$\left(\frac{\partial}{\partial t} + c\frac{\partial}{\partial z}\right)\mathcal{E}'^*(z, t) = -\frac{i\nu_2 N}{2\epsilon_0 V}\wp_{es}\frac{\Omega'^*}{\Delta_{\text{hf}}}\tilde{\rho}_{sg} \quad (2.104)$$

$$\partial_t\tilde{\rho}_{sg} = -[\gamma_0 - i(\delta - \delta_s)]\tilde{\rho}_{sg} + i\Omega^*\tilde{\rho}_{eg} + i\frac{\Omega'}{\Delta_{\text{hf}}}\alpha'^* \quad (2.105)$$

$$\partial_t\tilde{\rho}_{eg} = -[\gamma - i(\delta - 2\delta_s)]\tilde{\rho}_{eg} + i\Omega\tilde{\rho}_{sg} + i\alpha. \quad (2.106)$$

We will discuss the solutions and interpretation of Eqs. 2.103–2.106 in greater detail in Chapter 6.

CHAPTER 3

Experimental Arrangements

In this chapter, we describe the experimental arrangements; it is organized as follows. First, we discuss the physical properties of ^{87}Rb atoms and discuss the correspondence with the theoretical model. We then describe how we created the signal and control light beams for EIT-based experiments. We further describe the experimental apparatus and outline the experiments that were performed.

3.1 The atoms

There are no such things as three-level atoms. However, if one is clever about light polarizations and frequencies, then a three-level interaction can be experimentally realized in alkali atoms. In our experiments, we employ vapor cells of ^{87}Rb . In this section, we describe in detail these vapor cells and their contents.

There are two naturally occurring isotopes of Rb: ^{85}Rb , which is stable and has a natural abundance of 72.17(2)%, and radioactive ^{87}Rb , which has a natural abundance of 27.83(2)% and decays to $\beta^- + ^{87}\text{Sr}$ with a half-life of 4.88×10^{10} yr, making it effectively stable. The Rb atom has 37 electrons in the electronic configuration $[\text{Kr}]5s^1$, such that only one unbound electron is in the outermost shell,

much like Hydrogen. In Rb, the unbound electron is in the $5^2S_{1/2}$ ground state, thus, its quantum numbers are $n = 5$, $\ell = 0$, $s = \frac{1}{2}$, $m_s = \pm\frac{1}{2}$, and $j = \frac{1}{2}$. Because of selection rules, the ground state electron can be optically excited into the $5P$ orbital.

Due to the coupling of spin and orbital angular momentum (LS), the excited states are separated in energy. In particular, the total electron angular momentum, \mathbf{J} , is the vector sum of its orbital angular momentum \mathbf{L} and its spin angular momentum \mathbf{S} :

$$\mathbf{J} = \mathbf{L} + \mathbf{S}. \quad (3.1)$$

Using the convention that the expectation value for magnitude of \mathbf{J} is $\sqrt{J(J+1)}\hbar$ and the eigenvalue of the z -component, J_z is $m_j\hbar$, the corresponding quantum number J must lie in the range

$$|L - S| \leq J \leq L + S. \quad (3.2)$$

For the ground state of either isotope of Rb, $L = 0$ and $S = \frac{1}{2}$, so $J = \frac{1}{2}$. For the first excited state, $L = 1$, so $J = \frac{1}{2}$ or $J = \frac{3}{2}$. The optical transition $5S_{1/2} \rightarrow 5P_{1/2}$, commonly referred to as the D_1 line, has a wavelength of $\lambda = 794.978\,850\,9(8)$ nm with a radiative excited state lifetime of 27.70(4) ns, corresponding to natural line width of $\Gamma = (2\pi) 5.746(8)$ MHz (FWHM). The wavelength of the $5S_{1/2} \rightarrow 5P_{3/2}$ (D_2) line is $\lambda = 780.241\,209\,686(13)$ nm, with a lifetime of 26.24(4) ns [$\Gamma = (2\pi) 6.065(9)$ MHz (FWHM)] [1].

As a result of the coupling between the electron angular momentum \mathbf{J} and nuclear angular momentum \mathbf{I} , each of the fine-structure transitions have hyperfine structure. The total atomic angular momentum is:

$$\mathbf{F} = \mathbf{J} + \mathbf{I}, \quad (3.3)$$

whose magnitude can take values

$$|J - I| \leq F \leq J + I. \quad (3.4)$$

The actual structure depends on the isotope, as ^{85}Rb , which has 48 neutrons, has nuclear spin $I = \frac{5}{2}$ and ^{87}Rb , which has 50 neutrons, has $I = \frac{3}{2}$. At this point, we restrict our discussion to the D_1 transition of ^{87}Rb , since this is the transition relevant to the experiment. For the ^{87}Rb ground state, with $J = \frac{1}{2}$ and $I = \frac{3}{2}$, there are two hyperfine manifolds, $F = 1$ or $F = 2$, which are split by a frequency difference of 6.834 682 610 904 29(9) GHz [1]. Likewise, for the first excited state of the D_1 line ($5^2P_{1/2}$), $F = 1$ or $F = 2$, which are split by 816.656(30) MHz [1]. In Fig. 3.1, we plot the hyperfine structure of ^{87}Rb .

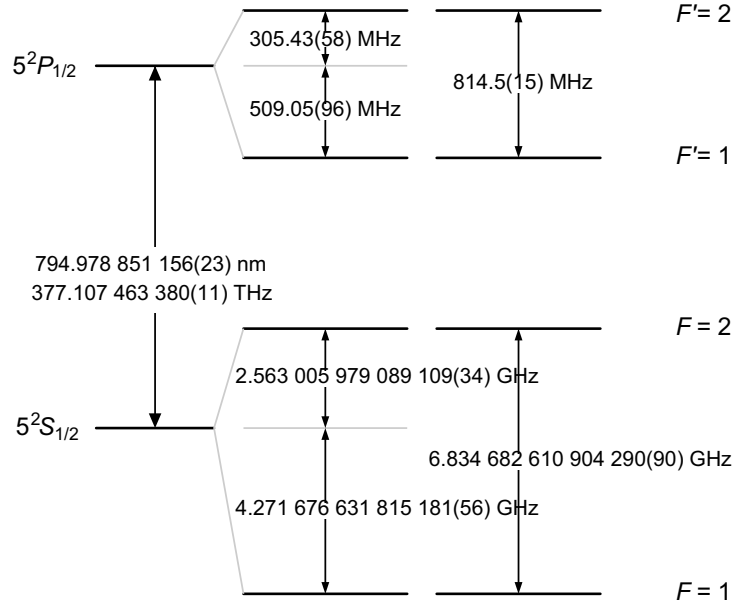


FIG. 3.1: ^{87}Rb D_1 hyperfine structure with frequency splitting between the hyperfine energy levels [1].

3.1.1 Zeeman sub-structure and transitions

Additionally, within each hyperfine manifold there are $2F + 1$ magnetic sub-levels, whose degeneracy is lifted by a magnetic field. These levels possess a magnetic quantum number m_F ranging from $-F$ to F . Specifically, we can compute the shift experienced by an atom in state $|F, m_F\rangle$ in the presence of an external magnetic field, $\mathbf{B} = B\hat{z}$ along the z -axis. The Hamiltonian describing this interaction is [88, 91]

$$\hat{H}_B = -\boldsymbol{\mu} \cdot \mathbf{B}, \quad (3.5)$$

where $\boldsymbol{\mu}$ is the magnetic dipole moment. For a weak magnetic field, the Zeeman splitting is small compared to the hyperfine splitting, and so F and m_F are a good quantum number [91]. In other words, the total angular momentum operator, $\mathbf{F} = \mathbf{I} + \mathbf{J}$ commutes with the interaction Hamiltonian. We can then relate the magnetic dipole moment, μ_B to the Bohr magneton, $\mu_B = e\hbar/(2m_e)$, via $\mu = g_F\mu_B F_z$. Here, e and m_e are the electron's charge and mass respectively, and g_F is called the total angular momentum g-factor. Finally, the energy shift experienced by state $|F, m_F\rangle$ in the presence of this external magnetic field is

$$E(F, m_F) = \frac{\mu_B}{\hbar} g_F \langle F, m_F | F_z B_z | F, m_F \rangle \quad (3.6)$$

$$= \mu_B g_F m_F B_z. \quad (3.7)$$

In the absence of the magnetic field, these m_F levels are degenerate, and we wish to study transitions between various hyperfine manifolds. Specifically, the probability of an electron in state $|F, m_F\rangle$ being excited to state $|F', m_{F'}\rangle$ is determined in part by the square of the electric dipole matrix element,

$$\wp = \langle F, m_F | \hat{\boldsymbol{\epsilon}} \cdot \mathbf{d} | F', m_{F'} \rangle. \quad (3.8)$$

It is useful to employ the Wigner-Eckart theorem [126, 127] to factor out the angular dependence and write φ as a product of a Clebsch-Gordan coefficient and a reduced matrix element,

$$\langle F, m_F | \hat{\epsilon} \cdot \mathbf{d} | F', m_{F'} \rangle = \langle F || \hat{\epsilon} \cdot \mathbf{d} || F' \rangle (-1)^{F'-1+m_F} \sqrt{2F+1} \begin{pmatrix} F & 1 & F' \\ m_F & q & -m_{F'} \end{pmatrix}, \quad (3.9)$$

where the double bars indicate a reduced matrix element, and the Wigner 3- j symbol is related to the Clebsch-Gordan coefficient, as we will show presently. The variable q indicates the ellipticity of the laser light ($q = \pm 1$ for right/left circularly polarized light, and $q = 0$ for linearly polarized light). The Wigner 3- j symbol is non-zero only if

$$m_{F'} = m_F + q, \quad (3.10)$$

which is essentially a transition selection rule effected by conservation of angular momentum.

We further simplify by factoring out the F and F' dependence into a Wigner 6- j symbol, which leaves us with a reduced matrix element in the J basis [126, 127]:

$$\begin{aligned} \langle F || \hat{\epsilon} \cdot \mathbf{d} || F' \rangle &= \langle J \ I \ F || \hat{\epsilon} \cdot \mathbf{d} || J' \ I' \ F' \rangle \\ &= \langle J || \hat{\epsilon} \cdot \mathbf{d} || J' \rangle (-1)^{F'+J+1+I} \sqrt{(2F'+1)(2J'+1)} \begin{Bmatrix} J & J' & 1 \\ F' & F & I \end{Bmatrix}. \end{aligned} \quad (3.11)$$

Combining Eqs. 3.9 and 3.11 we find [126],

$$\begin{aligned}
\wp &= \langle J || \hat{\epsilon} \cdot \mathbf{d} || J' \rangle (-1)^{2F'+J+I+m_F} \sqrt{(2F+1)(2F'+1)(2J+1)} \\
&\times \begin{pmatrix} F & 1 & F' \\ m_F & q & -m_{F'} \end{pmatrix} \begin{Bmatrix} J & J' & 1 \\ F' & F & I \end{Bmatrix} \\
&\equiv \text{CG}_{\wp_0},
\end{aligned} \tag{3.12}$$

where \wp is the reduced dipole matrix element and we have related the Clebsch-Gordan coefficients to the Wigner symbols. The reduced dipole matrix element can be calculated if the radial wavefunctions are known (*e.g.* for Hydrogen). It is more convenient to calculate them from the measurements of the lifetime of the excited state, τ , via [88, 91]

$$\frac{1}{\tau} = \frac{\nu^3}{3\pi\epsilon_0\hbar c^3} \frac{2J+1}{2J'+1} |\wp_0|^2. \tag{3.13}$$

For the D_1 line of ^{87}Rb [1],

$$\wp_0 = \langle J = \frac{1}{2} || \hat{\epsilon} \cdot \mathbf{d} || J' = \frac{1}{2} \rangle = 2.537(3) \times 10^{-29} \text{C} \cdot \text{m} \tag{3.14}$$

For the particular case of transitions driven by right-circularly polarized light (σ^+ , or $q = 1$), as depicted in Fig. 3.2. In this case, selection rules dictate that $m_{F'} = m_F + 1$. The Clebsch-Gordan coefficients for transitions $|F = 1, m_F\rangle \rightarrow |F', m_{F'} = m_F + 1\rangle$ are given in Table 3.1. The corresponding Clebsch-Gordan coefficients for transitions $|F = 2, m_F\rangle \rightarrow |F', m_{F'} = m_F + 1\rangle$ are given in Table 3.2.

3.1.2 Vapor cells

For our experiments, ^{87}Rb was housed in cylindrical Pyrex cell of length $L = 75$ mm and diameter 22 mm. At room temperatures, ^{87}Rb is in the solid phase, but it readily becomes liquid above its melting point of 39.31°C (312.46 K). Above this

	$m_F = -1$	$m_F = 0$	$m_F = +1$
$F' = 2$	$-\sqrt{\frac{1}{12}}$	$-\sqrt{\frac{1}{4}}$	$-\sqrt{\frac{1}{2}}$
$F' = 1$	$-\sqrt{\frac{1}{12}}$	$-\sqrt{\frac{1}{12}}$	0

TABLE 3.1: $^{87}\text{Rb } D_1$ ($5^2S_{1/2} \rightarrow 5^2P_{1/2}$) Clebsch-Gordan coefficients for σ^+ transitions, $|F = 1, m_F\rangle \rightarrow |F', m_{F'} = m_F + 1\rangle$

	$m_F = -2$	$m_F = -1$	$m_F = 0$	$m_F = +1$	$m_F = +2$
$F' = 2$	$\sqrt{\frac{1}{6}}$	$\sqrt{\frac{1}{4}}$	$\sqrt{\frac{1}{4}}$	$\sqrt{\frac{1}{6}}$	0
$F' = 1$	$\sqrt{\frac{1}{2}}$	$\sqrt{\frac{1}{4}}$	$\sqrt{\frac{1}{12}}$	0	0

TABLE 3.2: $^{87}\text{Rb } D_1$ ($5^2S_{1/2} \rightarrow 5^2P_{1/2}$) Clebsch-Gordan coefficients for σ^+ transitions, $|F = 2, m_F\rangle \rightarrow |F', m_{F'} = m_F + 1\rangle$

temperature, the dependence of the pressure, P_v [Torr] of the Rb vapor inside the cell on the temperature, T [K], is given by [1]

$$\log_{10} P_v = -94.048\ 26 - \frac{1961.258}{T} - 0.037\ 716\ 87\ T + 42.575\ 26\ \log_{10}\ T. \quad (3.15)$$

The atomic weight of ^{87}Rb is 86.909 atomic units, or 1.443×10^{-25} kg [1]. Assuming a classical gas of non-interacting atoms, the atomic speeds are described by a Maxwell-Boltzmann distribution about a most probable speed v_m [128]:

$$v_m = \sqrt{\frac{2kT}{m_{\text{Rb}}}} \quad (3.16)$$

The average speed in one dimension is computed as

$$\begin{aligned}\langle v \rangle &= \frac{4}{\sqrt{\pi} v_m^3} \int_0^\infty dv v^3 \exp\left(-\frac{v^2}{v_m^2}\right) \\ &= \frac{2}{\sqrt{\pi}} v_m = \sqrt{\frac{8}{\pi} \frac{kT}{m_{\text{Rb}}}}.\end{aligned}\tag{3.17}$$

For ^{87}Rb at a temperature of $T = 60^\circ\text{C}$ (333.15 K), $\langle v \rangle \approx 300$ m/s. Thus, even an atom that is traveling longitudinally down the cell will take less than 200 μs , which is too short for atomic memory experiments. As described in Sec. 3.3, typical laser beam diameters were on the order of 5 mm. Thus, a transversely-moving atom will leave the beam in only 20 μs . Collisions of atoms with the walls are generally undesirable, since the atom will experience an additional potential energy, which can result in shuffling of the Zeeman levels. Additionally, atoms experience a random phase shift during collisions, and dephasing of the collective spin state can occur.

3.1.3 Neon buffer gas

In order to curtail the loss of atoms out of the laser beam (and reduce the number of thermal atoms entering the laser beam), an inert buffer gas is added to the cell. Elastic collisions between Rb and Ne limit the mean free path of the Rb atoms while, at least to some extent, preserving any ground state coherence. The vapor cells are commercially filled, and the specifications indicate that the pressure of Neon is approximately 30 torr (4 kPa). For our operation temperature the estimated density of Ne atoms is found by the ideal gas law:

$$\begin{aligned}n_{\text{Ne}} &= \frac{P_{\text{Ne}}}{k_B T} \\ &= 8.7 \times 10^{17} \text{ cm}^{-3},\end{aligned}\tag{3.18}$$

where $k_B = 1.38066 \times 10^{-23}$ J/K is Boltzmann's constant.

3.1.4 Diffusion time

The diffusion time depends on several factors, including the Rb-Ne collisional cross section, σ_{RbNe} and the temperature. The collision rate of Rb with other Rb atoms produce a small correction to this term, which can become significant at higher temperature. Rb-Ne collisions typically preserve ground-state coherence at low buffer gas pressures, since Ne does not have a free electron. However, Rb-Rb collisions can result in an exchange of spin, which tends to destroy coherent states. We discuss this effect in more detail in Ch. 7. A detailed calculation would lead us too far astray, and so we ignore the effects of Rb-Rb collisions on diffusion. We can estimate the diffusion time for an atom to leave a laser beam of radius r as [128, 129]

$$\tau_{\text{diff}} = r^2/(4D), \quad (3.19)$$

where

$$D = \frac{1}{3}\langle\bar{v}\rangle l_{mf} \quad (3.20)$$

is the diffusion coefficient in three dimensions and $l_{mf} = 1/(n_{\text{Ne}}\sigma_{\text{RbNe}})$ is the mean free path. Here, $\langle\bar{v}\rangle$ is the mean relative speed of Rb and Ne, which is the same as the speed of a single atom with a reduced mass [129],

$$\mu = \frac{m_{\text{Rb}}m_{\text{Ne}}}{m_{\text{Rb}} + m_{\text{Ne}}}. \quad (3.21)$$

With $m_{\text{Ne}} = 3.35 \times 10^{-26}$, inserting Eq. 3.21 into Eq. 3.17, we find $\langle\bar{v}\rangle \approx 650$ m/s.

Rb-Ne collisional cross-section, σ_{RbNe}

A fair approximation of the collisional cross section is obtained by considering the area of a single Rb-Ne molecule of radius r_0 :

$$\sigma_{\text{RbNe}} = \pi r_0^2. \quad (3.22)$$

The potential energy curves of the ground-state Ne-Rb molecule [130, 131] allow for a rough estimate of $r_0 = 0.35$ nm. More difficult calculations assuming a Leonard-Jones interaction potential [132, 133] find that $r_0 = 0.366$ nm. Since these results agree approximately, we shall take the mean value to compute,

$$\sigma_{\text{RbNe}} \approx 4 \times 10^{-15} \text{ cm}^2. \quad (3.23)$$

It is important to note that this value is likely temperature-dependent, but we are only interested in an approximate value.

With Eqs. 3.18 and 3.23, we find that the diffusion coefficient (Eq. 3.20) is

$$D \approx 6.28 \text{ cm}^2/\text{s}. \quad (3.24)$$

The classic review of optical pumping by William Happer [134] notes that diffusion coefficients are typically determined experimentally, and are related to the buffer pressure P and a bare diffusion constant D_0 by an alternate expression,

$$D = \frac{760 \text{ Torr}}{P} D_0. \quad (3.25)$$

A value of $D_0 = 0.23 \text{ cm}^2/\text{s}$ is found in Ref. [135] which, with Eq. 3.25, yields $D \approx 5.83 \text{ cm}^2/\text{sec}$, which agrees fairly well with the previous analysis. Since we are simply interested in an approximation of the Rb diffusion rate out of the beam, we

will take $D = 6 \text{ cm}^2/\text{sec}$ to find that, for a typical beam diameter of 5 mm, Eq. 3.19 predicts,

$$\tau_{\text{diff}} = r^2/(4D) \approx 2.6 \text{ ms}, \quad (3.26)$$

Which is an improvement by several orders of magnitude compared to ballistic atomic motion.

3.1.5 Collisional broadening

For Rb atoms in a bath of Ne buffer gas, the energy splitting between two states, $\hbar\omega_{eg} = E_e - E_g$, is modified by the interaction potential between the two species, which typically depends upon the separation between atoms. An alternative, but equally valid picture, is that collisions cause random phase shifts in the time-dependent density matrix elements describing the Rb atoms, which collectively results in a spectral broadening of the absorption line. Quantitatively, this can be accounted for by appending an additional term to the dephasing rate of the corresponding coherence,

$$\gamma = \Gamma_{\text{sp}} + \gamma_{\text{coll}}, \quad (3.27)$$

where Γ_{sp} is the natural spontaneous emission rate from Eq. 3.13 and γ_{coll} is the correction due to buffer gas collisions, which depends on the buffer gas pressure via

$$\gamma_{\text{coll}} = aP_{\text{Ne}}. \quad (3.28)$$

The prefactor a is a constant that depends on the two species and is a non-trivial function of the collisional cross-section σ_{RbNe} , the reduced mass μ , and the temperature [136]. A full theoretical treatment of this process is complicated, and so γ_{coll} is typically determined experimentally. Here, we summarize a review of the literature and relate the experimental findings to our model.

Ottinger, *et al.* [137] investigated the broadening of both D_1 and D_2 Rb resonance lines in the presence of several pressurized inert gases (including Ne) at a temperature of $T = 320$ K and found that the FWHM of the D_1 broadening is $2\gamma^{\text{Ott.}} = 0.28 \pm 0.04 \text{ cm}^{-1}/n_{\text{Ne}}^{\text{Ott.}}$ in units of $1/\lambda$, where the Ne concentration was $n_{\text{Ne}}^{\text{Ott.}} = 2.69 \times 10^{19} \text{ cm}^{-3}$. Rotondaro, *et al.* [138] later used the temperature of $T = 320$ K to convert Ottinger's value to standard units:

$$2\gamma^{\text{Ott.}} = 9.4 \pm 1.3 \text{ MHz/Torr.} \quad (3.29)$$

Rotondaro, *et al.* also used high resolution laser absorption spectra to determine a more precise value for the broadening at $T = 394$ K:

$$2\gamma^{\text{Rot.}} = 9.84 \pm 0.1 \text{ MHz/Torr.} \quad (3.30)$$

The experiments described in this dissertation were conducted in a temperature range between $T = 50^\circ\text{C}$ (323 K) and $T = 80^\circ\text{C}$ (353 K). There is no simple formula for the temperature dependence of broadening, and it has not been carefully measured in this range. Ottinger, *et al.* [137] quotes an approximate theoretical dependence of $T^{0.3}$, but comments that this does not hold for Rb-Ne. Since this temperature dependence is unknown, we will use the more precise value from Rotondaro, *et al.*, and assume that it holds at our operating temperatures. Thus, the excited state depolarization rate is,

$$\begin{aligned} 2\gamma &= (2\pi) n_{\text{Ne}} \times 9.84 \text{ MHz/Torr} \\ &= (2\pi) 290 \text{ MHz,} \end{aligned} \quad (3.31)$$

where we have used our value Ne pressure of 30 Torr. Notice that this value is much larger than the FWHM of the natural linewidth, so we simply ignore the

contribution of the latter to the total linewidth.

3.1.6 Doppler broadening

In order to achieve sufficiently-high optical depth, it is necessary to heat the vapor cell to a high temperature, as described in more detail in Sec. 3.1.8. Atoms at higher temperatures are given more kinetic energy, which can result in broadening of absorption lines due to the Doppler effect, although for the operating temperature range for these experiments, changes in the Doppler width are negligible. Nevertheless, we consider the effects of Doppler broadening in this section.

Since atoms in a vapor cell are moving, they can experience different frequencies of light, depending on the relative difference in their velocity vector, \mathbf{v} , and \mathbf{k} , the wavevector of the laser light. Thus, laser light at a frequency of ν_0 in the lab frame will be Doppler shifted to

$$\nu' = \nu_0 - \mathbf{k} \cdot \mathbf{v} + \mathcal{O}(|v|^2), \quad (3.32)$$

where $\mathbf{k} = k\hat{z}$, with $k = 2\pi/\lambda$. Specifically, if the atom is moving in an opposite direction to \mathbf{k} , then the observed frequency will be shifted to the blue with respect to ν_0 . Likewise, the observed frequency will be red-shifted if $\mathbf{k} \cdot \mathbf{v} < 0$.

We recall the Maxwell-Boltzmann distribution of each velocity component from the discussion of Eq. 3.17. Here, we are only interested in the distribution of velocities v_z , so we integrate over the two other velocity components (in Cartesian coordinates) to find that the density of atoms with z -velocities between v_z and

$v_z + dv_z$ is [128]

$$\begin{aligned} n(v_z)dv_z &= n \left(\frac{1}{v_m \sqrt{\pi}} \right)^3 \left[\int_{-\infty}^{+\infty} e^{-v_x^2/v_m^2} dv_x \int_{-\infty}^{+\infty} e^{-v_y^2/v_m^2} dv_y \right] e^{-v_z^2/v_m^2} dv_z \\ &= \frac{n}{\sqrt{\pi} v_m} e^{-v_z^2/v_m^2} dv_z, \end{aligned} \quad (3.33)$$

where n is the total density of atoms and $v_m = \sqrt{\frac{2kT}{m_{\text{Rb}}}}$ (see Eq. 3.16). We use Eq. 3.32 to change variables, we find that the number of atoms with absorption frequencies shifted from ν_0 into the interval $[\nu, \nu + d\nu]$ is [136]

$$n(\nu)d\nu = \frac{n}{\sqrt{\pi} v_m} \exp \left[- \left(\frac{\nu - \nu_0}{k v_m} \right)^2 \right] d\nu. \quad (3.34)$$

This is a Gaussian profile with a HWHM

$$\begin{aligned} \Gamma_D &= \sqrt{\ln 2} k v_m \\ &= (2\pi) \frac{1}{\lambda} \sqrt{\frac{2k_B T}{m_{\text{Rb}}}} \ln 2. \end{aligned} \quad (3.35)$$

For ^{87}Rb at $T = 60^\circ\text{C}$ (333 K), this evaluates to $\Gamma_D = (2\pi) 264 \text{ MHz} \approx 1.8\gamma$. Since the collisional width and the Doppler width are roughly equal, we can justify ignoring the effects of Doppler broadening in our simple model. Thus, the value of the polarization decay rate γ from the model is related to only the pressure-broadened linewidth from Eq. 3.31.

3.1.7 Optical pumping

Let us consider in more detail the response of ^{87}Rb to strong σ^+ -polarized ($q = +1$) laser light in resonance with the D_1 $F = 2 \rightarrow F = 2$ transition, as depicted in Fig. 3.2. An atom prepared in the ground state sublevel $|F = 2, m_F = -2\rangle$ will “absorb” a σ^+ photon, and, with a probability proportional to the square of the

appropriate Clebsch-Gordan coefficient, be excited to state $|F' = 2, m_{F'} = -1\rangle$. The lifetime of this excited state is typically very short, and the atom will spontaneously decay into any dipole-allowed ground state, again with probability proportional to the square of the corresponding Clebsch-Gordan coefficient. In this case, the atom can decay into either $|F = 2, m_F = -2, -1, 0\rangle$ or $|F = 1, m_F = -1, 0\rangle$. If it decays into one of $|F = 2, m_F = -2, -1, 0\rangle$, the atom will then “absorb” another resonant photon of σ^+ polarization and the process will repeat. If the atom decays into the $|F = 1\rangle$ manifold, then it will not “see” the off-resonant light, so the atom will stay there.

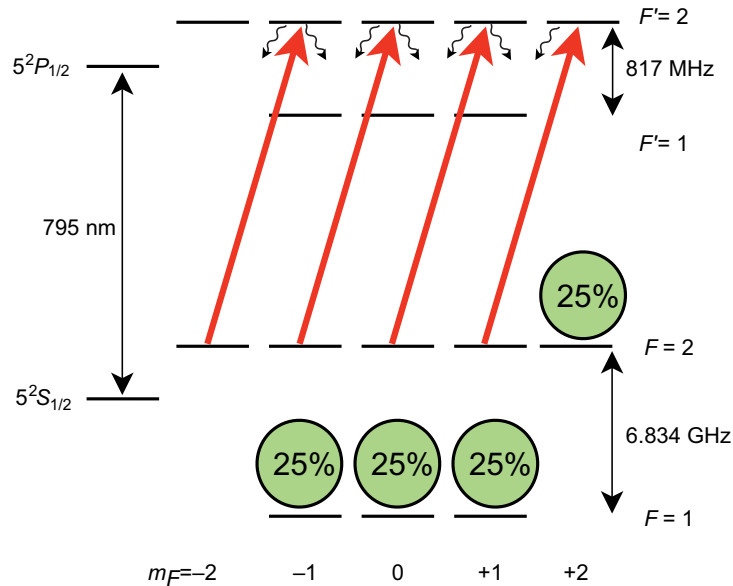


FIG. 3.2: ^{87}Rb D_1 hyperfine structure and Zeeman substructure with σ^+ light resonant to the $F = 2 \rightarrow F' = 2$ transition.

If the laser light illuminates a collection of these atoms for a sufficient time (determined by the spontaneous decay rate), the atoms are optically pumped into one of four states: $|F = 1, m_F = -1, 0, 1\rangle$, or $|F = 2, m_F = 2\rangle$. In reality, there is a redistribution of the population between the eight excited states, with an associated cross section on the order of the cross section that leads to collisional broadening.

The mixing of the F states is caused by mixing of the total electron angular momentum, J , which can be modeled by simple randomization [134, 139]. The relative rate of F mixing, γ_m , is on the order of the spontaneous emission rate, γ : $\gamma_m = \frac{35}{54}\gamma$ [140]. We solve the density matrix equations of motion for the 16 populations and 7 driven coherences, and allow excited state shuffling to find that the final population distributions are independent of the pumping field power, and the population distribution is,

$$p_{-1} = 0.24 \tag{3.36}$$

$$p_0 = 0.25 \tag{3.37}$$

$$p_{+1} = 0.255 \tag{3.38}$$

$$p_{\text{dark}} = 0.255. \tag{3.39}$$

In other words, we find that the atoms populate each state approximately equally:

$$p_{-1,0,1,\text{dark}} \approx 0.25.$$

3.1.8 Optical depth

In Section 2.4.1, we computed the optical depth of a medium comprised of two-level atoms in a near-resonant light field. This result was based on the linear susceptibility of a single transition. We consider the optical depth experienced by a weak signal field tuned to the $F = 1 \rightarrow F' = 2 D_1$ transition of ^{87}Rb , after the atoms have been optically pumped with a stronger control field, as in the previous section, and as shown in Fig. 3.4. The two laser fields differ in frequency by the hyperfine splitting, $\Delta_{\text{hf}} = 6.835$ GHz.

Since linear susceptibilities simply add, the contributions of different transitions to the optical depth simply add. We recall that the atoms equally populate each of

the three $|F = 1, m_F = -1, 0, 1\rangle$ ground states and the $|F = 2, m_F = 2\rangle$ state, the latter of which is dark since it cannot “see” the σ^+ light. Using the appropriate Clebsch-Gordan coefficients from Table 3.1, the optical depth (Eq. 2.57) becomes:

$$d = \frac{3}{8\pi} \lambda^2 L \frac{\Gamma_{\text{sp}}}{\gamma} n_{\text{Rb}} \left[p_1 \frac{1}{2} + p_0 \left(\frac{1}{4} + \frac{1}{12} \frac{\gamma^2}{\Delta_{\text{hf,P}}^2 + \gamma^2} \right) + p_{-1} \left(\frac{1}{12} + \frac{1}{12} \frac{\gamma^2}{\Delta_{\text{hf,P}}^2 + \gamma^2} \right) \right], \quad (3.40)$$

where $\Delta_{\text{hf,P}} = (2\pi) 817$ MHz is the hyperfine splitting of the $5^2P_{1/2}$ excited state, $\Gamma_{\text{sp}} = (2\pi) 5.7$ MHz is the spontaneous emission rate, $\gamma = (2\pi) 145$ MHz is the collisionally-broadened polarization decay rate from Eq. 3.31, $\lambda = 795$ nm is the wavelength corresponding to the D_1 transition, $L = 7.5$ cm is the cell length, and the total Rb concentration n_{Rb} is determined by calculating the vapor pressure at a given temperature from Eq. 3.15 and using the ideal gas law:

$$n_{\text{Rb}} = \frac{P_v(T)}{k_B T}. \quad (3.41)$$

In Fig. 3.3, we plot the value of d as a function of temperature. It is notable that since the signal field is weak, one might attempt to experimentally measure the optical depth by recording the intensity attenuation after the cell according

$$|\mathcal{E}_1(L)|^2 = |\mathcal{E}_1(0)|^2 e^{-2d}, \quad (3.42)$$

but this measurement is difficult for large d .

In Fig. 3.4, we plot the contribution to the optical depth from the three signal field transitions, and we signify the weight of each contribution by the corresponding line thickness. 10% of the contribution to the optical depth comes from the $|F = 1, m_F = -1\rangle \rightarrow |F' = 2, m_F = 0\rangle$ transition, 30% from the $|F = 1, m_F = 0\rangle \rightarrow |F' = 2, m_F = +1\rangle$ transition, and due to the large Clebsch-Gordan coefficient, 60%

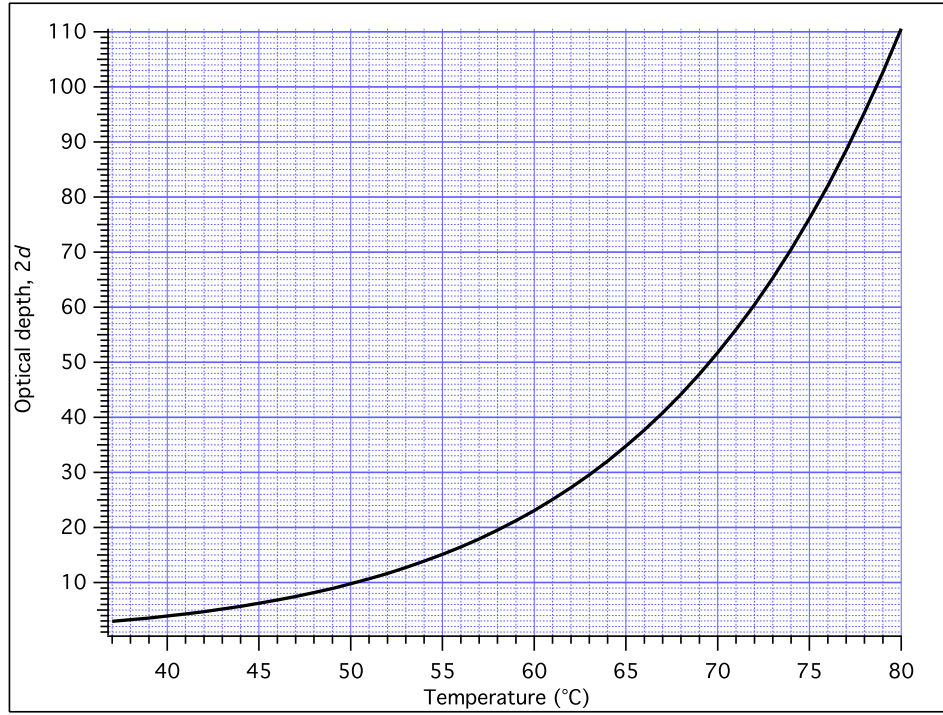


FIG. 3.3: Optical depth of the $^{87}\text{Rb } F = 1 \rightarrow F' = 2$ $^{87}\text{Rb } D_1$ transition as a function of temperature.

from the $|F = 1, m_F = +1\rangle \rightarrow |F' = 2, m_F = +2\rangle$ transition. Since the value of the optical depth determines the efficiency of the light storage process, the dominant single- Λ system will be formed with the signal field linking $|F = 1, m_F = 1\rangle \rightarrow |F' = 2, m_F = 2\rangle$ and the control field linking $|F = 2, m_F = 1\rangle \rightarrow |F' = 2, m_F = 2\rangle$.

Recalling the discussion of the simple Λ description from Sec. 2.3, we find that under the conditions described above, the D_1 structure of ^{87}Rb can approximate a single- Λ system with

$$|e\rangle = |5^2P_{1/2}, F' = 2, m_F = 2\rangle, \quad (3.43)$$

$$|s\rangle = |5^2S_{1/2}, F = 2, m_F = 1\rangle, \quad (3.44)$$

$$|g\rangle = |5^2s_{1/2}, F = 1, m_F = 1\rangle. \quad (3.45)$$

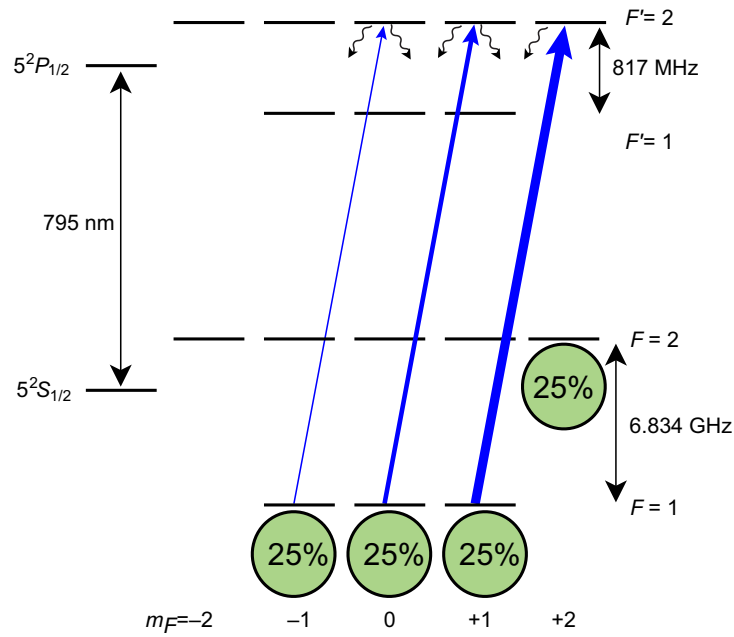


FIG. 3.4: A weak signal field tuned to the $F = 1 \rightarrow F' = 2$ $^{87}\text{Rb } D_1$ transition. 10% of the contribution to the optical depth comes from the $|F = 1, m_F = -1\rangle \rightarrow |F' = 2, m_F = 0\rangle$ transition, 30% from the $|F = 1, m_F = 0\rangle \rightarrow |F' = 2, m_F = +1\rangle$ transition, and due to the large Clebsch-Gordan coefficient, 60% from the $|F = 1, m_F = +1\rangle \rightarrow |F' = 2, m_F = +2\rangle$ transition.

3.1.9 Rabi frequency of the control field

With this approximation, we can calculate the Rabi frequency of the control field, Ω . From Eq. 2.26, we have:

$$\Omega = \wp_{es} E_2 / \hbar, \quad (3.46)$$

where $\wp_{es} = \frac{1}{\sqrt{6}} \wp_0$ is the dipole matrix element of the $|e\rangle \rightarrow |s\rangle$ transition, since $\frac{1}{\sqrt{6}}$ is the corresponding Clebsch-Gordan coefficient. We assume that the transverse intensity distribution of the laser beam is a uniform circle with radius R . It is standard practice to experimentally measure laser powers, P . Thus, the laser intensity is simply $P/(\pi R^2)$. We recall that the intensity of light depends on the square of the electric field, E_2 as [86]:

$$I = \epsilon_0 c \langle E_2^2 \rangle. \quad (3.47)$$

The oscillatory part of the electric field will average to $\frac{1}{2}$, so we have the following expression for the Rabi frequency,

$$|\Omega|^2 = \frac{P}{\pi R^2} \frac{|\wp_{eg}|^2}{2\hbar^2 \epsilon_0 c}. \quad (3.48)$$

In reality, the laser beam will have a Gaussian profile, so that different atoms at different radial positions experience different Rabi frequencies. In the experiments described later, we use an aperture to detect the central portion of the beam, which has a more or less uniform intensity distribution.

3.2 Experimental description

In this section, we provide a general overview of the experimental apparatus. We describe each individual component in more detail in subsequent sections. Mea-

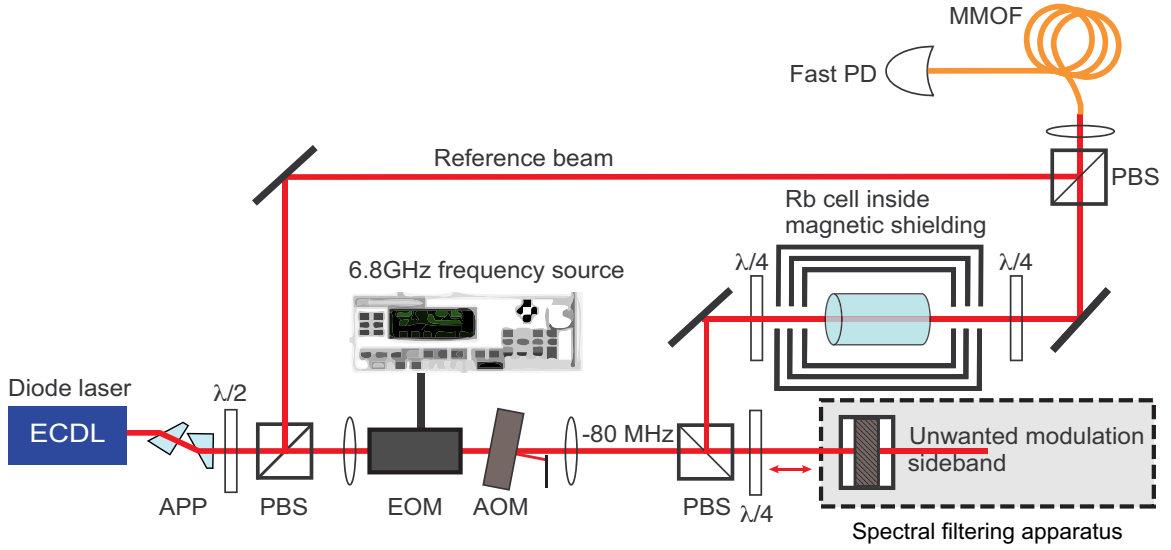


FIG. 3.5: A schematic of the experimental arrangements. See text for abbreviations.

measurements were performed using the configuration in Fig. 3.5. We tuned an External Cavity Diode Laser (ECDL) manufactured by Toptica Photonics (model number DL100) near the Rubidium D_1 transition ($\lambda = 795$ nm).

After sending the output through a pair of anamorphic prisms (APP) to correct for astigmatism, a polarizing beam splitter (PBS) was used to separate a fraction of the beam for use as a reference frequency. The main beam then passed through an electro-optical modulator (EOM), which modulated its phase near the frequency of the ground state hyperfine splitting of ^{87}Rb [$\Delta_{\text{hf}} = (2\pi) 6.835$ GHz], and produced sidebands separated by that frequency from the main beam. All optical fields then passed through an acoustic optical modulator (AOM) operating at 80 MHz, which shifted the frequencies of the fields to the red by that amount. We tuned the zeroth order (carrier frequency) field to the $5^2S_{1/2}F = 2 \rightarrow 5^2P_{1/2}F' = 2$ transition; this beam acted as the control field. The +1 modulation sideband functioned as the signal field, and was tuned near the $5^2S_{1/2}F = 1 \rightarrow 5^2P_{1/2}F = 2$ transition. The -1 sideband acted as the far-detuned Stokes field. A saturated absorption spectrum

through a vapor cell containing natural abundance of both ^{87}Rb and ^{85}Rb is shown in Fig. 3.6. We label the frequencies of the control and signal fields for convenience.

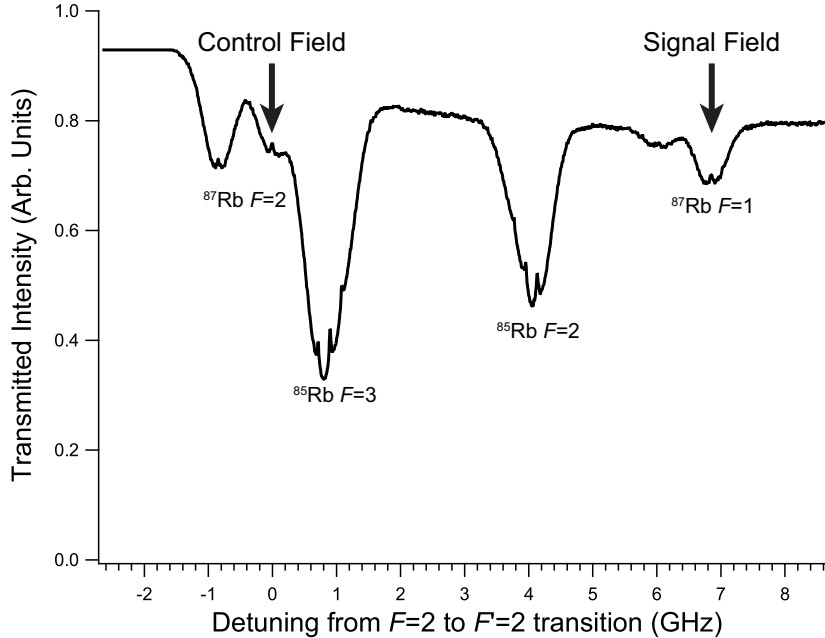


FIG. 3.6: Saturated absorption spectrum for a vapor cell containing natural abundance Rb. The control field is tuned near the $F = 2 \rightarrow F' = 2$ transition, as indicated. The signal field is tuned near the $F = 1 \rightarrow F' = 2$ transition, which is approximately $\Delta_{\text{hf}} = 6.835$ GHz away.

For spectral measurements, the control field was always on, thereby ensuring that most of the atoms were in $|g\rangle$, and we swept the modulation frequency of the EOM, which simultaneously swept the frequencies of the Stokes and signal field. For slow light measurements, we used the control field to optically pump the atoms into $|g\rangle$. We then adjusted the RF power of the EOM and AOM to produce Gaussian temporal pulses on the signal and Stokes channels.

Since, for some experiments, we were interested in observing the effects of resonant four-wave mixing, it was essential to independently manipulate the amplitudes of the signal (+1 sideband) and Stokes (-1 sideband) fields. The use of a temperature tunable Fabry-Pérot étalon (Free Spectral Range = 20 GHz, finesse ≈ 100)

enabled us to do this. By tuning the étalon (see Sec. 3.3.2) in resonance with the -1 sideband and reflecting the frequency comb off of the étalon, we were able to reduce the intensity of the Stokes field while preserving the intensity of both the control and signal fields.

The beam was weakly focused to either 2.6 mm or 4 mm diameter, as we indicate below, and circularly polarized with a quarter-wave plate ($\lambda/4$). Typical peak control field and signal field powers were approximately 19 mW and 50 μ W, respectively. A cylindrical Pyrex cell, of length 75 mm and diameter 22 mm, contained isotopically enriched ^{87}Rb and 30 Torr Ne buffer gas, so that the pressure-broadened optical transition linewidth was $2\gamma = 2\pi \times 290$ MHz [138] (see Sec. 3.1.5 for a discussion). The cell was mounted inside tri-layer magnetic shielding, as to reduce the effects of stray magnetic fields. The temperature of the cell (and thus the concentration of Rb in the vapor phase) was controlled via a bifilar resistive heater wound around the innermost magnetic shielding layer. The temperature range for this experiment was between 50°C and 80°C, which corresponded to Rb densities of 1.1×10^{11} atoms/cm³ and 1.2×10^{12} atoms/cm³, and to optical depths of 10 and 110, respectively.

After the cell, the output laser fields were recombined with the unshifted reference beam, coupled into a multi-mode optical fiber (MMOF), and sent to a fast photodetector, and the amplitude of each field was analyzed with a microwave spectrum analyzer. Because of the 80 MHz frequency shift introduced by the AOM, the beat note frequencies of the $+1$ and -1 modulation sidebands differed by 160 MHz, which allowed for independent measurement of the amplitudes of all three fields.

3.3 The light fields

A requirement for EIT is that signal and control fields have a stable relative phase with one another. In particular, if they are not in phase, then the atomic dark state (see Eq. 2.63),

$$|D\rangle = \frac{\Omega|g\rangle - \alpha e^{i\phi}|s\rangle}{\sqrt{|\Omega|^2 + |\alpha|^2}}, \quad (3.49)$$

can evolve into an atomic bright state,

$$|B\rangle = \frac{\Omega|g\rangle + \alpha|s\rangle}{\sqrt{|\Omega|^2 + |\alpha|^2}}, \quad (3.50)$$

if the phase difference between \mathcal{E} and Ω is π . Thus, whereas the dark state $|D\rangle$ was decoupled from the light fields, resulting in the effects of EIT, the bright state $|B\rangle$ (which is a basis vector along with $|D\rangle$ and $|e\rangle$), has an associated non-zero eigenenergy and is thus not a steady-state to which the atom evolves. In our experiments, we used opto-electronical devices to create a signal field from a control field, and ensure a steady relative phase. In this section, we describe the optics components used to create, manipulate, and detect the light fields.

3.3.1 Light field modulation

After the PBS, the main beam was focused with a lens to the center of an electro-optical modulator (EOM) operating at the frequency of the ground state hyperfine splitting of ^{87}Rb [$\Delta_{\text{hf}} = (2\pi) 6.835 \text{ GHz}$]. The EOM employed the electro-optic effect to phase-modulate the main beam, in turn producing sideband frequencies at multiples of $\pm\Delta_{\text{hf}}$ of nearly equal magnitudes and opposite phases.

More precisely, we can describe the incoming beam as a mono-chromatic plane wave of the form

$$\Psi_i = Ae^{i\nu t + i\phi}, \quad (3.51)$$

where A is the wave amplitude, and $\nu = c/\lambda$ is the frequency corresponding to the D_1 transition in ^{87}Rb ($\nu = (2\pi) 377.1$ THz), and ϕ is the phase. The EOM is made of lithium niobate (LiNbO_3) crystal with a nominal index of refraction which can be changed by applying a voltage, V , across the crystal. Thus, after traversing this device, we find that the outgoing wave has accrued a phase,

$$\Delta\phi = \frac{2\pi}{\lambda} \left(\frac{1}{2} n_0^3 r_{zz} \right) \frac{L}{d} V \equiv \beta, \quad (3.52)$$

where n_0 is the unperturbed refractive index, r_{zz} is the appropriate electro-optic tensor element, and L/d is the ratio of the crystal's length to thickness.

By modulating the voltage sinusoidally with a driving frequency ν_d , we can produce an outgoing wave of the form,

$$\Psi_o = A e^{i\nu t + i\beta \sin(\nu_d t)} \quad (3.53a)$$

$$= A e^{i\nu t} \left(J_0(\beta) + \sum_{k=1}^{\infty} J_k(\beta) e^{ik\nu_d t} + \sum_{k=1}^{\infty} (-1)^k J_k(\beta) e^{-ik\nu_d t} \right) \quad (3.53b)$$

$$= A J_0(\beta) e^{i\nu t} + A J_1(\beta) e^{i(\nu+\nu_d)t} - A J_1(\beta) e^{i(\nu-\nu_d)t} + \dots \quad (3.53c)$$

where J_i are Bessel functions of the first kind, and we have employed the Jacobi-Anger Identity in the second step [141]. For small $\beta \ll 1$, the main field amplitude (oscillating at frequency ν , first term in Eq. 3.53c) is largely unaffected (the power that remains in the first beam is proportional to $[J_0(\beta)]^2$). We clearly see that the main beam is accompanied by additional fields in a frequency comb with spacing determined by the driving frequency, ν_d . We note that since $\beta \ll 1$, the sideband amplitudes are significantly smaller than the main field amplitude (the power transferred to the first order beams is proportional to $[J_1(\beta)]^2$). For our experiments, $\nu_d = \Delta_{\text{hf}}$, so the +1 modulation sideband functioned as the signal field (oscillating

at $\nu + \Delta_{\text{hf}}$, second term in Eq. 3.53c), while the -1 sideband was the Stokes field (oscillating at $\nu - \Delta_{\text{hf}}$, third term in Eq. 3.53c). We note that the signal and Stokes field phases differ by π . Higher order sidebands, with smaller amplitudes and larger detunings from the atomic resonance, can be ignored for practical purposes.

All optical fields passed through an acousto-optical modulator (AOM) operating at 80 MHz. Thus, the -1 first diffraction order contained beams with frequencies shifted by this amount to the red. This resulted in the control field shifting back to the $^{87}\text{Rb } F = 2 \rightarrow F' = 2$ resonance and the signal field being tuned near the $^{87}\text{Rb } F = 1 \rightarrow F' = 2$ resonance, as shown in Fig. 3.6.

The total light power to the experiment (and, therefore, Rabi frequency Ω) was adjusted by changing the RF power to the AOM. In Sec. 3.3.5, we describe how we can modulate this RF power to produce a control field envelope, $\Omega(t)$. Since all fields traversed the AOM, the intensities and envelopes of all modulation comb fields were also changed. Thus, we accordingly adjusted the RF power at the EOM input, which controls the strength of the modulation sidebands, to compensate for any changes in the signal or Stokes field amplitudes caused by AOM modulation. In Sec. 3.3.5, we describe how we modulate the RF power to the EOM to produce the signal field envelope, $\mathcal{E}(t)$.

After the AOM, a lens was used to collimate the beam. All optical beams passed through another PBS and then were circularly-polarized with a quarter-wave plate ($\lambda/4$). In the next section, we discuss the mechanisms used to independently adjust the input signal and Stokes amplitude.

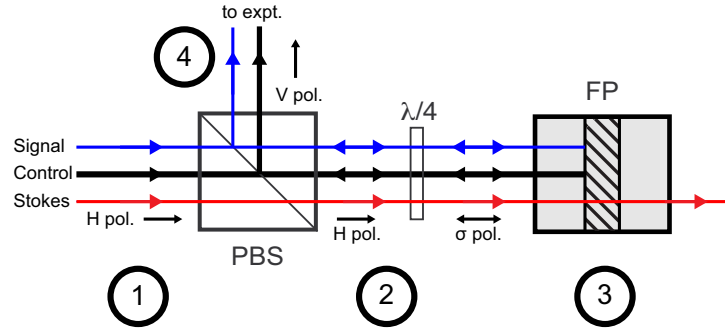


FIG. 3.7: A diagram of the Fabry-Pérot under filtering operation. (1) The three light fields are polarized horizontally (H) and are incident on a polarizing beam splitter (PBS), aligned to permit transmission of H polarized light. (2) After the PBS, the fields are circularly polarized with a quarter-wave plate ($\lambda/4$). (3) The Fabry-Pérot étalon in this case is tuned to permit the transmission of the Stokes frequency. The signal and Control field are reflected, and the $\lambda/4$ converts their polarization to vertical (V). (4) Since the polarizations are vertical, the PBS will reflect them into the experiment. The light fields are spatially separated for demonstration purposes only.

3.3.2 Spectral filtering with a temperature-tunable Fabry-Pérot Filter

Phase modulation of the main beam with the EOM produced signal and Stokes sidebands with equal amplitudes but opposite phases. To evaluate carefully the effects of four-wave mixing, we used a temperature-tunable Fabry-Pérot (FP) étalon to adjust the relative amplitudes of either pulse.

An étalon is an optical device that uses the phenomenon of light interference to permit transmission of certain frequencies of light, while other frequencies are reflected. This is the operating principle of our Fabry-Pérot étalon: we use temperature to tune the resonant frequency of an étalon mounted inside of a Fabry-Pérot-type cavity. The unwanted light field (with a frequency matching the transmission frequency of the étalon) will pass, while the other two light fields will reflect.

Figure 3.7 depicts the operation of the FP to filter the Stokes field, which, as we will discuss in Ch. 4, was necessary to suppress the effects of four-wave mixing. The three fields, separated in frequency by Δ_{hf} , are polarized horizontally, and thus

become transmitted through a polarizing beam splitter (PBS) (stage 1 in Fig. 3.7). After the PBS, the fields are circularly polarized with a quarter-wave plate ($\lambda/4$) (stage 2 in Fig. 3.7) and enter the FP device (stage 3 in Fig. 3.7). Since the resonant frequency of the étalon, in this case, was tuned to the frequency of the Stokes field, most of that field (approximately 95%) will transmit, while the signal and control fields will reflect. The two reflected fields will then pass through the $\lambda/4$ again, and become vertically polarized. The PBS will reflect vertically polarized beams into the experiment (stage 4 in Fig. 3.7). While it is not shown pictorially, in reality a small fraction of the Stokes field will enter the experiment, owing to imperfect transmission of the étalon.

The Fabry-Pérot étalon housing was constructed of a cylindrical tube of aluminum inner diameter 2.54 cm (1 in.), o.d. 3.82 cm (1.5 in.), length 6.35 cm (2.5 in.) mounted to a larger ($6.35 \times 6.35 \times 2.54$ cm³) block of aluminum, which operated as a heat sink. This assembly was mounted to a dual-axis stage. A 2.54 cm diameter étalon [Free Spectral Range (FSR) 20 GHz, finesse ≈ 100] was mounted inside the aluminum tube. Smaller aluminum spacers (o.d. 2.54 cm, i.d. 1.91 cm) were used to hold the étalon in place, and infrared-coated glass windows were inserted on the ends of the aluminum tube. We tuned the resonance frequency of the étalon by changing the temperature of the étalon with a Peltier element and a commercial Thermoelectric temperature controller (ThorLabs model TED200C) placed between the cylindrical tube and the heat sink.

For demonstration purposes, we show the filtering spectra when the FP was tuned to filter the amplitude of the signal field. We note that this example is not pertinent to the experiment, but it elucidates the operation of the filtering. For attenuation of the signal field, we tune the étalon to be in resonance with the ^{87}Rb $F = 1 \rightarrow F = 2$ frequency, as shown in Fig. 3.8. The black trace is from the saturated absorption reference cell. At the same time, the control and Stokes fields

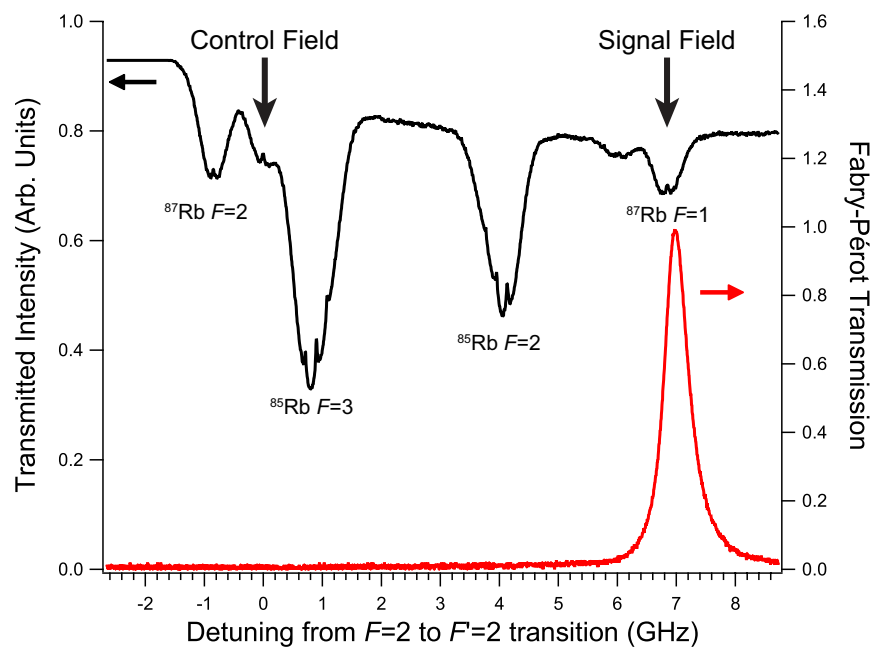


FIG. 3.8: Transmission spectrum of the Fabry-Pérot filter tuned to the signal field frequency. The black trace depicts the saturated absorption spectrum from a reference cell. The red curve shows the transmission after the FP, and demonstrates that, in this case, the signal field is filtered.

were far from the étalon resonance, and were reflected back with minimal losses. A photodiode after the FP detected the red curve, indicating that only the signal field was transmitted. Such filtering allowed for suppression of the unwanted sideband intensity by a factor of approximately 10.

3.3.3 Vapor cell enclosure

After the spectral filtering, the polarization of the reflected beams is converted to vertical, and so they are reflected by the PBS. We then used another $\lambda/4$ to convert the polarization to circular for the EIT experiment. The vapor cell described in Sec. 3.1.2 was mounted in three-layer magnetic shielding, which was constructed with a material with a large magnetic permeability, in order to reduce stray magnetic fields.

We controlled the temperature of the vapor cell (and correspondingly the optical depth) by adjusting the current through a bifilar resistive heater that was wound around the inner-most shield layer. Experimental temperatures ranged between 50°C to 80°C , which corresponded to changes in Rb density from $1.1 \times 10^{11} \text{ cm}^{-3}$ to $1.2 \times 10^{12} \text{ cm}^{-3}$, and to a range of optical depths $2d$ between 10 and 110. The temperature was set on a commercially available temperature controller (Newport Electronics, Inc. model i8-53).

3.3.4 Light detection

After the light beams exited the vapor cell housing, they were linearly polarized with a $\lambda/4$ wave plate, recombined with the reference beam, and coupled into a multi-mode optical fiber (MMOF). The fiber sent the light to a fast photodetector (PD) (New Focus model 1554). For EIT measurements, we are interested in independently monitoring the change in time of the signal and Stokes field amplitudes,

$\mathcal{E}(t)$ and $\mathcal{E}'(t)$, respectively. We employed a microwave spectrum analyzer (Agilent model E4405B) for this purpose.

Because of the frequency shift induced by the AOM, the act of combining the reference beam with the beams from the vapor cell created beat notes of $\Delta_{\text{hf}} \pm 80$ MHz. More precisely, the reference beam had a single frequency, which matched the output of the laser, ν_0 . The AOM induces a -80 MHz shift, and the EOM creates $\pm\Delta_{\text{hf}}$ sidebands, $\nu_0 - 80 \text{ MHz} \pm \Delta_{\text{hf}}$. Thus, the PD records beat notes of $|\Delta_{\text{hf}} \pm 80 \text{ MHz}|$. Thus, the signal field could be recorded by observing the spectrum around a frequency of 6.7547 GHz, while the Stokes field was recorded around 6.9107 GHz.

A wide span on the spectrum analyzer will show three beat notes in the vicinity of Δ_{hf} —a central one at Δ_{hf} , the amplitude of which is determined by the combined amplitudes of the signal, Stokes, and control fields; a peak at $\Delta_{\text{hf}} - 80$ MHz, whose amplitude is determined only by the signal field; and a peak at $\Delta_{\text{hf}} + 80$ MHz, whose amplitude is determined only by the Stokes field. Higher order harmonics (at frequencies $\sim 2\Delta_{\text{hf}}$) exist, while the amplitude of the beat note at 80 MHz is determined by the control field amplitude.

We are interested in measuring the time dependence of the signal (or Stokes) amplitude, and so we work with the spectrum analyzer in “zero-span mode” (actually a very small, 100 Hz span, for data acquisition convenience). A single sweep was completed in 1 s. The resolution bandwidth (RBW) was chosen to be 5 MHz, in order to encompass the entire EIT profile. In order to prevent clipping of the signal, a video bandwidth (VBW) of 3 MHz was chosen.

The spectrum analyzer was used to record the EIT spectra. In order to overcome the limitations of the slow sweep time of the spectrum analyzer, and collect information regarding pulse shapes for slow and stored light experiments, we attached the Auxiliary Video Out port of the Spectrum Analyzer to a digital oscillo-

scope (Tektronix model TDS 2014B). All electronic devices were synchronized with a nominal 10 MHz reference signal from the spectrum analyzer, and triggered using an additional function generator. The spectrum analyzer was connected to a computer with a GPIB cable, and traces were recorded with LabView software. The oscilloscope had a USB interface, and its traces were also recorded with LabView software.

3.3.5 Control of AOM and EOM inputs

The total power to the experiment was controlled by the amount of power in the first diffraction order from the AOM, which was driven by a commercial amplifier (IntraAction model ME). By controlling the driving voltage to the AOM, we could control the intensity of light in the -1 diffraction order. We could modulate the amplitude to the AOM with another arbitrary waveform generator (SRS model DS345), which was connected via GPIB to a computer. Thus, the overall amplitude of the light fields [A in Eq. 3.53c] is time-dependent. Additionally, the power to the EOM was driven by the an RF synthesizer (Agilent model E8257D) operating at $\Delta_{\text{hf}} = 6.8346932 \text{ GHz}$ ¹, which was capable of sweeping the driving frequency, $\nu_d = \nu_d(t)$ and also modulating the amplitude of $\beta = \beta(t)$ to produce pulses.

Thus, the fields entering the experiment can be described by a modified version of Eq. 3.53c(c):

$$\Psi_o = A(t)J_0[\beta(t)]e^{i\nu t} + A(t)J_1[\beta(t)]e^{i(\nu+\nu_d(t))t} - A(t)J_1[\beta(t)]e^{i(\nu-\nu_d(t))t} + \dots, \quad (3.54)$$

where the first term describes the control field amplitude, and the second and third

¹This value was experimentally determined to be the pressure-shifted EIT resonance by measuring the light shift as a function of control power and extrapolating to zero. We note that the unshifted resonance is at a frequency of 6.834 682 610 GHz [1]. The pressure shift that we measured (+11.4 kHz) is in good agreement with the literature (392 Hz/Torr, or +11.8 kHz for 30 Torr of Ne) [134].

terms describe the shapes of the signal and Stokes fields, respectively.

For cw (EIT) experiments, the RF frequency was swept around Δ_{hf} : $\nu_d(t) = \Delta_{\text{hf}} + \delta(t)$, where $\delta(t)$ is the two-photon detuning, while the amplitude modulation was off, keeping $A(t) = A$ and $\beta(t) = \beta$ constant. The span of the RF sweep was typically between 250 kHz and 1.5 MHz. For slow and stored light experiments, ν_d was parked at a desired two-photon detuning, while the collaboration of $A(t)$ and $\beta(t)$ produced control field and signal field envelopes.

3.3.6 Calibration of AOM and EOM

In this section, we describe the correspondence between the signal field's theoretical lineshape, $\mathcal{E}(t)$, and the amplitude produced from modulation, $A(t)J_1[\beta(t)]$. The desired lineshape was described by a function, *e.g.* a Gaussian of the form

$$y_0 + A \exp[-4 \ln 2 (x - x_0)^2 / w^2] \quad x \in [1, 1000], \quad (3.55)$$

where the data point $x \in [1, 1000]$ will correspond to a list of 1000 elements, y_0 is a vertical offset (background), x_0 is the horizontal offset, A is the amplitude, and w is the FWHM pulse duration, which we encode as a data list and send via a GPIB interface to an arbitrary waveform generator (SRS model DS345). The arbitrary waveform generator encoded this pulse in a carrier wave with frequency 10 MHz, so that 1 data point corresponded to $1/(10 \text{ MHz}) = 0.1 \mu\text{s}$. The modulation amplitude was 2.0 Vpp, and the offset was -1 Vpp .

Since the correspondence between $\mathcal{E}(t)$ and $A(t)J_1[\beta(t)]$ is not a trivial relation, it was more feasible to calibrate the EOM and AOM experimentally. Specifically, it was necessary to know the correspondence between the desired waveform sent from the computer to the function generator, which in turn provides a voltage, $V_{\text{AOM (EOM)}}$ to the AOM or EOM drivers, and the resultant power of laser pulse after the AOM

and EOM, $P_{\text{AOM (EOM)}}$. Equivalently, this is the correspondence between $A(t)$ and $J_i[\beta(t)]$ from Eq. 3.54] and the resultant shape of the laser pulse after the AOM and EOM [*e.g.*, $\mathcal{E}(t)$, $\mathcal{E}'(t)$, or $\Omega(t)$].

$A(t)$ is largely controlled by the AOM, which suffers from saturation effects, and thus providing more RF power to the AOM may not result in a linear increase in the power in the first order diffraction beam. Furthermore, the presence of the Bessel function indicates that the transfer function between input RF power to the EOM and output beam shape is not linear.

The strategy is to send simple lineshapes to the drivers and detect the pulse-shape of the signal field after it traverses the experiment. We first tune the laser far from any ^{87}Rb resonances, so that the laser is unaffected by the atoms and vice versa. We first describe the calibration of the AOM. We turn the RF synthesizer's modulation off, so that it creates cw signal and Stokes fields. We program a 'flat' data set of 10000 elements, $\{1, 1, 1, \dots, 1, 1\}$, to both the AOM and EOM function generators. We record the trace from the oscilloscope and determine the points x_{start} and x_{stop} as shown on Fig. 3.9(a). These points correspond to the start times and the stop of the pulse. We then loaded a 'ramp' data set of 10000 elements according to $f(x) = x/10000$ to the AOM function generator. We record the trace from the oscilloscope; this trace represents the light power after only the AOM, so we name these data P_{AOM} . A sample trace is shown in Fig. 3.9(b). Lastly, to calibrate the EOM, we load the 'flat' data set to the AOM function generator and the 'ramp' data set to the EOM function generator. We turn the RF synthesizer's modulation on and record the trace from the oscilloscope, which we name P_{EOM} . These data look qualitatively similar to the AOM data in Fig. 3.9(b).

We then process the data. We first subtract the background and cut all data in time according to the points x_{start} and x_{stop} and normalize the amplitude to 1. We plot V_{AOM} vs. P_{AOM} and fit the data with a polynomial of order eight,

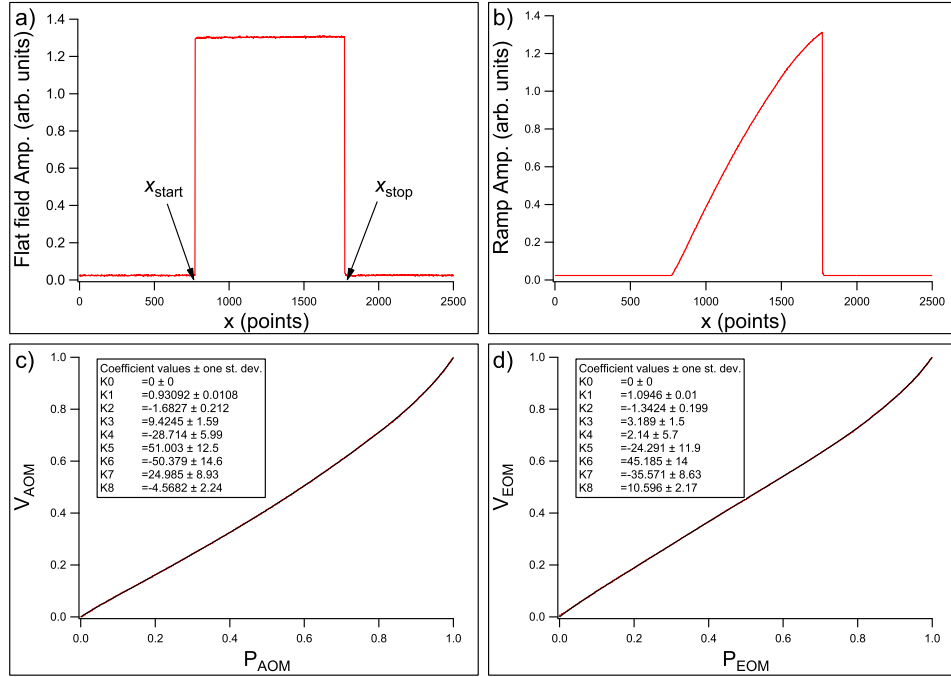


FIG. 3.9: Sample data from the calibration of the AOM and EOM. (a) Raw data from the timing measurement obtained with the ‘flat’ trace. (b) Sample raw data from the ‘ramp’ programmed to the AOM. These data are qualitatively similar for the EOM. (c) Fitting an eighth order polynomial to the V_{AOM} vs P_{AOM} . The red trace is the processed data; the black trace is the fit. (d) Fitting an eighth order polynomial to the V_{EOM} vs P_{EOM} . The red trace is the processed data; the black trace is the fit.

fit(x) = $\sum_{i=0}^8 K_i x^i$, as shown in Fig. 3.9(c). This fit represents the transfer function between the voltage sent to the function generator and the power measured after the AOM. We do the same thing for the EOM data, which are shown in Fig. 3.9(d).

3.3.7 A typical cw (EIT) experiment

In this section, we describe the experimental procedure for measuring a cw EIT spectrum. For these experiments, we were not interested in the behavior of pulses, so the EOM amplitude modulation was turned off at the RF synthesizer, and the AOM function generator’s amplitude modulation amplitude was 0 Vpp. We adjusted the power of the control field by changing the offset of the AOM function generator and

measuring the photo-current, i_{ph} produced by a photodiode whose responsivity was 0.56 at $\lambda = 795$ nm. Thus light power was then calculated as $P = 1.8 \times i_{\text{ph}}$.

As described in Sec. 3.2, we tuned the laser near the $^{87}\text{Rb } D_1 F = 2 \rightarrow F' = 2$ transition. We adjusted the FP étalon to filter the desired light field, as described in Sec. 3.3.2. We swept the RF output from the RF synthesizer by a desired ‘SPAN,’ which depended on the control power, and thus the width of the EIT window (see Eq. 2.62), and was typically on the order of 250 kHz to 3 MHz. The spectrum analyzer was used to record the spectrum of either the signal or the Stokes field. A sample data set, taken at a cell temperature of $T = 60^\circ\text{C}$ ($2d = 52$) and a control Rabi frequency of $\Omega = (2\pi) 9$ MHz (control power of 12 mW in a beam diameter of 4 mm) is shown in the black trace in Fig. 3.10. In this case, the Stokes seed was attenuated to approximately $\sqrt{0.05}$ of the signal field’s amplitude.

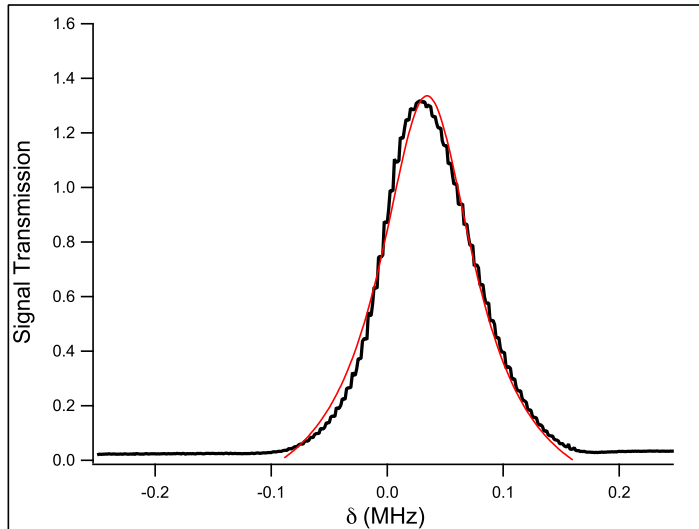


FIG. 3.10: Signal spectra at an optical depth of $2d = 52$ with a beam diameter of 4 mm and $\Omega = (2\pi) 9$ MHz. The black curve is experimental data. The red curve is a fit of the data to a Lorentzian function.

A fit to a Lorentzian profile (red trace) finds that the FWHM of the transparency window is $(2\pi) 100 \pm 34$ kHz. We can naïvely compare this to the predicted

FWHM of the EIT window, $\Gamma_E = |\Omega|^2/(\sqrt{d}\gamma) \approx (2\pi)106$ kHz. These results agree fairly well, considering that the spectrum that we measured in Fig. 3.10 demonstrates some of the effects of FWM, as evidenced in the slight asymmetry about the central frequency of $\delta_0 = 34.3 \pm 0.37$ kHz. It is notable that the central frequency is not exactly at the two-photon detuning of $\delta = 0$. This is because of the light shift (see Sec. 2.9), which shifts the resonant two-photon detuning by $\delta_s = 3|\Omega|^2/\Delta_{\text{hf}} \approx 35.6$ kHz, which agrees quite well with the measured resonance location. More of the spectral features of this trace will be discussed in Ch. 6.

3.3.8 A typical slow/stored light experiment

In this section, we describe the experimental procedure for a generic slow light or stored light experiment. The experimental variables that we changed were control field power (which determined Ω), the lineshape of the input signal pulse, the two-photon detuning δ , the storage time τ , and the amplitude ratio of the signal and Stokes pulses. As described in Sec. 3.2, we tuned the laser near the ^{87}Rb D_1 $F = 2 \rightarrow F' = 2$ transition. We adjusted the FP étalon to filter the desired light field, as described in Sec. 3.3.2, and dialed a desired δ on the RF synthesizer (typically several kHz). In the example below, and in many of the experiments, we were working with signal envelopes $\mathcal{E}_{\text{in}}(t)$ with Gaussian lineshapes, but in principle, we can use any reasonable function. We will discuss the details of pulse shaping in Ch. 4.

The pulseshapes that we sent to the AOM and EOM enable us to optically pump the atoms, obtain a cw reference level, and perform the three stages of light storage: 1) writing the signal pulse to the spin-wave, 2) storing for a time τ ($\tau = 0$ for slow light), and 3) reading out the spin coherence. We create a list of 6000 real numbers that describe the desired control field lineshape, as shown in the top graph

of Fig. 3.11. The level ‘1.0’ corresponds to the maximum possible Rabi frequency (*i.e.*, full laser power), and, as in this example, the level of ‘0.7’ corresponds to a control field Rabi frequency of $\Omega = 0.7\Omega_{\max}$. Similarly, we create a list of 6000 real numbers to describe the signal field trace, as plotted in the bottom graph of Fig. 3.11. We note that the levels discussed here take into account the calibration from Sec. 3.3.6.

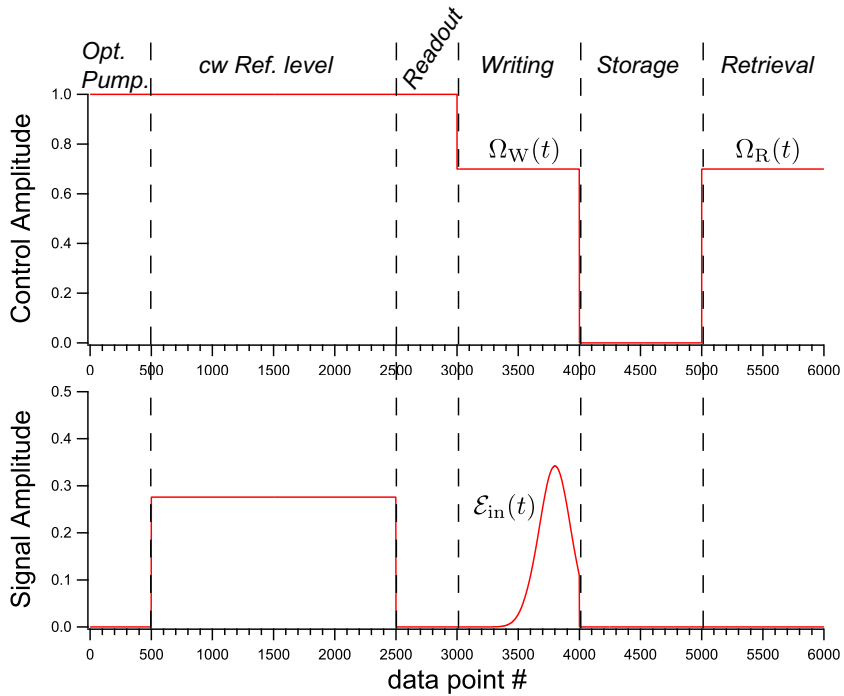


FIG. 3.11: The shapes of the control field train (top) and the signal field train (bottom) sent to the AOM and EOM function generators, respectively, during a typical stored light experiment.

During first 400 points, the signal field is off, and the Control field optically pumps the atoms to the desired state. For the next 1000 points, the control field is maximum, and the signal field is set to a nominal level of 0.3. Essentially, the light is cw during this time, so this allows us to compare the cw EIT lineshape from the spectrum analyzer to the light traces on the oscilloscope. This level also

allows us to normalize subsequent trials to a common level, so as to account for small fluctuations in the overall laser light intensity. After this (from 2500 to 3000), we turn off the signal field, in order to readout any spin coherence that was created during the cw reference portion, and prepares all of the atoms in state $|g\rangle$. Then, we perform the storage experiment by sending a desired writing control field envelope $\Omega_W(t)$ and the input signal field $\mathcal{E}_{in}(t)$. These functions are programmed for 1000 points. After the writing stage, we turn off the control field for the desired storage time—in this case, 1000 points. Again, $\tau = 0$ for slow light. Lastly, we retrieve the spin-wave into the signal field by turning on just the retrieval control field, $\Omega_R(t)$, which can be different than Ω_W , but in this case is the same. Figure 3.12 displays the raw data obtained from the oscilloscope during a stored light experiment.

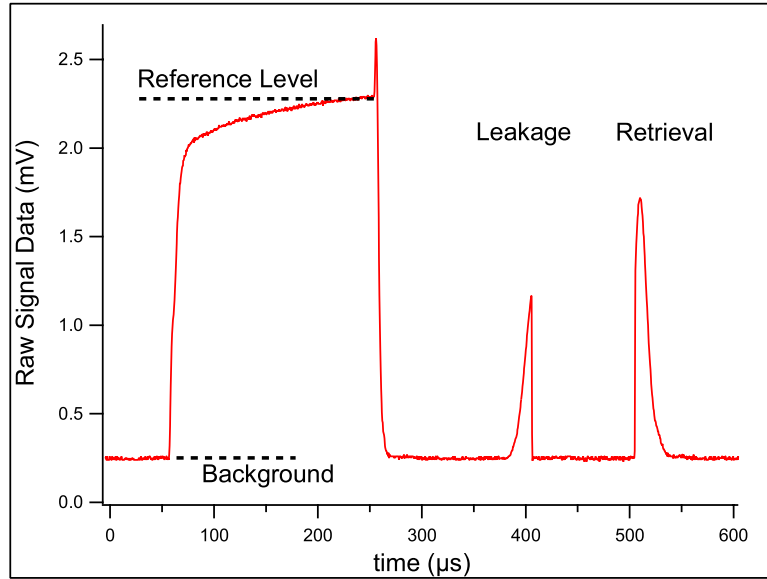


FIG. 3.12: An example trace from the oscilloscope which depicts the raw data obtained during a stored light experiment.

Post-processing of the raw data involves the standard practice of background subtraction, followed by a scaling to the reference level, which we show in Fig. 3.12. We detune the laser away from any ^{87}Rb resonances and retake the storage data,

and gives us a reference pulse which does not interact with the atoms. This tells us the actual shape of \mathcal{E}_{in} . We process the raw data from the reference pulse, and we then numerically compute the storage efficiency,

$$\eta = \frac{\int_{\tau}^{\tau+T} |\mathcal{E}_{\text{out}}(t)|^2}{\int_{\tau}^{\tau+T} |\mathcal{E}_{\text{in}}(t)|^2} \quad (3.56)$$

Figure 3.13 shows the post-processed data.

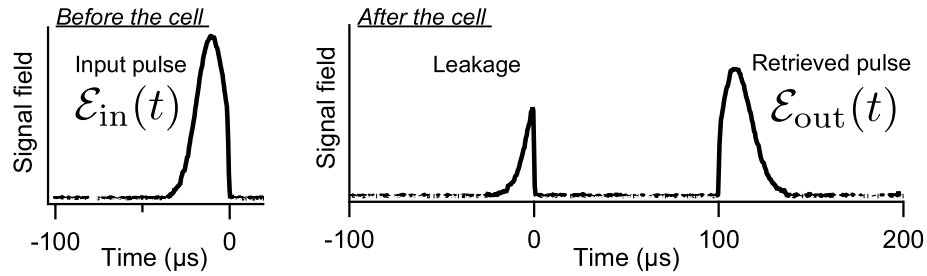


FIG. 3.13: Normalized off-resonant pulse, \mathcal{E}_{in} , the leakage, and the retrieval from storage, \mathcal{E}_{out} during a typical stored light experiment.

3.3.9 Measuring spin decay time

The remaining variable in the model is the spin decay time, γ_0 . In Chapter 7 we discuss experiments designed to investigate in detail the source of spin decay. In this section, we describe the experimental procedures used to extract the spin-wave decoherence time. We make an important assumption: that the duration of the pulses is short enough that spin decay during the writing and retrieval stages was negligible (although we do include this parameter in the numerical modeling). Thus, the spin-wave decay largely occurs in the dark—when all light fields are off during the storage time.

We varied the storage time between $\tau = 15 \mu\text{s}$ and $\tau = 1000 \mu\text{s}$ and then measured the reduction of the retrieved pulse energies as a function of storage time.

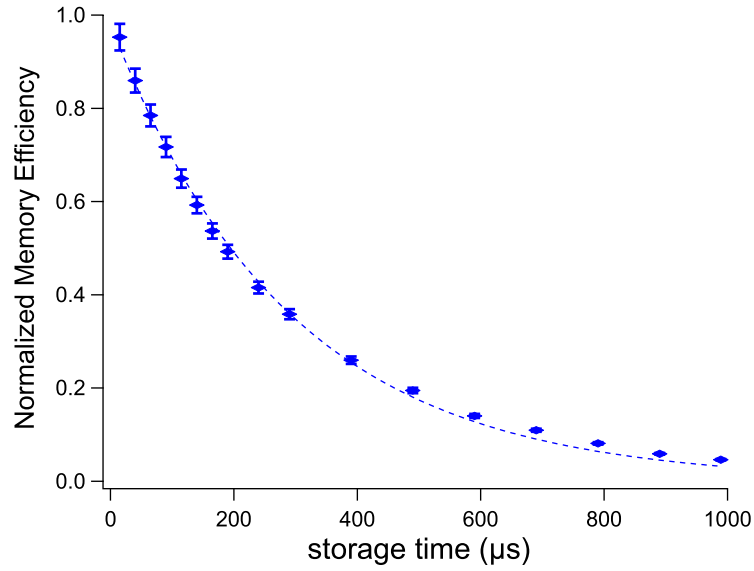


FIG. 3.14: Dependence of retrieved signal energies as a function of storage time at $T = 70^\circ\text{C}$ ($\alpha_0 L = 52$). Here, $\tau_s = 300 \pm 15 \mu\text{s}$. We normalized the memory efficiencies so that the zero-storage-time memory efficiency is unity.

The spin-wave decoherence time, τ_s was extracted by fitting the data to an exponential decay e^{-t/τ_s} . Fig. 3.14 presents a sample measurement of the decay rate at $T = 70^\circ\text{C}$ ($\alpha_0 L = 52$), for which we measured $\tau_s = 300 \pm 15 \mu\text{s}$.

CHAPTER 4

Optimization of memory efficiency

The ability to store light pulses in matter and then retrieve them while preserving their quantum state is an important step in the realization of quantum networks and certain quantum cryptography protocols [10, 13]. Mapping quantum states of light onto an ensemble of identical radiators (*e.g.*, atoms, ions, solid-state emitters, *etc.*) offers a promising approach to the practical realization of quantum memory [23, 28, 33, 42]. Recent realizations of storage and retrieval of single-photon wave packets [26, 27, 81], coherent states [28], and squeezed vacuum pulses [55, 56] constitute an important step in demonstrating the potential of this method. However, the efficiency and fidelity of the storage must be significantly improved before practical applications become possible.

In this chapter, we present a comprehensive analysis of two recently demonstrated memory optimization protocols [142] that are based on a recent theoretical proposal [40, 43, 97–99]. The first protocol iteratively optimizes the input pulse shape for any given control field [142]. The second protocol uses optimal control fields calculated for any given input pulse shape. We experimentally demonstrate their mutual consistency by showing that both protocols yield the same optimal

control-signal pairs and memory efficiencies. We also show that for moderate optical depths ($\lesssim 25$), the experimental results presented here are in excellent agreement with a simple three-level theoretical model [43, 99] with no free parameters (see Eqs. 2.41–2.43); we discuss the details of the correspondence between the actual atomic system and this simple model. Lastly, we study the dependence of memory efficiency on the optical depth. We show that for higher optical depths ($\gtrsim 25$), the experimental efficiency falls below the theoretically predicted values; we discuss possible effects, such as spin-wave decay and four-wave mixing, which may limit the experimentally observed memory efficiency.

4.1 Signal pulse optimization

One approach to the optimization of light storage is based on important time-reversal properties of photon storage that hold even in the presence of irreversible polarization decay [99]. In particular, for co-propagating¹ writing and retrieval control fields, the following is true under optimized conditions: if a signal pulse $\mathcal{E}_{\text{in}}(t)$ is mapped onto a spin wave using a particular control field $\Omega(t)$ and retrieved after some storage time τ using the time-reversed control field $\Omega(T - t)$, the retrieved signal pulse shape $\mathcal{E}_{\text{out}}(t)$ is proportional to the time-reversed input signal pulse $\mathcal{E}_{\text{in}}(T - t)$, but attenuated due to imperfect memory efficiency. This symmetry also gives rise to an experimentally realizable iteration procedure, which, for any given writing control field, determines the optimal incoming signal pulse shape. This procedure has been first demonstrated experimentally in Ref. [142]. The present experiment was performed independently on a different (although similar) exper-

¹The present experiment uses co-propagating writing and retrieval control fields, which corresponds to “forward retrieval,” using the terminology of Refs. [40, 43, 97–99]. Although backward retrieval is more efficient than forward retrieval for degenerate lower levels $|s\rangle$ and $|g\rangle$ of the Λ -system [43, 99], for the present experiment the hyperfine splitting between $|s\rangle$ and $|g\rangle$ makes forward retrieval more efficient [99]

imental setup. Therefore, in order to use this procedure in Sec. 4.3 to study the dependence of memory efficiency on the optical depth, we verify in this section its successful performance in the present experimental setup. In addition, the implementation of iterative signal optimization in this experimental setup will allow us, in Sec. 4.2, to compare and verify the consistency of signal and control optimizations.

The sequence of experimental steps for the iterative optimization procedure is shown in Fig. 4.1. The plots show the control field and the measured and simulated signal fields (solid red lines in the top panel, solid black lines, and dashed blue lines, respectively). Before each iteration, we optically pumped all atoms into the state $|g\rangle$ by applying a strong control field. We started the optimization sequence by sending an arbitrary signal pulse $\mathcal{E}_{\text{in}}^{(0)}(t)$ into the cell and storing it using a chosen control field $\Omega(t)$. In the particular case shown in Fig. 4.1, the group velocity was too high, and most of the input pulse escaped the cell before the control field was reduced to zero. However, a fraction of the pulse, captured in the form of a spin wave, was stored for a time period $\tau = 100 \mu\text{s}$. We then retrieved the excitation using a time-reversed control field $\Omega(t) = \Omega(\tau - t)$ and recorded the output pulse shape $\mathcal{E}_{\text{out}}^{(0)}(t)$. For the sample sequence shown, the control fields at the writing and retrieval stages were constant and identical. This completes the initial (zeroth) iteration step. The efficiency of light storage at this step was generally low, and the shape of the output pulse was quite different from the time-reverse of the initial pulse. To create the input pulse $\mathcal{E}_{\text{in}}^{(1)}(t)$ for the next iteration step, we digitally time-reversed the output $\mathcal{E}_{\text{out}}^{(0)}(t)$ of the zeroth iteration and renormalized it to compensate for energy losses during the zeroth iteration: $\mathcal{E}_{\text{in}}^{(1)}(t) \propto \mathcal{E}_{\text{out}}^{(0)}(\tau - t)$. Then, these steps were repeated iteratively until the rescaled output signal pulse became identical to the time-reversed profile of the input pulse. As expected, the memory efficiency grew with each iteration and converged to $43 \pm 2\%$.

To verify that the obtained efficiency is indeed the maximum possible at this

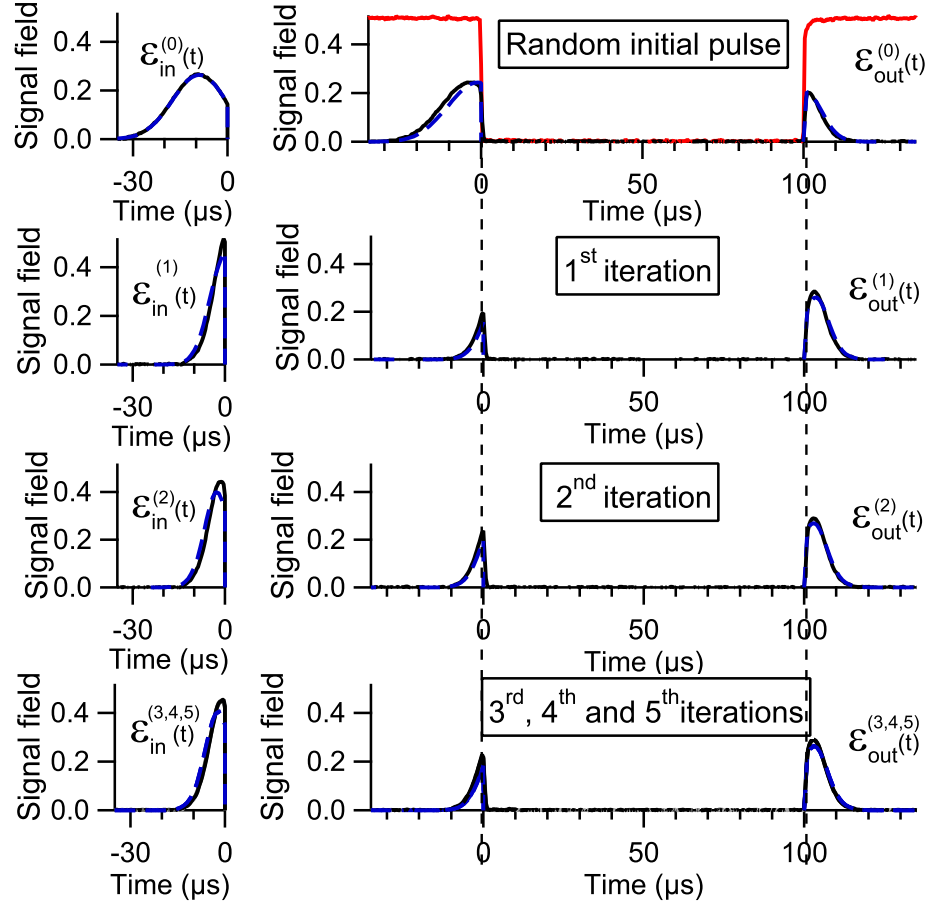


FIG. 4.1: Iterative signal pulse optimization. The experimental data (solid black lines) is taken at 60.5°C ($\alpha_0 L = 24$) using 16 mW constant control field during writing and retrieval (solid red line in the top panel) with a $\tau = 100\ \mu\text{s}$ storage interval. Numerical simulations are shown with blue dashed lines. *Left*: Input pulses for each iteration. *Right*: Signal field after the cell, showing leakage of the initial pulse for $t < 0$ and the retrieved signal field \mathcal{E}_{out} for $t > 100\ \mu\text{s}$. All pulses are shown on the same scale, and all input pulses are normalized to have the same area $\int_{-T}^0 |\mathcal{E}_{\text{in}}(t)|^2 dt = 1$, where t is time in μs .

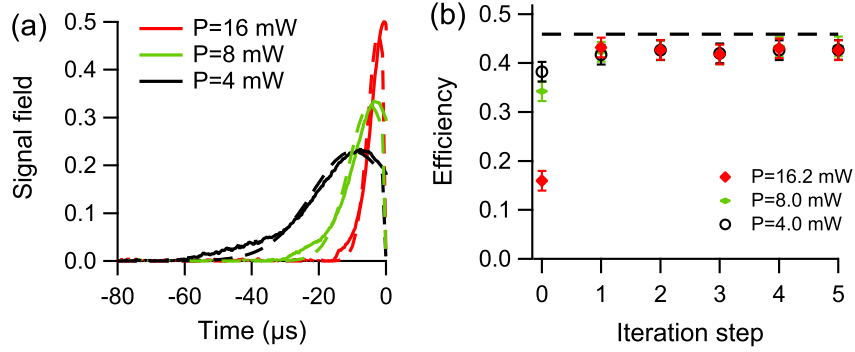


FIG. 4.2: (a) Experimental (solid) and theoretical (dashed) optimized signal pulses obtained after five steps of the iteration procedure for three different powers of the constant control fields during writing and retrieval stages. (b) Corresponding memory efficiencies determined for each iteration step. Theoretically predicted optimal efficiency value is shown by the dashed line. The temperature of the cell was $60.5\text{ }^{\circ}\text{C}$ ($\alpha_0 L = 24$).

optical depth and to confirm the validity of our interpretation of the results, we compare the experimental data to numerical simulations in Fig. 4.1. Using the calculated optical depth and the control Rabi frequency (see Secs. 3.1.8 and 3.1.9), we solve Eqs. 2.41–2.43 analytically in the adiabatic limit $T\alpha_0 L\gamma \gg 1$ [99], which is valid for the experiments discussed throughout this dissertation. There is a clear agreement between the calculated and measured lineshapes and amplitudes of the signal pulses. Also, theory and experiment converge to the optimal signal pulse shape in a similar number of iteration steps (2-3), and the experimental efficiency ($43 \pm 2\%$) converged to a value close to the theoretical limit of 45% (see below).

As in our previous study [142], we confirmed that the final memory efficiency and the final signal pulse after a few iteration steps are independent of the initial signal pulse $\mathcal{E}_{\text{in}}^{(0)}(t)$. We also confirmed that the optimization procedure yields the same memory efficiency for different control fields. While constant control fields of three different powers yield different optimal signal pulses [Fig. 4.2(a)], the measured efficiency [Fig. 4.2(b)] converged after a few iteration steps to the same value of $43 \pm 2\%$. With no spin-wave decay, the highest achievable memory efficiency for the

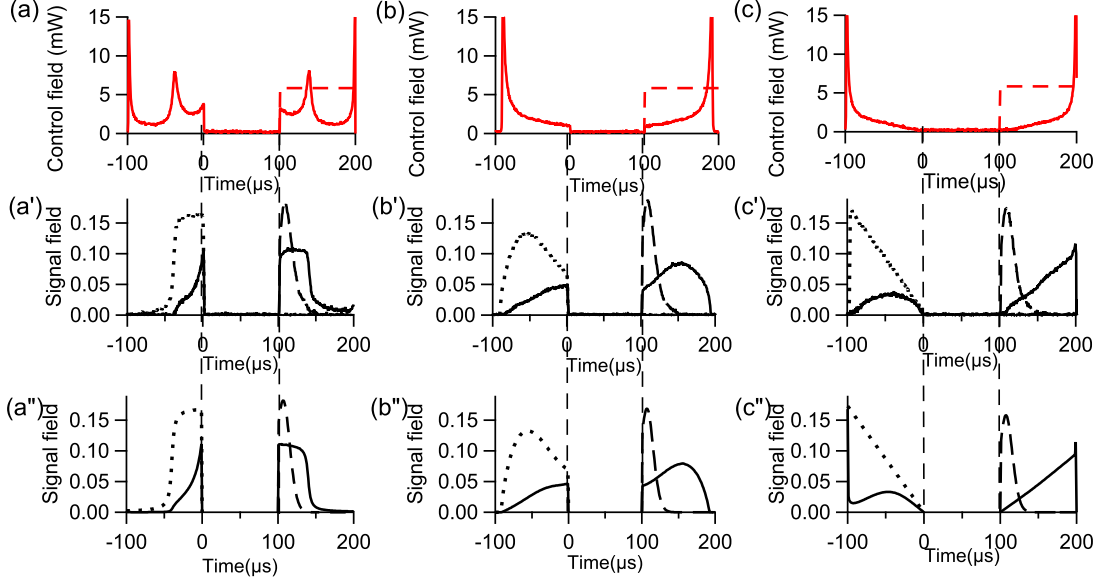


FIG. 4.3: Storage of three signal pulses (a' , b' , c') using calculated optimal storage ($t < 0$) control fields (a), (b), (c). Input signal pulse shapes are shown in black dotted lines. The same graphs also show the leakage of the pulses (solid black lines for $t < 0$) and retrieved signal pulses ($t > 100 \mu\text{s}$) using flat control fields at the retrieval stage (dashed red lines), or using time-reversed control fields (solid red lines). Graphs (a'' , b'' , c'') show the results of numerical calculations of (a' , b' , c'). The temperature of the cell was $60.5 \text{ }^\circ\text{C}$ ($\alpha_0 L = 24$).

optical depth $\alpha_0 L = 24$ is 54% [99]. Taking into account spin-wave decay during the $100 \mu\text{s}$ storage time by a factor of $\exp[-100\mu\text{s}/500\mu\text{s}] = 0.82$, the highest expected efficiency is 45% [dashed line in Fig. 4.2(b)], which matches our experimental results reasonably well.

4.2 Control pulse optimization

The iterative optimization procedure described in the previous section has an obvious advantage: the optimal signal pulse shape is found directly through experimental measurements without any prior knowledge of the system parameters (*e.g.*, optical depth, control field Rabi frequency, various decoherence rates, *etc.*). However, in some situations, it is difficult or impossible to shape the input signal

pulse (*e.g.*, if it is generated by parametric down-conversion [143]). In these cases, the *control field* temporal profile must be adjusted in order to optimally store and retrieve a given signal pulse.

To find the optimal writing control field for a given input pulse shape $\mathcal{E}_{\text{in}}(t)$, we maximize η (Eq. 5.1) within the three-level model (Eqs. 2.41–2.43). In this model, for a given optical depth $\alpha_0 L$ and a given retrieval direction (coinciding with the storage direction in the present experiment), there exists an optimal spin wave $S_{\text{opt}}(z)$, which gives the maximum memory efficiency. One way to calculate the control field required to map the input pulse onto this optimal spin wave is to first calculate an artificial “decayless” spin-wave mode $s(z)$, which, like $S_{\text{opt}}(z)$, depends only on the optical depth and not on the shape of the incoming pulse. This “decayless” mode $s(z)$ hypothetically allows for unitary reversible storage of an arbitrary signal pulse in a semi-infinite and polarization-decay-free atomic ensemble, in which the group velocity of the pulse is still given by Eq. 2.68. The unitarity of the mapping establishes a 1-to-1 correspondence between a given input signal pulse shape $\mathcal{E}_{\text{in}}(t)$ and an optimal writing control field that maps this input pulse onto $s(z)$. The same control field maps this input pulse onto the true optimal spin wave $S_{\text{opt}}(z)$, once polarization decay and the finite length of the medium are taken into account. The details of this construction are described in Ref. [99].

As an example of control field optimization, we consider the storage of three different initial pulse shapes, shown by dotted black lines in the middle row in Fig. 4.3: a step with a rounded leading edge (a’), a segment of the sinc-function (b’), and a descending ramp (c’). The top row (a,b,c) shows the corresponding calculated optimal writing ($t < 0$) control pulses. Since the shape and power of the *retrieval* control pulse do not affect the memory efficiency [43, 99], we show, in the top row of Fig. 4.3, two retrieval control fields for each input pulse: a flat control field (dashed) and the time-reverse of the writing control (solid). As expected, the flat control

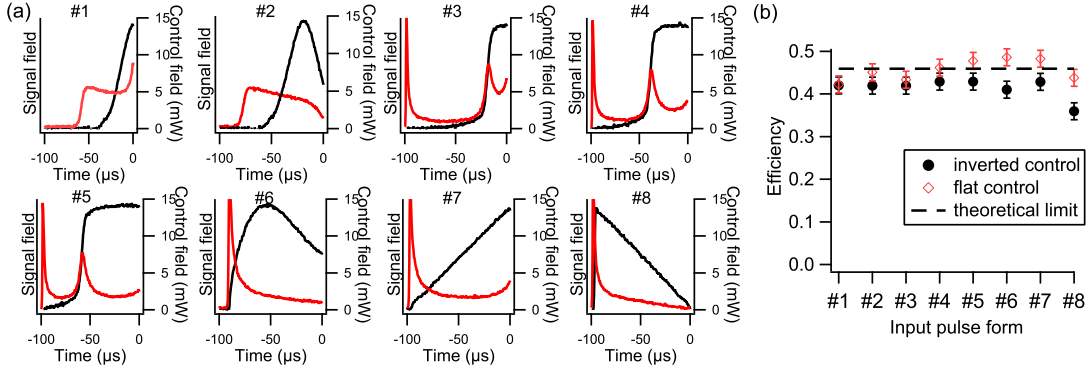


FIG. 4.4: (a) Eight randomly selected signal pulse shapes (black lines) and their corresponding optimal control fields (red lines). (b) Memory efficiency for the eight signal pulse shapes using calculated optimized control fields at the writing stage, and flat control fields (open red diamonds) or inverted writing control fields (solid black circles) at the retrieval stage. Theoretically predicted optimal memory efficiency is shown by a dashed line. The temperature of the cell was $60.5\text{ }^{\circ}\text{C}$ ($\alpha_0 L = 24$).

field (the same for all three inputs) results in the same output pulse [dashed in (a', b', c')] independent of the input signal pulse, because the excitation is stored in the same optimal spin wave in each case. On the other hand, using the time-reversed writing control field for retrieval yields output pulses that are time-reversed (and attenuated) copies of the corresponding input pulses. This means that the time-reversal iterations of Sec. 4.1 starting with these control-signal pairs converge on the zeroth iteration, which proves the consistency of the signal optimization of Sec. 4.1 with the control optimization of the present section. The experimental data also agrees very well with numerical simulations [bottom row (a'', b'', c'') in Fig. 4.3], supporting the validity of our interpretation of the data.

To further test the effectiveness of the control optimization procedure, we repeated the same measurements for eight different randomly selected pulse shapes, shown as black lines in Fig. 4.4(a). Pulses #4, #6, and #8 are the same as the input pulses (a'), (b'), and (c') in Fig. 4.3. For each of the eight input pulses, we calculated the optimal writing control [red lines in Fig. 4.4(a)] and then measured

the memory efficiency [Fig. 4.4(b)], retrieving with either a constant control pulse or a time-reversed writing control pulse (open red diamonds and solid black circles, respectively). The measured efficiencies are in good agreement with each other and with the theoretically calculated maximum achievable memory efficiency of 45% (horizontal dashed line) for the given optical depth.

By performing these experiments, we found that knowledge of accurate values for the experimental parameters, such as optical depth or control field intensity, is critical for calculations of the optimal control field. Even a few percent deviation in their values caused measurable decreases in the output signal pulse amplitude. In our experiment, effective optical depth and control field Rabi frequency were computed accurately directly from measurable experimental quantities with no free parameters. The accuracy of the parameters was also verified by the excellent agreement of experimental and theoretical results of iterative optimization in Sec. 4.1. We note that for some other systems, the necessary experimental parameters may be difficult to compute directly with high accuracy; in that case, they can be extracted from the iteration procedure of Sec. 4.1.

4.3 Dependence of memory efficiency on the optical depth

In the previous two sections, we verified at optical depth $\alpha_0 L = 24$, the consistency of the signal and control optimization methods and their agreement with the three-level theory. In this section, we study the dependence of memory efficiency on optical depth. To verify the theoretical prediction that the optimal efficiency depends only on the optical depth of the sample, we repeated the iterative signal optimization procedure (Secs. 3.1.8 and 3.1.9) for several constant control field pow-

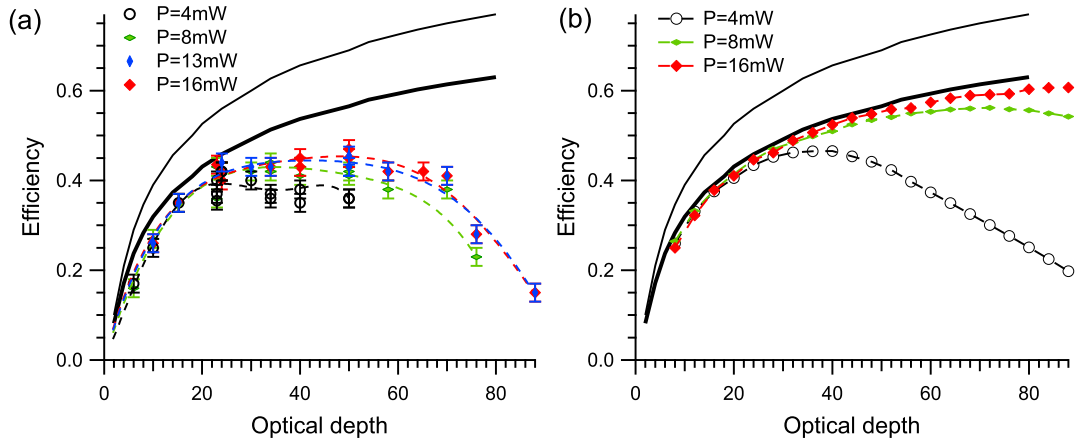


FIG. 4.5: Memory efficiency as a function of optical depth obtained by carrying out iterative signal optimization until convergence. (a) At each optical depth, we considered constant control fields at four different power levels (indicated on the graph) during writing and retrieval stages. Note that many experimental data points overlap since the converged efficiencies are often the same for different control fields. Dashed lines are to guide the eye. Thin and thick black solid lines show the theoretically predicted maximum efficiency assuming no spin-wave decay and assuming an efficiency reduction by a factor of 0.82 during the $100 \mu\text{s}$ storage period, respectively. (b) Thin and thick black lines are the same as in (a), while the three lines with markers are calculated efficiencies for three different control fields (indicated on the graph) assuming spin-wave decay with a $500 \mu\text{s}$ time constant during all three stages of the storage process (writing, storage, retrieval).

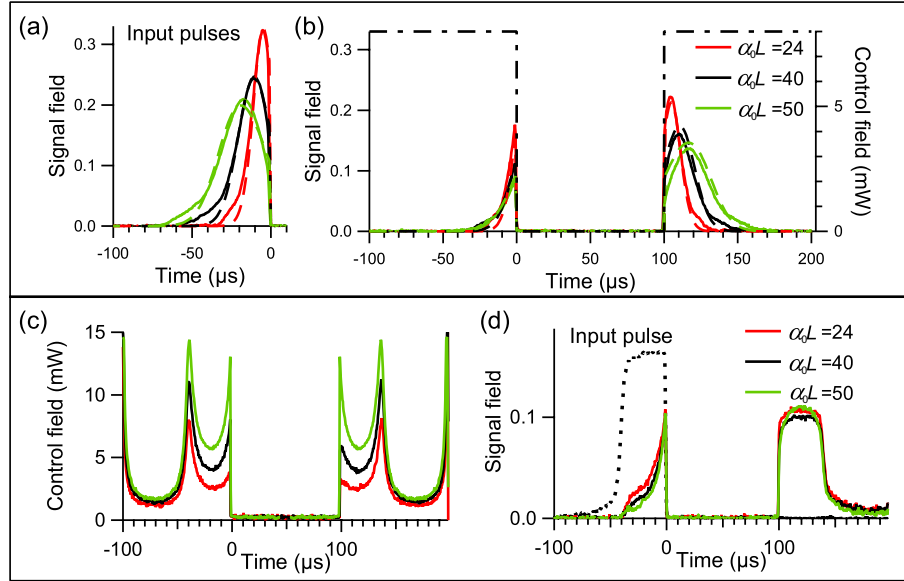


FIG. 4.6: Results of the optimization procedures for different optical depths: $\alpha_0 L = 24$ (red), $\alpha_0 L = 40$ (black), and $\alpha_0 L = 50$ (green). The top panel [(a) and (b)] shows storage and retrieval (b) of the optimized input signal pulses (a) obtained by running iterative optimization until convergence for a constant control field of power 8 mW [dash-dotted line in (b)]. Solid lines correspond to experimental results, while dashed lines show the results of numerical simulations. In the bottom panel [(c) and (d)], (c) shows the calculated optimal writing control fields ($t < 0$) for a step-like signal pulse [dotted line in (d)] and the time-reverses of these control fields used during retrieval ($t > 100 \mu\text{s}$), while (d) shows the resulting storage followed by retrieval.

ers at different temperatures of the Rb cell ranging from 45°C ($\alpha_0 L = 6$) to 77°C ($\alpha_0 L = 88$). In Fig. 4.5(a), we plot the measured efficiencies (markers) along with the maximum achievable efficiency predicated by the theory without spin decay (thin black line) and with spin decay during the storage time (thick black line). This graph allows us to make several important conclusions.

First of all, it demonstrates that for relatively low optical depths ($\alpha_0 L \leq 25$), the optimized memory efficiency for different control fields is the same, to within the experimental uncertainty, and approximately matches the theoretical value (thick black line). This confirms that the optimization procedure yields the maximum efficiency achievable for a given optical depth. However, for $\alpha_0 L > 20$, the efficiency obtained with the lowest control field power (black empty circles) dropped below

the efficiency obtained for higher control powers. As we will now show, the most probable reason for such deviation is spin-wave decay during writing and retrieval.

As the optical depth increases, the duration of the optimal input pulse increases as well, as shown in Fig. 4.6(a), following the underlying decrease of group velocity: $T \sim L/v_g \propto \alpha_0 L$ [99]. Thus, above a certain value of $\alpha_0 L$, the duration of the optimal pulse for a given control field becomes comparable with the spin wave lifetime, and the spin-wave decoherence during storage and retrieval stages can no longer be ignored. Further increase of the optical depth leads to a reduction of retrieval efficiency, even though the iterative optimization procedure is still valid [99] and produces signal pulses that are stored and retrieved with the highest efficiency possible for a given control field and $\alpha_0 L$. Fig. 4.5(b) shows the calculated maximum achievable efficiencies for different constant control powers as a function of the optical depth, taking into account spin-wave decay with a $500 \mu\text{s}$ time constant during all three stages of light storage. For each control field power, the efficiency peaks at a certain optical depth, and then starts to decrease as optical depth increases further. Since lower control powers require longer optimal input pulses $T \sim L/v_g \propto 1/|\Omega|^2$ [see Fig. 4.2(a)], the corresponding efficiency reaches its peak at lower optical depths. Thus, the problem of efficiency reduction posed by spin-wave decay during writing and retrieval can be alleviated by using higher control powers, and hence shorter optimal signal pulses. While this effect explains the reduction of maximum memory efficiency attained with the lowest control power for $\alpha_0 L > 20$ [Fig. 4.5(a)], other effects, discussed below, degrade the efficiency for all other control powers for $\alpha_0 L > 25$, as indicated by the divergence of experimental data in Fig. 4.5(a) from the corresponding theoretical efficiencies in Fig. 4.5(b) (red and green lines). Remarkably, at these optical depths, the iterative signal optimization procedure still yields efficiencies that grow monotonically at each iteration step for the three highest control powers. This suggests that iterative signal optimization

may still be yielding the optimum efficiency, although this optimum is lower than what the simple theoretical model predicts.

To further test the applicability of our optimization procedures at higher optical depths, we complemented the signal-pulse optimization [Fig. 4.6(a,b)] with the corresponding control field optimization [Fig. 4.6(c,d)]. We stored and retrieved input pulse #4 from Fig. 4.4(a) using calculated optimal writing control fields [$t < 0$ in Fig. 4.6(c)] at different optical depths $\alpha_0 L = 24, 40,$ and 50 . As expected, the overall control power was higher at higher optical depths to keep the group velocity unchanged: $L/T \sim v_g \propto \Omega^2/(\alpha_0 L)$. For each optical depth, we used a time-reversed writing control field to retrieve the stored spin wave. This resulted in the output signal pulse shape identical to the time-reversed (and attenuated) copy of the input pulse, as shown in Fig. 4.6(d). Although the memory efficiency drops below the theoretical value at these high optical depths [$\alpha_0 L = 50$ for the green lines in Fig. 4.6(c,d)], the results suggest that the calculated control field may still be optimal, since it yields the time-reverse of the input signal at the output.

To gain insight into what may limit the memory efficiency for $25 < \alpha_0 L < 60$, we investigated the effect of resonant four-wave mixing. Thus far, we have considered only the ground-state coherence created by the control and signal fields in the one-photon resonant Λ configuration (Fig. 2.1). However, the strong control field applied to the ground state $|g\rangle$ can also generate an additional Stokes field \mathcal{E}' , as shown in Fig. 4.7(a). This process is significantly enhanced in EIT media [110, 144–147]. In particular, it has been shown that a weak signal pulse traversing an atomic ensemble with reduced group velocity generates a complimentary Stokes pulse that travels alongside with a comparably low group velocity [148, 149].

To determine the effect of resonant four-wave mixing on light storage, we first carried out iterative signal optimization for a constant control field pulse of 16 mW power at different optical depths, but then detected not only the signal field, but also

the Stokes field, at the retrieval stage [see Fig. 4.7(b)]. We see that at low optical depths, the retrieved Stokes pulse [blue empty diamonds] is negligible compared to the output signal pulse [red filled diamonds, which are the same as the red filled diamonds in Fig. 4.5(a)]. However, at $\alpha_0 L \gtrsim 25$, the energy of the output pulse in the Stokes channel becomes significant. While the energy of the retrieved signal pulse stayed roughly unchanged for $25 < \alpha_0 L < 60$, the energy of the output Stokes pulse showed steady growth with increasing $\alpha_0 L$. Moreover, the combined energy (black empty circles) of the two pulses retrieved in the signal and Stokes channels added up to match well the theoretically predicted highest achievable efficiency (solid black line). We will study elsewhere whether this match is incidental and whether it can be harnessed for memory applications. For the purposes of the present work, we simply conclude that the effects of four-wave mixing become significant around the same value of $\alpha_0 L$ (~ 25) where experiment starts deviating from theory. Therefore, four-wave mixing may be one of the factors responsible for the low experimental efficiencies at high optical depths.

For $\alpha_0 L > 60$, iterative signal optimization still converges, but efficiency does not grow monotonically at each iteration step, which clearly indicates the breakdown of time-reversal-based optimization [99]. In addition, the final efficiency is significantly lower than the theoretical value (Fig. 4.5). Many factors, other than four-wave mixing, may be contributing to the breakdown of time-reversal-based optimization and to the rapid decrease of memory efficiency at $\alpha_0 L > 60$. First of all, the absorption of the control field at such high optical depths is significant (measured to be $> 50\%$). In that case, the reabsorption of spontaneous radiation contributes appreciably to spin-wave decoherence [150, 151] and can make the spin-wave decay rate γ_s grow with $\alpha_0 L$, reducing the light storage efficiency [152]. The spin-exchange collision rate [134], which destroys the spin-wave coherence, also becomes significant at high Rb density, reducing spin-wave lifetime even further, as we discuss in Ch. 7.

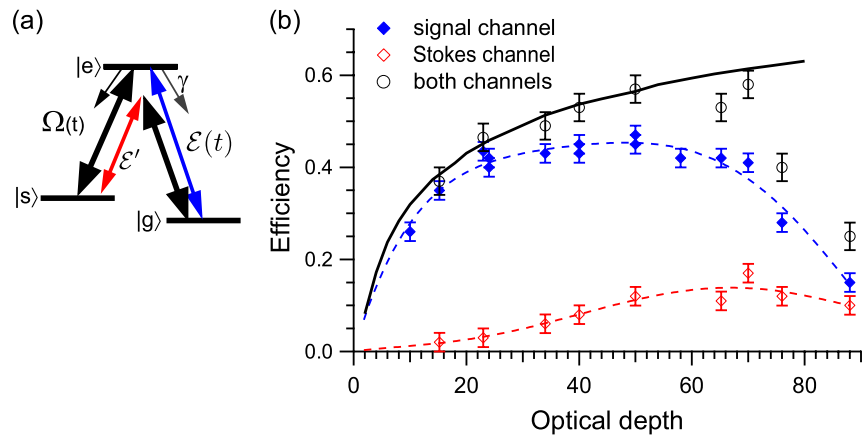


FIG. 4.7: (a) Level diagram illustrating Stokes field (\mathcal{E}') generation due to resonant four-wave mixing. (b) Memory efficiency for retrieval in the signal channel [same as the red filled diamonds in Fig. 4.5(a)], Stokes channel, and the total for both channels. The efficiencies are obtained by carrying out iterative optimization till convergence for constant writing and retrieval control fields of 16 mW power. Dashed lines are to guide the eye. The solid line (same as the thick black line in Fig. 4.5) shows the theoretically predicted maximum efficiency assuming an efficiency reduction by a factor of 0.82 during the 100 μ s storage period.

CHAPTER 5

Full control over storage and retrieval

Quantum memory for light is essential for the implementation of long-distance quantum communication [13] and of linear optical quantum computation [153]. Both applications put forth two important requirements for the quantum memory: (i) the memory efficiency is high (*i.e.*, the probability of losing a photon during storage and retrieval is low) and (ii) the retrieved photonic wavepacket has a well-controlled shape to enable interference with other photons. In this chapter, we report on the first experimental demonstration of this full optimal control over light storage and retrieval: by shaping an auxiliary control field, we store an incoming coherent signal pulse of arbitrary shape and then retrieve it into any desired output pulse shape with the maximum efficiency possible for the given memory. While our results are obtained in warm Rb vapor using electromagnetically induced transparency (EIT) [23, 26], the presented procedure is universal [43] and applicable to a wide range of systems, including ensembles of cold atoms [27, 81, 154] and solid-state impurities [155, 156], as well as to other light storage protocols (*e.g.*, the far-off-resonant Raman scheme [29]). Although our experiment uses weak classical pulses, the linearity of the corresponding equations of motion [43] allows us to expect that our results will

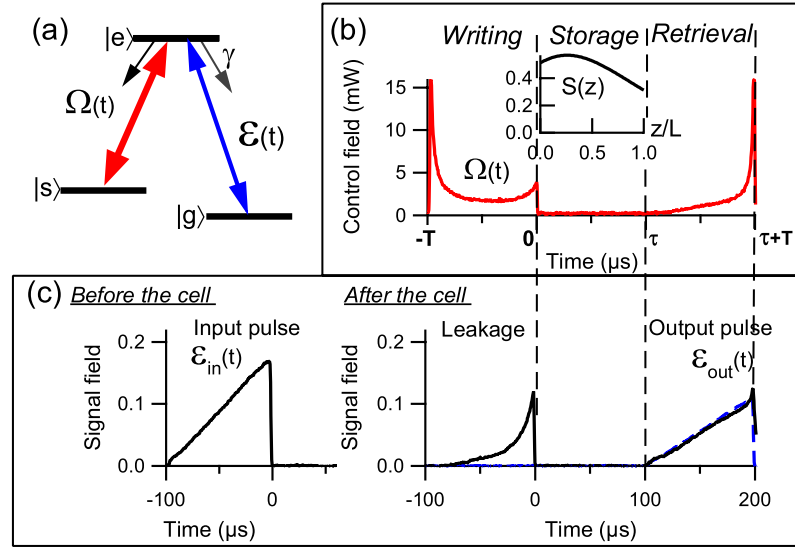


FIG. 5.1: (a) Schematic of the three-level Λ interaction scheme. Control (b) and signal (c) fields in pulse-shape-preserving storage of a “positive-ramp” pulse using a calculated optimal control field envelope $\Omega(t)$. During the *writing* stage ($t < 0$), the input pulse $\mathcal{E}_{in}(t)$ is mapped onto the optimal spin-wave $S(z)$ [inset in (b)], while a fraction of the pulse escapes the cell (leakage). After a *storage* time τ , the spin-wave $S(z)$ is mapped into an output signal pulse $\mathcal{E}_{out}(t)$ during the *retrieval* stage. The dashed blue line in (c) shows the target output pulse shape.

be applicable to quantum states confined to the mode defined by the classical pulse.

In this chapter, we experimentally demonstrate the capability to satisfy both quantum memory requirements in an ensemble with a limited optical depth. Specifically, by adjusting the control field envelopes for several arbitrarily selected input pulse shapes, we demonstrate precise retrieval into any desired output pulse shape with experimental memory efficiency very close to the fundamental limit [43, 99]. This ability to achieve maximum efficiency for any input pulse shape is crucial when optimization with respect to the input pulse [142] is not applicable (*e.g.*, if the photons are generated by parametric down-conversion [143]). At the same time, control over the outgoing mode, with precision far beyond the early attempts [24, 69, 70, 157] is essential for experiments based on the interference of photons stored under different experimental conditions (*e.g.*, in atomic ensembles with different optical depths),

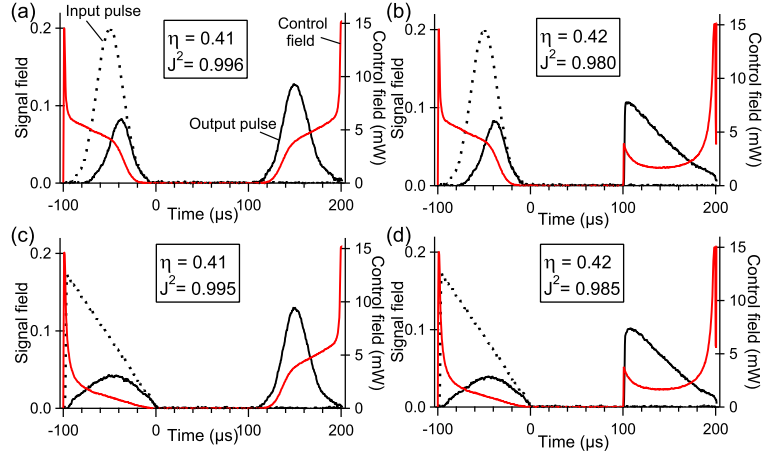


FIG. 5.2: An input Gaussian pulse was optimally stored and retrieved either into its original pulse shape (a) or into a ramp pulse shape (b). Similarly, the incoming ramp pulse was optimally stored and retrieved into a Gaussian (c) or into an identical ramp (d). Input and output signal pulses are shown as dotted and solid black lines, respectively, while the optimal control fields are shown in solid red lines.

or stored a different number of times. In addition, control over the output pulse duration may also allow one to reduce sensitivity to mechanical noise. It is important to note that shaping the output mode via the control pulse avoids additional losses that would be present if one were to post-process the retrieved photon with an electro-optical modulator [121].

An example of optimized light storage with controlled retrieval is shown in Fig. 5.1(b,c). In this measurement, we chose the input pulse $\mathcal{E}_{\text{in}}(t)$ to be a “positive ramp”. According to theory [43, 99], the maximum memory efficiency is achieved only if the input pulse is mapped onto a particular optimal spin wave $S(z)$, unique for each $\alpha_0 L$. The calculated optimal spin-wave for $\alpha_0 L = 24$ is shown in the inset in Fig. 5.1(b). Then, we used the method described in Ref. [99] to calculate the *writing* control field $\Omega(t)$ ($-T < t < 0$) that maps the incoming pulse onto the optimal spin-wave $S(z)$. To calculate the *retrieval* control field $\Omega(t)$ ($\tau < t < \tau + T$) that maps $S(z)$ onto the target output pulse $\mathcal{E}_{\text{tgt}}(t)$, we employ the same

writing control calculation together with the following time-reversal symmetry of the optimized light storage [43, 99, 142]. A given input pulse, stored using its optimal writing control field, is retrieved in the time-reversed and attenuated copy of itself [$\mathcal{E}_{\text{out}}(t) \propto \mathcal{E}_{\text{in}}(\tau - t)$] when the time-reversed control is used for retrieval [$\Omega(t) = \Omega(\tau - t)$]. Thus the control field that retrieves the optimal spin-wave $S(z)$ into $\mathcal{E}_{\text{tgt}}(t)$ is the time-reversed copy of the control that stores $\mathcal{E}_{\text{tgt}}(\tau - t)$ into $S(z)$. As shown in Fig. 5.1(b,c), we used this method to achieve pulse-shape-preserving storage and retrieval, *i.e.*, the target output pulse was identical to the input pulse (“positive ramp”). The measured output pulse [solid black line in Fig. 5.1(c)] matches very well the target shape [dashed blue line in the same figure]. This qualitatively demonstrates the effectiveness of the proposed control method.

To describe the memory quantitatively, we define memory efficiency η as the probability of retrieving an incoming photon after some storage time, or, equivalently, as the energy ratio between retrieved and initial signal pulses:

$$\eta = \frac{\int_{\tau}^{\tau+T} |\mathcal{E}_{\text{out}}(t)|^2 dt}{\int_{-T}^0 |\mathcal{E}_{\text{in}}(t)|^2 dt}. \quad (5.1)$$

To characterize the quality of pulse shape generation, we define an overlap integral J^2 as [39]

$$J^2 = \frac{|\int_{\tau}^{\tau+T} \mathcal{E}_{\text{out}}(t) \mathcal{E}_{\text{tgt}}(t) dt|^2}{\int_{\tau}^{\tau+T} |\mathcal{E}_{\text{out}}(t)|^2 dt \int_{\tau}^{\tau+T} |\mathcal{E}_{\text{tgt}}(t)|^2 dt}. \quad (5.2)$$

The measured memory efficiency for the experiment in Fig. 5.1 is 0.42 ± 0.02 . This value closely approaches the predicted highest achievable efficiency 0.45 for $\alpha_0 L = 24$ [43, 99], corrected to take into account the spin wave decay during the storage time. The measured value of the overlap integral between the output and the target is $J^2 = 0.987$, which indicates little distortion in the retrieved pulse shape.

The definitions of efficiency η and overlap integral J^2 are motivated by quantum

information applications. Storage and retrieval of a single photon in a non-ideal passive quantum memory produces a mixed state that is described by a density matrix $\rho = (1 - \eta)|0\rangle\langle 0| + \eta|\phi\rangle\langle\phi|$ [40], where $|\phi\rangle$ is a single photon state with envelope $\mathcal{E}_{\text{out}}(t)$, and $|0\rangle$ is the vacuum state. Then the fidelity between the target single-photon state $|\psi\rangle$ with envelope $\mathcal{E}_{\text{tgt}}(t)$ and the single-photon state $|\phi\rangle$ is given by the overlap integral J^2 [Eq. (5.2)], while $F = \langle\psi|\rho|\psi\rangle = \eta J^2$ is the fidelity of the output state ρ with respect to the target state $|\psi\rangle$. The overlap integral J^2 is also an essential parameter for optical quantum computation and communication protocols [13, 153], since $(1 - J^2)/2$ is the coincidence probability in the Hong-Ou-Mandel [158] interference between photons $|\psi\rangle$ and $|\phi\rangle$ [39]. One should be cautious in directly using our classical measurements of η and J^2 to predict fidelity for single photon states because single photons may be sensitive to imperfections that do not significantly affect classical pulses. For example, four-wave mixing processes may reduce the fidelity of single-photon storage, although our experiments [120] found these effects to be relatively small at $\alpha_0 L < 25$.

Fig. 5.2 shows more examples of optimal light storage with full output-pulse-shape control. For this experiment, we stored either of two randomly selected input signal pulse shapes — a Gaussian and a “negative ramp” — and then retrieved them either into their original waveforms (a,d) or into each other (b,c). Memory efficiency η and overlap integral J^2 are shown for each graph. Notice that the efficiencies for all four input-output combinations are very similar (0.42 ± 0.02) and agree well with the highest achievable efficiency (0.45) for the given optical depth $\alpha_0 L = 24$. The overlap integrals are also very close to 1, revealing an excellent match between the target and the retrieved signal pulse shapes. Note that different input pulses stored using corresponding (different) optimized writing control fields but retrieved using identical control fields [pairs (a,c) and (b,d)] had identical output envelopes, very close to the target one. This observation, together with the fact

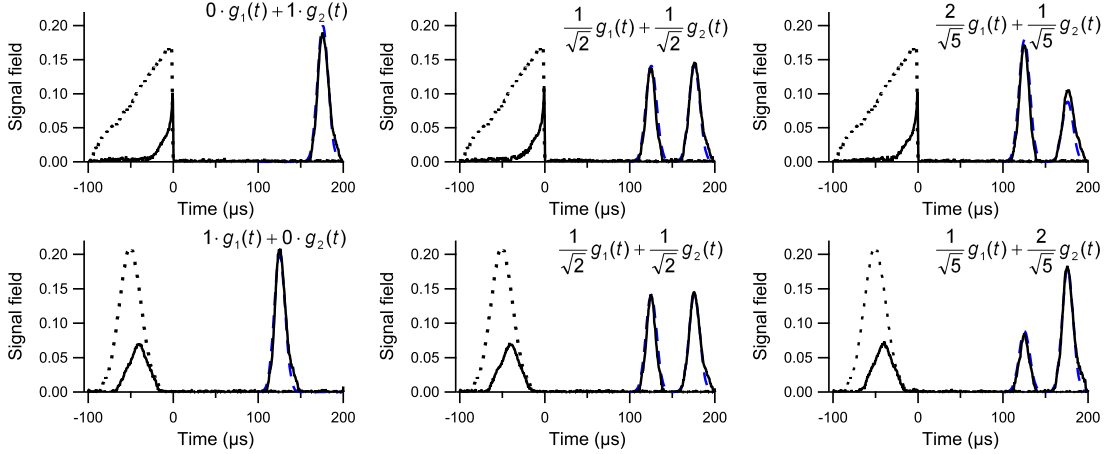


FIG. 5.3: Examples of storage of signal input pulses with Gaussian and triangular envelopes, followed by retrieval in a linear combination of two time-resolved Gaussian pulse shapes $g_1(t)$ and $g_2(t)$. Input and output signal fields are shown in dotted and solid black lines, respectively. Dashed blue lines show the target envelopes.

that the measured memory efficiency is close to the fundamental limit, suggests that indeed different initial pulses were mapped onto the same optimal spin-wave. This indirectly confirms our control not only over the output signal light field but also over the spin-wave.

Our full control over the outgoing pulse shape opens up an interesting possibility to convert a single photon into a so-called “time-bin” qubit — a single photon excitation delocalized between two time-resolved wavepackets (bins). The state of the qubit is encoded in the relative amplitude and phase between the two time bins [159]. Such time-bin qubits are advantageous for quantum communication since they are insensitive to polarization fluctuations and depolarization during propagation through optical fibers [159]. We propose to efficiently convert a single photon with an arbitrary envelope into a time-bin qubit by optimally storing the photon in an atomic ensemble, and then retrieving it into a time-bin output envelope with well-controlled relative amplitude and phase using a customized retrieval control field.

To illustrate the proposed output pulse shaping, in Fig. 5.3, we demonstrate

storage of two different classical input pulses (a Gaussian and a positive ramp), followed by retrieval into a time-bin-like classical output pulse, consisting of two distinct Gaussian pulses $g_{1,2}(t)$ with controllable relative amplitude and delay. We obtained the target output independently of what the input pulse shape was. We also attained the same memory efficiency as before (0.41 ± 0.02) for all linear combinations. Also, regardless of the input, the output pulse shapes matched the target envelopes very well, as characterized by the value of the overlap integral close to unity $J^2 = 0.98 \pm 0.01$. We also verified that the envelopes of the two retrieved components of the output pulse were nearly identical by calculating the overlap integral $J^2(g_1, g_2)$ between the retrieved bins g_1 and g_2 . This parameter is important for applications requiring interference of the two qubit components [159]. The average value of $J^2(g_1, g_2) = 0.94 \pm 0.02$ was consistently high across the full range of target outputs. The relative phase of the two qubit components can be adjusted by controlling the phase of the control field during retrieval. The demonstrated control over the amplitude ratio and shape of the two output pulses is essential for achieving high-fidelity time-bin qubit generation. Our scheme is also immediately applicable to high-fidelity partial retrieval of the spin wave [24], which forms the basis for a recent promising quantum communication protocol [11].

To conclude, we have reported the experimental demonstration of optimal storage and retrieval of arbitrarily shaped signal pulses in an atomic vapor at an optical depth $\alpha_0 L = 24$ by using customized writing control fields. Our measured memory efficiency is close to the highest efficiency possible at that optical depth. We also demonstrate full precision control over the retrieved signal pulse shapes, achieved by shaping the retrieval control field. A high degree of overlap between the retrieved and target pulse shapes was obtained (overlap integral $J^2 = 0.98 - 0.99$) for all input and target pulse shapes tested in the experiments. We also demonstrated the potential application of the presented technique to the creation of optical time-bin

qubits and to controlled partial retrieval. Finally, we observed excellent agreement between our experimental results and theoretical modeling. The optimal storage and pulse-shape control presented here are applicable to a wide range of experiments, since the underlying theory applies to other experimentally relevant situations such as ensembles enclosed in a cavity [40, 154], the off-resonant regime [40, 43, 99], non-adiabatic storage (*i.e.*, storage of pulses of high bandwidth) [97], and ensembles with inhomogeneous broadening [98], including Doppler broadening [26] and line broadening in solids [33]. Thus, we expect this pulse-shape control to be indispensable for applications in both classical [160] and quantum optical information processing.

CHAPTER 6

The effects of four-wave mixing on pulse propagation through an EIT medium

In this chapter, we investigate the propagation and storage of weak optical signal pulses in an optically thick hot atomic vapor under conditions of electromagnetically induced transparency (EIT) and four-wave mixing (FWM). As we have reported on in Ch. 4, optimal performance of an EIT-based memory requires operation at a high optical depth in order to yield improved memory efficiency. For example, 90% memory efficiency requires an optical depth $\alpha_0 L > 100$ [99]. On the other hand, an optically dense coherent atomic medium is also known to enhance competing undesired effects, such as resonant four-wave mixing (FWM) in a double- Λ configuration. In this FWM process, the far-detuned interaction of the control field, which resonantly drives the $|s\rangle \rightarrow |e\rangle$ transition (see Fig. 2.4), with the atomic ground-state coherence enhances the generation of an off-resonant Stokes optical field (α' in Fig. 2.4). In turn, the presence of the Stokes field strongly affects

pulse propagation.

This chapter is organized as follows. We first start from the four equations of motion derived in Eqs. 2.103–2.106 and develop a novel theoretical model of the EIT-FWM interference phenomenon. We first investigate the modification of the two-photon resonant transmission peak and the dynamics of pulse propagation in the case of a seeded Stokes field, which was produced simultaneously with the signal field by phase modulating the original monochromatic laser field. Specifically, we show that the resulting signal and Stokes spectra are well-described by a double- Λ system. Additionally, we show that this model accurately portrays the dynamics of signal and Stokes field propagation. We then analyze the regime of stored light under conditions of EIT and FWM, both experimentally and theoretically. We will find that the spin wave is only weakly affected by the Stokes field, and we will develop an intuitive analytical picture of the effects of FWM on the signal and Stokes pulses and on the atomic spin coherence. We note that, in order to avoid carrying extra factors of 2, we employ the optical depth notation of $2d$ in Sec. 6.1, but notate the optical depth as $\alpha_0 L$ in Sec. 6.4.

6.1 Theoretical description of FWM in the steady-state

As a starting point, we pick up from Eqs. 2.103–2.106. We remind the reader that we are working in the undepleted pump approximation and assume that the Rabi frequencies of the strong control fields Ω and Ω' are not affected by the atoms, so that $\Omega(z, t) = \Omega(z)$ and $\Omega'(z, t) = \Omega'(z)$ are constants. We show presently that when the control field is static in time, as in cw and slow light experiments, that there is an analytic solution. For simplicity, we move to a frame that is moving with

the pulse phase velocity, c , so that $\partial_t + c\partial_z \rightarrow c\partial_z$. We perform a Fourier transform in time ($t \rightarrow \omega$, $\partial_t \rightarrow -i\omega$) to find,

$$\left(-i\omega + c\frac{\partial}{\partial z}\right)\mathcal{E}(z, \omega) = \frac{i\nu_1 N}{2\epsilon_0 V}\wp_{eg}\tilde{\rho}_{eg} \quad (6.1)$$

$$\left(-i\omega + c\frac{\partial}{\partial z}\right)\mathcal{E}'^*(z, \omega) = -\frac{i\nu_2 N}{2\epsilon_0 V}\wp_{es}\frac{\Omega'^*}{\Delta_{\text{hf}}}\tilde{\rho}_{sg} \quad (6.2)$$

$$-i\omega\tilde{\rho}_{sg} = -[\gamma_0 - i(\delta - \delta_s)]\tilde{\rho}_{sg} + i\Omega^*\tilde{\rho}_{eg} + i\frac{\Omega'}{\Delta_{\text{hf}}}\alpha'^* \quad (6.3)$$

$$-i\omega\tilde{\rho}_{eg} = -[\gamma - i(\delta - 2\delta_s)]\tilde{\rho}_{eg} + i\Omega\tilde{\rho}_{sg} + i\alpha. \quad (6.4)$$

As before, \mathcal{E} , \mathcal{E}' are the slowly-varying electric field envelopes of the signal and Stokes fields, respectively, $\alpha = \mathcal{E}\wp_{eg}/\hbar$ and $\alpha' = \mathcal{E}'\wp_{es}/\hbar$ are the corresponding Rabi frequencies, and \wp_{eg} and \wp_{es} are the (real) dipole matrix elements of the transitions. In the continuous-wave (cw) regime, the atomic coherences have essentially reached a steady state, and the left hand side of the coherence equations can be set to zero. We then solve for the Fourier-transform of the coherences to find:

$$\begin{pmatrix} \tilde{\rho}_{sg}(z, \omega) \\ \tilde{\rho}_{eg}(z, \omega) \end{pmatrix} = \frac{i}{F} \begin{pmatrix} \Gamma & i\Omega^* \\ i\Omega & \Gamma_0 \end{pmatrix} \begin{pmatrix} \frac{\Omega'}{\Delta_{\text{hf}}}\alpha'^*(z, \omega) \\ \alpha(z, \omega) \end{pmatrix} \quad (6.5)$$

where, similar to before, $\Gamma_0 = [\gamma_0 - i(\delta - \delta_s + \omega)]$, $\Gamma = [\gamma - i(\delta - 2\delta_s + \omega)]$, and $F = |\Omega|^2 - \Gamma\Gamma_0$. We restrict ourselves to the experimental configuration described in this dissertation, where the Clebsch-Gordan coefficients are such that $\Omega' = -\sqrt{3}\Omega$, and $\wp_{es} = -\wp_{eg}/\sqrt{3}$; thus, $\Omega'\wp_{es} = \Omega\wp_{eg}$.

Inserting Eqs. 6.5 into Eqs. 6.1–6.2, we find that the Fourier components of the signal field $\mathcal{E}(\omega)$ and the Stokes field $\mathcal{E}'(\omega)$ propagate according to the coupled

differential equations, to linear order in α and α' [109, 110, 144]:

$$\begin{aligned} \frac{\partial}{\partial z} \begin{pmatrix} \mathcal{E}(z, \omega) \\ \mathcal{E}'^*(z, \omega) \end{pmatrix} &= \frac{i\nu}{2c} \begin{pmatrix} \chi_{11}(\omega) & \chi_{12}(\omega) \\ \chi_{21}(\omega) & 0 \end{pmatrix} \begin{pmatrix} \mathcal{E}(z, \omega) \\ \mathcal{E}'^*(z, \omega) \end{pmatrix} \\ &= \frac{d\gamma}{FL} \begin{pmatrix} \delta + \delta_s + i\gamma_0 & -\Omega^2/\Delta_{\text{hf}} \\ \Omega^{*2}/\Delta_{\text{hf}} & 0 \end{pmatrix} \begin{pmatrix} \mathcal{E}(z, \omega) \\ \mathcal{E}'^*(z, \omega) \end{pmatrix}, \end{aligned} \quad (6.6)$$

where we have used $\nu_1 \approx \nu_2$, and as before, $\gamma = \frac{\nu_1^3 \rho_{eg}^2}{3\pi\epsilon_0 \hbar c^3}$ and defined the optical depth $d = \frac{3}{8\pi} \frac{N}{V} \lambda^2 L$, since the Clebsch-Gordan coefficient corresponding to the $|g\rangle \rightarrow |e\rangle$ transition is $\frac{-1}{\sqrt{2}}$. Further assuming that Ω is real, which is usually the case for electronic transitions in atoms, Eq. 6.6 can be solved analytically for $\mathcal{E}(z, \omega)$ and $\mathcal{E}'^*(z, \omega)$ by integrating with respect to dummy variable z' along the interaction length (*i.e.*, from 0 to point z). Defining $\Delta_{\text{R}} = -\Omega^2/\Delta_{\text{hf}}$, we obtain

$$\begin{pmatrix} \mathcal{E}(z, \omega) \\ \mathcal{E}'^*(z, \omega) \end{pmatrix} = \exp \left[i \frac{d\gamma}{F} \begin{pmatrix} \delta + \delta_s + i\gamma_0 & \Delta_{\text{R}} \\ -\Delta_{\text{R}} & 0 \end{pmatrix} \right] \begin{pmatrix} \mathcal{E}(0, \omega) \\ \mathcal{E}'^*(0, \omega) \end{pmatrix} \quad (6.7)$$

The matrix, which we define as M , is diagonalizable, so we can write $\exp[M] = \exp[PD P^{-1}] = P \text{diag}[e^{\lambda_-}, e^{\lambda_+}] P^{-1}$, where $\text{diag}[\lambda_-, \lambda_+]$ represents a diagonal matrix comprised of the exponential of the eigenvalues, λ_{\pm} . We first define

$$\sigma(\omega) = i \frac{d\gamma}{2FL} \Gamma_0 \quad (6.8)$$

$$\beta(\omega) = \sqrt{\Gamma_0^2 + 4\Delta_{\text{R}}^2} \quad (6.9)$$

$$\xi(\omega) = \frac{d\gamma}{2FL} \beta(\omega), \quad (6.10)$$

and find $\lambda_{\pm} = i\sigma \pm |\xi|$. Thus,

$$\exp[M] = \frac{1}{\xi} e^{i\sigma z} \begin{pmatrix} \xi \cosh[\xi z] + i\sigma \sinh[\xi z] & i\frac{d\gamma\Delta_R}{F} \sinh[\xi z] \\ -i\frac{d\gamma\Delta_R}{F} \sinh[\xi z] & \xi \cosh[\xi z] - i\sigma \sinh[\xi z] \end{pmatrix}, \quad (6.11)$$

For the conditions corresponding to our experiment: $\mathcal{E}'^*(0, \omega) = -f\mathcal{E}(0, \omega)$, in which, as a byproduct of phase-modulation, the Stokes seed has the same initial temporal lineshape as the signal pulse, but with an opposite phase and with some amplitude scaling factor $0 < f \leq 1$. We find the following analytic expressions for the Fourier components of the signal and Stokes fields [109, 161]:

$$\mathcal{E}(z, \omega) = e^{i\sigma z} \left\{ \mathcal{E}(0, \omega) \left[\cosh(\xi z) + i\frac{\sigma}{\xi} \sinh(\xi z) \right] + \frac{2\Delta_R}{\beta} \sinh(\xi z) \mathcal{E}'^*(0, \omega) \right\}, \quad (6.12)$$

$$\mathcal{E}'^*(z, \omega) = e^{i\sigma z} \left\{ \mathcal{E}'^*(0, \omega) \left[\cosh(\xi z) - i\frac{\sigma}{\xi} \sinh(\xi z) \right] - i\frac{2\Delta_R}{\beta} \sinh(\xi z) \mathcal{E}(0, \omega) \right\}. \quad (6.13)$$

Eqs. 6.12 and 6.13 fully describe the propagation of the light fields through the atomic medium. Theoretically, the measured transmission spectra of the signal and Stokes fields are computed as $|\mathcal{E}(L)|$ and $|\mathcal{E}'(L)|$, respectively using Eqs. 6.12 and 6.13. We interpret equations 6.12 and 6.13 by first applying a few simplifications, similar to Ref. [161], by first shifting the two-photon detuning by the light shift, defining $\tilde{\delta} = \delta - \delta_s$ (setting $\omega = 0$ for continuous wave measurements), and considering large $|\tilde{\delta}| \gg 2|\Delta_R|$, but also $|\tilde{\delta}| \ll \Omega$, and $|\tilde{\delta}| \gg \gamma_0$. Under these assumptions, $\beta \approx i\tilde{\delta}$, and for our parameters, $2\xi L = 2i\sigma L \approx i\frac{\tilde{\delta}}{\Omega^2/(d\gamma)} - \frac{\tilde{\delta}^2}{[\Omega^2/(\sqrt{d\gamma})]^2}$, where the denominators of the two terms represent, respectively, the inverse of the EIT group delay and the square of the width of the EIT transparency window. Under these approximations, which hold well in our experiments, the signal and Stokes amplitudes

after the cell are:

$$|\mathcal{E}(L)| = \mathcal{E}(0) \left| e^{2i\sigma L} - f \frac{\Omega^2}{\Delta_{\text{hf}} \tilde{\delta}} (1 - e^{2i\sigma L}) \right|, \quad (6.14)$$

$$|\mathcal{E}'(L)| = \mathcal{E}(0) \left| \frac{\Omega^2}{\Delta_{\text{hf}} \tilde{\delta}} (1 - e^{2i\sigma L}) - f \right|. \quad (6.15)$$

These expressions allow us to interpret the transmission spectra for both fields in terms of an interference between EIT and FWM effects, where the FWM effect is represented by the terms proportional to $1/\Delta_{\text{hf}}$ [161]. At small optical depth, the effect of FWM on the signal field transmission is negligible, and we observe a typical symmetric EIT transmission peak (not shown). As optical depth increases, the FWM term ($\propto 1/\Delta_{\text{hf}}$) in Eq. 6.14 becomes more noticeable relative to the EIT term, which reduces with d due to the shrinking of the EIT window. Since the phase of $e^{2i\sigma L}$ in Eq. 6.14 is $\approx \tilde{\delta}/(v_g/L)$, for $\tilde{\delta} > 0$, $\tilde{\delta} = n\pi v_g/L$ gives destructive interference (and hence dips in the spectrum) for even n , and constructive interference for odd n . For $\tilde{\delta} < 0$, the opposite case is true: even n yields constructive interference; odd n yields destructive interference. Thus, for example, one expects to see one more destructive interference fringe at negative detunings than at positive detunings—as evidenced in the spectra below.

6.2 Spectral Measurements

We record the transmission spectra for continuous signal and Stokes fields by sweeping the EOM frequency, which changes the two-photon detuning δ , and measuring their amplitude variations after the cell. Fig. 6.1(a,b) depicts the experimental results for an optical depth of $2d = 52$. Solid lines represent the spectra corresponding to the signal field transmission; dashed lines correspond to the Stokes field transmission spectra. Black lines are with no Stokes filtering (*i.e.*, $f = 1$); red

lines are with a Stokes intensity attenuation so that $f = \sqrt{0.05}$. These two values of f (1 and $\sqrt{0.05}$) are shown by horizontal dashed blue lines in Figs. 6.1(b,b') and represent the input Stokes amplitude.

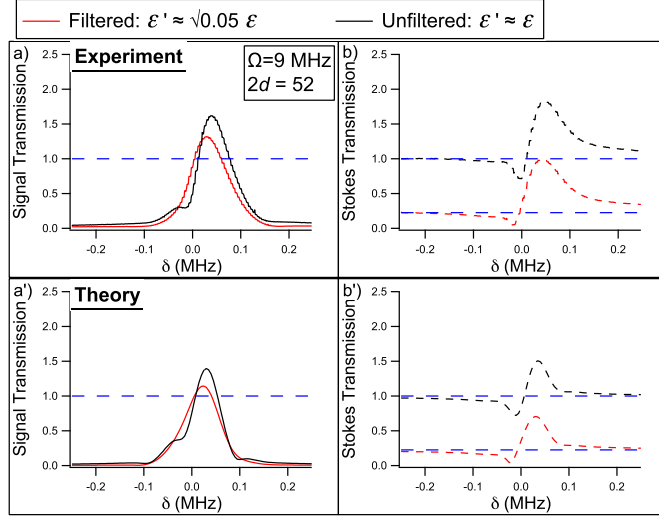


FIG. 6.1: (a, b) Signal and Stokes amplitude spectra at an optical depth of $2d = 52$ with a beam diameter of 4 mm and $\Omega/2\pi = 9$ MHz. Black traces are with a full Stokes seed present. Red traces are with the Stokes seed amplitude attenuated to $\approx \sqrt{0.05}$ of the signal field's amplitude. (a', b') Corresponding theoretical predictions.

With the reduced Stokes seed (red curves), the effects of FWM are suppressed, and we observe a slightly amplified and nearly symmetric EIT transmission peak. However, when the full Stokes seed field is present (black curves), on one hand we observe more gain in the signal field, but on the other hand the FWM/EIT destructive interference becomes more evident by the presence of a “knee” in the signal spectra for small negative detunings. These results are in very good agreement with the predictions of the theory [see Fig. 6.1(a', b')], which are calculated from the full expressions in Eqs. 6.12 and 6.13 with no free parameters, where Ω , γ_0 , d , and γ were computed as we describe in Ch. 3.

Spectra taken at higher optical depth reveal more clear evidence of the constructive and destructive interference between EIT and FWM. Fig. 6.2(a,b) presents

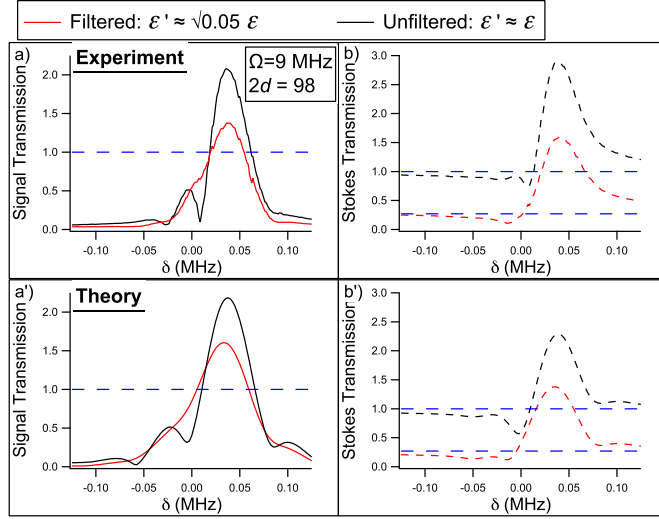


FIG. 6.2: Same as Fig. 6.1, but at with an optical depth of $2d = 98$.

similar spectra recorded for the same signal and Stokes fields, but at an optical depth of $2d = 98$. In the case of no Stokes attenuation (black curves), the theoretical curve in Fig. 6.2(b') exhibits, as expected, destructive interference at $\tilde{\delta} = \delta - \delta_s = n\pi v_g/L$ for $n = -3, -1$, and 2 [here $\pi v_g/L = (2\pi)31$ kHz and $\delta_s = (2\pi)36$ kHz]. While slightly shifted, these three points of destructive interference are also clearly visible in the experimental measurement of Fig. 6.2(a). Even when the Stokes seed field is suppressed, its presence leads to significant distortions in the signal transmission resonance.

We repeated similar spectral measurements after reducing the diameter of the beam by a factor of 1.5, which increased the control field Rabi frequency to $\Omega/2\pi = 14$ MHz, and corresponded to a larger light shift of $\delta_s/2\pi \approx 85$ kHz. Larger control intensity and smaller beam size allowed us to reduce the control field absorption at high optical depths and stay within the theoretical model's approximations, but the smaller interaction volume likely exacerbated the detrimental effects of atomic diffusion. Figs. 6.3 and 6.4 show the experimental and corresponding theoretical

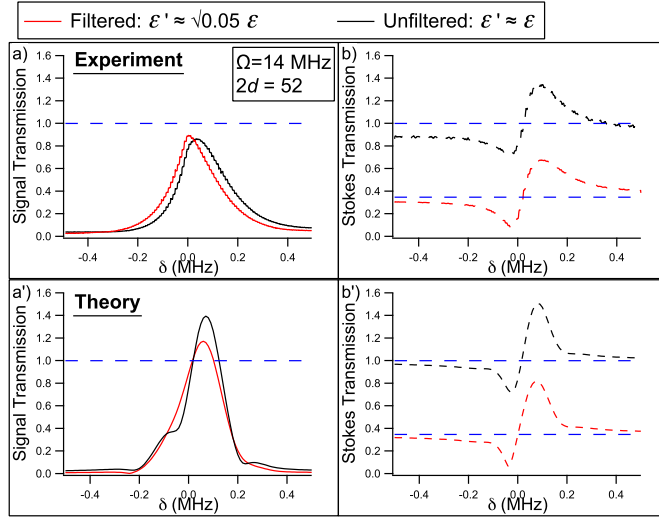


FIG. 6.3: (a, b) Signal and Stokes amplitude spectra at an optical depth of $2d = 52$ with a beam diameter of 2.6 mm and $\Omega/2\pi = 14$ MHz. Black traces are with a full Stokes seed present. Red traces are with the Stokes seed amplitude attenuated to $\approx \sqrt{0.05}$ of the signal field's amplitude. (a', b') Corresponding theoretical predictions.

spectra for optical depths of 52 and 110. The larger Rabi frequency results in a larger v_g than above, and thus more closely spaced spectral dips and peaks. There is an excellent agreement between the experiment and the theory for the Stokes spectra, and for the signal spectra at negative detuning. However, the theoretical model for signal transmission diverges from experimental observations at positive detuning, indicating the presence of some unaccounted mechanisms such as nonunity control field refractive index, atomic diffusion [162], or the effects of the multi-level structure of the atoms.

6.3 Slow Light Measurements

In this section we discuss the slow light regime for the signal field pulses in the presence of the co-propagating seeded Stokes field. In particular, we are interested in the prospect of manipulating the signal pulse group delay and amplitude via the

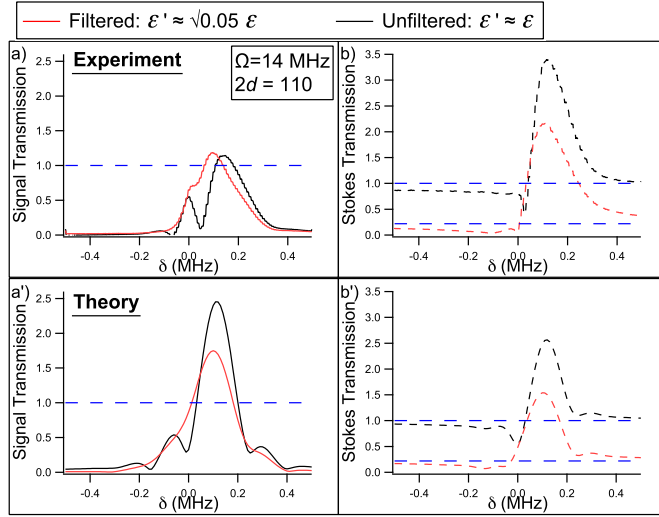


FIG. 6.4: Same as Fig. 6.3, but at with an optical depth of $2d = 98$.

controllable amplitude of the input Stokes field. It is convenient to use Eqs. 6.12, 6.13 to analyze the dynamics of each pulse propagation through the medium by calculating the variation in the complex amplitudes of both fields for each spectral component of the input pulse and then by Fourier transforming the resulting expressions back into the temporal domain. The group delay of the signal field is determined from the acquired phase, which consists of two contributions. The first from the first exponential in Eq. 6.12, and it is the same for all spectral components of the pulse: $\tau_0 = \frac{d}{d\omega} \text{Re}[\sigma(\omega)z] \approx \frac{d\gamma z}{2L\Omega^2}$. Notably, this value is exactly half of the pulse delay expected from the pure EIT system. The second contribution is from the expression in brackets in Eq. 6.12. The value of this additional delay depends explicitly on the detuning of the signal pulse from resonance and may vary significantly for different spectral components of the pulse. Below we discussed three distinct scenarios for the pulse two-photon detuning: $\delta = 2|\Delta_R|$, $\delta = 2\delta_s$, and $\delta = 0$.

Figures 6.5(a,b) and 6.6(a,b) correspondingly present the experimental data for 6 μs -long (FWHM) signal and Stokes pulses (which corresponds to a bandwidth of

$\pm(2\pi)31$ kHz around the carrier frequency) when the full Stokes field is present, and when the Stokes field is suppressed. Respective graphs (a') and (b') give the prediction of the calculations based on the complete solutions of Eqs. 6.12,6.13. In these calculations, we use a control field with Rabi frequency $\Omega/2\pi = 14$ MHz, corresponding to $\delta_s/2\pi = 84$ kHz and $\Delta_R/2\pi = -28$ kHz.

For more insight into the spectral dynamics of the pulse, we also plot the calculated time delay experienced by the signal field spectral components ω [Figs. 6.5(c) and 6.6(c)], and the spectral gain $|\mathcal{E}(\omega, L)|/|\mathcal{E}(\omega, 0)|$ [Figs. 6.5(d) and 6.6(d)]. These last graphs also show the spectral bandwidth of the input pulse (the blue, dashed curve) for reference.

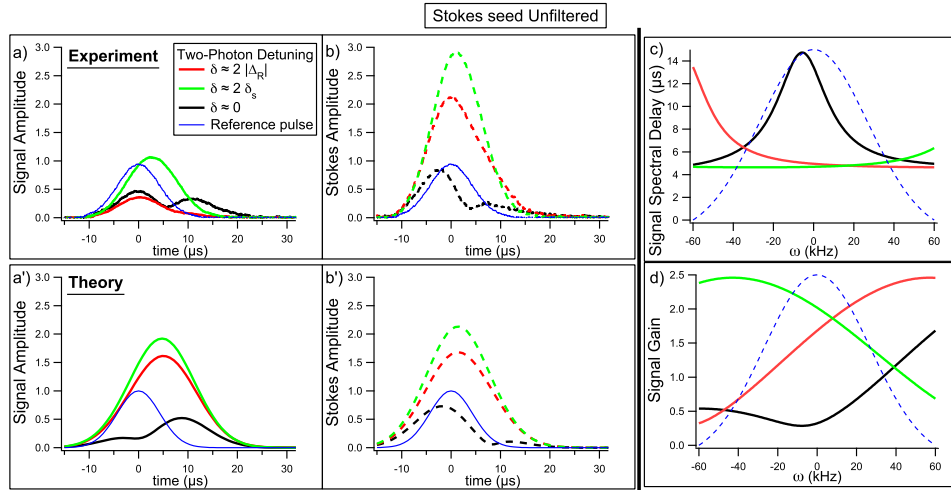


FIG. 6.5: (a) Slow light on the signal channel at an optical depth of $2d = 110$ with no Stokes seed attenuation (*i.e.*, $f = 1$) for signal detunings $\delta = 2|\Delta_R|$ (red curves), $\delta = 2\delta_s$ (green curves), and $\delta = 0$ (black curves). The thin blue curve is the initial reference pulse. (b) Corresponding Stokes channel. (a', b') Corresponding theoretical predictions from Eqs 6.12,6.13. (c) Theoretical total delay dispersion experienced by the signal pulse frequency components after traversing length L . The blue dashed curve depicts the frequency spread of the input signal pulse. (d) Predicted signal gain dispersion.

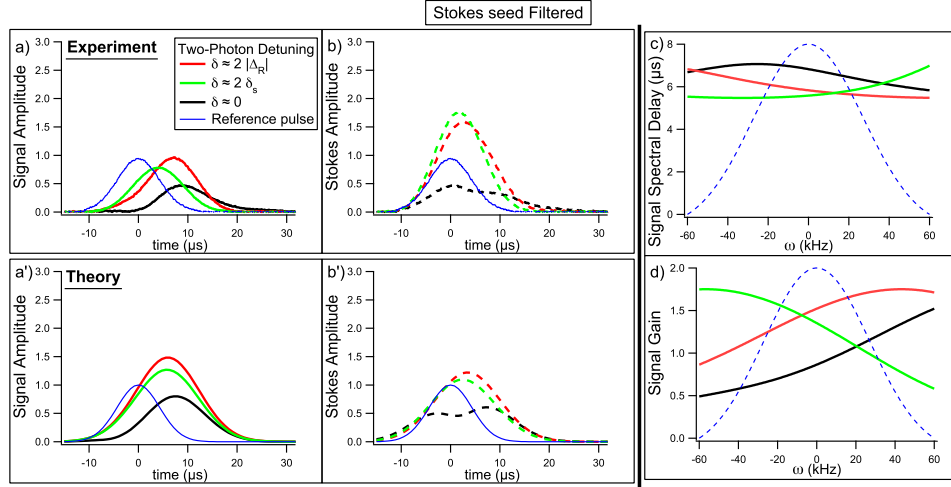


FIG. 6.6: Same as Fig. 6.5, but with Stokes seed attenuation ($f = \sqrt{0.05}$).

6.3.1 Case I: $\delta = 2|\Delta_R|$.

The data corresponding to the case $\delta = 2|\Delta_R| = (2\pi)56$ kHz are shown in Figs. 6.5 and 6.6 in red. Although the theoretical calculations predict only a weak dependence of the signal pulse on the amplitude of the Stokes seed, the experimental data show much stronger dependence: for the full seeded Stokes field the experimental pulse shows small delay and noticeable attenuation, while when the Stokes field is small, the signal pulse experiences some small gain and much larger delay. The latter is much closer to the theoretical expectations of gain of ≈ 1.5 and the delay of $\approx 6\mu\text{s}$. The experimental results for the Stokes field, however, match the theory much more accurately, which may indicate that the absorption of the signal field is underrepresented by the model.

The analysis of the spectral gain and delay for both cases ($f = 1$ and $f = \sqrt{0.05}$) provides some qualitative understanding of the observed pulse behavior. For the case of the full Stokes field, Fig. 6.5(c) shows that all the signal spectral components with $\omega > 0$ experience a roughly uniform delay of $\approx 5\mu\text{s}$, whereas the components

$\omega < 0$ experience a longer delay, resulting in the pulse spreading as it traverses the cell. However, this effect is somewhat suppressed by lower spectral gain for $\omega < 0$ (Fig. 6.5d). With the Stokes field attenuated [Fig. 6.6(c,d)], we expect that all signal spectral components ω experience a uniform delay of $\approx 6\mu\text{s}$, and a slight gain, resulting in delayed propagation with little pulseshape distortion, as corroborated well in Fig. 6.6(a).

6.3.2 Case II: $\delta = 2\delta_s$.

The green curves in Figs. 6.5 and 6.6 depict the results of slow light experiments with a two-photon detuning of $\delta = 2\delta_s = (2\pi)168$ kHz. Figs. 6.5(c,d) illustrate that for the unfiltered Stokes field ($f = 1$), all frequency components of the initial signal pulse experience a nearly identical delay of $\approx 5\mu\text{s}$ —indicating very little pulse spread. Simultaneously, the central component should be amplified by a factor of ≈ 1.8 . This prediction matches well with both the experimental [Figs. 6.5(a,b)] and theoretical [Figs. 6.5(a',b')] pulses. When the Stokes seed is attenuated ($f = \sqrt{0.05}$), the signal pulse experiences a slightly longer delay of approximately $5.8\mu\text{s}$, but will also be less amplified, according to Fig. 6.6(d). The experimental result [green curve in Fig. 6.6(a)] reproduces this predicted delay, but shows a small attenuation rather than gain, possibly indicating the presence of an additional decay mechanism.

6.3.3 Case III: $\delta = 0$.

The black curves in Figs. 6.5 and 6.6 depict the results of slow light experiments with a two-photon detuning of $\delta = 0$. This case most clearly demonstrates the merits of Stokes seed attenuation. For the unfiltered Stokes seed $f = 1$, different spectral components will acquire very different phase and gain while propagating through the interaction region. In particular, Fig 6.5(c) shows large variation in the

spectral delay — from $14 \mu\text{s}$ for central frequencies to $5\mu\text{s}$ for the farther detuned components. When combined with the gain curve, shown in Fig. 6.5(d), such variations should greatly distort the shape of the output pulses. In fact, the expected output closely resembles a double-peaked pulse, and is quite similar to that observed in the experiment. When the Stokes seed is filtered ($f = \sqrt{0.05}$), as in Fig. 6.6, the differential delay is suppressed, and all spectral components experience a common delay of nearly $7 \mu\text{s}$, but at the sacrifice of gain, which is < 1 . Figs. 6.6(a,b) show excellent agreement with the corresponding theoretical curves.

6.4 FWM under Stored Light conditions

As we have seen in Sec. 6.3, under certain experimental conditions, both the signal and Stokes pulses appear to be delayed during propagation in the slow light regime. Thus, it is reasonable to expect that the control field could be turned off while portions of both pulses are within the medium, thus mapping the pulses to a single memory. In this section, we investigate the prospect of the light storage of both fields; that is, a process in which both signal and Stokes pulses are reversibly mapped onto a long-lived spin coherence and thus can be faithfully recreated after some storage period. Recent experiments [124] have shown that a spontaneously generated Stokes field can be detected upon retrieval of a signal field from a spin coherence. Based on these results, one might anticipate that the spin wave might function, at least to some extent, as a memory for both pulses.

6.4.1 Coupled propagation of signal and Stokes fields in a double- Λ system

In order to match the equations of motion for quantum fields (*c.f.*, Eqs. 2.41–2.43), we define $g\sqrt{N} = \sqrt{\gamma\alpha_0 c/2}$ as the coupling constant between the signal field and the atomic ensemble. We rescale the light field envelopes by defining dimensionless light field envelopes $\frac{\mu}{\hbar g}\mathcal{E} \rightarrow \mathcal{E}$ and $\frac{\mu}{\hbar g}\mathcal{E}' \rightarrow \mathcal{E}'$. We define the optical polarization $P(z, t) = \rho_{eg}(z, t)\sqrt{N}$ and the spin coherence $S(z, t) = \rho_{sg}(z, t)\sqrt{N}$, where $\rho_{ij}(z, t)$ is the appropriate slowly-varying position-dependent collective density matrix element and N is the number of atoms in the interaction volume.

In the dipole approximation, assuming that at all times most of the atoms are in $|g\rangle$, and to linear order in the weak light fields \mathcal{E} and \mathcal{E}' , the atomic evolution and light propagation equations read [109, 110, 124, 161, 163]:

$$(\partial_t + c\partial_z)\mathcal{E} = ig\sqrt{N}P, \quad (6.16)$$

$$(\partial_t + c\partial_z)\mathcal{E}'^* = -ig\sqrt{N}\frac{\Omega}{\Delta_{\text{hf}}}S, \quad (6.17)$$

$$\partial_t S = -\Gamma_0 S + i\Omega P + i\frac{\Omega}{\Delta_{\text{hf}}}g\sqrt{N}\mathcal{E}'^*, \quad (6.18)$$

$$\partial_t P = -\Gamma P + i\Omega S + ig\sqrt{N}\mathcal{E}, \quad (6.19)$$

where we have defined $\Gamma_0 = \gamma_0 - i(\delta - \delta_s)$ and $\Gamma = \gamma - i(\delta - 2\delta_s)$. The polarization decay rate γ and the spin decay rate γ_0 have been introduced.

Equations 6.16–6.19 fully describe the propagation of the light fields and the dynamics of the spin wave and of the optical polarization during all stages of light storage. As we have demonstrated, in the slow light regime, when the control field is constant in time [$\Omega(t) = \Omega$], Eqs. 6.16–6.19 can be solved analytically using Fourier transformation in time [109, 110, 124, 161, 163]. In the stored light regime, when the control field intensity is time-dependent, these equations can be solved numerically.

6.4.2 Correspondence between experiment and theory

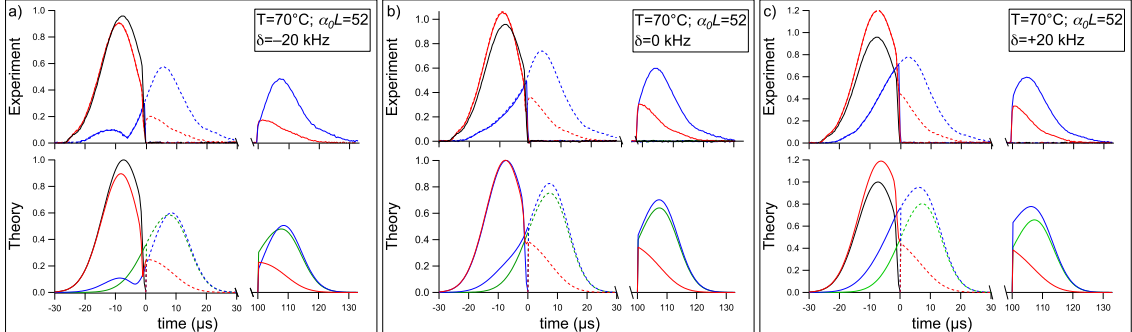


FIG. 6.7: Storage and retrieval of 16 μs -long (FWHM) truncated Gaussian pulses at $T = 70^\circ\text{C}$ ($\alpha_0 L = 52$), for a two-photon detuning of (a) $\delta = -20$ kHz, (b) $\delta = 0$ kHz, and (c) $\delta = +20$ kHz. In all plots, the top graphs are experimental data and the bottom graphs are the theoretical predictions from Eqs. 6.16–6.19. The black curve is a far-detuned reference pulse; the blue (red) traces are the signal (Stokes) pulses. Dashed (solid) lines correspond to slow (stored) light experiments. In the theory plots, the green curve corresponds to a model consisting only of EIT, to provide contrast with the EIT-FWM model.

Figure 6.7 displays the results of storage experiments with 16 μs -long truncated Gaussian pulses at $T = 70^\circ\text{C}$ (optical depth $\alpha_0 L = 52$) along with the corresponding theoretical predictions, which are obtained by numerically solving Eqs. 6.16–6.19 with the appropriate parameters. We measured the control field power to be 4.7 mW, and the beam diameter was 2.67 mm, which corresponded to $\Omega/(2\pi) = 9.6$ MHz, and induced a light shift of $\delta_s = 17$ kHz. The spin-wave decay rate was measured to be approximately 300 μs , thus $\gamma_0/(2\pi) \approx 270$ Hz. The results from the slow light experiment (dashed lines) and the stored light experiment (solid lines) are overlaid to facilitate shape comparison.

For a small negative two-photon detuning $\delta = -20$ kHz [Fig. 6.7(a)], the signal field (in blue) experiences some distortion during propagation [as evidenced by the bumps in the leakage portion of the pulse (when $t < 0$), which exits the cell before the control field is extinguished], but the shape of the slow pulse is preserved during the storage process. Likewise, the fraction of the Stokes field that exits the medium

at $t > 0$ in the slow light experiment (dashed red) matches the retrieved Stokes field in the stored light experiment (solid red). There is an excellent agreement between the experimental observations and the numerical model predictions. The green trace in the theory plot corresponds to standard EIT-based light storage of the signal field, where the FWM process has been artificially turned off. To compute this trace, the Stokes contribution in Eq. 6.18 is set to zero, and Eqs. 6.16, 6.18, and 6.19 are solved numerically. We include this trace in order to showcase the effects of four-wave mixing on signal pulse shape and delay.

Figure 6.7(b) demonstrates the excellent correspondence between experiment and theory for a two-photon detuning of $\delta = 0$ kHz. For this value of δ , the signal pulse is less distorted during propagation, but the pulse shape is still distinct from the bare-EIT model. Likewise, Fig. 6.7(c) depicts the results for $\delta = +20$ kHz $\approx \delta_s$, where the two-photon detuning effectively cancels the light shift during the writing and retrieval stages. Under this condition, the signal pulse will experience the least amount of distortion due to FWM, since the EIT transmission peak is, at least for a sufficiently narrow pulse bandwidth, symmetric about $\delta = \delta_s$. As a result, the dispersion experienced by the pulse is mostly linear. In all cases, the theoretical model matches the experimental data very well.

The correspondence between slow light pulseshapes (dashed lines) and the shapes of the retrieved pulses (solid lines) illustrates an important result—when the writing and retrieval control field amplitudes are constant in time, the process of switching the control field off and on has little effect on the signal and Stokes fields, apart from a delay and the spin-wave decay during storage time. In this case, we can further understand the effects of FWM by using the closed form solutions to the Fourier transformed versions of Eqs. 6.16–6.19 [109, 124, 161, 163]. In Appendix B, we detail the derivation of the following two approximate equations, which intuitively describe the effects of FWM and EIT on pulse propagation for the

case $\delta = \delta_s$. Although these equations make a set of strong assumptions, including the assumption of an infinitely wide EIT transmission window $\Gamma_E \rightarrow \infty$, they preserve the essential physics in the limit of weak FWM. Defining $\Delta_R = -\Omega^2/\Delta_{\text{hf}}$, the equations are

$$\begin{aligned} \mathcal{E}(L, t) \approx & \mathcal{E}(0, t - L/v_g) + \Delta_R^2 \int_0^{L/v_g} dt' \mathcal{E}(0, t - t')t' \\ & + i\Delta_R \int_0^{L/v_g} dt' \mathcal{E}'^*(0, t - t'), \end{aligned} \quad (6.20)$$

$$\begin{aligned} \mathcal{E}'^*(L, t) \approx & \mathcal{E}'^*(0, t) + \Delta_R^2 \int_0^{L/v_g} dt' \mathcal{E}'^*(0, t - t')(L/v_g - t') \\ & - i\Delta_R \int_0^{L/v_g} dt' \mathcal{E}(0, t - t'). \end{aligned} \quad (6.21)$$

These equations clearly show how the effects of FWM grow with optical depth $\alpha_0 L$. The first term on the RHS of Eq. 6.20 describes the delay that the signal field experiences during propagation in an EIT medium, where $v_g = 2\Omega^2/(\alpha_0\gamma)$ is the EIT group velocity [90]. Due to the effects of FWM, the signal field acquires a small in-phase gain of order $\Delta_R^2(L/v_g)^2 \sim (\alpha_0 L)^2 \gamma^2 / \Delta_{\text{hf}}^2$ from times up to L/v_g earlier. The times farthest away are weighted more heavily. Additionally, the signal field acquires an *i*-out-of-phase contribution of order $|\Delta_R|L/v_g \sim \alpha_0 L\gamma/\Delta_{\text{hf}}$ from the Stokes field up to L/v_g earlier with all times contributing equally. The Stokes field propagates undistorted and largely undelayed, but gets a small [order $(\alpha_0 L)^2 \gamma^2 / \Delta_{\text{hf}}^2$] in-phase gain from times up to L/v_g earlier, with closest times weighted more heavily, and also an *i*-out-of-phase contribution of order $\alpha_0 L\gamma/\Delta_{\text{hf}}$ from the signal field, with all times weighted equally. Notice that in both equations, in the regime where the first term on the RHS is large, small in-phase $(\alpha_0 L)^2 \gamma^2 / \Delta_{\text{hf}}^2$ terms and small *i*-out-of-phase $\alpha_0 L\gamma/\Delta_{\text{hf}}$ terms contribute at the same $(\alpha_0 L)^2 \gamma^2 / \Delta_{\text{hf}}^2$ order to the absolute value of the field (which is what our experiment measures).

However, the first terms on the RHS are not always dominant. In particular,

for $t > 0$, the first term on the RHS of Eq. 6.21 vanishes, in which case $|\mathcal{E}'^*(L, t)|$ is dominated by the third term with a small correction from the second term. This means, as we will confirm experimentally, that the retrieved Stokes field is largely determined by the input signal, and not by the input Stokes field. Similarly, if EIT group delay is comparable to the signal pulse duration, then, for $t < 0$, the RHS of Eq. 6.20 is small and $|\mathcal{E}(L, t)|$ is significantly affected by the third term. This means, as we will confirm experimentally, that the signal pulse leakage can be strongly affected by the Stokes input, in contrast to the retrieved signal pulse, which is only weakly affected by the Stokes input. Equations 6.20 and 6.21 also show that the perturbative treatment of the effects of FWM, employed to derive them, breaks down when $|\Delta_{\text{R}}L/v_g| \gtrsim 1$, *i.e.*, when the optical depth is $\alpha_0L \gtrsim 2\Delta_{\text{hf}}/\gamma \approx 100$.

To test the validity of Eqs. 6.20 and 6.21, in Fig. 6.8(a), we compare the solutions obtained by numerically solving Eqs. 6.16–6.19 (solid lines) to the predictions of Eqs. 6.20 and 6.21 (dotted lines). In the dashed traces, we include the results of a useful intermediate approximation, which does not assume infinite Γ_{E} and is described by Eqs. B.4–B.5 and B.11–B.15 in Appendix B. For these plots, $\Omega/(2\pi) = 10$ MHz and $\alpha_0L = 80$; the pulse bandwidth was $\Delta\omega = 0.1\Gamma_{\text{E}}$. From the excellent correspondence between theoretical models, it is evident that the approximations made in deriving Eqs. 6.20 and 6.21 are valid.

6.4.3 The effect of four-wave mixing on the spin wave

While the solutions of Eqs. 6.16–6.19 accurately describe the evolution of light pulses and atomic variables under slow light and storage conditions, we have not yet used them to elucidate the role that the Stokes field plays in the creation of the spin coherence. Specifically, it is not yet clear whether the quantum memory description based on the dark state polariton principle [22, 42] is valid under EIT-

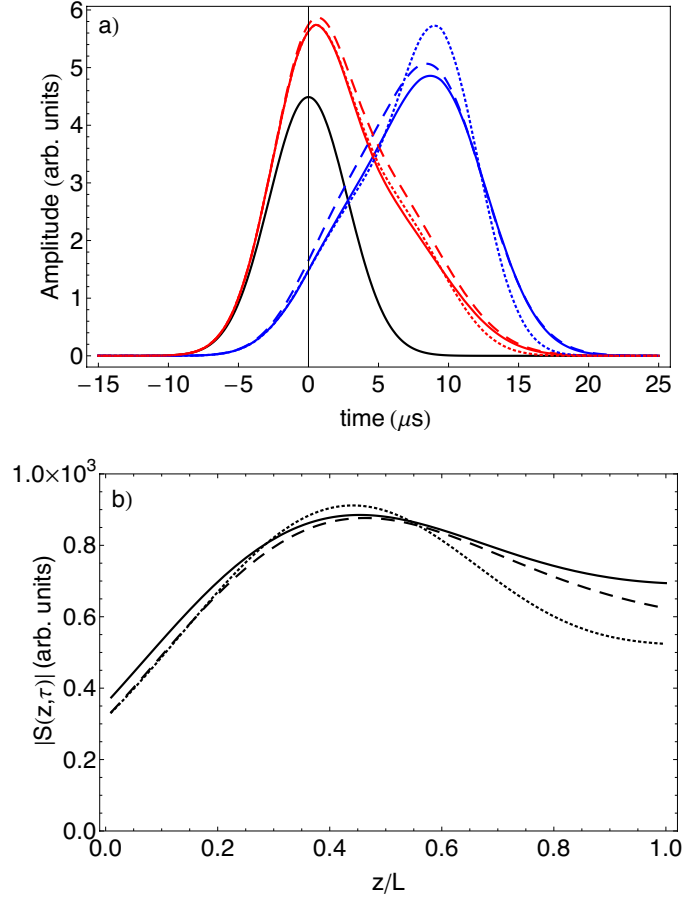


FIG. 6.8: (a) Results of a numerical investigation of slow light with a $6.6 \mu\text{s}$ -long pulse (reference in black), with $\Omega/(2\pi) = 10 \text{ MHz}$ and $\alpha_0 L = 80$, so that the bandwidth of the pulse $\Delta\omega = 0.1\Gamma_E$. Blue traces are the signal field; red traces are the Stokes field. Solid lines are the result of numerically solving Eqs. 6.16–6.19. Dotted lines are the result of the infinite- Γ_E approximation in Eqs. 6.20–6.21. Dashed lines correspond to results obtained using numerical integration of expressions in Eqs. B.4–B.5, and B.11–B.15 in Appendix B. (b) The spin waves created at time $T = 5 \mu\text{s}$ in Fig. 6.8(a). The solid black line is the result of numerically solving Eqs. 6.16–6.19. Dotted lines are the results from Eq. 6.29. Dashed lines are the results from Eqs. B.17 and B.23.

FWM conditions. In what follows, we develop a more transparent description of light storage in a double- Λ system and show that in this case, the spin wave is determined by a particular combination of signal and Stokes fields.

We obtain this result by adiabatically eliminating the optical polarization $P(z, t)$. We set the time derivative to zero in Eq. 6.19 and find

$$P(z, t) \approx i\frac{\Omega}{\Gamma}S(z, t) + i\frac{g\sqrt{N}}{\Gamma}\mathcal{E}(z, t). \quad (6.22)$$

Inserting Eq. 6.22 into Eq. 6.18, we obtain the following equation for time evolution of the spin wave $S(z, t)$:

$$\partial_t S(z, t) = -\left(\Gamma_0 + \frac{\Omega^2}{\Gamma}\right)S(z, t) - g\sqrt{N}\frac{\Omega}{\Gamma}\mathcal{F}(z, t). \quad (6.23)$$

It is easy to see that the spin wave depends only on a combination $\mathcal{F}(z, t)$ of signal and Stokes optical fields, defined as

$$\mathcal{F}(z, t) = \mathcal{E}(z, t) - i\frac{\Gamma}{\Delta_{\text{hf}}}\mathcal{E}'^*(z, t). \quad (6.24)$$

Eq. 6.23 is analogous to the spin-wave expression obtained through a similar treatment of a standard three-level light storage model [22, 42],

$$\partial_t S(z, t) = -\left(\Gamma_0 + \frac{\Omega^2}{\Gamma}\right)S(z, t) - g\sqrt{N}\frac{\Omega}{\Gamma}\mathcal{E}(z, t), \quad (6.25)$$

but with one modification—the single light field (signal) is now replaced by a combined signal-Stokes field \mathcal{F} . Thus, one might expect that it should be possible to store information about this joint mode in the spin coherence. However, only a small $(\alpha_0 L)^2 \gamma^2 / \Delta_{\text{hf}}^2$ fraction of the Stokes field [the second term on the RHS of Eq. 6.21] exits the medium at $t > 0$ after the input Stokes has been turned off, while

the signal pulse is delayed in its entirety (the first term on the RHS of Eq. 6.20). As a result, in contrast to the information encoded in the signal field, most of the information encoded in the Stokes field is lost to leakage, which leaves the interaction region before the control field is shut off.

The similarity between Eq. 6.23 and Eq. 6.25 motivates a more detailed comparison of our EIT-FWM system with the traditional EIT configuration. The propagation equation for \mathcal{F} is easily obtained from the appropriate combination of Eqs. 6.16 and 6.17:

$$(\partial_t + c\partial_z)\mathcal{F} = -\frac{g^2N}{\Gamma}\mathcal{F} - \Omega\frac{g\sqrt{N}}{\Gamma}S - i\frac{g^2N}{\Delta_{\text{hf}}}\mathcal{E}'^*. \quad (6.26)$$

This equation is also similar to the signal propagation expression in the classic stored light model [22, 42],

$$(\partial_t + c\partial_z)\mathcal{E} = -\frac{g^2N}{\Gamma}\mathcal{E} - \Omega\frac{g\sqrt{N}}{\Gamma}S, \quad (6.27)$$

except for the optical-depth-dependent Stokes term, which describes the generation of signal from Stokes during propagation through a sufficiently optically-thick medium.

When the two-photon detuning is chosen such that the light shift is canceled (*i.e.*, $\delta = \delta_s$), the propagation equation becomes, to $\mathcal{O}(1/\Delta_{\text{hf}})$,

$$[\partial_t + c\cos^2\theta(t)\partial_z]\mathcal{F}(z, t) \approx i\Delta_{\text{R}}\mathcal{E}'^*(z, t) \quad (6.28)$$

with the angle $\theta(t)$ given by $\tan^2\theta(t) = \frac{g^2N}{\Omega^2(t)}$.

Analysis of above equations demonstrates two regimes for light storage under EIT-FWM conditions. At low optical depths, the contribution of the Stokes field on the RHS of Eqs. 6.26 and 6.28 is negligible. In this case, the equations for the

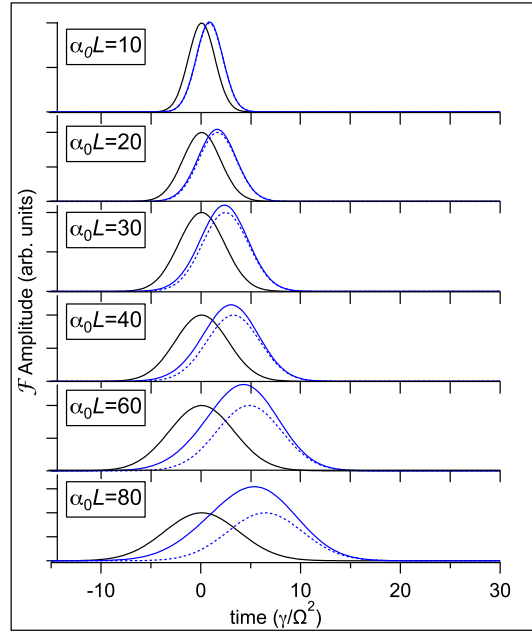


FIG. 6.9: Results from numerical evaluation of Eqs. 6.17, 6.23 and 6.28 (solid blue lines) and of the homogeneous version of Eq. 6.28 (dashed blue lines) for a range of optical depths $\alpha_0 L$, as indicated in the legends. The bandwidth of each input pulse was $\Delta\omega = 0.05\Gamma_E = \Omega^2/(20\sqrt{\alpha_0 L/2\gamma})$.

joint field \mathcal{F} and spin wave S become identical to those for \mathcal{E} and S in the regular EIT configuration. For example, if we replace the RHS of Eq. 6.28 with zero, it would describe the propagation of \mathcal{F} without distortion at a reduced group velocity $v_g = c \cos^2 \theta \approx \frac{2\Omega^2}{\alpha_0 \gamma}$. However, at low optical depths and $t > 0$ (after the input Stokes pulse has been turned off), the contribution of the Stokes field into \mathcal{F} is also negligible: it is small not only because of the small factor $\Gamma/\Delta_{\text{hf}}$ in Eq. (6.24) but also because $\mathcal{E}'(z, t)$ itself is small [since the first term on the RHS of Eq. 6.21, generalized to arbitrary z , vanishes for $t > 0$]. Thus, signal field propagation can be analyzed using a three-level single Λ , even though the Stokes field can be significantly affected by control and signal fields, as is evident from the dominance of the last term on the RHS of Eq. 6.21 for $t > 0$.

However, at higher optical depths, the term on the RHS of Eq. 6.28 becomes significant. Specifically, this term results in gain or loss of the signal field due to

the Stokes field. The dashed blue lines in Fig. 6.9 depict the results of numerical calculations of the homogeneous form of Eq. 6.28. Solid blue lines show the results of the numerical evaluation of the full form of Eq. 6.28 with Eqs. 6.17 and 6.23. For these calculations, $\Omega/(2\pi) = 8$ MHz, $\gamma/(2\pi) = 150$ MHz, and the signal pulse was chosen so that its bandwidth, $\Delta\omega = 0.05\Gamma_E$. It is evident from this graph that the Stokes contribution is not negligible for optical depths $\alpha_0 L \gtrsim 25$, when the simple slow propagation of \mathcal{F} breaks down due to the Stokes term on the RHS of Eq. 6.28.

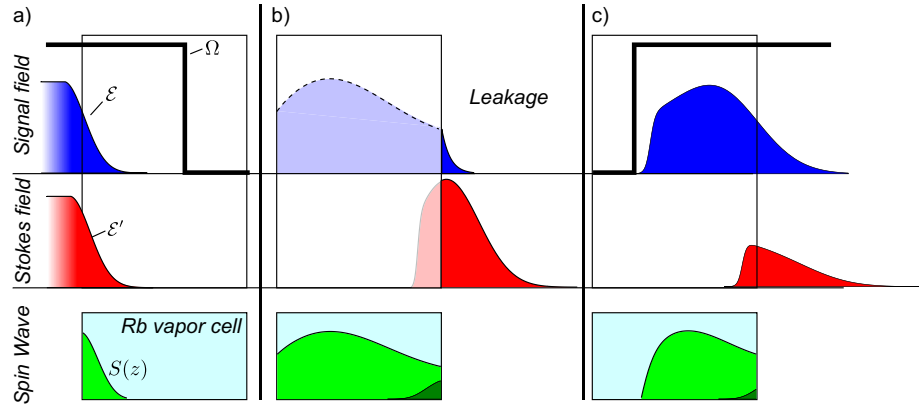


FIG. 6.10: An illustration of the modified storage description. (a) During the writing stage, the input signal field \mathcal{E} (*top*) and Stokes field \mathcal{E}' (*middle*) propagate at different group velocities through the atomic medium, creating a spin wave (*bottom*). (b) During the storage stage, the control field is turned off and no light fields are present. Some portion of the signal field has propagated through the cell and leaks out before the control field is extinguished. At the same time, most of the information in the Stokes field is lost in the leakage, since, in the regime $(\alpha_0 L)\gamma/\Delta \ll 1$, the propagation of the Stokes field is affected by the atoms only weakly (see Eq. 6.21). The spin wave is preserved during storage. (c) During retrieval, the control field is turned on, releasing the spin wave into both the signal and Stokes fields, which exit the vapor cell.

As shown in Appendix B, the same approximations that lead to Eqs. 6.20 and 6.21 give the following expression for the spin wave $S(z, t)$ in the limit when $\Gamma_E \rightarrow \infty$:

$$S(z, t) \approx -\frac{g\sqrt{N}}{\Omega} \left[\mathcal{E}(0, t - \frac{z}{v_g}) + \Delta_R^2 \int_0^{\frac{z}{v_g}} dt' \mathcal{E}(0, t - t')t' + i\Delta_R \int_0^{\frac{z}{v_g}} dt' \mathcal{E}'^*(0, t - t') \right]. \quad (6.29)$$

In Fig. 6.8(b), we compare the shape of the spin wave that is obtained by numerically solving Eqs. 6.16–6.19 (solid lines) to the predictions of Eq. 6.29 (dotted lines). As in Fig. 6.8(a), we also include the predictions of an intermediate approximation, which does not assume an infinite Γ_E and is described in Eqs. B.17 and B.23 in Appendix B. The reasonable agreement between the three curves in Fig. 6.8(b) implies that Eq. 6.29 does indeed contain the essential physics. In particular, under this approximation, the spin wave is proportional to the signal field only, as in a traditional three-level single- Λ EIT system (see Eq. B.23 in Appendix B),

$$S(z, t) \approx -\frac{g\sqrt{N}}{\Omega}\mathcal{E}(z, t). \quad (6.30)$$

Moreover, under this approximation, $\mathcal{E}(z, t)$ [and hence $S(z, t)$] is mostly determined by the usual slowed-down version of the input signal (first term in square brackets in Eq. 6.29) with small corrections of order $|\Delta_R|L/v_g \sim \alpha_0 L\gamma/\Delta_{\text{hf}}$ (third term in square brackets in Eq. 6.29) and $(\alpha_0 L)^2\gamma^2/\Delta_{\text{hf}}^2$ (second term in the square brackets in Eq. 6.29).

Fig. 6.10 illustrates an intuitive way to understand storage under EIT-FWM conditions. At the beginning of the writing stage, shown in Fig. 6.10(a), the control field (in black) prepares the atoms and causes the input signal field \mathcal{E} (in blue, *top*) to propagate at a reduced group velocity. The Stokes pulse (in red, *middle*) enters the cell and is not completely extinguished inside the medium even after the reference pulse would have left the medium. A collective spin coherence is created in the atomic vapor cell (in green, *bottom*). As the pulses propagate through the atomic medium, as shown in column (b), they experience mutual interference effects and may become distorted. The spin wave propagates along with the signal field. The contributions to the spin wave are determined by the joint mode \mathcal{F} , and we can distinguish between the contributions to the spin wave from the signal field (shown

in light green) and those of the Stokes field (shown in dark green) (see Eq. 6.29). In the regime of weak FWM, the propagation of the Stokes field is only weakly affected by the atoms (see Eq. 6.21), so that much of the Stokes field leaves the end of the vapor cell as leakage. Any information contained in this leaked field is lost for the storage process, which commences when the control field is shut down. After some time [column (c)], the control field is turned on, and the spin wave is released into both the signal and Stokes fields. It is important to note that, since the joint mode \mathcal{F} is not a normal mode, the proportion of Stokes to signal is not fixed.

In the regime of weak FWM ($\alpha_0 L \leq 25$), the joint mode $\mathcal{F}(z, t)$ is determined mostly by the input signal field \mathcal{E} . Thus, the propagation dynamics experienced by the signal pulse will be only slightly sensitive to the amplitude of the seeded Stokes pulse (of order $\alpha_0 L \gamma / \Delta_{\text{hf}}$, see the last term in Eq. 6.20), and consequently the spin wave created will have the same weak dependence on the seeded Stokes field (see the last term in Eq. 6.29). Since the spin wave is only weakly dependent on the input Stokes field, it is possible to create approximately the same spin wave for different input combinations of signal and Stokes fields. The retrieval from the spin wave into the light fields will consequently have this same weak dependence on the input Stokes field.

Equations 6.20 and 6.21 support this conclusion. Specifically, the amplitude of the retrieved signal field (Eq. 6.20) is determined primarily by the input signal field (the first term on the RHS) with a small $(\alpha_0 L \gamma / \Delta_{\text{hf}})^2$ correction from the input Stokes field (the third term on the RHS). Similarly, since the first term on the RHS of Eq. 6.21 vanishes for $t > 0$, the retrieved Stokes field is also determined primarily by the input signal (the third term on the RHS) with a small $(\alpha_0 L \gamma / \Delta_{\text{hf}})^2$ correction from the input Stokes (the second term on the RHS). At the same time, signal and Stokes outputs are more strongly affected by the Stokes input for $t < 0$ (leaked pulses) than for $t > 0$ (retrieved pulses). This statement is obvious for the Stokes

field, since the first term on the RHS of Eq. 6.21 does not vanish for $t < 0$. The reason this statement holds for the output signal is that the first term on the RHS of Eq. 6.20 is smaller for $t < 0$ than for $t > 0$ for a sufficiently large group delay, while the third term on the RHS of Eq. 6.20 is larger for $t < 0$ than for $t > 0$ since $\mathcal{E}'(0, t - t')$ vanishes for $t - t' > 0$.

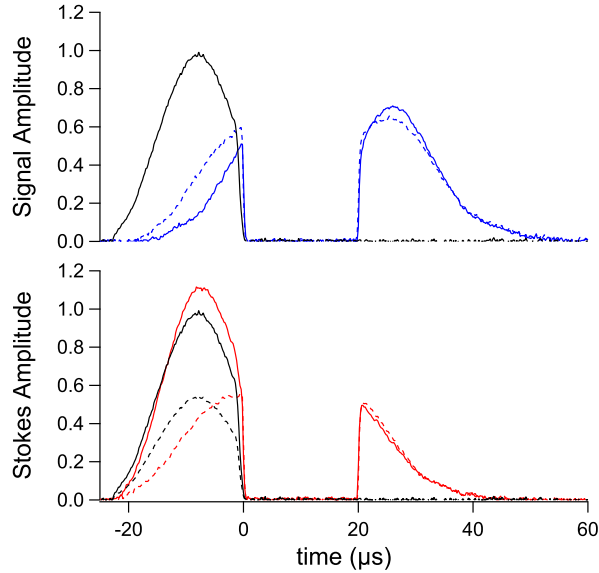


FIG. 6.11: Storage of a $15 \mu\text{s}$ (FWHM) truncated Gaussian pulse at $T = 70^\circ\text{C}$ ($\alpha_0 L = 52$) under different Stokes seeding conditions. Solid lines depict storage when the Stokes seed amplitude is the same as the signal amplitude. The dashed lines correspond to the case of a reduced input Stokes field. The black traces show reference (input) pulses, and the dashed black trace in the bottom plot illustrates the reduced Stokes seed amplitude.

In Fig. 6.11, we display the results of an experiment designed to test these conclusions. The top graph [Fig. 6.11(a)] depicts the storage of a $15 \mu\text{s}$ -long (FWHM) truncated Gaussian signal field at $T = 70^\circ\text{C}$ ($\alpha_0 L = 52$). The solid trace corresponds to approximately equal amplitudes of input signal and Stokes optical pulses, while the dashed traces correspond to a reduced initial Stokes amplitude $\mathcal{E}'^*(0, t) = -0.55\mathcal{E}(0, t)$.

Notice the difference in the leakage portion ($t < 0$) of both the signal pulse and the Stokes pulse as we go from solid curves to dashed curves, which exemplifies that

both signal and Stokes outputs for $t < 0$ do depend strongly on the amplitude of the seeded Stokes pulse, as we have explained theoretically above and as we have reported previously [163]. At the same time, the retrieved ($t > 0$) Stokes and signal pulses are both almost independent of the amplitude of the seeded Stokes field, which is consistent with the theoretical explanation above. We repeated similar measurements many times under a wide range of experimental conditions and found the retrieved pulses to be weakly affected by the seeded Stokes amplitude as long as the input signal field is comparable to or stronger than the input Stokes field.

6.5 Optical depth dependence of the Stokes field

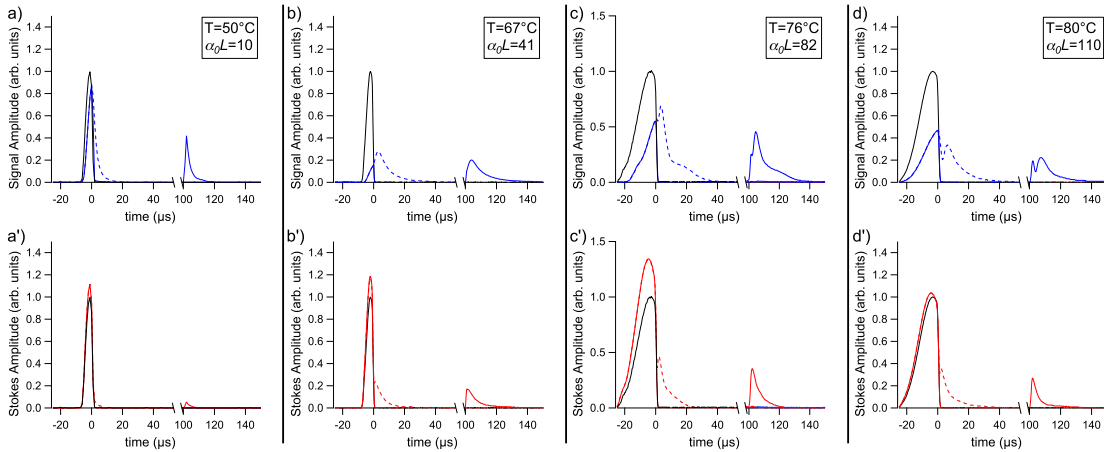


FIG. 6.12: Stokes behavior for increasing optical depths. For all cases, the two-photon detuning $\delta = 0$. The black trace is a reference pulse; the blue (red) trace is the signal (Stokes) pulse. (a, a') Storage and retrieval of a $6 \mu\text{s}$ -long (FWHM) truncated Gaussian pulse at $T = 50^\circ$, which corresponds to an optical depth of $\alpha_0 L = 10$. Here, $\Omega/(2\pi) = 8.3$ MHz. (b, b') $T = 67^\circ$ ($\alpha_0 L = 41$), pulse duration is $6 \mu\text{s}$, $\Omega/(2\pi) = 7.1$ MHz. (c, c') $T = 76^\circ$ ($\alpha_0 L = 82$), pulse duration is $20 \mu\text{s}$, $\Omega/(2\pi) = 12.7$ MHz. (d, d') $T = 80^\circ$ ($\alpha_0 L = 110$), pulse duration is $20 \mu\text{s}$, $\Omega/(2\pi) = 7.8$ MHz.

In this section, we present the results of storage experiments at increasing optical depths.

Figure 6.12 depicts the evolution of the Stokes and signal fields under storage conditions as optical depth increases. The general features of these results are

well-explained by the simple signal and Stokes expressions in Eqs. 6.20–6.21, as described below. In Figs. 6.12(a, a'), we show the results of slow light and stored light experiments using a 6 μs -long (FWHM) truncated Gaussian pulse at a temperature of $T = 50^\circ\text{C}$, which corresponds to an optical depth of $\alpha_0 L = 10$. The signal pulse [blue trace in Fig. 6.12(a)] experiences a reduction in group velocity during propagation, as seen by comparing the dashed trace (slow light) to the black trace, which is a far-detuned reference pulse. The Stokes pulse [red trace in Fig. 6.12(a')] closely mimics the far-detuned reference pulse, indicating that four-wave mixing is not a dominant process at this optical depth. In a separate run, we investigate storage of these pulses by turning off the control field for 100 μs . Upon retrieval, the signal field [solid blue trace in Fig. 6.12(a)] is recovered with a modest reduction in amplitude due to spin-wave decay during the storage time, but its shape is preserved. Additionally, we retrieve a small pulse on the Stokes channel [solid red trace in Fig. 6.12(a')]. Equation 6.20 predicts that at low optical depths [$(\alpha_0 L \gamma / \Delta_{\text{hf}}) \ll 1$] the retrieved signal pulse will be a delayed version of the input pulse (if one accounts for the storage time), but with a slight modification due to the Stokes field (the last term in Eq. 6.20). Likewise, the Stokes field will be mostly unaffected by the atoms (the first term on the RHS of Eq. 6.21), so most of it will leak out (see $t < 0$). However, a small Stokes pulse $\propto (\alpha_0 L / \Delta_{\text{hf}})$ generated from the input signal (the last term in Eq. 6.21) will be retrieved.

Figures 6.12(b, b') show the results of similar experiments at $T = 67^\circ\text{C}$, corresponding to an optical depth of $\alpha_0 L = 41$. Here, the signal shape is again preserved by the storage process. The four-wave mixing effects are exhibited by the Stokes gain in the leakage portion of the pulse [see Fig. 6.12(b')], which leaves the interaction region before the storage stage occurs. This gain is described by the last two terms in Eq. 6.21. At this increased optical depth, the last term in Eq. 6.21 also predicts an increased Stokes output for $t > 0$. The effects of FWM are also apparent

in the distortion that the signal field experiences during propagation.

Figures 6.12(c, c') depict the storage experiments at $T = 76$ ($\alpha_0 L = 82$). We used a longer pulse (FWHM of $20 \mu\text{s}$). At this optical depth, the Stokes pulse experiences more gain during propagation. Storage and retrieval, however, still preserve the shapes of both the signal and the Stokes pulse. Again, it is clear that the Stokes field gain predicted by Eq. 6.21 becomes more apparent at higher optical depths. We also see that, at $\alpha_0 L = 110$ [column (d)], the Stokes field amplitude is smaller than at $\alpha_0 L = 82$ [column (c)]. This effect is most likely due to the absorption of the control field by unprepared atoms that enter the interaction region during the waiting time. We also note that, at $\alpha_0 L \approx 100$, the perturbative expansion used to derive Eqs. 6.20 and 6.21 breaks down.

CHAPTER 7

Experimental investigations of spin decay mechanisms

In this chapter, we present the details of several experiments that were designed to investigate causes for spin decay. As described in Sec. 3.3.9, we extracted the decay rate of the spin wave by performing consecutive storage experiments with the same signal pulse and control field, but varying the storage time. We fit the retrieved pulse energy as a function of storage time to an exponential decay e^{-t/τ_s} . The spin decay rate is $\gamma_s = 1/(2\tau_s)$.

This chapter is organized as follows. We first review mechanisms that are known to affect the rate of ground-state decoherence and discuss relevant experimental observations. We have observed that the memory decay rate is dependent on many experimental parameters that are not considered in the literature. We present data from spin decay experiments conducted with different control field Rabi frequencies, Ω ; input signal pulses, $\mathcal{E}_{\text{in}}(t)$; two-photon detunings, δ ; optical depths, $2d$; and Stokes relative input amplitudes, f . While analysis of these experiments has not determined a single cause of memory decay, we discuss some physical mechanisms

that may contribute.

7.1 Mechanisms that affect the rate of spin decay

7.1.1 Diffusion and $2d$ -dependence

In theory, since the memory decay value that we measure characterizes spin decay that occurs in the dark—when all light fields are off, it should only depend on fundamental atomic decoherence rates. Ultimately, atomic diffusion puts an upper-bound on the $1/e$ decay time of several milliseconds (see Sec. 3.1.4). In most vapor cell experiments, an inert buffer gas is employed to mitigate diffusivity of Rb atoms through the laser beam. Nevertheless, the ground-state decoherence rate due to diffusion is [134, 164]

$$\gamma_0^{\text{diff.}} = 2.405^2 \frac{D}{a^2} \frac{1}{1 + 6.8l_{mf}/a}, \quad (7.1)$$

where, as in Sec. 3.1.4, $D = D_0 p_0 / p$ is the diffusion constant for the motion of the atom through the buffer gas, $l_{mf} = 1/(n_{\text{Ne}} \sigma_{\text{RbNe}})$ is the mean free path, p is the buffer gas pressure, a is the laser beam radius, and p_0 and D_0 are the corresponding values at one atmosphere. The prefactor, 2.405 is the lowest zero of the zeroth-order Bessel function [164], and the factor of 6.8 is employed for a hard-sphere collisions model [134]. Thus, for the experiments described in this dissertation, with $a \approx 2.5$ mm, and using the appropriate values from Sec. 3.1.4, we find that $\gamma_0^{\text{diff.}} \approx 500$ Hz, which corresponds to a diffusion time of approximately 2 ms, as we saw in Sec. 3.1.4. Our observed value of τ_s was on the order of 500 μs , so diffusion is not the main culprit of spin decay.

7.1.2 Collisions

The buffer gas that was used to limit the diffusion time out of the laser beam also introduces additional collisions. Since the inert buffer atoms do not possess an unbound electron, Rb-Ne collisions generally preserve coherence at low buffer gas pressures of 30 Torr, although at higher pressures, more frequently-occurring ballistic collisions can thermalize the hyperfine level populations of the Rb atoms. However, spin-exchange collisions between Rb atoms can destroy the fragile coherence [134, 152, 165–167]. The rate of spin-exchange collisions (and also the efficiency at which the exchange of spin states occurs) is not a well-characterized phenomenon. One might suspect that this rate depends on the concentration of Rb, which is temperature dependent (see Sec. 3.15), but that also the Rb-Rb collisional-cross section might have temperature dependence [134].

Shuker, *et al.* [166] investigated this phenomenon by measuring the decay rates between the hyperfine and Zeeman sublevels in the ground state of ^{87}Rb in vapor cells similar to the ones employed presently. They prepared a spin coherence and measured its relaxation in the dark with a series of weak, short laser probe pulses, and then extracted the relevant decay rates. They found that the hyperfine decoherence rate scales inversely with optical depth, as $\tau_s \sim 80 \text{ ms}/(2d)$.

Motivated by these findings, we conducted experiments to investigate the dependence of the measured spin decay rate on optical depth. Figure 7.1 shows the results of these experiments. At each temperature, we measured the memory decay after storage of several different signal pulses. We present data from experiments with two different control fields, $\Omega = 7 \text{ MHz}$ (red) and $\Omega = 10 \text{ MHz}$ (black). The graph represents the average spin decay time at each optical depth. It is clear that an increased optical depth has a detrimental effect on the decay time.

We fit our data to an inverse function, and we find that if we ignore the two

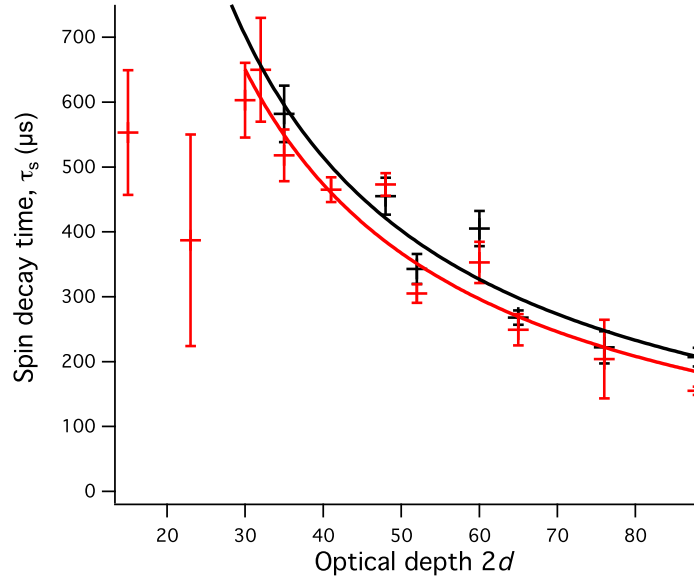


FIG. 7.1: The dependence of spin decay time, τ_s . Black points correspond to a control field Rabi frequency of $\Omega = 10$ MHz. Red points correspond to $\Omega = 7$ MHz. We fit the data to an inverse function with respect to $2d$.

seemingly anomalous points for $\Omega = 7$ MHz, then

$$\tau_s \sim \frac{20 \text{ ms}}{2d}, \quad (7.2)$$

with a slight power dependence [$21.23 \pm 0.22 \text{ ms}/(2d)$ for $\Omega = 7$ MHz, $22.58 \pm 0.33 \text{ ms}/(2d)$ for $\Omega = 10$ MHz]. This is a factor of 4 faster than Shuker, *et al.* measured. Thus, we conclude that the spin decay rate that we measure is not the decoherence rate between ground-state levels, which is dominated by spin-exchange collisions between Rb atoms. We investigate the control field power dependence in more detail Sec. 7.2.1.

7.1.3 Magnetic fields

Stray magnetic fields are commonly cited as culprits for spin decay. Uniform magnetic fields will induce Zeeman shifts of the m -sublevels of the hyperfine manifold, causing coherences to precess at different Larmor frequencies. The result is that the dependence of the retrieved pulse energy on the storage time will have a beat-note structure, as these different coherences interfere constructively and destructively [168, 169]. This non-exponential decay has been observed experimentally [170]. Magnetic shielding mitigated this effect in our experiment, and we do not observe the beating phenomenon in our spin decay graphs. Thus, we rule out this mechanism of decay.

Nevertheless, magnetic field gradients can cause a similar phenomenon, which can result in a dephasing of the spin coherence. This can cause a population shuffling amongst Zeeman levels in the same hyperfine state, but not between the $F = 1$ and $F = 2$ states. In order to avoid these effects in the experiment, care was taken to degauss the magnetic shielding regularly. Thus, while this is a known mechanism, we do not expect that stray magnetic fields are the main cause of the spin decay that we observe.

7.2 Experimental evidence for spin decay mechanisms

7.2.1 Ω and \mathcal{E}_{in} dependences

In Sec. 7.1.1 we discussed the dependence of spin decay rate on the optical depth (and hence Rb concentration). The data were collected with a variety of input signal pulses, and the measured decay rates at each optical depth were averaged together

to create Fig. 7.1. In the next two sections, we discuss results from experiments in which different input signal pulses and different control field powers yield dissimilar memory decay times.

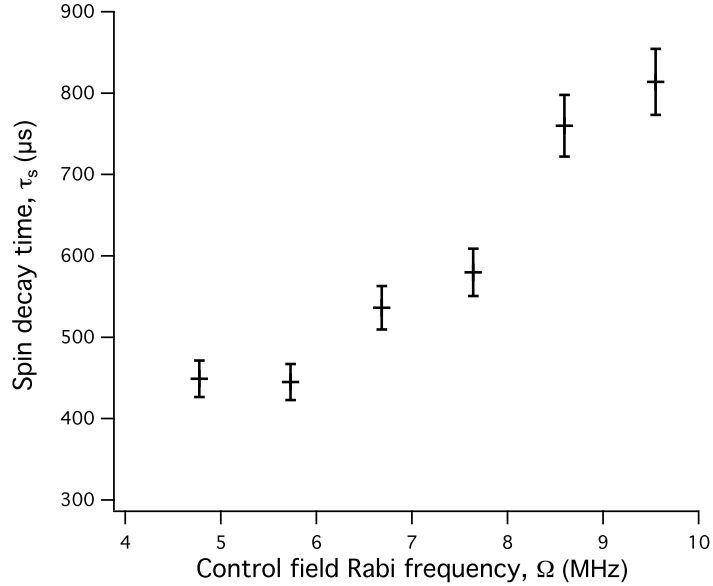


FIG. 7.2: The dependence of spin decay during storage time as a function of the Rabi frequency of the writing control field, Ω . These experiments were performed with $T = 65^\circ\text{C}$ ($2d = 34$) and with an input signal pulse of approximately $20 \mu\text{s}$ duration.

Figure 7.2 depicts the dependence of the spin decay time extracted using $20 \mu\text{s}$ -long signal pulses with various control field powers at $T = 65^\circ\text{C}$ ($2d = 34$). It is evident that a longer decay time is obtained by using stronger writing and retrieval control fields. This result is surprising. Certainly, as we discussed in Ch. 4, careful matching of the control power and the input signal pulseshape is necessary to achieve maximum storage efficiency. Failure to match $\Omega(t)$ and $\mathcal{E}_{\text{in}}(t)$ will still create a spin coherence, but the memory efficiency will be low (see, for instance, the first iteration step in Sec. 4.1). Regardless of the memory efficiency, we are interested in the memory decay time—and the dominant decay process occurs when all light fields are off. Theoretically, the decay rate should be independent of one’s ability to achieve optimal efficiency. However, it appears from Fig. 7.2 that different spin

waves decay at different rates.

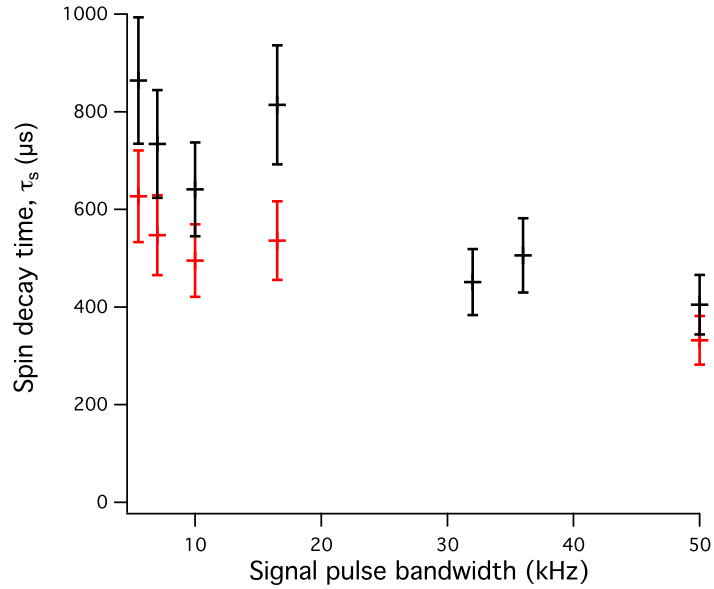


FIG. 7.3: The dependence of spin decay on the bandwidth of the input signal pulse. Stored pulses were typically truncated Gaussians, and we computed the bandwidth as the FWHM of the Fourier transform of the pulse in time. Here, $T = 65^\circ\text{C}$ ($2d = 34$).

Figure 7.3 provides further data that support the hypothesis that different spin waves decay at different rates. Here, we are operating at $T = 65^\circ\text{C}$ ($2d = 34$) and with a control field $\Omega = 10$ MHz. We measure the spin decay rate after storage of several different pulses. Input signal pulses were truncated Gaussians, and we computed the bandwidth by determining the FWHM of the pulse Fourier transform. At this optical depth, the measured FWHM of the EIT spectrum was approximately 300 kHz, so all pulses fit inside the window of transparency. However, even if this were not the case—and a temporally narrow signal pulse (broad bandwidth) was used, any portion of the pulse’s bandwidth that was outside of the EIT window would be absorbed by the atoms, and not stored. The resultant spin wave would simply decay during the storage waiting time. It is suggestive from this graph that a pulse with a narrower bandwidth (longer temporally) will produce a spin wave that decays slowly.

7.3 Possible physical mechanisms

These results are quite curious. The input signal pulses were typically short enough so that any spin decay during the writing and retrieval stages was negligible. *i.e.*, the dominant decoherence mechanism occurs in the dark, when all lights are off. Thus, it is surprising that the spin decay rate depends on parameters of the pulses. We now investigate several possible explanations for these observations.

7.3.1 Power broadening

The off-resonant interaction of the control field on the $|e\rangle \rightarrow |g\rangle$ transition acts as a background AC electric field, and induces AC Stark shifts of the $|e\rangle$ and $|g\rangle$ levels, as we have discussed in Sec. 2.9. Additionally, the strong control field will broaden the EIT linewidth [171] and resultantly increase the spin decay rate [96],

$$\gamma_s = \gamma_0 + \gamma \frac{|\Omega'|^2}{\Delta_{\text{hf}}^2} \quad (7.3)$$

However, this additional broadening only occurs during the writing and retrieval stages. We have checked numerically that the inclusion of this additional decay correction¹ is insufficient to explain the observations.

7.3.2 Radiation trapping and diffusion effects

In Sec. 7.1.1, we computed the time for an atom to leave the interaction region to be 2 ms, which is approximately 20 times longer than the storage time. Thus, we suspect that loss of coherence out of the beam is not the largest contributing factor to spin-wave decay [131]. However, during the storage time, unprepared atoms can enter the interaction region and affect the storage process.

¹We note that the correction to γ_s is $\mathcal{O}(1/\Delta_{\text{hf}}^2)$, whereas our theoretical model is accurate to $\mathcal{O}(1/\Delta_{\text{hf}})$, so more careful analysis could be justified.

In optically thick atomic vapor, the reabsorption of spontaneously emitted photons (*i.e.*, radiation trapping) [150, 151] can destroy an atomic coherence by incoherently pumping the atoms out of the dark state. Although this effect is absent during the storage time, it might lead to a breakdown of an important approximation. We assume that the control field only varies temporally, and is spatially uniform. However, the control field used to retrieve the spin wave can be absorbed by unprepared atoms that enter the interaction region during the waiting time. These atoms then re-emit incoherent light, which can detrimentally effect the retrieval of the atomic coherence.

For example, as the retrieval process begins, the optical pumping of fresh atoms results in an attenuation of the retrieval control field intensity, which develops an exponentially-decaying spacial profile from $z = 0$ to $z = L$. Since the control field's intensity is lower, then v_g is also lower upon retrieval than during writing, and it takes longer to complete the retrieval stage, which in turn, can lead to an apparent reduction of spin-wave coherence time. Further, since the control field is spatially-varying longitudinally, the atomic coherence can experience spatially-dependent AC Stark shifts. Thus, the retrieved signal pulse can have a spatially and temporally-varying phase, leading to an apparent reduction in spin decay time.

We can test these hypotheses by numerically reconstructing the shape and phase of the spin wave. Specifically, we use Eqs. 2.41-2.43 to compute $S(z)$ after the writing stage. A spin wave with a larger amplitude near $z = 0$ will be affected more than a spin wave with a smaller amplitude near $z = 0$, since the control field spatial gradient is sharpest near $z = 0$. Thus, a larger spatial gradient is accumulated due to the larger Stark shift gradient.

In Fig. 7.4(a), we plot the numerical solutions to Eqs. 2.41-2.43 for experimental parameters relevant to Fig. 7.2 {in particular, $T = 65^\circ\text{C}$ ($2d = 34$), and $\mathcal{E}_{\text{in}}(t) \propto e^{-4 \ln 2(t-0.9)^2/0.2^2}$, $t \in [0, 1]$ }. We see that the spin wave created with the weaker

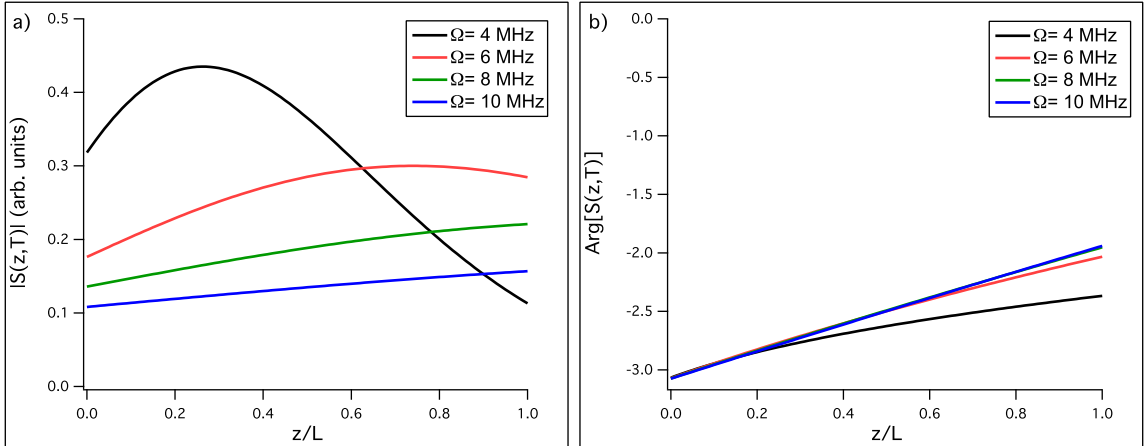


FIG. 7.4: The spin-wave (a) shape and (b) phase computed by solving Eqs. 2.41-2.43 for a $20 \mu\text{s}$ -long input signal pulse and a control field Rabi frequency of $\Omega = 4$ MHz (black), $\Omega = 6$ MHz (red), $\Omega = 8$ MHz (green), $\Omega = 10$ MHz (blue). Here, $T = 65^\circ\text{C}$ ($2d = 35$). These control fields were selected to correspond with Fig. 7.2.

control field has a greater amplitude near $z = 0$ than the spin waves created with more powerful control fields. Indeed, the “flattest” spin wave is created with $\Omega = 10$ MHz, which we observe from Fig. 7.2 has the longest decay time. Figure 7.4(b) depicts the phase of the computed spin wave. We see that the phases of each spin wave do not depict disparate behavior.

These results appear to support the theory that diffusion of fresh atoms into the interaction region during the storage time, which results in longitudinally-varying AC Stark shifts, can possibly explain the dependence of τ_s on Ω .

In Fig. 7.5, we use the same theoretical techniques to observe the spin-wave shape and phase for different input pulses, but using the same control field $\Omega = 10$ MHz, as in Fig. 7.3. The conclusion drawn from the Fig. 7.3 was that pulses with a narrower bandwidth produce a spin wave that has a longer decay time, however, these observations are tenuous, given the size of the error bars. Nevertheless, we observe in Fig. 7.5 that there is no clear trend in the spin-wave shape. The “flattest” spin wave is created by using the narrowest pulse (5 kHz, in black), which yielded a decay time of approximately $700 \mu\text{s}$. Likewise, the red lineshape (8 kHz) and

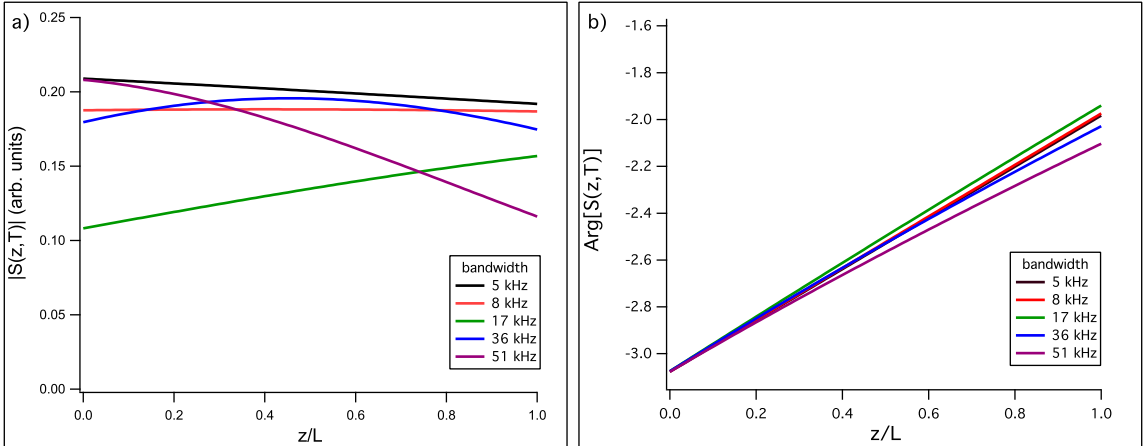


FIG. 7.5: The spin-wave (a) shape and (b) phase computed by solving Eqs. 2.41-2.43 for several signal pulses and a control field of $\Omega = 10$ MHz. The signal pulse bandwidths were 5 kHz (black), 8 kHz (red), 17 kHz (green), 36 kHz (blue), and 51 kHz (magenta). Here, $T = 65^\circ\text{C}$ ($2d = 35$). These experimental parameters were selected to correspond with Fig. 7.3.

blue lineshape (36 kHz) are also quite flat, and yielded respective decay times of approximately $650 \mu\text{s}$ and $550 \mu\text{s}$. The spin-shape with the largest amplitude near $z = 0$ and the most spatial variation was produced with an input pulse of 51 kHz (magenta), and resulted in the shortest decay time of approximately $400 \mu\text{s}$. We see in Fig. 7.5(b) that the phase of the spin waves are all approximately the same. These results provide support to the hypothesis that the spatially-varying AC Stark shift can result in shorter decay times. However, there is not a clear, direct correlation between pulse bandwidth and spin decay time.

7.3.3 Transverse AC Stark shifts

In order to simplify the theoretical model, we assumed that the light fields had a uniform and circular cross-sectional profile. However, light fields exiting from an optical fiber are typically Gaussian in profile. As a result, atoms at the same longitudinal position, z , but at different radial positions r in the interaction region will experience slightly different control field intensities (and hence Ω). Correspond-

ingly, there are transversely-varying AC Stark shifts associated with the transverse variation in the control field.

Simon *et al.* [154] has investigated this phenomenon. They consider atoms along the transverse profile of the signal field and compute the relative phase accumulated (during the retrieval) between the atoms, due to the transversely-varying Stark shifts,

$$\phi_r \sim T \frac{|\Omega'|^2}{\Delta_{\text{hf}}}, \quad (7.4)$$

where T is the time required to read out the spin wave. They then compute the fidelity between the initial spin wave and the final spin wave and determine that this can severely reduce the read-out efficiency at high optical depth. This mechanism could contribute to the optical depth-dependence of the spin decay rate, but likely does not explain the dependence on control power, since T is determined by $1/v_g \propto 1/|\Omega|^2 \propto 1/|\Omega'|^2$, so this relative phase should be independent of the maximum control power.

We attempted to mitigate this effect by using a pinhole aperture to detect the central-most portion of the light beams. One could verify this interpretation by using a control field with a larger diameter than the signal field, but this is not possible with the experimental setup described in this dissertation, since all light beams were derived from the same laser output and co-propagated at all times.

7.3.4 Two-photon detuning (δ) dependence

In this section, we discuss the results of experiments designed to determine if the two-photon detuning of the input pulse affected the rate of spin-wave decay. These experiments were motivated by the fact that during writing and retrieval, when the control field is on, the atoms experience an AC Stark shift, but when the control field is off, they relax to the natural energy splitting. We can select a

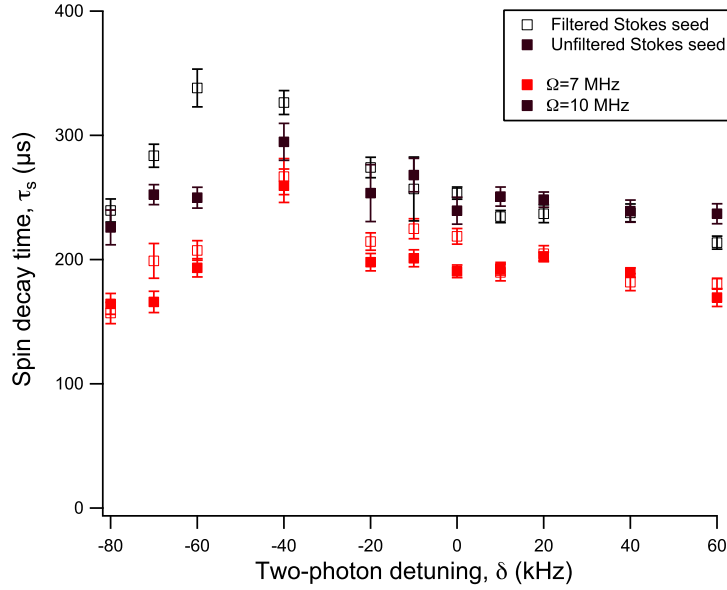


FIG. 7.6: Results from an investigation of the dependence of spin decay time on the amplitude of the seeded Stokes pulse and the dialed two-photon detuning, δ . Here, $T = 75^\circ\text{C}$ ($2d = 76$) and a $15 \mu\text{s}$ -long signal pulse was used. Red points correspond to a control field $\Omega = 7 \text{ MHz}$, while black points correspond to $\Omega = 10 \text{ MHz}$. Solid squares are data from experiments with the full Stokes seed ($f = 1$), while empty squares are data with $f = \sqrt{0.05}$.

two-photon detuning $\delta = \delta_s$ to account for this effect. As a result of the relaxation, the spin wave should have a spatially-dependent phase,

$$\phi = i \frac{(\delta - \delta_s)z}{v_g}. \quad (7.5)$$

The coherence can be carried longitudinally by atomic diffusion along z . In Sec. 7.1.1, we calculated that an atom would leave the interaction region in approximately 2 ms, which was much longer than the spin decay time that we measured. However, even moderate dephasing due to longitudinal diffusion can result in memory deficiency, since the relative phase and amplitude of the spin wave is essentially washed out. As a result, one might expect that spin waves with a spatially-uniform phase and amplitude [*e.g.*, $S(z) = 1$] will have a longer decay time than one with a rapidly-varying amplitude or phase. The spin wave with the most spatially-uniform

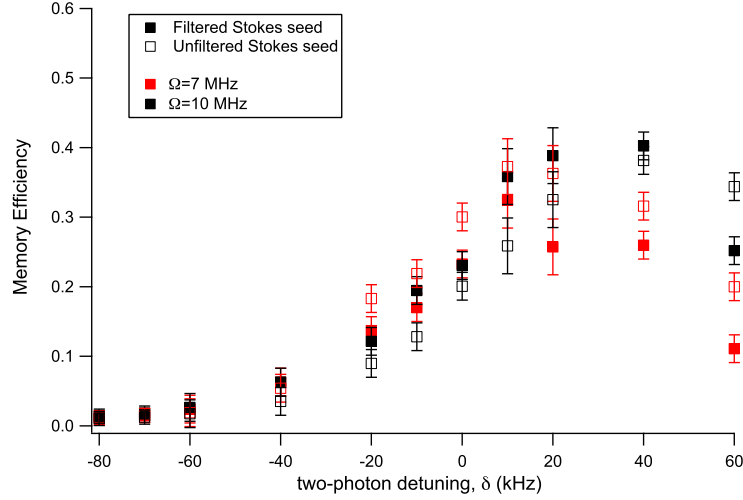


FIG. 7.7: The memory efficiency obtained by storing a $17 \mu\text{s}$ -long signal pulse with $\Omega = 7$ MHz (red) and $\Omega = 10$ MHz (black) as a function of two-photon detuning (δ) and the amplitude of the seeded Stokes field [(■) corresponds to $f = 1$, while (□) corresponds to $f = \sqrt{0.05}$]. The temperature was $T = 75$, ($2d = 76$).

phase would be created with a signal pulse at $\delta = \delta_s$.

We see from Fig. 7.6 that this interpretation is not supported by the data. The best spin decay time is achieved at negative two-photon detunings ($\delta \approx -40$ kHz). We note that $\delta_s = 21$ kHz for $\Omega = 7$ MHz (red points), and $\delta_s = 44$ kHz for $\Omega = 10$ MHz (black points). Clearly, the Stark shift is in the opposite δ -direction as the two-photon detuning that yields the longest memory decay rate. We conclude that longitudinal phase shuffling due to diffusion is not a main contributor to the spin decay that we measure.

We include a graph of the storage efficiency vs δ (see Fig. 7.7) to show that the best memory efficiency is obtained when $\delta = \delta_s$. *i.e.*, the two-photon detuning is chosen to match the location of the center of the shifted EIT peak. This agrees with intuition. Even though FWM effects distort the EIT transmission peak at high optical depths (and thus create a refractive index with non-linear δ dependence near $\delta = 0$, which in turn results in pulse distortion during propagation), we can account for this effect, to some degree, by choosing $\delta = \delta_s$, near which the EIT

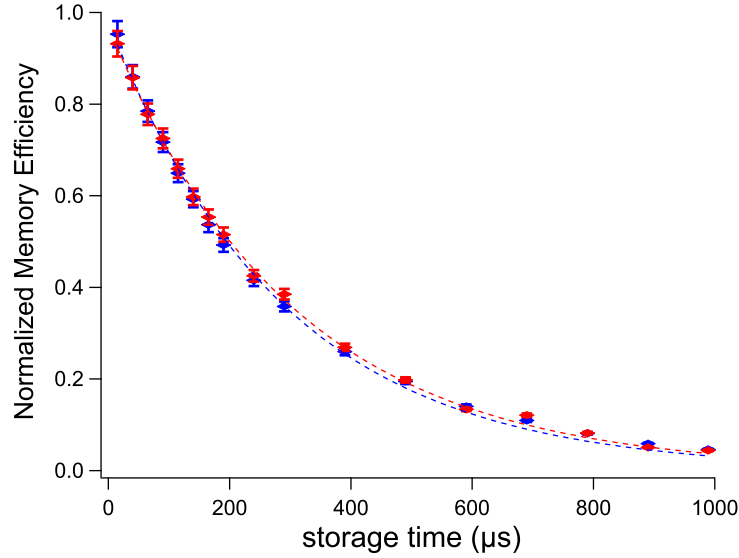


FIG. 7.8: Dependence of retrieved signal (blue) and Stokes (red) pulse energies as a function of storage time at $T = 70^\circ\text{C}$ ($\alpha_0 L = 52$). Here, $\tau_s = 300 \mu\text{s}$. We normalized the memory efficiencies so that the zero-storage-time memory efficiency is unity. Experimentally, we were not operating under optimal storage conditions, and the zero-storage-time memory efficiency was $\approx 40\%$ for the signal pulse and $\approx 5\%$ for the Stokes pulse.

peak is most symmetric. Nevertheless, while there is an intuitive understanding of the dependence of memory efficiency on two-photon detuning, an explanation of the spin-decay rate δ -dependence remains elusive.

7.3.5 FWM dependence

In this section, we discuss the possible dependence of the spin-wave decay rate on the FWM. Based on the findings presented in Sec. 6.4.3, where we discovered that the input Stokes field's contribution to the spin wave is $\mathcal{O}(\gamma/\Delta_{\text{hf}}) \ll 1$, one might conclude that there is little dependence. Because of this weak dependence, FWM could be used in a Ramsey-type experiment to probe the coherence [165].

We begin by presenting a measurement of the spin decay rate via the reduction of retrieved pulse energies of both the Stokes and the signal fields as a function of storage time. We show typical data in Fig. 7.8. Here, the cell temperature was

$T = 70^\circ\text{C}$ ($2d = 52$), and we measure $\tau_s \approx 300 \mu\text{s}$ with both fields. While the storage efficiency of the pulses is not commensurate (approximately 40% for the signal field and 5% for the Stokes field, in this case), the spin decay rate that we measure is the same, within experimental uncertainty. This observation that both the signal field and Stokes fields yield the same spin decay rate has been observed with a wide range of experimental parameters. This observation is supported by the interpretation from Sec. 6.4.3 that the retrieved Stokes pulse is seeded by the spin wave.

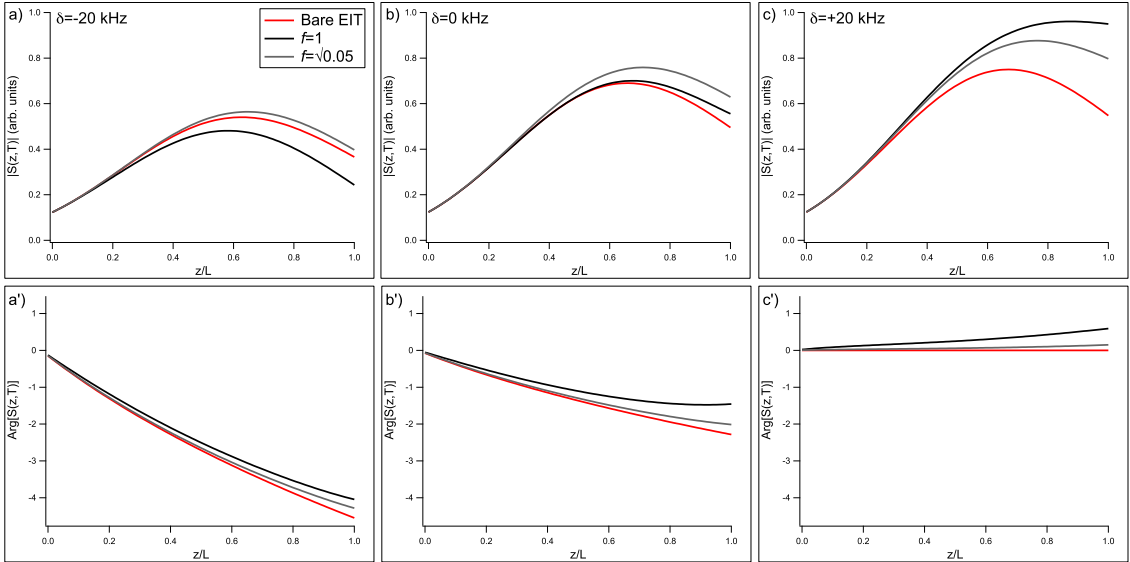


FIG. 7.9: Numerical solutions to Eqs. 6.16-6.19 provide the calculated spin-wave (*top*) shapes and (*bottom*) phases for two-photon detunings of (a, a') $\delta = -20$ kHz, (b, b') $\delta = 0$ kHz, (c, c') $\delta = +20$ kHz. Here, $\Omega = 7$ MHz, so that $\delta_s \approx 20$ kHz. $T = 75^\circ$ ($2d = 76$). Black curves are with the full Stokes seed, $f = 1$. Gray curves are for the filtered case $f = \sqrt{0.05}$, and the red curve corresponds to the bare EIT model (Eqs. 2.41-2.43).

We now present data from an experiment where we attenuated the input Stokes seed and measured the corresponding spin-wave decay time, as seen in Fig. 7.6. The red points correspond to $\Omega = 7$ MHz; the black points correspond to $\Omega = 10$ MHz. We observe the dependence of τ_s on Ω , as discussed in Sec. 7.2.1. We also note the dependence on δ as discussed in Sec. 7.3.4. Here, the full squares (■) correspond

to data taken with the full Stokes seed ($f = 1$), while empty squares (\square) were with $f = \sqrt{0.05}$. For the majority of data points, the decay times for the filtered ($f = \sqrt{0.05}$) and unfiltered ($f = 1$) cases agree to within the error bars. It is evident that the relative amplitude of the input Stokes pulse (with respect to the amplitude of the signal pulse) is not a large factor in determining the spin decay rate.

In Fig. 7.9, we show the results from numerically solving Eqs. 6.16-6.19 for the experimental conditions that were used to produce Fig. 7.6. Namely, $\Omega = 7$ MHz, and with $\delta = -20$ kHz [Fig. 7.9(a, a')], $\delta = 0$ kHz [Fig. 7.9(b, b')], and $\delta = +20$ kHz [Fig. 7.9(c c')]. The spin-wave amplitudes are shown in the top graphs; the phases are shown in the bottom graphs. We also investigate the effects of the input Stokes field amplitude on the spin wave. Black curves correspond to $f = 1$; gray curves correspond to $f = \sqrt{0.05}$, and the red curves correspond to the limit of pure EIT (*c.f.* Eqs. 2.41-2.43)]

Here, we clearly see from the bottom graphs that the phases of the spin wave with the longer decay time ($\delta = -20$ kHz) has the largest spatial-variation in phase. This result rules out longitudinal shuffling of phase via diffusion as a major contributor to spin decay. We clearly see that the phase of the spin wave varies according to Eq. 7.5. More precisely, $\delta = \delta_s$ produces a uniform phase variation, $\phi(z) \approx 0$ [see Fig. 7.9(c')]. For $\delta = 0$, we expect that the phase should vary by $-\delta_s L/v_g = -3d\gamma/\Delta_{\text{hf}} \approx 2.5$ rad, which agrees qualitatively with the graph. Likewise, for $\delta = -\delta_s$, we expect the phase to vary by twice this amount, $\Delta\phi \approx 5$ rad, as Fig. 7.9(a') confirms.

Additionally, at this optical depth when Stokes gain during propagation is still small, we see that the Stokes field contribution to the spin wave is minimal. There is very little qualitative difference in the three filtering cases in the top graphs. It is notable that on the light-shifted two-photon resonance $\delta = \delta_s \approx 20$ kHz, the spin-wave amplitude is largest, which results in a larger memory efficiency, as we

reported in Fig. 7.7. The data presented in this section seem to indicate that the effects of FWM are not a major contributor to spin decay.

7.4 Summary and conclusions

In this chapter, we have presented the results of experiments that investigated the memory decay rate in ^{87}Rb under EIT conditions. It is essential to understand the parameters that affect this rate, since it ultimately governs the storage time. We have observed that the memory decay time is typically shorter than predicted by collisional models; thus, we conclude that other effects are present. We have ruled out diffusion of the spin coherence as a major contributor. However, the most likely explanation of our observations involves diffusion of unprepared atoms into the interaction region. Fresh atoms into the interaction region absorb the retrieval control field and produce longitudinally-varying AC Stark shifts. Additionally, the Gaussian intensity distribution of the control field results in radially-dependent AC Stark shifts, which reduce the fidelity of the spin coherence. Although these hypotheses appear to resolve some discrepancies, they fail to explain the dependence on the input signal field, and the two-photon detuning. The mechanisms that are responsible for these observations remain elusive.

CHAPTER 8

Conclusion and Outlook

This dissertation has presented the results of studies pertaining to the optimization of quantum memory based on EIT in atomic vapors. We have studied in detail two quantum memory optimization protocols in warm Rb vapor and demonstrated their consistency for maximizing memory efficiency. We have also observed good agreement between our experimental data and theoretical predictions for relatively low optical depths (< 25), both in terms of the highest memory efficiency and in terms of the optimized pulse shapes. At higher optical depths, however, the experimental efficiency was lower than predicted. We observed that resonant four-wave mixing processes became important at these higher optical depths.

We have reported on the experimental demonstration of optimal storage and retrieval of arbitrarily shaped signal pulses in an atomic vapor at an optical depth $2d = 24$ by using customized writing control fields. Our measured memory efficiency is close to the highest efficiency possible at that optical depth. We also demonstrate full precision control over the retrieved signal pulse shapes, achieved by shaping the retrieval control field. A high degree of overlap between the retrieved and target pulse shapes was obtained (overlap integral $J^2 = 0.98 - 0.99$) for all input and

target pulse shapes tested in the experiments. We also demonstrated the potential application of the presented technique to the creation of optical time-bin qubits and to controlled partial retrieval. Finally, we observed excellent agreement between our experimental results and theoretical modeling.

The optimal storage and pulse-shape control presented here are applicable to a wide range of experiments, since the underlying theory applies to other experimentally relevant situations such as ensembles enclosed in a cavity [40, 154], the off-resonant regime [40, 43, 99], non-adiabatic storage (*i.e.*, storage of pulses of high bandwidth) [97], and ensembles with inhomogeneous broadening [98], including Doppler broadening [26] and line broadening in solids [33]. Thus, we expect this pulse-shape control to be indispensable for applications in both classical [160] and quantum optical information processing.

We also have presented the results of detailed experimental and theoretical investigations of the effects of resonant four-wave mixing (FWM) in an EIT medium. In particular, we have demonstrated that both steady-state and dynamic (slow light and stored light) properties of the signal field propagating under the EIT conditions are strongly effected by resonant four-wave mixing that arise under the conditions of EIT at high optical depth. This process is well-modeled by a simple double- Λ system, where the output signal and stokes field amplitudes are the results of interference of “traditional” EIT and FWM. We have shown that by attenuating the amplitude of the seeded Stokes field, we can partially control the optical properties of the medium for the signal field. Moreover, by adjusting the central frequency of the input signal field around two-photon resonance, in the presence of Stokes seed field we can achieve longer pulse delay and/or amplification of the signal pulse.

We have studied the phenomenon of stored light under conditions of electromagnetically induced transparency (EIT) and four-wave mixing (FWM) in an ensemble of hot Rb atoms. In particular, we have investigated the prospect of simultaneously

storing both a signal and a Stokes pulse in a single atomic coherence, and have shown that independent storage of two modes is not possible. The reason is that most of the Stokes pulse leaks out of the medium during the writing stage, so that during retrieval both output fields are determined primarily by the input signal field and depend on the input Stokes field only very weakly. We presented a theoretical model based on a simple double- Λ system, which agreed very well with experimental observations. This model allowed us to derive a simple relationship between input and output fields, which explained the above mentioned impossibility of two-mode storage. Furthermore, we showed that a particularly convenient description of storage in an EIT-FWM system involves a joint signal-Stokes mode, whose dynamics we also studied. Lastly, we have presented the results of experiments designed to further understand the mechanisms that govern the spin decay time. While these findings were not conclusive, we have identified several mechanisms that may contribute.

APPENDIX A

Details of control field shaping

In this appendix, we provide the details of the control field shaping computation employed for optimal storage in the experiments discussed in Sec. 4.2. The scope of the program is this: at a given optical depth, it is desired to optimally store an input signal field $\mathcal{E}_{\text{in}}(t)$, which is described by some reasonable function. For additional details, we direct the curious reader to Ref. [99], on which this appendix is based.

As a starting point, we choose the three equations of motion that describe the propagation of a signal pulse envelope through a Λ -type medium and the response of the atomic coherences, $P(z, t)$ and $S(z, t)$, as detailed in Eqs. (2.41–2.43). For simplicity, we employ dimensionless variables, in which time is in units of the excited state decay rate, γ , and position is in units of cell length, L . We employ a frame of reference that is co-moving at with the control field, and we assume two-photon resonance ($\delta = 0$), but allow the single-photon detuning, Δ to be non-zero:

$$\tilde{t} = \gamma \left(t - \frac{z}{c} \right) \quad (\text{A.1})$$

$$\tilde{z} = z/L \quad (\text{A.2})$$

$$\tilde{\Omega} = \Omega/\gamma \quad (\text{A.3})$$

$$\tilde{\Delta} = \Delta/\gamma \quad (\text{A.4})$$

$$\tilde{T} = T\gamma. \quad (\text{A.5})$$

We remind the reader that the optical depth is defined as $d = g^2 \frac{NL}{\gamma c}$, where $g^2 N$ is the collective-enhanced coupling constant of the signal field. Thus, the three equations of motion become,

$$\partial_{\tilde{z}} \mathcal{E} = i\sqrt{d}P \quad (\text{A.6})$$

$$\partial_{\tilde{t}} P = -(1 + i\tilde{\Delta})P + i\sqrt{d}\mathcal{E} + i\tilde{\Omega}(\tilde{t})S \quad (\text{A.7})$$

$$\partial_{\tilde{t}} S = i\tilde{\Omega}^*(\tilde{t})P, \quad (\text{A.8})$$

Our equations are subject to some initial and boundary conditions:

$$\mathcal{E}(\tilde{z} = 0, \tilde{t}) = \mathcal{E}_{\text{in}}(\tilde{t}) \quad (\text{A.9})$$

$$P(\tilde{z}, \tilde{t} = 0) = 0 \quad (\text{A.10})$$

$$S(\tilde{z}, \tilde{t} = 0) = 0, \quad (\text{A.11})$$

where we re-emphasize that $\mathcal{E}_{\text{in}}(\tilde{t})$ is our normalized signal field, which is defined on some interval $\tilde{t} \in [0, T\gamma]$, with T being the writing time (*e.g.*, 100 μ s):

$$\int_0^{\tilde{T}} d\tilde{t} |\mathcal{E}_{\text{in}}(\tilde{t})|^2 = 1. \quad (\text{A.12})$$

Thus, the retrieval efficiency is simply,

$$\eta_r = \int_{\tilde{T}_r}^{\infty} d\tilde{t} |\mathcal{E}(1, \tilde{t})|^2 = 1. \quad (\text{A.13})$$

We make a distinction between the efficiency of the writing and retrieval processes: η_r , and the efficiency of the storage, η_s , such that the total memory efficiency is the product of the two, $\eta = \eta_r \eta_s$. In general, Eqs. (A.9–A.11) cannot be solved analytically. By applying the adiabatic approximation,

$$\partial_{\tilde{t}} P = \frac{\partial t}{\partial \tilde{t}} \partial_t P = \frac{1}{\gamma} \partial_t P \ll 1, \quad (\text{A.14})$$

we can solve for \mathcal{E}_{out} as a function of $\tilde{\Omega}$, d , S , and $\tilde{\Delta}$. We define

$$h(t, t') = \int_t^{t'} |\tilde{\Omega}(t'')|^2 dt'', \quad (\text{A.15})$$

and change variables, $\tilde{t} \rightarrow h(\tilde{T}_r, \tilde{t})$ in order to eliminate the dependence of Ω . Thus, it is possible to find an Ω -independent solution to Eqs. (A.9–A.11), and rescale for any given Ω . We find that the retrieved signal field shape is,

$$\mathcal{E}(1, \tilde{t}) = -\sqrt{d\tilde{\Omega}} \int_0^1 d\tilde{z} \frac{1}{1 + i\tilde{\Delta}} \exp \left[-\frac{h(0, \tilde{t}) + \tilde{z}d}{1 + i\tilde{\Delta}} \right] I_0 \left[2 \frac{\sqrt{h(0, \tilde{t})\tilde{z}d}}{1 + i\tilde{\Delta}} \right] S(1 - \tilde{z}), \quad (\text{A.16})$$

which, in the limit of no spin-wave decay, becomes:

$$\mathcal{E}(1, \tilde{t}) = i\sqrt{d\tilde{\Omega}} \int_0^1 d\tilde{z} \frac{1}{\tilde{\Delta}} \exp \left[i \frac{h(0, \tilde{t}) + \tilde{z}d}{\tilde{\Delta}} \right] J_0 \left[2 \frac{\sqrt{h(0, \tilde{t})\tilde{z}d}}{\tilde{\Delta}} \right] S(1 - \tilde{z}) \quad (\text{A.17})$$

In a similar fashion, we can solve for the spin-wave, S , in terms of \mathcal{E}_{in} :

$$S(\tilde{z}, \tilde{T}) = -\sqrt{d} \int_0^{\tilde{T}} dt \tilde{\Omega}^*(\tilde{t}) \frac{1}{1+i\tilde{\Delta}} \exp \left[-\frac{h(\tilde{t}, \tilde{T}) + \tilde{z}d}{1+\tilde{\Delta}} \right] I_0 \left[2 \frac{\sqrt{h(\tilde{t}, \tilde{T})\tilde{z}d}}{1+i\tilde{\Delta}} \right] \mathcal{E}_{\text{in}} \quad (\text{A.18})$$

It can be shown [99] that the optimal memory efficiency depends only on the optical depth. At a given optical depth, there is a unique spin-wave S_d that, when created yields this optimal efficiency. This optimal spin-wave can be found by finding the eigenvector with the largest eigenvalue of the following integral equation:

$$\eta_r S(1-\tilde{z}) = \int_0^1 d\tilde{z}' k_r(\tilde{z}, \tilde{z}') S(1-\tilde{z}'), \quad (\text{A.19})$$

where the kernel k_r is defined as

$$k_r(\tilde{z}, \tilde{z}') = \frac{d}{2} e^{-d[(\tilde{z}'+\tilde{z})/2]} I_0(d\sqrt{\tilde{z}\tilde{z}'}), \quad (\text{A.20})$$

where I_0 is the zeroth-order modified Bessel function of the first kind. This eigenvalue problem can be solved by starting with a trial $S(\tilde{z})$ and iterating the integral several times until convergence [99].

Once this optimal spin-wave shape is found, it is possible to find the matching pair of input signal field, $\mathcal{E}_{\text{in}}(\tilde{t})$, and control field, $\tilde{\Omega}(\tilde{t})$ which creates it. We outline this calculation presently. We first define the following function, which appears in both of the equations for \mathcal{E} and S :

$$m[\tilde{\Omega}(\tilde{t}), \tilde{t}, \tilde{z}] \equiv -\frac{\sqrt{d}\tilde{\Omega}}{1+i\tilde{\Delta}} \exp \left[-\frac{h(0, \tilde{t}) + \tilde{z}d}{1+i\tilde{\Delta}} \right] I_0 \left[2 \frac{\sqrt{h(0, \tilde{t})\tilde{z}d}}{1+i\tilde{\Delta}} \right]. \quad (\text{A.21})$$

Ignoring decay, we can make the following definitions and arrive at the ‘‘decayless’’

storage equation, which assumes that $\Delta \gg 1$:

$$q(\tilde{z}, \tilde{t}) \equiv m(\tilde{z}, \tilde{t})_{\text{decayless}} \quad (\text{A.22})$$

$$= \frac{i\sqrt{d}\tilde{\Omega}^*(\tilde{t})}{\tilde{\Delta}} \exp\left[\frac{ih(\tilde{t}, \tilde{T}) + \tilde{z}d}{\tilde{\Delta}}\right] J_0\left[2\frac{\sqrt{h(\tilde{t}, \tilde{T})\tilde{z}d}}{\tilde{\Delta}}\right] \quad (\text{A.23})$$

$$s(\tilde{z}) = \int_0^{\tilde{T}} d\tilde{t} q(\tilde{z}, \tilde{t}) \mathcal{E}_{\text{in}}(\tilde{t}). \quad (\text{A.24})$$

Using orthogonality properties of Bessel functions, we can invert Eq. A.18 to solve for \mathcal{E}_{in} :

$$\mathcal{E}_{\text{in}}(\tilde{t}) = \int_0^\infty d\tilde{z} q^*(\tilde{z}, \tilde{t}) s(\tilde{z}) \quad (\text{A.25})$$

Now, to solve for $\tilde{\Omega}$, we integrate the norm squared of both sides of the equation:

$$\int_0^{\tilde{t}} d\tilde{t}' |\mathcal{E}_{\text{in}}(\tilde{t}')|^2 = \int_0^{\tilde{t}} d\tilde{t}' \left| \int_0^\infty d\tilde{z} q^*(\tilde{z}, \tilde{t}') s(\tilde{z}) \right|^2, \quad (\text{A.26})$$

and the RHS simplifies to,

$$\left| \int_0^\infty d\tilde{z} q^*(\tilde{z}, \tilde{t}') s(\tilde{z}) \right|^2 = \left(\int_0^\infty d\tilde{z} q^*(\tilde{z}, \tilde{t}') s(\tilde{z}) \right) \left(\int_0^\infty d\tilde{z}' q(\tilde{z}', \tilde{t}') s(\tilde{z}') \right) \quad (\text{A.27})$$

$$= \int_0^\infty \int_0^\infty d\tilde{z} d\tilde{z}' q^*(\tilde{z}, \tilde{t}') q(\tilde{z}', \tilde{t}') s^*(\tilde{z}') s(\tilde{z}), \quad (\text{A.28})$$

where

$$q(\tilde{z}', \tilde{t}') = i \frac{\sqrt{d} \tilde{\Omega}^*(\tilde{t}')}{\tilde{\Delta}} \exp \left[\frac{i \left(h(\tilde{t}', \tilde{T}) + \tilde{z}' d \right)}{\tilde{\Delta}} \right] \times J_0 \left[2 \frac{\sqrt{h(\tilde{t}', \tilde{T}) \tilde{z}' d}}{\tilde{\Delta}} \right] \quad (\text{A.29})$$

$$q^*(\tilde{z}, \tilde{t}') = -i \frac{\sqrt{d} \tilde{\Omega}(\tilde{t}')}{\tilde{\Delta}} \exp \left[\frac{-i \left(h(\tilde{t}', \tilde{T}) + \tilde{z} d \right)}{\tilde{\Delta}} \right] \times J_0^* \left[2 \frac{\sqrt{h(\tilde{t}', \tilde{T}) \tilde{z} d}}{\tilde{\Delta}} \right] \quad (\text{A.30})$$

$$q^*(\tilde{z}, \tilde{t}') q(\tilde{z}', \tilde{t}') = + \frac{d |\tilde{\Omega}(\tilde{t}')|^2}{\tilde{\Delta}} \left| \exp \left[-i \frac{\tilde{z} d}{\tilde{\Delta}} \right] J_0 \left[2 \frac{\sqrt{h(\tilde{t}', \tilde{T}) \tilde{z} d}}{\tilde{\Delta}} \right] \right|^2. \quad (\text{A.31})$$

Therefore,

$$\int_0^{\tilde{t}} d\tilde{t}' |\mathcal{E}_{\text{in}}(\tilde{t}')|^2 = \int_0^{\tilde{t}} d\tilde{t}' \frac{|\tilde{\Omega}(\tilde{t}')|^2 d}{\tilde{\Delta}} \left| \int_0^\infty d\tilde{z} s(\tilde{z}) \exp \left[-i \frac{\tilde{z} d}{\tilde{\Delta}} \right] J_0 \left[2 \frac{\sqrt{h(\tilde{t}', \tilde{T}) \tilde{z} d}}{\tilde{\Delta}} \right] \right|^2. \quad (\text{A.32})$$

We make the change of variables $\tilde{t}' \rightarrow h' \equiv h(\tilde{t}', \tilde{T})$ and $|\tilde{\Omega}(\tilde{t}')|^2 d\tilde{t}' \rightarrow dh'$ to arrive at,

$$\int_0^{\tilde{t}} d\tilde{t}' |\mathcal{E}_{\text{in}}(\tilde{t}')|^2 = \int_{h(0, \tilde{T})}^{h(\tilde{t}, \tilde{T})} dh' \frac{d}{\tilde{\Delta}} \left| \int_0^\infty d\tilde{z} s(\tilde{z}) \exp \left[-i \frac{\tilde{z} d}{\tilde{\Delta}} \right] J_0 \left[2 \frac{\sqrt{h' \tilde{z} d}}{\tilde{\Delta}} \right] \right|^2. \quad (\text{A.33})$$

We can solve this equation numerically for $h(\tilde{t}, \tilde{T})$. We then invert our definition, $h(\tilde{t}, \tilde{T}) = \int_{\tilde{t}}^{\tilde{T}} |\tilde{\Omega}(t')|^2 dt'$ to get:

$$\tilde{\Omega}(\tilde{t}) = \sqrt{-\frac{dh}{d\tilde{t}}}. \quad (\text{A.34})$$

APPENDIX B

Derivation of Eqs. 6.20, 6.21, 6.29, and 6.30

In Ch. 6, we omitted the derivations of Eqs. 6.20, 6.21, 6.29, and 6.30. In this Appendix, we present these derivations.

Since experiments and numerics show that turning the control field off and back on has a negligible effect on the fields except for a delay and spin-wave decay during the storage time, we solve Eqs. 6.16–6.19 in the main text assuming a constant control field. In the co-moving frame ($\partial_t + c\partial_z \rightarrow c\partial_z$), Fourier transforming in time ($t \rightarrow \omega$ and $\partial_t \rightarrow -i\omega$), Eqs. 6.16–6.19 can be written as

$$\begin{aligned} \partial_z \begin{pmatrix} \mathcal{E}(z, \omega) \\ \mathcal{E}'^*(z, \omega) \end{pmatrix} &= i \frac{\alpha_0 \gamma}{2F} \begin{pmatrix} \omega + i\Gamma_0 & -\frac{\Omega^2}{\Delta_{\text{hf}}} \\ \frac{\Omega^2}{\Delta_{\text{hf}}} & -\frac{\Omega^2}{\Delta_{\text{hf}}}(\omega + i\Gamma) \end{pmatrix} \begin{pmatrix} \mathcal{E}(z, \omega) \\ \mathcal{E}'^*(z, \omega) \end{pmatrix} \\ &= M \begin{pmatrix} \mathcal{E}(z, \omega) \\ \mathcal{E}'^*(z, \omega) \end{pmatrix}, \end{aligned} \tag{B.1}$$

where $F = \Omega^2 + (\Gamma - i\omega)(\Gamma_0 - i\omega)$ (*c.f.*, Eq. 6.6 with $\alpha_0 L = 2d$).

To gain some intuition for how FWM may result in amplification, one can

consider a simple case, in which the diagonal terms in the matrix M in Eq. B.1 vanish (equivalently, one could consider the case where the Stokes field also propagates in its own EIT medium). Approximating further $F \rightarrow \Omega^2$, we find that

$$M \approx i \frac{\alpha_0 \gamma}{2\Delta_{\text{hf}}} \begin{pmatrix} 0 & -1 \\ 1 & 0 \end{pmatrix} \quad (\text{B.2})$$

and has eigenvectors $(1, \pm i)$ with eigenvalues $\pm \frac{\alpha_0 \gamma}{2\Delta_{\text{hf}}}$, corresponding to an exponentially growing solution and an exponentially decaying solution. In our experiment, however, the diagonal terms for the signal and the Stokes fields are very different. Moreover, the effect of FWM is rather small and can, in fact, be treated perturbatively, as we will show below.

We checked numerically that the last entry in the matrix M in Eq. B.1 does not significantly affect our results. For example, it gives a contribution to $\mathcal{E}'(L, \omega)$ of order $\alpha_0 L \gamma^2 / \Delta_{\text{hf}}^2$, which will be negligible relative to other contributions of order $(\alpha_0 L)^2 \gamma^2 / \Delta_{\text{hf}}^2$ since $\alpha_0 L \gg 1$. We will therefore neglect the last entry in the matrix M in Eq. B.1 for the rest of this Appendix.

Eq. B.1 can then be solved to give [109, 110, 124, 161, 163]

$$\begin{pmatrix} \mathcal{E}(z, \omega) \\ \mathcal{E}'^*(z, \omega) \end{pmatrix} = e^{i\sigma z} \begin{pmatrix} \cosh(\xi z) + i \frac{\sigma}{\xi} \sinh(\xi z) & i \frac{2\Delta_{\text{R}}}{\beta} \sinh(\xi z) \\ -i \frac{2\Delta_{\text{R}}}{\beta} \sinh(\xi z) & \cosh(\xi z) - i \frac{\sigma}{\xi} \sinh(\xi z) \end{pmatrix} \begin{pmatrix} \mathcal{E}(0, \omega) \\ \mathcal{E}'^*(0, \omega) \end{pmatrix}, \quad (\text{B.3})$$

where $\Delta_{\text{R}} = -\Omega^2 / \Delta_{\text{hf}}$, $\beta = \sqrt{(\Gamma_0 - i\omega)^2 + 4\Delta_{\text{R}}^2}$, $\sigma = \frac{\alpha_0 \gamma}{4F}(i\Gamma_0 + \omega)$, and $\xi = \frac{\alpha_0 \gamma}{4F}\beta$.

Using the convolution theorem [172], we then obtain

$$\begin{aligned} \mathcal{E}(z, t) &= \int dt' \mathcal{E}(0, t - t') f_1(z, t') + \int dt' \mathcal{E}(0, t - t') f_2(z, t') \\ &\quad + \int dt' \mathcal{E}'^*(0, t - t') f_3(z, t'), \end{aligned} \quad (\text{B.4})$$

$$\begin{aligned} \mathcal{E}'^*(z, t) &= \mathcal{E}'^*(0, t) + \int dt' \mathcal{E}'^*(0, t - t') g_2(z, t') \\ &\quad + \int dt' \mathcal{E}(0, t - t') g_3(z, t'), \end{aligned} \quad (\text{B.5})$$

where

$$f_1(z, t') = \frac{1}{2\pi} \int d\omega e^{2i\sigma z} e^{-i\omega t'}, \quad (\text{B.6})$$

$$f_1(z, t') + f_2(z, t') = \frac{1}{2\pi} \int d\omega e^{i\sigma z} \left[\cosh(\xi z) + i \frac{\sigma}{\xi} \sinh(\xi z) \right] e^{-i\omega t'}, \quad (\text{B.7})$$

$$f_3(z, t') = \frac{1}{2\pi} \int d\omega e^{i\sigma z} i \frac{2\Delta_R}{\beta} \sinh(\xi z) e^{-i\omega t'}, \quad (\text{B.8})$$

$$\delta(t') + g_2(z, t') = \frac{1}{2\pi} \int d\omega e^{i\sigma z} \left[\cosh(\xi z) - i \frac{\sigma}{\xi} \sinh(\xi z) \right] e^{-i\omega t'}, \quad (\text{B.9})$$

$$g_3(z, t') = -f_3(z, t'). \quad (\text{B.10})$$

Here f_1 and f_2 are defined in such a way that f_1 captures pure EIT, while f_2 describes how FWM changes the relationship between the input signal and the output signal. f_3 describes the effect of the input Stokes field on the output signal. Similarly, the first term in Eq. B.5 describes pure undistorted propagation of the Stokes field in the absence of FWM. g_2 describes how FWM changes the relationship between the input Stokes field and the output Stokes field. Finally, g_3 describes the effect of the input signal on the output Stokes field.

To get some insight into the behavior of f_i and g_i , we consider the case $\delta = \delta_s$ (generalization to arbitrary δ is straightforward). We further take the limit $\gamma_0 = 0$, which is a reasonable approximation in our experiment, except during the waiting

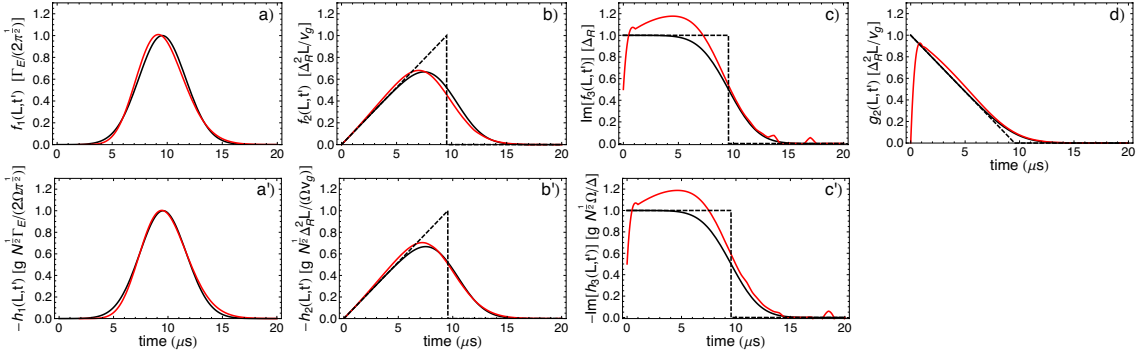


FIG. B.1: Graphs of (a) $f_1(L, t)$, (a') $-h_1(L, t)$, (b) $f_2(L, t)$, (b') $-h_2(L, t)$, (c) $\text{Im}[f_3(L, t)] = -\text{Im}[g_3(L, t)]$, (c') $-\text{Im}[h_3(L, t)]$, and (d) $g_2(L, t)$. For the calculations, $\Omega/(2\pi) = 10$ MHz, $\alpha_0 L = 80$. Red curves show the result of numerical integration of the respective expression in Eqs. B.6–B.10 and B.18–B.20. Solid black curves show the approximate forms of the integrals given in Eqs. B.11–B.15 and B.23, without taking the limit $\Gamma_E \rightarrow \infty$. The dashed black curves incorporate the $\Gamma_E \rightarrow \infty$ approximations in Eqs. B.11–B.15 and B.23.

time between writing and retrieval (however, again one can easily generalize the derivation below to $\gamma_0 \neq 0$). Furthermore, we expand f_2 and g_2 to second order in $1/\Delta_{\text{hf}}$, and expand f_3 and g_3 to first order in $1/\Delta_{\text{hf}}$; in other words, we treat FWM perturbatively, which is a good approximation in our experiment, except in Figs. 6.12(c, d). Furthermore, we approximate $2i\sigma \rightarrow i\frac{\omega}{v_g} - \frac{\omega^2}{L\Gamma_E^2}$, where $v_g = \frac{2\Omega^2}{\alpha_0\gamma}$ is the EIT group velocity and $\Gamma_E = \frac{\Omega^2}{\gamma\sqrt{\alpha_0 L/2}}$ is the width of the EIT transparency window.

We then find

$$f_1(z, t') \approx \frac{\Gamma_E e^{-\Gamma_E^2 \frac{L}{4z} (t' - z/v_g)^2}}{2\sqrt{\pi z/L}} \approx \delta(t' - z/v_g), \quad (\text{B.11})$$

$$\begin{aligned} f_2(z, t') &\approx \Delta_R^2 \left[-\frac{e^{-\Gamma_E^2 \frac{L}{4z} (t' - z/v_g)^2}}{2\Gamma_E \sqrt{\pi L/z}} + \frac{1}{2}|t'| + \frac{1}{2}t' \text{Erf} \left\{ \frac{\Gamma_E(z/v_g - t')}{2\sqrt{z/L}} \right\} \right] \\ &\approx \Delta_R^2 t' \Pi[0, z/v_g](t'), \end{aligned} \quad (\text{B.12})$$

$$\begin{aligned} f_3(z, t') &\approx \frac{i\Delta_R}{2} \left(\text{Sign}[t'] + \text{Erf} \left\{ \frac{\Gamma_E(z/v_g - t')}{2\sqrt{z/L}} \right\} \right) \\ &\approx i\Delta_R \Pi[0, z/v_g](t'), \end{aligned} \quad (\text{B.13})$$

$$\begin{aligned} g_2(z, t') &\approx \Delta_R^2 \left[-\frac{z\delta(t')}{\Gamma_E^2 L} + \frac{e^{-\Gamma_E^2 \frac{L}{4z} (t' - z/v_g)^2}}{\Gamma_E \sqrt{\pi L/z}} \right. \\ &\quad \left. + \frac{z/v_g - t'}{2} \left(\text{Erf} \left\{ \frac{\Gamma_E(z/v_g - t')}{2\sqrt{z/L}} \right\} + \text{Sign}[t'] \right) \right] \\ &\approx \Delta_R^2 (z/v_g - t') \Pi[0, z/v_g](t'), \end{aligned} \quad (\text{B.14})$$

$$g_3(z, t') = -f_3(z, t'). \quad (\text{B.15})$$

Here Erf is the error function, the sign function $\text{Sign}[t'] = 1$ for $t' \geq 0$ and -1 otherwise, and the box function $\Pi[x, y](t) = 1$ for $x < t < y$ and 0 otherwise. The second approximation in Eqs. B.11–B.15 is done in the limit $\Gamma_E \rightarrow \infty$ (the case of an infinitely wide EIT window). Using the $\Gamma_E \rightarrow \infty$ expressions, we arrive at Eqs. 6.20 and 6.21.

In Fig. B.1(a–d), we plot functions f_j and g_j for $j = 1, 2, 3$ and the two approximate forms described above. Red curves depict the results of numerical integration of Eqs. B.6–B.10, with experimental variables $\alpha_0 L = 80$ and $\Omega/(2\pi) = 10$ MHz, so that $\Delta_R/(2\pi) = -14.6$ kHz, $\Gamma_E/(2\pi) = 105$ kHz, and $v_g/(2\pi L) = 16.7$ kHz. Because the light pulses \mathcal{E} and \mathcal{E}'^* have a finite bandwidth, we chose an integration bandwidth of $(2\pi)160$ MHz, and we have checked that a larger range does not significantly affect the results. Solid black curves in Fig. B.1(a–d) plot the first approximations in Eqs. B.11–B.15; dashed black lines show the corresponding $\Gamma_E \rightarrow \infty$

expressions in Eqs. B.11–B.15.

Let us now compute $S(z, t)$. From Eqs. 6.18 and 6.19, we have

$$S(z, \omega) = -\frac{g\sqrt{N}\Omega}{F} \left[\mathcal{E}(z, \omega) - i\frac{\Gamma - i\omega}{\Delta_{\text{hf}}} \mathcal{E}'^*(z, \omega) \right], \quad (\text{B.16})$$

where $\mathcal{E}(z, \omega)$ and $\mathcal{E}'^*(z, \omega)$ are given in Eq. B.3.

We can then write

$$\begin{aligned} S(z, t) &= \int dt' \mathcal{E}(0, t - t') h_1(z, t') \\ &\quad + \int dt' \mathcal{E}(0, t - t') h_2(z, t') \\ &\quad + \int dt' \mathcal{E}'^*(0, t - t') h_3(z, t'), \end{aligned} \quad (\text{B.17})$$

where h_1 describes pure EIT, while h_2 and h_3 are the results of FWM. Functions h_j can be computed as

$$h_1(z, t') = \frac{1}{2\pi} \int d\omega \frac{-g\sqrt{N}\Omega}{F} e^{2i\sigma z} e^{-i\omega t'}, \quad (\text{B.18})$$

$$\begin{aligned} h_1(z, t') + h_2(z, t') &= \frac{1}{2\pi} \int d\omega \frac{-g\sqrt{N}\Omega}{F} e^{i\sigma z} e^{-i\omega t'} \\ &\quad \times \left[\cosh(\xi z) + \left(i\frac{\sigma}{\xi} - \frac{2\Delta_{\text{R}}(\Gamma - i\omega)}{\beta\Delta_{\text{hf}}} \right) \sinh(\xi z) \right], \end{aligned} \quad (\text{B.19})$$

$$\begin{aligned} h_3(z, t') &= \frac{1}{2\pi} \int d\omega \frac{g\sqrt{N}\Omega}{F} e^{i\sigma z} e^{-i\omega t'} \left[i\frac{\Gamma - i\omega}{\Delta_{\text{hf}}} \cosh(\xi z) \right. \\ &\quad \left. + \left(\frac{\sigma(\Gamma - i\omega)}{\xi\Delta_{\text{hf}}} - i\frac{2\Delta_{\text{R}}}{\beta} \right) \sinh(\xi z) \right]. \end{aligned} \quad (\text{B.20})$$

Expanding h_2 to $\mathcal{O}(1/\Delta_{\text{hf}}^2)$ and h_3 to $\mathcal{O}(1/\Delta_{\text{hf}})$, the above expressions simplify

to

$$h_2(z, t') \approx \frac{1}{2\pi} \int d\omega \frac{g\sqrt{N}\Omega^3 (F + e^{2i\sigma z} (2i\Omega^2 \sigma z - F))}{F\Delta_{\text{hf}}^2 (\omega + i\Gamma_0)^2} e^{-i\omega t'}, \quad (\text{B.21})$$

$$h_3(z, t') \approx \frac{1}{2\pi} \int d\omega \frac{g\sqrt{N}\Omega (\Omega^2 e^{2i\sigma z} - F)}{\Delta_{\text{hf}} (\omega + i\Gamma_0) F} e^{-i\omega t'}. \quad (\text{B.22})$$

Taking $\delta = \delta_s$, $\gamma_0 = 0$, $2i\sigma \approx i\frac{\omega}{v_g} - \frac{\omega^2}{L\Gamma_E^2}$, and $F \approx \Omega^2$, we have

$$h_j(z, t') \approx -\frac{g\sqrt{N}}{\Omega} f_j(z, t') \quad (\text{B.23})$$

for $j = 1, 2, 3$, where the expressions for $f_j(z, t')$ are given in Eqs. (B.11–B.13). Plugging Eq. B.23 into Eq. B.17 yields an expression that is proportional to the signal field $\mathcal{E}(z, t)$ in Eq. B.4. Thus, under these approximations, we obtain Eq. (6.30), which is, remarkably, the usual EIT relation. Specifically, in the limit of an infinitely wide EIT window, $S(z, t)$ can be found by plugging Eq. B.23 (with the corresponding $\Gamma_E \rightarrow \infty$ expressions for f_j from Eqs. B.11–B.13) into Eq. B.17 to yield Eq. 6.29. The expressions for $|h_1(L, t)|$, $|h_2(L, t)|$, and $|\text{Im}[h_3(L, t)]|$ are plotted in Fig. B.1 (a', b', and c'), respectively. As before, red traces depict the results of numerical integration of Eqs. B.18–B.20 with the same input parameters as in the f_j and g_j analysis. Solid black curves plot Eq. B.23 using finite Γ_E expressions for f_j from Eqs. B.11–B.13. Dashed black lines show the corresponding $\Gamma_E \rightarrow \infty$ expressions.

BIBLIOGRAPHY

- [1] D. A. Steck (2010), revision 2.1.4, URL <http://steck.us/alkalidata/>.
- [2] W. K. Wootters and W. H. Zurek, “A single quantum cannot be cloned,” *Nature* **299**, 802 (1982).
- [3] D. Dieks, “Communication by EPR devices,” *Physics Letters A* **92**, 271 (1982).
- [4] C. Bennett, G. Brassard, et al., “Quantum cryptography: Public key distribution and coin tossing,” *Proceedings of IEEE International Conference on Computers, Systems and Signal Processing* **175** (1984).
- [5] A. I. Lvovsky, B. C. Sanders, and W. Tittel, “Optical quantum memory,” *Nature Photonics* **3**, 706 (2009).
- [6] E. Knill, R. Laflamme, and G. Milburn, “A scheme for efficient quantum computation with linear optics,” *Nature* **409**, 46 (2001).
- [7] A. P. Lund and T. C. Ralph, “Nondeterministic gates for photonic single-rail quantum logic,” *Phys. Rev. A* **66**, 032307 (2002).
- [8] D. Berry, A. Lvovsky, and B. Sanders, “Interconvertibility of single-rail optical qubits,” *Opt. Lett.* **31**, 107 (2006).
- [9] I. Marcikic, H. de Riedmatten, W. Tittel, V. Scarani, H. Zbinden, and N. Gisin, “Time-bin entangled qubits for quantum communication created by femtosecond pulses,” *Phys. Rev. A* **66**, 062308 (2002).
- [10] H.-J. Briegel, W. Dür, J. I. Cirac, and P. Zoller, “Quantum repeaters: The role of imperfect local operations in quantum communication,” *Phys. Rev. Lett.* **81**, 5932 (1998).
- [11] N. Sangouard, C. Simon, B. Zhao, Y.-A. Chen, H. de Riedmatten, J.-W. Pan, and N. Gisin, “Robust and efficient quantum repeaters with atomic ensembles and linear optics,” *Phys. Rev. A* **77**, 062301 (2008).
- [12] N. Sangouard, C. Simon, H. De Riedmatten, and N. Gisin, “Quantum repeaters based on atomic ensembles and linear optics,” *Rev. Mod. Phys.* **83**, 33 (2011).

- [13] L. M. Duan, M. D. Lukin, J. I. Cirac, and P. Zoller, “Long-distance quantum communication with atomic ensembles and linear optics,” *Nature* **414**, 413 (2001).
- [14] H. J. Kimble, “The quantum internet,” *Nature* **453**, 1023 (2008).
- [15] J. I. Cirac, P. Zoller, H. J. Kimble, and H. Mabuchi, “Quantum state transfer and entanglement distribution among distant nodes in a quantum network,” *Phys. Rev. Lett.* **78**, 3221 (1997).
- [16] A. S. Parkins, P. Marte, P. Zoller, and H. J. Kimble, “Synthesis of arbitrary quantum states via adiabatic transfer of Zeeman coherence,” *Phys. Rev. Lett.* **71**, 3095 (1993).
- [17] S. Van Enk, J. Cirac, and P. Zoller, “Photonic channels for quantum communication,” *Science* **279**, 205 (1998).
- [18] M. Hijlkema, B. Weber, H. Specht, S. Webster, A. Kuhn, and G. Rempe, “A single-photon server with just one atom,” *Nature Physics* **3**, 253 (2007).
- [19] M. Keller, B. Lange, K. Hayasaka, W. Lange, and H. Walther, “Continuous generation of single photons with controlled waveform in an ion-trap cavity system,” *Nature* **431**, 1075 (2004).
- [20] J. McKeever, A. Boca, A. Boozer, R. Miller, J. Buck, A. Kuzmich, and H. Kimble, “Deterministic generation of single photons from one atom trapped in a cavity,” *Science* **303**, 1992 (2004).
- [21] R. Fleischhaker and J. Evers, “Nonlinear effects in pulse propagation through Doppler-broadened closed-loop atomic media,” *Phys. Rev. A* **77**, 043805 (2008).
- [22] M. Fleischhauer and M. D. Lukin, “Dark-state polaritons in electromagnetically induced transparency,” *Phys. Rev. Lett.* **84**, 5094 (2000).
- [23] M. D. Lukin, “Colloquium: Trapping and manipulating photon states in atomic ensembles,” *Rev. Mod. Phys.* **75**, 457 (2003).
- [24] C. Liu, Z. Dutton, C. H. Behroozi, and L. V. Hau, “Observation of coherent optical information storage in an atomic medium using halted light pulses,” *Nature* **409**, 490 (2001).
- [25] D. F. Phillips, A. Fleischhauer, A. Mair, R. L. Walsworth, and M. D. Lukin, “Storage of light in atomic vapor,” *Phys. Rev. Lett.* **86**, 783 (2001).
- [26] M. D. Eisaman, A. Andre, F. Massou, M. Fleischhauer, A. S. Zibrov, and M. D. Lukin, “Electromagnetically induced transparency with tunable single-photon pulses,” *Nature* **438**, 837 (2005).

- [27] T. Chanelière, D. N. Matsukevich, S. D. Jenkins, S. Y. Lan, T. A. B. Kennedy, and A. Kuzmich, “Storage and retrieval of single photons transmitted between remote quantum memories,” *Nature* **438**, 833 (2005).
- [28] B. Julsgaard, J. Sherson, J. I. Cirac, J. Fiurasek, and E. S. Polzik, “Experimental demonstration of quantum memory for light,” *Nature* **432**, 482 (2004).
- [29] A. E. Kozhekin, K. Mølmer, and E. Polzik, “Quantum memory for light,” *Phys. Rev. A* **62**, 033809 (2000).
- [30] J. Nunn, K. Reim, K. C. Lee, V. O. Lorenz, B. J. Sussman, I. A. Walmsley, and D. Jaksch, “Multimode memories in atomic ensembles,” *Phys. Rev. Lett.* **101**, 260502 (2008).
- [31] S. A. Moiseev and S. Kröll, “Complete reconstruction of the quantum state of a single-photon wave packet absorbed by a Doppler-broadened transition,” *Phys. Rev. Lett.* **87**, 173601 (2001).
- [32] P. Hemmer, A. Turukhin, M. Shahriar, and J. Musser, “Raman-excited spin coherences in Nitrogen-vacancy color centers in diamond,” *Opt. Lett.* **26**, 361 (2001).
- [33] B. Kraus, W. Tittel, N. Gisin, M. Nilsson, S. Kröll, and J. I. Cirac, “Quantum memory for nonstationary light fields based on controlled reversible inhomogeneous broadening,” *Phys. Rev. A* **73**, 020302 (2006).
- [34] J. J. Longdell, E. Fraval, M. J. Sellars, and N. B. Manson, “Stopped light with storage times greater than one second using electromagnetically induced transparency in a solid,” *Phys. Rev. Lett.* **95**, 063601 (2005).
- [35] M. Kroutvar, Y. Ducommun, D. Heiss, M. Bichler, D. Schuh, G. Abstreiter, and J. J. Finley, “Optically programmable electron spin memory using semiconductor quantum dots,” *Nature* **432**, 81 (2004).
- [36] M. Eisaman, M. Fleischhauer, M. Lukin, and A. Zibrov, “Toward quantum control of single photons,” *Optics and Photonics News* **17**, 22 (2006).
- [37] P. Berman and V. Malinovsky, *Principles of laser spectroscopy and quantum optics* (Princeton Univ Press, 2010).
- [38] C. Simon, M. Afzelius, J. Appel, A. B. de la Giroday, S. J. Dewhurst, N. Gisin, C. Y. Hu, F. Jelezko, S. Kröll, J. H. Müller, et al., “Quantum memories,” *Eur. Phys. J. D* **58**, 1 (2010).
- [39] R. Loudon, *The Quantum Theory of Light* (Oxford University Press, 2000).
- [40] A. V. Gorshkov, A. André, M. D. Lukin, and A. S. Sørensen, “Photon storage in Λ -type optically dense atomic media. I. Cavity model,” *Phys. Rev. A* **76**, 033804 (2007).

- [41] L. Jiang, J. M. Taylor, and M. D. Lukin, “Fast and robust approach to long-distance quantum communication with atomic ensembles,” *Phys. Rev. A* **76**, 012301 (2007).
- [42] M. Fleischhauer and M. D. Lukin, “Quantum memory for photons: Dark-state polaritons,” *Phys. Rev. A* **65**, 022314 (2002).
- [43] A. V. Gorshkov, A. André, M. Fleischhauer, A. S. Sørensen, and M. D. Lukin, “Universal approach to optimal photon storage in atomic media,” *Phys. Rev. Lett.* **98**, 123601 (2007).
- [44] L. V. Hau, S. E. Harris, Z. Dutton, and C. H. Behroozi, “Light speed reduction to 17 metres per second in an ultracold atomic gas,” *Nature* **397**, 594 (1999).
- [45] D. Budker, D. F. Kimball, S. M. Rochester, and V. V. Yashchuk, “Nonlinear magneto-optics and reduced group velocity of light in atomic vapor with slow ground state relaxation,” *Phys. Rev. Lett.* **83**, 1767 (1999).
- [46] M. M. Kash, V. A. Sautenkov, A. S. Zibrov, L. Hollberg, G. R. Welch, M. D. Lukin, Y. Rostovtsev, E. S. Fry, and M. O. Scully, “Ultraslow group velocity and enhanced nonlinear optical effects in a coherently driven hot atomic gas,” *Phys. Rev. Lett.* **82**, 5229 (1999).
- [47] A. S. Zibrov, A. B. Matsko, O. Kocharovskaya, Y. V. Rostovtsev, G. R. Welch, and M. O. Scully, “Transporting and time reversing light via atomic coherence,” *Phys. Rev. Lett.* **88**, 103601 (2002).
- [48] R. H. Hadfield, “Single-photon detectors for optical quantum information applications,” *Nature Photonics* **3**, 696 (2009).
- [49] G. Hétet, O. Glöckl, K. A. Pilypas, C. C. Harb, B. C. Buchler, H.-A. Bachor, and P. K. Lam, “Squeezed light for bandwidth-limited atom optics experiments at the Rubidium D1 line,” *J. Phys. B* **40**, 221 (2007).
- [50] Y. Takeno, M. Yukawa, H. Yonezawa, and A. Furusawa, “Observation of -9 dB quadrature squeezing with improvement of phase stability in homodyne measurement,” *Opt. Express* **15**, 4321 (2007).
- [51] S. Burks, J. Ortalo, A. Chiummo, X. Jia, F. Villa, A. Bramati, J. Laurat, and E. Giacobino, “Vacuum squeezed light for atomic memories at the D₂ Cesium line,” *Opt. Express* **17**, 3777 (2009).
- [52] J. Thompson, J. Simon, H. Loh, and V. Vuletić, “A high-brightness source of narrowband, identical-photon pairs,” *Science* **313**, 74 (2006).
- [53] P. Kolchin, S. Du, C. Belthangady, G. Y. Yin, and S. E. Harris, “Generation of narrow-bandwidth paired photons: Use of a single driving laser,” *Phys. Rev. Lett.* **97**, 113602 (2006).

- [54] D. Akamatsu, K. Akiba, and M. Kozuma, “Electromagnetically induced transparency with squeezed vacuum,” *Phys. Rev. Lett.* **92**, 203602 (2004).
- [55] J. Appel, E. Figueroa, D. Korystov, M. Lobino, and A. I. Lvovsky, “Quantum memory for squeezed light,” *Phys. Rev. Lett.* **100**, 093602 (2008).
- [56] K. Honda, D. Akamatsu, M. Arikawa, Y. Yokoi, K. Akiba, S. Nagatsuka, T. Tanimura, A. Furusawa, and M. Kozuma, “Storage and retrieval of a squeezed vacuum,” *Phys. Rev. Lett.* **100**, 093601 (2008).
- [57] M. Arikawa, K. Honda, D. Akamatsu, S. Nagatsuka, K. Akiba, A. Furusawa, and M. Kozuma, “Quantum memory of a squeezed vacuum for arbitrary frequency sidebands,” *Phys. Rev. A* **81**, 021605 (2010).
- [58] A. Peng, M. Johnsson, W. P. Bowen, P. K. Lam, H.-A. Bachor, and J. J. Hope, “Squeezing and entanglement delay using slow light,” *Phys. Rev. A* **71**, 033809 (2005).
- [59] E. Figueroa, F. Vewinger, J. Appel, and A. I. Lvovsky, “Decoherence of electromagnetically induced transparency in atomic vapor,” *Opt. Lett.* **31**, 2625 (2006).
- [60] Y.-A. Chen, S. Chen, Z.-S. Yuan, B. Zhao, C.-S. Chuu, J. Schmiedmayer, and J.-W. Pan, “Memory-built-in quantum teleportation with photonic and atomic qubits,” *Nature Physics* **4**, 103 (2008).
- [61] R. Brown and R. Twiss, “Correlation between photons in two coherent beams of light,” *Nature* **177**, 27 (1956).
- [62] M. Eisaman, Ph.D. thesis, Harvard University (2006).
- [63] R. J. Glauber, “The quantum theory of optical coherence,” *Phys. Rev.* **130**, 2529 (1963).
- [64] R. J. Glauber, “Coherent and incoherent states of the radiation field,” *Phys. Rev.* **131**, 2766 (1963).
- [65] A. Kuzmich, W. P. Bowen, A. D. Boozer, A. Boca, C. W. Chou, L. M. Duan, and H. J. Kimble, “Generation of nonclassical photon pairs for scalable quantum communication with atomic ensembles,” *Nature* **423**, 731 (2003).
- [66] C. van der Wal, M. Eisaman, A. André, R. Walsworth, D. Phillips, A. Zibrov, and M. Lukin, “Atomic memory for correlated photon states,” *Science* **301**, 196 (2003).
- [67] V. Balić, D. A. Braje, P. Kolchin, G. Y. Yin, and S. E. Harris, “Generation of paired photons with controllable waveforms,” *Phys. Rev. Lett.* **94**, 183601 (2005).

- [68] D. N. Matsukevich, T. Chanelière, S. D. Jenkins, S.-Y. Lan, T. A. B. Kennedy, and A. Kuzmich, “Deterministic single photons via conditional quantum evolution,” *Phys. Rev. Lett.* **97**, 013601 (2006).
- [69] S. Du, P. Kolchin, C. Belthangady, G. Y. Yin, and S. E. Harris, “Subnatural linewidth biphotons with controllable temporal length,” *Phys. Rev. Lett.* **100**, 183603 (2008).
- [70] M. D. Eisaman, L. Childress, A. André, F. Massou, A. S. Zibrov, and M. D. Lukin, “Shaping quantum pulses of light via coherent atomic memory,” *Phys. Rev. Lett.* **93**, 233602 (2004).
- [71] Y. O. Dudin, S. D. Jenkins, R. Zhao, D. N. Matsukevich, A. Kuzmich, and T. A. B. Kennedy, “Entanglement of a photon and an optical lattice spin wave,” *Phys. Rev. Lett.* **103**, 020505 (2009).
- [72] D. N. Matsukevich, T. Chanelière, M. Bhattacharya, S.-Y. Lan, S. D. Jenkins, T. A. B. Kennedy, and A. Kuzmich, “Entanglement of a photon and a collective atomic excitation,” *Phys. Rev. Lett.* **95**, 040405 (2005).
- [73] D. Matsukevich and A. Kuzmich, “Quantum state transfer between matter and light,” *Science* **306**, 663 (2004).
- [74] C. W. Chou, H. de Riedmatten, D. Felinto, S. V. Polyakov, S. J. van Enk, and H. J. Kimble, “Measurement-induced entanglement for excitation stored in remote atomic ensembles,” *Nature* **438**, 828 (2005).
- [75] C. Chou, J. Laurat, H. Deng, K. Choi, H. De Riedmatten, D. Felinto, and H. Kimble, “Functional quantum nodes for entanglement distribution over scalable quantum networks,” *Science* **316**, 1316 (2007).
- [76] D. Felinto, C. W. Chou, J. Laurat, E. W. Schomburg, H. de Riedmatten, and H. J. Kimble, “Conditional control of the quantum states of remote atomic memories for quantum networking,” *Nature Physics* **2**, 844 (2006).
- [77] J. Laurat, K. S. Choi, H. Deng, C. W. Chou, and H. J. Kimble, “Heralded entanglement between atomic ensembles: Preparation, decoherence, and scaling,” *Phys. Rev. Lett.* **99**, 180504 (2007).
- [78] D. N. Matsukevich, T. Chanelière, S. D. Jenkins, S.-Y. Lan, T. A. B. Kennedy, and A. Kuzmich, “Entanglement of remote atomic qubits,” *Phys. Rev. Lett.* **96**, 030405 (2006).
- [79] S. Chen, Y.-A. Chen, T. Strassel, Z.-S. Yuan, B. Zhao, J. Schmiedmayer, and J.-W. Pan, “Deterministic and storable single-photon source based on a quantum memory,” *Phys. Rev. Lett.* **97**, 173004 (2006).

- [80] A. Kuhn, M. Hennrich, and G. Rempe, “Deterministic single-photon source for distributed quantum networking,” *Phys. Rev. Lett.* **89**, 067901 (2002).
- [81] K. S. Choi, H. Deng, J. Laurat, and H. J. Kimble, “Mapping photonic entanglement into and out of a quantum memory,” *Nature* **452**, 67 (2008).
- [82] S. Lan, A. Radnaev, O. Collins, D. Matsukevich, T. Kennedy, and A. Kuzmich, “A multiplexed quantum memory,” *Opt. Express* **17**, 13639 (2009).
- [83] R. Zhao, Y. O. Dudin, S. D. Jenkins, C. J. Campbell, D. N. Matsukevich, T. A. B. Kennedy, and A. Kuzmich, “Long-lived quantum memory,” *Nature Physics* **5**, 100 (2009).
- [84] A. Radnaev, Y. Dudin, R. Zhao, H. Jen, S. Jenkins, A. Kuzmich, and T. Kennedy, “A quantum memory with telecom-wavelength conversion,” *Nature Physics* **6**, 894 (2010).
- [85] M. Lettner, M. Mücke, S. Riedl, C. Vo, C. Hahn, S. Baur, J. Bochmann, S. Ritter, S. Dürr, and G. Rempe, “Remote entanglement between a single atom and a Bose-Einstein condensate,” *Phys. Rev. Lett.* **106**, 210503 (2011).
- [86] J. Jackson, *Classical Electrodynamics* (Wiley, 1999), 3rd ed.
- [87] M. Scully, M. Zubairy, and I. Walmsley, *Quantum Optics* (Cambridge University Press, 1999).
- [88] D. A. Steck (2010), revision 0.2.3, URL <http://steck.us/teaching/>.
- [89] C. Cohen-Tannoudji, J. Dupont-Roc, and G. Grynberg, *Atom-Photon Interactions: Basic Processes and Applications*, vol. 1 (Wiley, 1998).
- [90] M. Fleischhauer, A. Imamoglu, and J. Marangos, “Electromagnetically induced transparency: Optics in coherent media,” *Rev. Mod. Phys.* **77**, 633 (2005).
- [91] D. Griffiths, *Introduction to Quantum Mechanics* (Pearson Prentice Hall, 2005).
- [92] R. Boyd and D. Gauthier, “‘Slow’ and ‘fast’ light,” *Progress in Optics* **43**, 497 (2002).
- [93] A. Dantan, J. Cviklinski, M. Pinard, and P. Grangier, “Dynamics of a pulsed continuous-variable quantum memory,” *Phys. Rev. A* **73**, 032338 (2006).
- [94] A. Dantan, A. Bramati, and M. Pinard, “Atomic quantum memory: Cavity versus single-pass schemes,” *Phys. Rev. A* **71**, 043801 (2005).
- [95] A. Dantan and M. Pinard, “Quantum-state transfer between fields and atoms in electromagnetically induced transparency,” *Phys. Rev. A* **69**, 043810 (2004).

- [96] A. André, Ph.D. thesis, Harvard University (2005).
- [97] A. V. Gorshkov, T. Calarco, M. D. Lukin, and A. S. Sørensen, “Photon storage in Λ -type optically dense atomic media. IV. Optimal control using gradient ascent,” *Phys. Rev. A* **77**, 043806 (2008).
- [98] A. V. Gorshkov, A. André, M. D. Lukin, and A. S. Sørensen, “Photon storage in Λ -type optically dense atomic media. III. Effects of inhomogeneous broadening,” *Phys. Rev. A* **76**, 033806 (2007).
- [99] A. V. Gorshkov, A. André, M. D. Lukin, and A. S. Sørensen, “Photon storage in Λ -type optically dense atomic media. II. Free-space model,” *Phys. Rev. A* **76**, 033805 (2007).
- [100] A. Mair, J. Hager, D. F. Phillips, R. L. Walsworth, and M. D. Lukin, “Phase coherence and control of stored photonic information,” *Phys. Rev. A* **65**, 031802 (2002).
- [101] I. Novikova, Y. Xiao, D. F. Phillips, and R. L. Walsworth, “EIT and diffusion of atomic coherence,” *Journal of Modern Optics* **52**, 2381 (2005).
- [102] S. Manz, T. Fernholz, J. Schmiedmayer, and J.-W. Pan, “Collisional decoherence during writing and reading quantum states,” *Phys. Rev. A* **75**, 040101 (2007).
- [103] Y. Qi, H. Gao, and S. Zhang, “Fidelity of light storage in warm atomic gases at different storage time,” *Chinese Opt. Lett.* **8**, 1 (2010).
- [104] R. W. Boyd, D. J. Gauthier, A. L. Gaeta, and A. E. Willner, “Maximum time delay achievable on propagation through a slow-light medium,” *Phys. Rev. A* **71**, 023801 (2005).
- [105] G. S. Agarwal, T. N. Dey, and D. J. Gauthier, “Competition between electromagnetically induced transparency and Raman processes,” *Phys. Rev. A* **74**, 043805 (2006).
- [106] K.-i. Harada, T. Kanbashi, M. Mitsunaga, and K. Motomura, “Competition between electromagnetically induced transparency and stimulated Raman scattering,” *Phys. Rev. A* **73**, 013807 (2006).
- [107] H. Kang, G. Hernandez, and Y. Zhu, “Resonant four-wave mixing with slow light,” *Phys. Rev. A* **70**, 061804 (2004).
- [108] V. Wong, R. S. Bennink, A. M. Marino, R. W. Boyd, C. R. Stroud, and F. A. Narducci, “Influence of coherent Raman scattering on coherent population trapping in atomic sodium vapor,” *Phys. Rev. A* **70**, 053811 (2004).

- [109] M. D. Lukin, A. B. Matsko, M. Fleischhauer, and M. O. Scully, “Quantum noise and correlations in resonantly enhanced wave mixing based on atomic coherence,” *Phys. Rev. Lett.* **82**, 1847 (1999).
- [110] M. D. Lukin, P. R. Hemmer, M. Löffler, and M. O. Scully, “Resonant enhancement of parametric processes via radiative interference and induced coherence,” *Phys. Rev. Lett.* **81**, 2675 (1998).
- [111] A. Eilam, A. D. Wilson-Gordon, and H. Friedmann, “Slow and stored light in an amplifying double- Λ system,” *Opt. Lett.* **33**, 1605 (2008).
- [112] Q. Glorieux, R. Dubessy, S. Guibal, L. Guidoni, J.-P. Likforman, T. Coudreau, and E. Arimondo, “Double- Λ microscopic model for entangled light generation by four-wave mixing,” *Phys. Rev. A* **82**, 033819 (2010).
- [113] C. Li, Y. Zhang, Z. Nie, Y. Du, R. Wang, J. Song, and M. Xiao, “Controlling enhancement and suppression of four-wave mixing via polarized light,” *Phys. Rev. A* **81**, 033801 (2010).
- [114] O. S. Mishina, N. V. Larionov, A. S. Sheremet, I. M. Sokolov, and D. V. Kupriyanov, “Stimulated Raman process in a scattering medium applied to the quantum memory scheme,” *Phys. Rev. A* **78**, 042313 (2008).
- [115] A. Raczynski and J. Zaremba, “Controlled light storage in a double lambda system,” *Opt. Commun.* **209**, 149 (2002).
- [116] A. Raczynski, M. Rzepecka, J. Zaremba, and S. Zielinska-Kaniasty, “Polariton picture of light propagation and storing in a tripod system,” *Opt. Commun.* **260**, 73 (2006).
- [117] F. Zimmer, A. André, M. Lukin, and M. Fleischhauer, “Coherent control of stationary light pulses,” *Opt. Commun.* **264**, 441 (2006).
- [118] F. E. Zimmer, J. Otterbach, R. G. Unanyan, B. W. Shore, and M. Fleischhauer, “Dark-state polaritons for multicomponent and stationary light fields,” *Phys. Rev. A* **77**, 063823 (2008).
- [119] E. Cerboneschi and E. Arimondo, “Propagation and amplitude correlation of pairs of intense pulses interacting with a double- Λ system,” *Phys. Rev. A* **54**, 5400 (1996).
- [120] N. B. Phillips, A. V. Gorshkov, and I. Novikova, “Optimal light storage in atomic vapor,” *Phys. Rev. A* **78**, 023801 (2008).
- [121] P. Kolchin, C. Belthangady, S. Du, G. Y. Yin, and S. E. Harris, “Electro-optic modulation of single photons,” *Phys. Rev. Lett.* **101**, 103601 (2008).
- [122] V. Boyer, A. M. Marino, R. C. Pooser, and P. D. Lett, “Entangled images from four-wave mixing,” *Science* **321**, 544 (2008).

- [123] A. Matsko, D. Strekalov, and L. Maleki, “On the dynamic range of optical delay lines based on coherent atomic media,” *Opt. Express* **13**, 2210 (2005).
- [124] R. M. Camacho, P. K. Vudyasetu, and J. C. Howell, “Four-wave-mixing stopped light in hot atomic rubidium vapour,” *Nature Photonics* **3**, 103 (2009).
- [125] K. Drese and M. Holthaus, “Floquet theory for short laser pulses,” *Eur. Phys. J. D* **5**, 119 (1999).
- [126] D. Brink and G. Satchler, *Angular Momentum* (Clarendon Press, Oxford, UK, 1993), 3rd ed.
- [127] H. Metcalf and P. Van der Straten, *Laser Cooling and Trapping* (Springer Verlag, 1999).
- [128] F. Sears and G. Salinger, *Thermodynamics, Kinetic Theory, and Statistical Thermodynamics* (Addison-Wesley, 1975).
- [129] L. Landau and E. Lifshitz, *Statistical Physics*, vol. 1 (Pergamon Press, 1980).
- [130] D. L. Drummond and A. Gallagher, “Potentials and continuum spectra of Rb-noble gas molecules,” *J. Chem. Phys.* **60**, 3426 (1974).
- [131] M. Erhard and H. Helm, “Buffer-gas effects on dark resonances: Theory and experiment,” *Phys. Rev. A* **63**, 043813 (2001).
- [132] R. M. Herman, “Noble-gas-induced Rubidium spin disorientation,” *Phys. Rev.* **136**, A1576 (1964).
- [133] D. Gray, *American Institute of Physics (AIP). Handbook*, vol. 1 (Mcgraw-Hill, 1972).
- [134] W. Happer, “Optical pumping,” *Rev. Mod. Phys.* **44**, 169 (1972).
- [135] J. Vanier and C. Audoin, *The quantum physics of atomic frequency standards* (A. Hilger, 1989).
- [136] W. Demtröder, *Laser Spectroscopy: Basic Concepts and Instrumentation* (Springer, 2003).
- [137] C. Ottinger, R. Scheps, G. W. York, and A. Gallagher, “Broadening of the Rb resonance lines by the noble gases,” *Phys. Rev. A* **11**, 1815 (1975).
- [138] M. D. Rotondaro and G. P. Perram, “Collisional broadening and shift of the rubidium D_1 and D_2 lines ($5^2S_{1/2} \rightarrow 5^2P_{1/2}$, $5^2P_{3/2}$) by rare gases, H_2 , D_2 , N_2 , CH_4 and CF_4 ,” *Journal of Quantitative Spectroscopy and Radiative Transfer* **57**, 497 (1997).
- [139] F. A. Franz and J. R. Franz, “Excited-state mixing in the optical pumping of alkali-metal Vapors,” *Phys. Rev.* **148**, 82 (1966).

- [140] M. D. Rotondaro and G. P. Perram, “Collision-induced transitions between the Zeeman-split (J, m) levels of Rb ($5^2P_{1/2}$, $5^2P_{3/2}$),” *Phys. Rev. A* **58**, 2023 (1998).
- [141] M. Abramowitz and I. Stegun, *Handbook of Mathematical Functions with Formulas, Graphs, and Mathematical Tables* (Dover publications, 1964).
- [142] I. Novikova, A. V. Gorshkov, D. F. Phillips, A. S. Sørensen, M. D. Lukin, and R. L. Walsworth, “Optimal control of light pulse storage and retrieval,” *Phys. Rev. Lett.* **98**, 243602 (2007).
- [143] J. S. Neergaard-Nielsen, B. M. Nielsen, H. Takahashi, A. I. Vistnes, and E. S. Polzik, “High purity bright single photon source,” *Opt. Express* **15**, 7940 (2007).
- [144] M. D. Lukin, M. Fleischhauer, A. S. Zibrov, H. G. Robinson, V. L. Velichansky, L. Hollberg, and M. O. Scully, “Spectroscopy in dense coherent media: line narrowing and interference effects,” *Phys. Rev. Lett.* **79**, 2959 (1997).
- [145] S. E. Harris, J. E. Field, and A. Imamoglu, “Nonlinear optical processes using electromagnetically induced transparency,” *Phys. Rev. Lett.* **64**, 1107 (1990).
- [146] Y. qing Li and M. Xiao, “Enhancement of nondegenerate four-wave mixing based on electromagnetically induced transparency in Rubidium atoms,” *Opt. Lett.* **21**, 1064 (1996).
- [147] M. D. Lukin, S. F. Yelin, M. Fleischhauer, and M. O. Scully, “Quantum interference effects induced by interacting dark resonances,” *Phys. Rev. A* **60**, 3225 (1999).
- [148] E. E. Mikhailov, Y. V. Rostovtsev, and G. R. Welch, “Group velocity study in hot ^{87}Rb vapour with buffer gas,” *Journal of Modern Optics* **50**, 2645 (2003).
- [149] V. Boyer, C. F. McCormick, E. Arimondo, and P. D. Lett, “Ultraslow propagation of matched pulses by four-wave mixing in an atomic vapor,” *Phys. Rev. Lett.* **99**, 143601 (2007).
- [150] A. B. Matsko, I. Novikova, M. O. Scully, and G. R. Welch, “Radiation trapping in coherent media,” *Phys. Rev. Lett.* **87**, 133601 (2001).
- [151] A. B. Matsko, I. Novikova, and G. R. Welch, “Radiation trapping under conditions of electromagnetically induced transparency,” *J. Mod. Optics* **49**, 367 (2002).
- [152] M. Klein, Y. Xiao, A. V. Gorshkov, M. Hohensee, C. D. Leung, M. R. Browning, D. F. Phillips, I. Novikova, and R. L. Walsworth, in *Advances in Slow and Fast Light*, edited by S. M. Shahriar, P. R. Hemmer, and J. R. Lowell (SPIE, 2008), vol. 6904, p. 69040C.

- [153] P. Kok, W. J. Munro, K. Nemoto, T. C. Ralph, J. P. Dowling, and G. J. Milburn, “Linear optical quantum computing with photonic qubits,” *Rev. Mod. Phys.* **79**, 135 (2007).
- [154] J. Simon, H. Tanji, J. K. Thompson, and V. Vuletić, “Interfacing Collective Atomic Excitations and Single Photons,” *Phys. Rev. Lett.* **98**, 183601 (2007).
- [155] A. L. Alexander, J. J. Longdell, M. J. Sellars, and N. B. Manson, “Photon echoes produced by switching electric fields,” *Phys. Rev. Lett.* **96**, 043602 (2006).
- [156] M. U. Staudt, S. R. Hastings-Simon, M. Nilsson, M. Afzelius, V. Scarani, R. Ricken, H. Suche, W. Sohler, W. Tittel, and N. Gisin, “Fidelity of an optical memory based on stimulated photon echoes,” *Phys. Rev. Lett.* **98**, 113601 (2007).
- [157] A. K. Patnaik, F. L. Kien, and K. Hakuta, “Manipulating the retrieval of stored light pulses,” *Phys. Rev. A* **69**, 035803 (2004).
- [158] C. K. Hong, Z. Y. Ou, and L. Mandel, “Measurement of subpicosecond time intervals between two photons by interference,” *Phys. Rev. Lett.* **59**, 2044 (1987).
- [159] J. Brendel, N. Gisin, W. Tittel, and H. Zbinden, “Pulsed energy-time entangled twin-photon source for quantum communication,” *Phys. Rev. Lett.* **82**, 2594 (1999).
- [160] R. Tucker, P.-C. Ku, and C. Chang-Hasnain, “Slow-light optical buffers: capabilities and fundamental limitations,” *Lightwave Technology, Journal of* **23**, 4046 (2005).
- [161] T. Hong, A. V. Gorshkov, D. Patterson, A. S. Zibrov, J. M. Doyle, M. D. Lukin, and M. G. Prentiss, “Realization of coherent optically dense media via buffer-gas cooling,” *Phys. Rev. A* **79**, 013806 (2009).
- [162] O. Firstenberg, M. Shuker, N. Davidson, and A. Ron, “Elimination of the diffraction of arbitrary images imprinted on slow light,” *Phys. Rev. Lett.* **102**, 043601 (2009).
- [163] N. B. Phillips, A. V. Gorshkov, and I. Novikova, “Slow light propagation and amplification via electromagnetically induced transparency and four-wave mixing in an optically dense atomic vapor,” *J. Mod. Optics* **56**, 1916 (2009).
- [164] E. Arimondo, “Relaxation processes in coherent-population trapping,” *Phys. Rev. A* **54**, 2216 (1996).
- [165] M. Oberst, F. Vewinger, and A. Lvovsky, “Time-resolved probing of the ground state coherence in Rubidium,” *Opt. Lett.* **32**, 1755 (2007).

- [166] M. Shuker, O. Firstenberg, Y. Sagi, A. Ben-kish, N. Davidson, and A. Ron, “Ramsey-like measurement of the decoherence rate between Zeeman sub-levels,” *Phys. Rev. A* **78**, 063818 (2008).
- [167] F. A. Franz and C. Volk, “Spin relaxation of rubidium atoms in sudden and quasimolecular collisions with light-noble-gas atoms,” *Phys. Rev. A* **14**, 1711 (1976).
- [168] S. D. Jenkins, D. N. Matsukevich, T. Chanelière, A. Kuzmich, and T. A. B. Kennedy, “Theory of dark-state polariton collapses and revivals,” *Phys. Rev. A* **73**, 021803 (2006).
- [169] T. Peters, Y.-H. Chen, J.-S. Wang, Y.-W. Lin, and I. A. Yu, “Optimizing the retrieval efficiency of stored light pulses,” *Opt. Express* **17**, 6665 (2009).
- [170] D. N. Matsukevich, T. Chanelière, S. D. Jenkins, S.-Y. Lan, T. A. B. Kennedy, and A. Kuzmich, “Observation of dark state polariton collapses and revivals,” *Phys. Rev. Lett.* **96**, 033601 (2006).
- [171] L. Yang, L. Zhang, Q. Guo, and G. Fu, “The linewidth and contrast of electromagnetically induced transparency in a homogeneously broadened system,” *Journal of Luminescence* **122-123**, 552 (2007).
- [172] M. Boas, *Mathematical Methods in the Physical Sciences* (John Wiley & Sons New York, 1983).

VITA

Nathaniel Blair Phillips

Nathaniel Blair Phillips was born on the nineteenth day of March, 1981 in Lancaster, PA. He attended Hempfield High School in Landisville, Pennsylvania and graduated in 1999. During the same year, he began pursuing a degree in Physics Education at the Pennsylvania State University. After three semesters, he transferred to Millersville University in Millersville, Pennsylvania, from which he received a Bachelor of Arts degree in Physics in 2004 with a magna cum laude distinction.

He entered the College of William and Mary in Williamsburg, Virginia in the Fall of 2004 to pursue a Ph.D. in physics. He received his Master of Science degree in Physics in 2006, and he began working for Dr. Irina Novikova in the Spring of 2007. This dissertation was defended on the twenty-fourth day of June, 2011 in Williamsburg, VA.

SLOW AND STORED LIGHT UNDER CONDITIONS OF ELECTROMAGNETICALLY
INDUCED TRANSPARENCY AND FOUR WAVE MIXING IN AN ATOMIC VAPOR

ABSTRACT PAGE

The recent prospect of efficient, reliable, and secure quantum communication relies on the ability to coherently and reversibly map nonclassical states of light onto long-lived atomic states. A promising technique that accomplishes this employs Electromagnetically Induced Transparency (EIT), in which a strong classical control field modifies the optical properties of a weak signal field in such a way that a previously opaque medium becomes transparent to the signal field. The accompanying steep dispersion in the index of refraction allows for pulses of light to be decelerated, then stored as an atomic excitation, and later retrieved as a photonic mode. This dissertation presents the results of investigations into methods for optimizing the memory efficiency of this process in an ensemble of hot Rb atoms. We have experimentally demonstrated the effectiveness of two protocols for yielding the best memory efficiency possible at a given atomic density. Improving memory efficiency requires operation at higher optical depths, where undesired effects such as four-wave mixing (FWM) become enhanced and can spontaneously produce a new optical mode (Stokes field). We present the results of experimental and theoretical investigations of the FWM-EIT interaction under continuous-wave (cw), slow light, and stored light conditions. In particular, we provide evidence that indicates that while a Stokes field is generated upon retrieval of the signal field, any information originally encoded in a seeded Stokes field is not independently preserved during the storage process. We present a simple model that describes the propagation dynamics and provides an intuitive description of the EIT-FWM process.

NATHANIEL BLAIR PHILLIPS

DEPARTMENT OF PHYSICS

THE COLLEGE OF WILLIAM AND MARY IN VIRGINIA

ASSISTANT PROFESSOR IRINA NOVIKOVA, PHYSICS